VNIVERSITAT DE VALÈNCIA

Beam Loading Effects in Linear Accelerators: Modelization and Implications on the Beam-Dynamics-based Design of a Compact Neutron Source

PROGRAMA DE DOCTORAT EN FÍSICA - 3126

IFIC / DEPARTAMENT DE FÍSICA APLICADA I ELECTROMAGNETISME

PhD dissertation by:

Javier Olivares Herrador

Under the supervision of:

Dr. Andrea Latina

Dra. Nuria Fuster Martínez

Dr. Benito Gimeno Martínez

VALENCIA, JULY 2025

Dr. ANDREA LATINA, Senior Staff at the Beams Department in the European Organization for Nuclear Research (CERN), as DIRECTOR,

Dra. NURIA FUSTER MARTÍNEZ, *Contratada Investigadora con Experiencia Internacional (CDEIGENT)* at *Instituto de Física Corpuscular* (IFIC) in *Consejo Superior de Investigaciones Científicas* (CSIC), as DIRECTOR,

Dr. BENITO GIMENO MARTÍNEZ, Professor at the Applied Physics and Electromagnetism Department in Valencia University and member of IFIC, as TUTOR,

HEREBY CERTIFY:

That the present dissertation, entitled *Beam Loading Effects in Linear Accelerators: Modelization and Implications on the Beam-Dynamics-based Design of a Compact Neutron Source* has been elaborated under their direction and tutorship at CERN, IFIC, and Valencia University by Javier Olivares Herrador, and constitutes his Doctoral Thesis.

Signed:

BENITO RAMON\| GIMENO\| MARTINEZ

Firmado digitalmente por BENITO RAMON\|GIMENO\|MARTINEZ
Fecha: 2025.07.09 18:54:21 +09'00'

Dr. Benito Gimeno Martínez

FUSTER MARTINEZ NURIA - 48409567H

Firmado digitalmente por FUSTER MARTINEZ NURIA - 48409567H
Fecha: 2025.07.09 09:57:29 +02'00'

Dra. Nuria Fuster Martínez

Andrea Latina

Dr. Andrea Latina

Acknowledgements

This document is a product of my work, and reflects the knowledge I have adquired during these last four years. Therefore, my gratitude extends not only to those who have helped me develop these results, but to all of those from whom I was able to learn, expand my knowledge, and engage in discussions.

In first place, I would like to thank my PhD supervisor, Dr. Andrea Latina, for the trust deposited in me, for the patience during the well-needed debugging processes, and for the rigor with which my work has been supervised. I am certain that your guidance has brought me closer to the professional I want to become. My university supervisors, Dra. Nuria Fuster, Dr. Benito Gimeno, and Dr. Daniel Esperante, have also been a crucial part of this process, always open to explore with me new challenges, to support my path, and to offer an analytical and constructive feedback when necessary.

During these years, I have had the opportunity to participate in workshops and discussions with sounded experts in the field: Dr. Alexej Grudiev, Dr. Walter Wuensch, Dr. Roberto Corsini, Dr. Steinar Stapnes, Dr. Avni Aksoy, Dr. Lawrence M. Wroe, and more. Thank you all for your generosity and your invaluable help.

Learning how to deal with uncertainty has been the major achievement of my PhD. This would have been impossible without a solid support network, and I am grateful I had the best: Sara, Pablo, Paula, Laura, Eduardo, Juan Carlos, Marta, María, my CERN and Úbeda *amigos*, thank you very much. Also my psychotherapist Marta has been a crucial support, and for your professionalism and support I am grateful.

Lastly, I have to give credits to my family, especially to my parents and my sister. Not only your hard work brought me here, but your love made me grow. Migue, you have also been crucial: Your attention and support have been invaluable. I really hope to carry this life lesson forever with me.

Resumen

Introducción y objetivos

Esta tesis se enmarca en el contexto de las aplicaciones derivadas del proyecto del Colisionador Lineal Compacto (CLIC), una propuesta de la Organización Europea de la Investigación Nuclear (CERN) para un colisionador electrón-positrón de energías del orden de los tera electron-voltio (TeV). Este estudio ha desarrollado unidades de aceleración de alto gradiente, las cuales son compactas y eficientes energéticamente. Los componentes para constuir dichas unidades, incluyendo las fuentes de radiofrecuencia (RF), están disponibles en la industria y ofrecen una alternativa económica para la fabricación de *linacs* de electrones eficientes y compactos.

El interés por estos aceleradores es creciente debido a la diversidad de aplicaciones científicas, médicas e industriales que ofrecen. Destacan fuentes de fotones como las *Free-Electron-Laser light sources* o las fuentes de rayos X por Scattering Compton inverso; *linacs* medicos para radioterapia tipo FLASH; o fuentes de neutrones compactas.

Las fuentes de neutrones son instalaciones con una amplia oferta de aplicaciones en ciencia de materiales, medicina nuclear, espectroscopía, imagenología, etc. Tradicionalmente, estas fuentes dependían de reactores nucleares, algunos de los cuales están desapareciendo en la actualidad. Por tanto, surge la necesidad de generar neutrones para tales fines, y los aceleradores de partículas poseen dicha capacidad. Distinguimos dos tipos de fuentes de neutrones basadas en aceleradores: Fuentes de espalación, y fuentes compactas.

Las fuentes de espalación son instalaciones eficientes donde las partículas, generalmente protones, son aceleradas a muy altas energías para obtener haces intensos de neutrones ($> 1 \times 10^{16}\,\mathrm{n/s}$). Las fuentes compactas, por su parte, ocupan un es-

pacio más reducido y consumen menor energía, proporcionando un haz de intensidad moderada de hasta $\sim 5 \times 10^{15}\,\mathrm{n/s}$. El panorama actual de fuentes de neutrones basadas en aceleradores compactos muestra como las propuestas más competentes se basan en aceleradores de protones.

Sin embargo, por los motivos presentados anteriormente, la tecnología desarrollada en el contexto de CLIC permitiría desarrollar fuentes de neutrones basada en aceleradores lineales de electrones (*electron linacs*) con flujos de neutrones similares. Así, el primer objetivo de esta tesis es explorar la viabilidad de estos *linacs* de electrones como generadores de neutrones para fuentes compactas.

La tecnología CLIC es de alto gradiente, lo cual entraña varios desafíos desde el punto de vista de la dinámica de haces, en especial, cuando se opera con alta intensidad de haz, como el caso para las fuentes de neutrones. Concretamente, existe un fenómeno, conocido como *Beam Loading*, que compromete el funcionamiento del acelerador. Por tanto, se hace necesario desarrollar un código de simulación que permita reproducir tal efecto y explorar soluciones en estas estructuras de tipo onda viajera (TW). Esto plantea el segundo desafío y objetivo de esta tesis: Modelizar este fenómeno y desarrollar una herramienta que permita analizarlo.

Otro objetivo perseguido ha sido la integración y validación del modelo de *Beam Loading* en el código de tracking RF-Track, que permite transportar partículas de especie arbitraria en aceleradores bajo el efecto de fuerzas externas o auto-inducidas, también conocidas como fenómenos colectivos.

Finalmente, el último objetivo ha sido convenir un diseño preliminar de una fuente de neutrones compacta basada en un acelerador lineal de electrones en banda X; en particular, proporcionar una serie de parámetros de diseño basados en la dinámica de haces que garanticen estabilidad en la operación del *linac*, así como máxima transmisión de electrones y producción de neutrones.

Metodología y resultados

El efecto de *Beam Loading* se define como la reducción del gradiente de aceleración en las cavidades como consecuencia del paso de haz a través de estas, que provoca la excitación del modo fundamental en fase decelerante y, por consiguiente, la pérdida de energía de las partículas del haz. Para entender y modelizar el mismo, ha sido necesario realizar una revisión bibliográfica y formalizar la definición de: la propagación de ondas electromagnéticas (EM) en cavidades aceleradoras, los parámetros

de diseño que definen su funcionamiento, el formalismo de *wakefields* e impedancia que permite describir los efectos colectivos detrimentales que sufre el haz de partículas; y la terminología básica acerca del espacio de fase para describir las propiedades del haz.

Tal y como se demostrará, el fenómeno de *Beam Loading* exhibe una respuesta transitoria. Una descripción rigurosa de este efecto exige, por tanto, asumir que la amplitud de campos electromagnéticos que se propagan en las cavidades disminuye con el tiempo. Para admitir tal comportamiento, se hace necesario describir los campos EM bajo el formalismo fasorial quasi-estático, en virtud del cual, la variación de la amplitud es más lenta que la oscilación de radiofrecuencia. Con esto, se redefinen el gradiente de aceleración, la energía electromagnética almacenada y la potencia disipada por unidad de longitud como se expone en la Tabla 2.

Formalismo fasorial estándar	**Formalismo fasorial quasi-estático**
$\bar{u}(\boldsymbol{r}) \equiv \frac{1}{2}\varepsilon_0 \|\|\tilde{\boldsymbol{E}}(\boldsymbol{r})\|\|^2_{\mathbb{C}^3} + \frac{1}{2}\mu_0 \|\|\tilde{\boldsymbol{H}}(\boldsymbol{r})\|\|^2_{\mathbb{C}^3}$	$\bar{u}(\boldsymbol{r},t) \equiv \frac{1}{2}\varepsilon_0 \|\|\tilde{\boldsymbol{E}}(\boldsymbol{r},t)\|\|^2_{\mathbb{C}^3} + \frac{1}{2}\mu_0 \|\|\tilde{\boldsymbol{H}}(\boldsymbol{r},t)\|\|^2_{\mathbb{C}^3}$
$\bar{P}_{\text{diss}}(z_k) := \frac{1}{2}\int_{V_k} R_s \|\|\tilde{\boldsymbol{H}}_{\tan}(\boldsymbol{r})\|\|^2_{\mathbb{C}^3}\ \mathrm{d}V$	$\bar{P}_{\text{diss}}(z_k,t) \equiv \frac{1}{2}\int_{V_k} R_s \|\|\tilde{\boldsymbol{H}}_{\tan}(\boldsymbol{r},t)\|\|^2_{\mathbb{C}^3}\ \mathrm{d}V$
$G(z_k) = \frac{1}{L}\int_{z_k}^{z_k+L} \|\tilde{E}_z(z)\|\mathrm{d}z$	$G(z_k,t) = \frac{1}{L}\int_{z_k}^{z_k+L} \|\tilde{E}_z(z,t)\|\mathrm{d}z$
$G_{\text{eff}}(z_k) = \frac{1}{L}\int_{z_k}^{z_k+L} \mathrm{Re}\left[\tilde{E}_z(z)\exp\left(j\omega t_q(z)\right)\right]\mathrm{d}z$	$G_{\text{eff}}(z_k,t) = \frac{1}{L}\int_{z_k}^{z_k+L} \mathrm{Re}\left[\tilde{E}_z(z,t)\exp\left(j\omega t_q(z)\right)\right]\mathrm{d}z$

Table 2: Parámetros de diseño en el formalismo quasi-estático.

Tal extensión del formalismo fasorial permite estudiar la conservación de la energía en las cavidades de aceleración y, partiendo del Teorema de Poynting, derivar las siguiente expresiones para la reducción de gradiente en cavidades aceleradoras de onda viajera (TW) y onda estacionaria (SW) respectivamente:

$$-\frac{\partial G(z,t)}{\partial t} = v_g(z)\frac{\partial G(z,t)}{\partial z} + \left(\frac{\partial v_g(z)}{\partial z} - \frac{v_g(z)}{\frac{r}{Q}(z)}\frac{\partial \frac{r}{Q}(z)}{\partial z} + \frac{\omega}{Q(z)}\right)\frac{G(z,t)}{2} + \frac{\omega\frac{r}{Q}(z)\mathcal{T}(z,t)\tilde{I}(z,t)}{2}. \tag{1}$$

$$-\frac{\partial G(z,t)}{\partial t} = \frac{\omega}{2Q(z)}G(z,t) - \frac{\omega}{2Q(z)}G_{\text{end}}(z) + \frac{\omega\frac{r}{Q}(z)\mathcal{T}(z,t)\tilde{I}(z,t)}{2}. \tag{2}$$

Ambas ecuaciones comparten interpretación: El gradiente en una cavidad disminuye en el tiempo como consecuencia de las pérdidas por disipación ohmica (términos exclusivamente dependientes del factor de calidad, Q); de la propagación de potencia a las celdas adyacentes (términos dependientes de la velocidad de grupo, v_g,

en TW); y como consecuencia de la presencia de haz, como refleja el último término de las Ecuaciones (1) y (2), $\frac{\omega \frac{r}{Q} \mathcal{T} \tilde{I}}{2}$.

Este término recoge el efecto del *Beam Loading*, mostrando que hay una reducción en el gradiente que depende de la intensidad promedio del haz, $\tilde{I}$, de la frecuencia de resonancia, ω, y de la *shunt impedance* normalizada, r/Q. Esto implica que el fenómeno de *beam loading* tiene un mayor impacto en estructuras aceleradoras compactas, ya que operan a altas frecuencias y poseen altos valores de $\frac{r}{Q}$ por diseño.

Este modelo ha sido implementado en el código RF-TRACK como un fenómeno colectivo. La implementación se basa en la resolución de las Ecuaciones (1) y (2) mediante diferencias finitas en el dominio del tiempo, cuya estabilidad numérica ha sido debidamente analizada con el método de Von Neummann. Con esto, se puede calcula la fuerza que sufre una partícula como consecuencia de los campos auto-inducidos que intervienen en el efecto de *Beam Loading* como:

$$F_{z,\mathrm{BL}}(z) = -\frac{1}{L_{\mathrm{total}}} \int_{-\infty}^{\infty} \mathrm{d}s \lambda_q(s) w_l(z-s). \tag{3}$$

El wakefield longitudinal, w_l, informa de la variación de momento longitudinal (debidamente normalizada) como consecuencia de la acción de una única partícula del haz. Para calcularlo, se usa la solución de las ecuaciones (1) y (2) para una única partícula, G_{single}, y se aplica la definición:

$$w_l(s) = \frac{c}{e} \int_{-\infty}^{\infty} \mathrm{d}t E_z(ct-s,t), \text{ con } E_z(z,t) = \mathrm{Re}\left[G_{\mathrm{single}}(z,t) e^{j(\omega t - \frac{\omega}{c} z)} \right]. \tag{4}$$

Por cuestiones de eficiencia numérica, los efectos *bunch*-to-*bunch* (de largo alcance) se pueden calcular siguiendo una estrategia diferente que los de corto alcance o intra-*bunch*. Para ello, se asume que dos *bunches* lejanos se ven el uno al otro como una única macropartícula que contiene toda la información en carga y posición del mismo, lo cual permite simplificar la expresión como:

$$\begin{aligned} F_{z,\mathrm{BL}}(t_{\mathrm{part}}) &= -\sum_{i=1}^{N_{\mathrm{bunches}}} \frac{1}{L_{\mathrm{total}}} \int_{-\infty}^{\infty} \mathrm{d}s \lambda_q(s)^{(i)} w_l(ct_{\mathrm{part}} - s) \\ &= \underbrace{-\frac{1}{L_{\mathrm{total}}} \int_{-\infty}^{\infty} \mathrm{d}s \lambda_q(s)^{(j)} w_l(ct_{\mathrm{part}} - s)}_{\text{Corto alcance}} \underbrace{- \frac{1}{L_{\mathrm{total}}} \sum_{i \neq j} q_{\mathrm{bunch}}^{(i)} w_l(ct_{\mathrm{part}} - z_i)}_{\text{Largo alcance}}, \end{aligned} \tag{5}$$

con i el índice del propio *bunch* de la partícula en cuestión, y j el índice sobre el resto de *bunches*.

El desempeño de la herramienta creada ha sido comparado con resultados previos de diversos estudios donde se aborda el *Beam Loading* en aceleradores de onda viajera, tratando de reproducir los mismos. En este punto, se recalca, al menos hasta donde el conocimiento del autor y los supervisores alcanza, la inexistencia de códigos que integren de forma global y autocontenida dicho efecto en TW y SW, y lo incorporen al transporte de partículas. En concreto, los resultados obtenidos muestran que:

- Para el caso de estructuras aceleradoras de onda viajera y haces ultrarelativistas, el módulo desarrollado en RF-Track reproduce con acierto el cálculo de la reducción de gradiente de aceleración que se expone en la Referencia [62] basado en métodos analíticos. Se distinguen dos regímenes de este efecto: El estado transitorio y el estado estacionario; y el tiempo de transición entre uno y otro, determinado por el tiempo de llenado, t_{fill}, es calculado con acierto.

- El transporte de haces bajo este efecto se compara con Placet para el caso del *drive beam* de CLIC, implementado de forma específica en dicho software, donde es únicamente aplicable a estructuras pasivas, i.e sin campo eléctrico de aceleración externo. Aquí, la herramienta de *Beam Loading* calcula, con una desviación inferior al 1%, la pérdida de energía relativa del haz, y por tanto la capacidad de extracción de energía a las cavidades primarias de CLIC, que es del 90%.

- El cálculo de la función *wakefield* longitudinal es preciso, como muestra la comparación frente a GdFidl para el caso de las estructuras aceleradoras de CLIC alimentadas por klystrons. El cálculo del *wakefield* en GdFidl involucra la computación de campos EM tridimensionales, lo cual tomó $16\,\text{días}$ en un servidor de 32 nodos. Por su parte, RF-Track y su modelo monodimensional para el cálculo del wake fundamental, se demoraron segundos, lo cual pone en valor dos aspectos: Uno, el dinamismo que esta herramienta ofrece en el diseño y optimización de cavidades teniendo en cuenta dicho efecto de forma inmediata sobre el transporte de partículas; y dos, la versatilidad de la herramienta, que además de transporte, puede calcular en cuestión de segundos una estimación bastante precisa del *wakefield* longitudinal para estructuras SW y TW.

Además, desde el punto computacional, se presentan los mecanismos de compensación del *Beam Loading* tanto en estructuras TW como SW, y se implementan los mismos en el módulo de RF-Track. Estos se basan en el estudio de las condiciones iniciales y de contorno de las Ecuaciones (1) y (2). Para el caso de SW, la compensación se produce al inyectar el haz en el acelerador mientras el gradiente de RF se está cons-

truyendo, para que la dinámica de construcción y de deceleración auto-inducida se compensen. Para el caso TW, la idea es similar, pero también hay que modular convenientemente la forma del pulso de RF que alimenta la cavidad. Aprovechando la interfaz de RF-TRACK en OCTAVE, se muestran varios casos de optimización de la forma del pulso de alimentación de cavidades de banda X, consiguiendo la cancelación de este efecto para trenes de carga constante y una cancelación de hasta el 60% para haces con carga diferente *bunch*-to-*bunch*.

Para constatar la validez del modelo en SW, en particular en el régimen no-ultrarelativista, ha sido necesario acudir a resultados experimentales llevados a cabo en CLEAR, el acelerador lineal de electrones del CERN destinado a investigación y desarrollo de tecnologías aceleradoras. La línea particular donde se han realizado los experimentos que se exponen en esta tesis consta de un fotocátodo de Cs_2Te y una primera cavidad SW de banda S, que junto con un solenoide focalizador, constituyen el inyector, al cual siguen tres estructuras TW, también de banda S, que aceleran el haz hasta $200\,\mathrm{MeV}$. A lo largo de la línea, se integran diversos cuadrupolos de focalización, pantallas y monitores de posición, y un espectrómetro de masas, llamado VESPER, que mide la energía del haz.

Para llevar a cabo las campañas experimentales, ha sido necesario, en primer lugar, calibrar las estructuras aceleradoras, lo que permite cuantificar con precisión el gradiente de ace-leración de las estructuras y, por ende, cuánto gradiente de aceleración se pierde por efecto de *Beam Loading*. Tanto para el inyector como para las estructuras TW, la metodología seguida ha sido la misma: Basados en los campos calculados en SUPERFISH, cortesía de Dr. Avni Aksoy, se ha simulado el transporte de un único *bunch* de baja carga (donde el *Beam Loading* es despreciable) con RF-TRACK. Para varios valores de máximo campo eléctrico, $E_z^{\max}$ y fase de RF, φ, se calcula la ganancia de energía de dicho *bunch*, $F(E_z^{\max}, \varphi)$. Para varios valores de φ, se calcula la ganancia de energía de dicho *bunch*, tanto al final del inyector como en VESPER, y los datos experimentales se ajustan, mediante el método de Gauss-Newton, a la curva F para determinar el valor de $E_z^{\max}$ óptimo.

Esto permite establecer la operación del inyector en la fase que mayor acuerdo con la curva F proporciona, $\varphi_{\text{gun}} = 200\,\mathrm{deg}$, y en la fase que maximiza la ganancia de energía para las estructuras TW. En esta condiciones, se han hecho pasar haces de número variable de *bunches* ($N_{\text{bunches}} = 1 - 150$) y carga por *bunch*, q_{bunch}, variable; y se han medido la disminución de voltaje de aceleración en el inyector, así como la ganancia de energía en VESPER.

En ambos casos, se constata una pérdida de voltaje de aceleración, o equivalentemente energía, que es proporcional a la intensidad del haz, cuantificada por el número de *bunches* o la carga por *bunch*. Los resultados experimentales y el código de RF-TRACK se comparan en la Tabla 3, donde se muestran las pendientes de las regresiones lineales de los datos para cada caso, la desviación relativa de ambos valores, y el coeficiente lineal de regresión.

Case (y,x)	m_{exp} **[keV/pC]**	$m_{\text{RF-Track}}$ **[keV/pC]**	δ_m	r^2
$(\mathcal{E}_{\text{loss, BL}}\ ,\ q_{\text{bunch}})$	0.56 ± 0.03	0.577 ± 0.024	$3.4\,\%$	> 0.99
$(\mathcal{E}_{\text{loss, BL}}\ ,\ N_{\text{bunches}})$	-	-	-	0.98
$(\langle\mathcal{E}\rangle\ ,\ q_{\text{bunch}})$	-22.5 ± 2.4	-23.67 ± 0.17	$5.2\,\%$	> 0.98
$(\mathcal{E}_{\text{range}}\ ,\ q_{\text{bunch}})$	42 ± 5	44.8 ± 0.3	$5.9\,\%$	> 0.99

Table 3: Indicadores estadísticos de concordancia simulación-experimento.

Estos permiten validar la adecuación del modelo desarrollado, fundamentalmente para las medidas correspondientes al inyector. No obstante, se recalca que los resultados, mostrados con mayor detalle en el Capítulo 4, se encuadran dentro del rango de validez de causalidad de los *wakefields*: Se encuentra que el *wakefield* originado por un electrón en la cola del bunch no afecta a electrones situados por delante de él.

Tras un estudio exhaustivo del fenómeno de *Beam Loading* y su implementación en el código RF-TRACK, el Capítulo 5 explora las posibilidades y el desempeño de los aceleradores lineales de electrones como generadores de neutrones de fuentes compactas.

Para producir neutrones a partir de electrones, el mejor proceso es la espalación. Esta se consigue al hacer incidir electrones frente a un material de alto número atómico, lo cual genera rayos X y gamma por Bremsstrahlung. Estos fotones crea, entre otras, neutrones como producto de una serie de reacciones nucleares que acontecen en cadena en un rango de energías de entre algunos MeV hasta los GeV. Para estudiar la producción de neutrones con haces de electrones, se hace necesario emplear un código de simulación MonteCarlo que simule estos procesos nucleares, en este caso, G4BEAMLINE.

El primer resultado obtenido, en lo que a la producción de neutrones refiere, son las dimensiones óptimas de un blanco de tungsteno para maximizar el *yield*, definido como el número de neutrones producido por electrón incidente. El blanco óptimo posee $40\,\text{mm}$ de radio y $80\,\text{mm}$ de largo. También se analizan la distribución angu-

lar de los neutrones emitidos, así como su espectro energético, y se concluye: que el espectro de energías es Maxwelliano, con pico en $\sim 0.5\,\mathrm{MeV}$; y que la emisión es mayor en direcciones traseras, es decir, en la región del espacio donde el vector posición del electrón incidente y el vector posición del neutrón emergente forman un ángulo superior a $90\,\mathrm{deg}$.

Para estudiar el desempeño de fuentes de neutrones, la principal magnitud que se compara es la fuerza de fuente, definida como la intensidad de neutrones emergente del blanco en todas las direcciones del espacio. Esta cantidad depende tanto del *yield* como de la intensidad de electrones que incide sobre el blanco. Por tanto, además de la optimización del blanco de tungsteno, se hace necesario producir neutrones a partir de un acelerador de electrones con suficiente intensidad. La solución a esta necesidad la encontramos en el contexto de CLIC, donde se han desarrollado *linacs* de electrones de tecnología resistiva, compactos, y de operación pulsada, lo cual es beneficioso para la mayoría de aplicaciones de ciencia de neutrones mencionadas anteriormente.

En particular, se han estudiado y optimizado dos posibles aceleradores lineales de electrones: El *linac* del *drive beam* de CTF3 (Instalación de Prueba de CLIC-3), y el Inyector Pulsado de alta Corriente (HPCI, del inglés *High-Pulse-Current-Injector*). Ambos operan en alta intensidad, aunque presentan diferencias en compacidad y en esquema de inyección.

Por un lado, el *linac* de *drive beam* de CTF3 consiste en una pistola termoiónica seguida de estructuras de aceleración TW en banda S. Este *linac* operó entre 2004 y 2016, y probó su operación con hasta $2.33\,\mathrm{nC/bunch}$. Por otro lado, HPCI consta de un fotoinyector en banda S seguido de varias estructuras TW de banda X. Es un diseño más compacto con diveras aplicaciones médicas e industriales. Haciendo uso de ambas propuestas y el blanco de tungsteno previamente optimizado, se han estudiado las limitaciones y desafíos en la operación de estos *linacs* a alta intensidad, así como la fuerza de fuente y la eficiencia energética.

La producción de neutrones se beneficia de máxima intensidad. Sin embargo, esta carga por *bunch* que un *linac* puede tolerar está limitada, entre otras, por el *Beam Loading*. Cuando este límite se alcanza, toda la energía EM almacenada en la cavidad es consumida por el haz e invertida en su aceleración. Esto, aunque provoca pérdidas notables en el gradiente de aceleración, conlleva un aumento de la eficiencia de transferencia de energía RF-haz, $\eta_{\text{RF-beam}}$. Para CTF3, la operación en estas condiciones ya fue demostrada, llegando a una carga por *bunch* de $2.33\,\mathrm{nC}$, 2100 *bunches* por

tren, y $\eta_{\text{RF-beam,av}} = 90\%$. Para HPCI, el módulo desarrollado en RF-TRACK permite optimizar el pulso de RF, compensar el *Beam Loading*, y maximizar la carga hasta $600\,\text{pC/bunch}$ en banda X; todo ello con una eficiencia $\eta_{\text{RF-beam,av}} = 88\%$, con una distancia *bunch*-to-*bunch* de $100\,\text{mm}$, y con trenes de hasta 1000 *bunches*.

Otro desafío que presenta la operación a alta intensidad es la deposición de calor en el blanco, ya que se puede producir dilatación térmica hasta sobrepasar el umbral elástico. Cuando la deformación es inelástica, se producen rupturas irreversibles en el blanco. En particular, para el tungsteno, dicho límite de deposición de energía se encuentra en $35.1\,\text{J/g}$. Para no sobrepasar dicho umbral, se ha conducido un estudio de deposición de energía con G4BEAMLINE, revelando que, para haces de electrones de hasta $500\,\text{MeV}$ con la carga por *bunch* anteriormente convenida, existe un límite inferior en el tamaño transversal del haz de $0.4\,\text{mm}$ para el caso de HPCI y $3.5\,\text{mm}$ para CTF3.

Un diseño que satisfaga estas restricciones tanto en carga como en focalización es plausible, tal y como mostrará el capítulo 6. En esas condiciones, se ha estudiado la fuerza de fuente de ambas propuestas con energía variable entre $20\,\text{MeV}$ y $500\,\text{MeV}$. Se encuentra que las fuentes propuestas ofrecen flujos comparables a otras basadas en aceleradores de protones y electrones, siendo la mayor producción para el caso en que el *drive beam linac* de CTF3 opera con $500\,\text{MeV}$, produciendo hasta $1.51 \times 10^{15}\,\text{n/s}$. Además, en el rango de potencias de haz de $0.57\,\text{kW}$ hasta $245\,\text{kW}$, las fuentes propuestas exhiben mayor producción de neutrones que los diseños e instalaciones presentes en el panorama actual, como se comprueba en la Figura 1.

La Figura 1 muestra que la producción de neutrones viene condicionada por la potencia de haz, lo cual depende, a su vez, de cuanta energía se esté dispuesto a consumir. Donde realmente se encuentra una ventaja en el uso de *linacs* de electrones para la producción de neutrones es en la eficiencia energética, es decir, en cuantos Julios de energía son necesarios para producir un neutrón. Esto lo cuantifica la energía consumida por neutrón producido, E_{pn}.

Para estimar la eficiencia, se ha realizado un estudio donde se han tenido en cuenta: la eficiencia RF-haz dada por el *Beam Loading*; las especificaciones de los klystrons, compresores de pulsos, y divisores de potencia; la frecuencia de ciclo de los distintos *linacs*, así como la intensidad y la longitud de pulso de RF. Con todo, se han encontrado valores preliminares de E_{pn} de hasta $5.65 \times 10^{-10}\,\text{J/n}$ para el HPCI-linac, y $E_{\text{pn}} = 6.76 \times 10^{-10}\,\text{J/n}$ para CTF3 *drive beam linac*, una década por debajo de los valores de otras fuentes compactas. Sólo se encuentran más eficientes las fuentes de

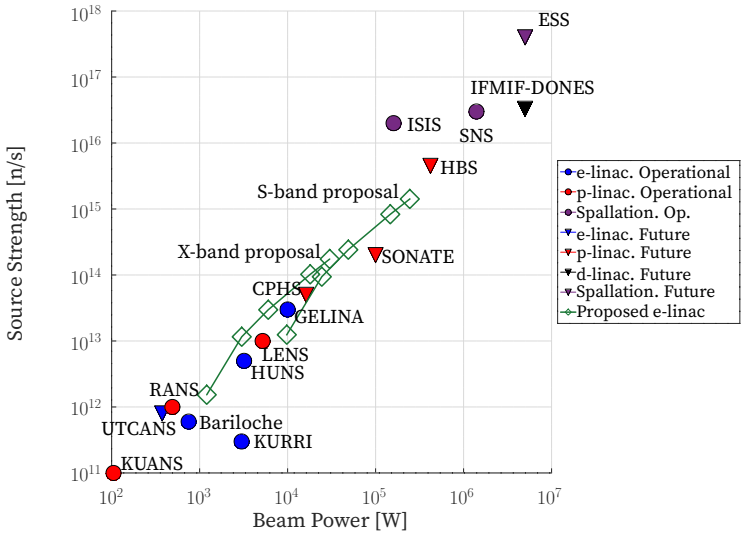

Figure 1: Comparación de la fuerza de fuente frente a la potencia de haz para distintas fuentes de neutrones del panorama actual.

espalación de protones, donde la ventaja proviene del blanco y los procesos nucleares más que en la tecnología aceleradora.

Esto permite convenir que, para aplicaciones que requieran flujos intermedios ($<$ 10^{16} n/s), las fuentes de neutrones basadas en aceleradores lineales de electrones son una alternativa más compacta, más eficiente, y, por lo tanto, competente.

El último aspecto que presenta el Capítulo 5 es un diseño preliminar de un ensamblaje blanco-moderador para producción de neutrones con aplicaciones en espectrografía e imagenología. Tales prácticas requiren del uso de neutrones de energías del orden de los meV. Para ello, se estudian dos esquemas de moderación: uno térmico, consistente en una cubierta de polietileno, y otro frío, donde la cubierta es de hidrógeno líquido.

Con tales ensamblajes, se exploran las figuras de mérito que permiten comparar fuentes entre sí, la *brightness* promedio y pico. Se halla que las fuentes de neutrones - basadas en los aceleradores de electrones anteriormente presentados - poseen la capacidad de producir espectros con *brightness* comparable a los diseños más prometedores de fuentes compactas. No obstante, tal conclusión queda supeditada a mejoras en el material moderador para neutrones fríos, y otros desafíos del ensamblaje desde el punto de vista mecánico.

Desde el punto de vista de la dinámica de haces, los límites en focalización dados por la deposición de calor son plausibles, pero este punto evidencia la necesidad de estudiar detenidamente la dinámica y el transporte de haces intensos en dichos aceleradores, a fin de garantizar una operación estable, máxima transmisión, y una focalización controlada. Esto fue demostrado en CTF3 durante su periodo de operación, pero no para el caso de la tecnología de banda X. Por tanto, en el capítulo 6, se analizan los desafíos de la operación del *linac* HPCI con altas intensidades.

Para ello, la metodología empleada ha sido, por un lado, simulaciones de transporte con RF-TRACK, prestando especial atención a los fenómenos: de *space charge*, especialmente relevante a bajas energías; de *Beam Loading*, gracias al módulo desarrollado; y a los *wakefields* de corto alcance, dados por el formalismo de Karl Bane. Por otro lado, se ha realizado una revisión bibliográfica de los fenómenos colectivos dependientes de la intensidad que comprometen la estabilidad transversal del haz. En particular, se ha prestado especial atención al fenómeno de *Single-bunch Beam Breakup Instability* (BBU) en presencia de aceleración, así como a estrategias para su mitigación.

En primer lugar, para el inyector en banda S, se optimizan los parámetros del láser, la cavidad aceleradora, y el solenoide para *bunches* de $500\,\mathrm{pC}$, $550\,\mathrm{pC}$ y $600\,\mathrm{pC}$. La optimización revela que los tamaños de haz, así como la emitancia, crecen con la carga. El inconveniente de altas cargas por *bunch* viene dado por las dimensiones de las estructuras de aceleración TW en banda X, que en este caso, poseen una diámetro modulado de $4.6\,\mathrm{mm}$ a $3.0\,\mathrm{mm}$, lo cual impone una limitación estricta en el máximo tamaño permitido.

Esto da pie al segundo resultado: el diseño y la optimización de una línea de aceleración de electrones hasta $500\,\mathrm{MeV}$. La fenomenología anteriormente explicada res-tringe el estudio a cargas por *bunch* de $550\,\mathrm{pC}$. Los grados de libertad para esta optimización son las fases de RF de las estructuras aceleradoras, ϕ_{RF}, así como la fuerza de los cuadrupolos de focalización, k; y el resultado muestra como una aceleración fuera de cresta, esto es, $\phi_{\mathrm{RF}} \neq 0$, permite transportar, sin pérdidas, el haz de 1000 *bunches* hasta una energía de $509\,\mathrm{MeV}$ (es decir, una potencia de $28\,\mathrm{kW}$), y focalizarlo en el blanco con $\sigma_x \simeq \sigma_y \simeq 0.78\,\mathrm{mm}$.

Conviene resaltar que, la función objetivo en el proceso de optimización, además de maximizar la potencia de haz incidente en el blanco, garantizar la condición $|\sigma_x - \sigma_y| < 0.1\,\mathrm{mm}$, y minimizar las pérdidas para el caso de un haz centrado en la cavidad; exigía el cumplimiento de tales condiciones para fluctuaciones de hasta el 5% en el

offset inicial del haz tanto en posición como en momento.

Como resultado, el diseño presenta una tolerancia de hasta el 7% en fluctuación en la posición inicial del haz, es decir, tales desviaciones se traducen en una pérdida de potencia de haz inferiores al 1%. Complementariamente, se ha realizado un estudio de sensibilidad a desalineamientos en los componentes del *linac*, es decir, las cavidades de aceleración TW y los cuadrupolos. Se encuentra que, desviaciones rms de $100\,\mu\mathrm{m}$ - razonables desde el punto de vista de la puesta en servicio - no inducen pérdidas y producen un descentramiento mínimo del haz en el blanco que no afecta a la producción de neutrones.

Finalmente, se han repetido simulaciones de G4BEAMLINE para reproducir la producción de neutrones con el haz emergente del diseño anterior. El *yield* encontrado es de $(4.53\pm0.02)\cdot10^{-1}$ n/e, lo que repercute en una intensidad de fuente de $(1.56\pm0.07)\cdot10^{14}$ n/s, con una disposición espacial y espectro en energías similar al mencionado anteriormente. Se comprueba satisfactoriamente que no se alcanza el umbral de deposición de energía, y que el valor de energía consumida por neutrón producido es de $(8.57 \pm 0.03) \cdot 10^{-10}$ J/n, siendo una alternativa compacta y más eficiente desde el punto de vista del consumo energético que las fuentes de neutrones compactas del panorama mencionadas anteriormente.

Conclusiones

La necesidad de alcanzar altas energías en aceleradores de partículas ha ocasionado el desarrollo de nuevas tecnologías. Un ejemplo particular son las estructuras resisitivas de alto gradiente en banda X desarrolladas por la colaboración de CLIC. La compacidad y eficiencia energética de estas estructuras las convierten en candidatas para futuros *linacs* de investigación, precursores de fuentes de rayos X compactas por IBS, o fuentes de neutrones. En concreto, esta tesis se ha enfocado en esta última aplicación, donde se requiren altas intensidades de haz. En estas condiciones, aparecen fenómenos de *Beam Loading*, y una reducción de gradiente, dependiente de la intensidad, decelera el haz como consecuencia de la interacción del mismo con la geometría que lo circunda.

El primer objetivo de esta tesis, abordado en los capítulos 2-4, es la implementación de un módulo de *Beam Loading* en el código RF-TRACK. Para conseguir esto, se ha derivado un modelo de difusión de potencia basado en el Teorema de Poynting, válido para estructuras TW y SW. Además, como este efecto exhibe una re-

spuesta transitoria, las figuras de mérito que describen el funcionamiento de los aceleradores han sido reformuladas en el marco de la aproximación quasi-estática. Esto limita la validez del modelo desarrollado a escenarios donde el decaimiento en amplitud de los campos EM es notoriamente inferior a la oscilación armónica de los mismos.

Del modelo difusivo se extrae una Ecuación en Derivadas Parciales (EDP), que se resuelve con un esquema de diferencias finitas en paso de avance y cuya estabilidad numérica ha sido estudiada. La solución a la misma se interpreta como el gradiente del armónico de Floquet, l^*, del modo fundamental TM_{01}, cuya propagación se sincroniza con el vuelo de la partícula en la cavidad. A raíz de esta interpretación, se calcula el *wakefield* longitudinal correspodiente a la excitación del modo fundamental, permitiendo reproducir los efectos que se derivan de este en el corto y largo alcance. Para esta última, se asume una interacción *bunch*-partícula, lo cual circunscribe la validez de los cálculos a situaciones donde la forma de los *bunches* esté bien definida y no se solapen.

La validez del modelo desarrollado ha sido comprobada mediante comparaciones con resultados teóricos previos para el caso de estructuras TW y haces ultrarelativistas, mostrando gran acierto en la reproducción de la respuesta transitoria y estacionaria. Además, el transporte de partículas bajo la influencia de este efecto ha sido comparado con el código PLACET para el caso particular de los CLIC-PETS, encontrándose que RF-TRACK reproduce el coeficiente de extracción de potencia, magnitud altamente dependiente del fenómeno de BL, con una desviación inferior al 1%. Además, se han realizado comprobaciones del cálculo de la función *wakefield* longitudinal, correspondiente al modo fundamental: Para el caso de las estructuras CLIC-K, se reproduce con precisión los resultados de GDFIDL en menor tiempo de computación.

La validez del módulo para estructuras SW también se ha contrastado con medidas experimentales del fenómeno de *Beam Loading* en el acelerador de electrones CLEAR del CERN. Se encuentra que RF-TRACK reproduce, con desviaciones de hasta el 5.9%, la dependencia con la carga de la pérdida de energía al final de la línea de aceleración y la dependencia con la carga del voltage de aceleración de la primera cavidad inyectora.

El resultado de este estudio, avalado por las comprobaciones, es una herramienta flexible que permite considerar el *Beam Loading* para haces multi-especie, con cargas arbitrarias; a la vez que implementar esquemas que permitan su compensación. Esto

abre la puerta a nuevos diseños de aceleradores donde este fenómeno es relevante y esta herramienta ha sido empleada, como en fuentes de positrones para futuros colisionadores (FCC-ee o CLIC), fuentes de rayos-X por efecto ICS, o la optimización de la secciones *ring-to-main-linac* de CLIC.

El segundo objetivo de la tesis ha sido abordado en el capítulo 5, donde se muestra que los aceleradores lineales resistivos de alto gradiente son buenos candidatos como precursores de fuentes de neutrones compactas. Un estudio extensivo de simulaciones con G4BEAMLINE muestra que las dimensiones óptimas que maximizan la producción de neutrones de un blanco de tungsteno son $L = 80\,\mathrm{mm}$ and $r = 40\,\mathrm{mm}$. Haciendo uso del mismo, se comprueba el desempeño del *linac* de *drive beam* de CTF3, en banda S; y el *linac* HPCI, en banda X; como precursores de tales fuentes. Se encuentra que aumentar la carga por *bunch* hasta llegar al *full beam loading* maximiza la emisión de neutrones hasta $1.51 \times 10^{15}\,\mathrm{n/s}$, así como la eficiencia RF-haz hasta el 91%.

La comparación con el estado del arte muestra que las fuentes basadas en aceleradores de electrones son, en general, igual de compactas y más eficientes que las fuentes basadas en protones o deuterones, lo que las convierte en alternativas valiosas para escenarios de producción moderada de neutrones, como las aplicaciones médicas e industriales. En particular, sin moderación, la fuente propuesta, cuyos neutrones son mayormente del orden de los MeV, podría servir mayormente para estudios de irradiación en componentes electrónicos.

Para otras aplicaciones industriales y médicas en las que se requiera moderación, se ha propuesto un diseño preliminar de un conjunto moderador-objetivo que demuestra que puede alcanzar valores de *brightness* comparables a los diseños de fuentes compactas más avanzados. Sin embargo, los trabajos futuros deberán centrarse en el diseño mecánico de dicho conjunto, así como en una comprensión más profunda de los moderadores fríos que podría dar lugar a valores de *peak brightness* más elevados para una aplicación específica de neutrones.

Finalmente, en el capítulo 6, se analizan los desafíos en la operación estable de haces de alta intensidad para la producción de neutrones con el HPCI *linac*. Se presenta el diseño de una línea de aceleración y se ofrecen parámetros basados en la dinámica de haces, la cual restringe la carga por *bunch* a $550\,\mathrm{pC}$ y el espaciado entre *bunches* a $100\,\mathrm{mm/c}$. El diseño resultante exhibe una tolerancia a la fluctuación en la posición inicial del haz de hasta un 7%, lo que significa que desviaciones por debajo de este umbral conllevan pérdidas inferiores al 1%. De forma complementaria, se ha estudiado

la sensibilidad a desalineamientos de las estructuras TW y cuadrupolos, asegurando un 100% de transmisión para desalineamientos de $100\,\mu\mathrm{m}$ en media cuadrática. Tal *linac* produciría $I_n = (1.56 \pm 0.07) \cdot 10^{14}$ n/s y consumiría una energía por neutrón de $E_{\mathrm{pn}} = (8.57 \pm 0.03) \cdot 10^{-10}$ J/n, lo cual lo convierte en una alternativa eficiente y compacta para producir neutrones para fines médicos e industriales, como los que se muestran en la Figura 2.

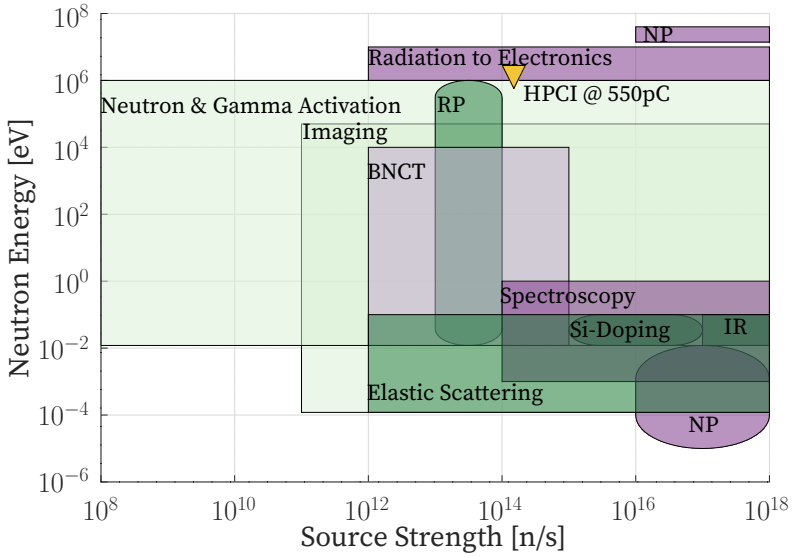

Figure 2: Diagrama de aplicaciones de neutrones con el desempeño del *linac* HPCI a $@550\,\mathrm{pC/bunch}$. El acrónimo BNCT refiere a Terapia por Captura de Neutrones, NP refiere a Investigación en Física Nuclear, RP a Producción de Radioisótopos, e IR a Experimentos de Irradiación.

Abstract

The need to achieve high energies in particle accelerators has led to the development of new accelerator technologies, being one particular example the high-gradient, normal-conducting accelerating structures, developed within the Compact Linear Collider (CLIC) collaboration. These can serve for diverse industrial and medical applications, like compact neutron sources. For this case, high beam intensities are required, and charge-dependent collective effects, in particular beam loading effects, arise, compromising the accelerator performance. This establishes the necessity of reliable tracking codes that can take this effect into account, and sets the two objectives for this thesis: To model the Beam Loading effect in linear accelerator, implementing this in the tracking code RF-Track; and to assess the impact of this effect in beam dynamics of an electron linac based on CLIC accelerating structures that could serve for neutron production.

The first objective is addressed in chapters 2, 3 and 4. First, the figures of merit accounting for accelerator performance, the wakefield formalism, and the quasi-static assumption is re-visited to then, derive a power-diffusive model. This model, which is obtained starting from the Poynting theorem, leads to a Partial Differential Equation (PDE) which considers Beam Loading Effects in travelling- and standing- wave structures. Its resolution is implemented in the tracking code RF-Track, which allows to account for this effect in the short- and long-range for arbitrarely charged and multi-species beams, and to study compensation algorithms based on the initial and boundary conditions of the derived PDE. The performance of the designed tool is successfully benchmarked against: other theoretical results for beam-induced EM field calculation, the Placet tracking code for energy-extraction efficiency calculations, and the Electro Magnetic (EM) solver GdFidl for longitudinal wakefield calculations of the fundamental accelerating mode. The evaluation of the developed module is completed by comparison against experimental measurements carried out

in the CLEAR facility at European Organization for Nuclear Research (CERN), where it is found that RF-Track reproduces accurately the charge-dependent energy loss due to Beam Loading effects.

In chapter 5, a G4beamline study is carried out to optimize a tungsten target for neutron production. The optimal target exhibits maximal backward neutron production with a Maxwellian neutron spectrum with peak energy in the order of the MeV. This allows the assessment of the performance of two high-gradient normal-conducting compact linacs as drivers for compact neutron sources: The CLIC Test Facility 3 (CTF3) drive-beam linac, and the High-Pulse-Current-Injector (HPCI) linac. The full beam loading regime is explored for maximum neutron production and RF-to-beam efficiency, and safe thresholds in the transverse size are proposed to prevent target malfunctioning. When compared to the state of the art, it is found that these sources are, in general, equally compact and more energy-efficient than proton-based compact sources, making them valuable alternatives for moderate neutron production scenarios, like medical and industrial applications.

Finally, in chapter 6, a beam-dynamics based design of an X-band linear accelerator for neutron production is presented. A set of beamline element parameters is obtained as a result of an optimization process aiming for: maximal beam power at the target, full transmission, and safe transversal focusing at the target. The resulting design minimizes the impact of space-charge, beam loading, and the single bunch breakup instability, showing solid stability against initial beam offset jitter and element misalignments. This linac would drive neutron generation for a source with a strength of $I_n = (1.56 \pm 0.07) \cdot 10^{14}$ n/s and an energy per neutron produced of $E_{\text{pn}} = (8.57 \pm 0.03) \cdot 10^{-10}$ J/n, being a compact, energy-efficient source with a wide variety of potential medical and industrial applications.

⋆ ⋆ ⋆ ⋆ ⋆

La necesidad de alcanzar altas energías en los aceleradores de partículas ha llevado al desarrollo de nuevas tecnologías de aceleración, siendo un ejemplo concreto las estructuras aceleradoras resistivas de alto gradiente desarrolladas en el marco de la colaboración del Colisionador Lineal Compacto (CLIC). Estas pueden servir para diversas aplicaciones industriales y médicas, como las fuentes compactas de neutrones. En este caso, se requieren intensidades de haz elevadas y surgen efectos colectivos dependientes de la carga, en particular efectos de *Beam Loading*, que comprometen el rendimiento del acelerador. Esto establece la necesidad de códigos de transporte fiables que puedan tener en cuenta este efecto, y fija los dos objetivos de esta tesis:

Modelizar el efecto *Beam Loading* en aceleradores lineales e implementarlo en el código de transporte RF-Track; y evaluar el impacto de este efecto en la dinámica de haces de un linac de electrones basado en estructuras aceleradoras CLIC que sirva para la producción de neutrones.

El primer objetivo se aborda en los capítulos 2, 3 y 4. Primeramente, se revisan las figuras de mérito que describen el funcionamiento de los aceleradores, el formalismo de *wakefields* y la hipótesis cuasiestática para, después, derivar un modelo de difusión de potencia. Este modelo, a obtenido del Teorema de Poynting, conduce a una Ecuación en Derivadas Parciales (EDP) que considera el efecto de *Beam Loading* en estructuras de onda viajera y estacionaria. Su resolución se implementa en el código de transporte RF-Track, y permite considerar este efecto en el corto y largo alcance para haces arbitrariamente cargados y multi-especies; así como estrategias para la compensación de este efecto basadas en las condiciones iniciales y de contorno de la EDP. El desempeño del módulo diseñado se ha contrastado satisfactoriamente con: otros estudios teóricos para el cálculo de campos electromagnéticos (EM) auto-inducidos por el haz, el código de transporte Placet par el cálculo del coeficiente de extracción energética, y el *solvers* EM GdFidl para el cálculo de la función *wakefield* longitudinal asociada al modo de aceleración fundamental. La evaluación del desempeño del módulo se ha completado con el contraste frente a medidas experimentales en el acelerador CLEAR de la Organización Europea de la Investigación Nuclear (CERN). Se encuentra que RF-Track reproduce con adecuación la pérdida de energía dependiente de la carga que surge como consecuencia del fenómeno de *Beam Loading*.

En el capítulo 5, se lleva a cabo un estudio con G4beamline para optimizar un blanco de tungsteno para la producción de neutrones. El blanco óptimo posee máxima producción en la dirección trasera, y el espectro de energía posee energía pico del orden de los MeV. Con esto, se evalúa el rendimiento de dos *linacs* compactos, resistivos, y de alto gradiente como precursores de fuentes compactas de neutrones: El *drive beam linac* de la Infraestructura de Prueba de CLIC 3 (CTF3), y el *linac* inyector de pulsos de alta corriente (HPCI). Presentamos un estudio exhaustivo de la condición de *full Beam Loading*, así como una discusión acerca del tamaño mínimo de haz, en el eje transversal, para evitar rupturas indeseadas del blanco. Cuando se comparan con el panorama actual, se encuentra que las fuentes propuestas son, en general, igual de compactas y más eficientes energéticamente que las fuentes basadas en protones, lo que las convierte en opciones competentes para la producción de neutrones con flujos intermedios para aplicaciones médicas e industriales.

Por último, en el capítulo 6, se presenta un diseño de un acelerador lineal de banda X para la producción de neutrones. Para los distintos elementos de la línea de aceleración, se ofrece una serie de parámetros como resultado de un proceso de optimización cuyos objetivos han sido: maximizar la potencia de haz en el blanco, transmisión total, y un tamaño de haz por encima del umbral convenido. El diseño resultante minimiza el impacto del *space-charge, beam loading* y la inestabilidad *Single Bunch Breakup*, y muestra una sólida estabilidad frente a la fluctuación inicial del haz y los desajustes de los elementos. El *linac* resultante podría producir neutrones con una fuerza de fuente de $I_n = (1.56 \pm 0.07) \cdot 10^{14}$ n/s y una energía consumida por neutrón producida de $E_{\text{pn}} = (8.57 \pm 0.03) \cdot 10^{-10}$ J/n, siendo una fuente compacta, eficiente energéticamente, y con una amplia variedad de aplicaciones potenciales en medicina e industria.

⋆ ⋆ ⋆ ⋆ ⋆

La necessitat d'aconseguir altes energies en els acceleradors de partícules ha portat al desenvolupament de noves tecnologies d'acceleració, sent un exemple concret les estructures acceleradores resistives d'alt gradient desenrotllades en el marc de la col·laboració del Colisionador Lineal Compacte (CLIC). Estes poden servir per a diverses aplicacions industrials i mèdiques, com les fonts compactes de neutrons. En este cas, es requerixen intensitats de feix elevades i sorgixen efectes col·lectius dependents de la càrrega, en particular efectes de *Beam Loading*, que comprometen el rendiment de l'accelerador. Això establix la necessitat de codis de transport fiables que puguen tindre en compte este efecte, i fixa els dos objectius d'esta tesi: Modelitzar l'efecte *Beam Loading* en acceleradors lineals i implementar-lo en el codi de transport RF-Track; i avaluar l'impacte d'este efecte en la dinàmica de feixos d'un *linac* d'electrons basat en estructures acceleradores CLIC que servisca per a la producció de neutrons.

El primer objectiu s'aborda en els capítols 2, 3 i 4. Primerament, es revisen les figures de mèrit que descriuen el funcionament dels acceleradors, el formalisme de *wakefields* i la hipòtesi cuasiestática per a, després, derivar un model de difusió de potència. Este model, obtingut del Teorema de Poynting, conduïx a una Equació en Derivades Parcials (EDP) que considera l'efecte de *Beam Loading* en estructures d'ona viatgera i estacionària. La seua resolució s'implementa en el codi de transport RF-Track, i permet considerar este efecte en el curt i llarg abast per a fas arbitràriament carregats i multi-espècies; així com estratègies per a la compensació d'este efecte basades en les condicions inicials i de contorn de l'EDP. L'acompliment del mòdul dissenyat s'ha

contrastat satisfactòriament amb: altres estudis teòrics per al càlcul de camps electromagnètics (EM) acte-induïts pel feix, el codi de transport PLACET parell el càlcul del coeficient d'extracció energètica, i el *solvers* EM GDFIDL per al càlcul de la funció *wakefield* longitudinal associada al mode d'acceleració fonamental. L'avaluació de l'acompliment del mòdul s'ha completat amb el contrast enfront de mesures experimentals en l'accelerador CLEAR de l'Organització Europea de la Investigació Nuclear (CERN). Es troba que RF-TRACK reproduïx amb adequació la pèrdua d'energia dependent de la càrrega que sorgix a conseqüència del fenomen de *Beam Loading*.

En el capítol 5, es du a terme un estudi amb G4BEAMLINE per a optimitzar un blanc de tungsté per a la producció de neutrons. El blanc òptim posseïx màxima producció en la direcció posterior, i l'espectre d'energia posseïx energia pic de l'orde dels MeV. Amb això, s'avalua el rendiment de dos *linacs* compactes, resistius, i d'alt gradient com a precursors de fonts compactes de neutrons: El *drive beam linac* de la Infraestructura de Prova de CLIC 3 (CTF3), i el *linac* injector de polsos d'alt corrent (HPCI). Presentem un estudi exhaustiu de la condició de *full Beam Loading*, així com una discussió sobre la grandària mínima de feix, en l'eix transversal, per a evitar ruptures indesitjades del blanc. Quan es comparen amb el panorama actual, es troba que les fonts proposades són, en general, igual de compactes i més eficients energèticament que les fonts basades en protons, la qual cosa les convertix en opcions competents per a la producció de neutrons amb fluxos intermedis per a aplicacions mèdiques i industrials.

Finalment, en el capítol 6, es presenta un disseny d'un accelerador lineal de banda X per a la producció de neutrons. Per als diferents elements de la línia d'acceleració, s'oferix una sèrie de paràmetres com a resultat d'un procés d'optimització els objectius de la qual han sigut: maximitzar la potència de feix en el blanc, transmissió total, i una grandària de feix per damunt del llindar convingut. El disseny resultant minimitza l'impacte del *space-charge, beam loading* i la inestabilitat *Single Bunch Breakup*, i mostra una sòlida estabilitat enfront de la fluctuació inicial del feix i els desajustaments dels elements. El *linac* resultant podria produir neutrons amb una força de font de $I_n = (1.56 \pm 0.07) \cdot 10^{14}$ n/s i una energia consumida per neutró produïda de $E_{\mathrm{pn}} = (8.57 \pm 0.03) \cdot 10^{-10}$ J/n, sent una font compacta, eficient energèticament, i amb una àmplia varietat d'aplicacions potencials en medicina i indústria.

Contents

1. Introduction

The present PhD dissertation addresses the beam dynamics challenges in the simulation of high-gradient linear accelerators which suffer from the Beam Loading (BL) effect, and explores their feasibility as drivers for a compact neutron sources. Accordingly, this introductory chapter presents the context of nowadays compact linear accelerators and their applications, as well as the state-of-the-art in neutron production. Finally, this chapter concludes with the motivation and the outline of the thesis.

1.1 Accelerating technology and its applications

Particle accelerators are devices designed to impart kinetic energy to charged particles beams. The first experiment towards a Radiofrequency (RF) Linear Accelerator (linac) was done in 1928 by R. Wideroe [1], who accelerated a group of potassium ions to 50 Kilo electron-volt (keV) in a system of drift tubes in an evacuated glass cylinder.

In parallel to Wideroe's advancements, around 1930, Lawrence built the first cyclotron, achieving particle acceleration along a curved trajectory for the first time [2]. Then, the synchrotron [3], the betatron [4] and the Alvarez linac were invented. By 1950, protons and electrons had been accelerated to a kinetic energy of some 300 Mega electron-volt (MeV) [5]. The chronological evolution of accelerating technology and the energies achieved over the last 70 years is shown in Fig. 1.1.

Nuclear Physics and High Energy Particle Physics have motivated the design and construction of particle colliders based on accelerators that target a center of mass energy as high as possible, as seen in Fig. 1.1. The latest proposals for future particle colliders are the Future Circular Collider (FCC) [6], the Compact Linear Collider (CLIC) [7], the International Linear Collider (ILC) [8], and the Muon Collider [9], as seen in Fig. 1.1.

This need for higher energies imposed tighter requirements on particle accelerators, such as compactness, energy efficiency, and higher beam quality - since achieving and controlling high-energy beams requires low emittance and small energy spread to ensure precise focusing and stable operation. Thanks to these advancements, particle accelerators became increasingly relevant devices for industrial and medical applications, extending beyond fundamental research.

Some examples of this are X-ray and gamma sources (*light sources*) such as the European X-Ray Free-Electron Laser Facility (XFEL) [10], which are based on the undulation of electrons accelerated in a superconducting linac; radiotherapy accelerators for cancer treatments such as Turning Linac for Proton Therapy (TULIP) [11], which is based on a proton linac; and spallation neutron sources, such as the European Spallation Source (ESS) [12].

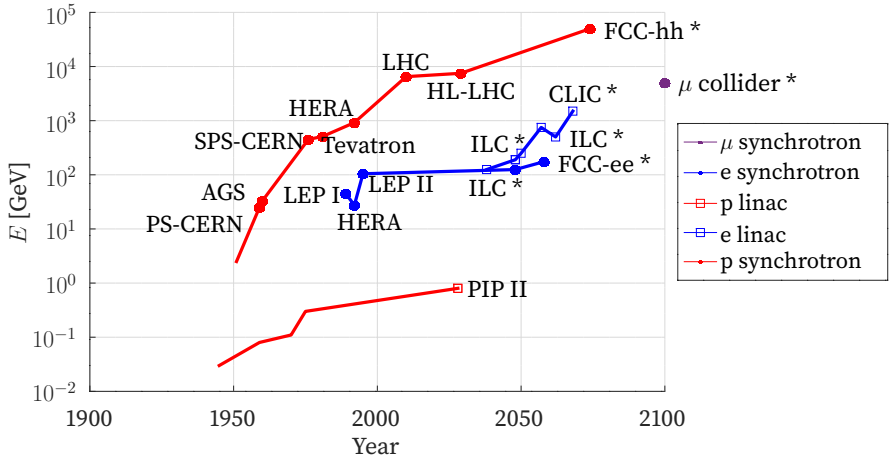

Figure 1.1: Chronological evolution of the maximal energy reached by particles accelerators in the latest century [5]. The facilities marked with a star (*) are under design but their comissioning is pending final approval.

1.1.1 Linear accelerators

Radiofrequency Linear Accelerators are devices in which particles move along a linear path and are accelerated by RF fields. These fields allow achieving high energies by repeating acceleration through steps in energy which, individually, are much smaller than the final energy reached [13].

Linacs are versatile devices which can provide high-intensity beams and/or high-quality beams, that is, beams whose bunches present small sizes and low energy

spread. Other advantages of these machines are the absence of losses due to synchrotron radiation and the avoidance of errors resulting from the beam passing through the same elements multiple times, as it traverses the accelerator in a single pass.

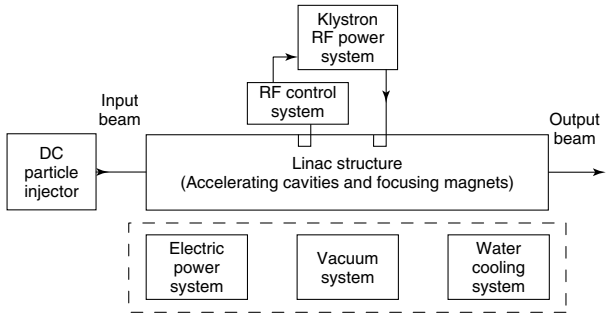

Figure 1.2: Simplified linac layout. Figure extracted from [14].

A schematic of a linac is shown in Fig. 1.2. The main components of these devices are:

- **Accelerating structures**, which are periodic structures where Electromagnetic (EM) fields are confined so that they transfer energy to the beam.

- **Focusing magnets**, which are electromagnetic devices which use current-carrying coils to generate magnetic fields. These elements compress the beam, providing a focusing effect and increasing the quality of the beam.

- **External RF-power tubes**, which feed the accelerating structures. For the considered designs through the document, the RF fields exciting the accelerating cavities are produced by klystrons. These are high-power microwave generators which are based on the amplification of the signal left in the klystron cavity by an initial electron bunch.

- **Electric power, vacuum and water cooling systems** which control the hardware performance.

- **RF control system and beam instrumentation**, which allows monitoring the properties of the beam and the basic set of parameters of the machine to control and ensure the general functionality of the accelerator.

High-gradient normal-conducting linear accelerating technology

Greater energies are expected from particle accelerators, resulting in the need to develop new accelerating techniques such as superconducting cavities [15], plasma-wakefield acceleration [16] or high-gradient normal-conducting technology. Here, we focus our work on the last one.

The most recent developments in normal-conducting accelerating technology have been achieved in the context of CLIC, an international collaboration of 32 countries that has studied a Multi-TeV linear collider. It has been shown that normal conducting technology can achieve gradients of up to $150\,\mathrm{MeV/m}$ [17] by reducing surface field geometries, utilising alternative materials [18] and choosing the right frequency band, depending on the application. Table 1.1 shows the common frequency ranges for linac operation.

Frequency range	216 - 450 MHz	1 - 2 GHz	2 - 4 GHz	4 - 8 GHz	8 - 12 GHz
Microwave band	P-band	L-band	S-band	C-band	X-band

Table 1.1: Most extended bands for RF accelerators [19].

The high accelerating gradients that characterise X-band technology translate into compactness, thus decreasing the footprint of the accelerator. However, its Technology Readiness Level (TRL) is inferior to conventional L- and S-band technology, as its supporting RF and mechanical technologies are less mature for large-scale use, facing still some engineering challenges. For this reason, one of the missions of the European Organization for Nuclear Research (CERN) in recent years has been to increase the TRL of X-band technology, developing highly efficient X-band klystrons [20] or designing and manufacturing new prototypes [21].

Applications

Linac applications can be subdivided into three major categories: fundamental research in Nuclear Physics and High-Energy Particle Physics, medical applications, and industrial applications.

Linacs for elementary particle physics research. Proposals for a future electron and positron linear collider such as CLIC [7] or ILC [8] are under study in international collaborations to bring electrons and positrons up to several TeVs. In particular, linear technology minimizes synchrotron radiation losses for light particles, while

single-beam-passage reduces cumulative beam degradations.

Another feature of interest is their strong focusing capabilities, which translate into high beam quality, necessary for a high luminosity [22]. This figure of merit, which is proportional to the number of collisions per second taking place, characterizes the performance of a collider.

In addition, when it comes to complementary colliders based on synchrotron accelerators, linacs play an important role as injectors in the early stages. Examples of these are LINAC4 [23], the first stage in acceleration for protons in the Large Hadron Collider (LHC) [24], and injectors under design for projects such as FCC-ee [25].

Linacs for medical purposes More than 10,000 electron linacs are currently used worldwide to treat patients with cancer [26]. The basis of this treatment is energy deposition of particles as they spread through human tissue, thus leading to the death of tumoral cells. Depending on the tumor requirements, several therapies can be found based on different accelerated particles such as electrons [27], protons [28] or carbon ions [29].

Linacs for industrial purposes Non-destructing material testing and microscopy experiments require photon sources with high average photon flux density. To serve these means, linear accelerators can perform as photon drivers in Free Electron Laser (FEL), such as the European XFEL [10], or Inverse Compton Scattering (ICS) sources, like the one presented in Ref [30]. Both installations make use of an electron linac, and photons are obtained from the accelerated electron bunches by backscattering processes in ICS sources or with undulator magnets in FELs. Beyond microscopy experiments, electron and light sources find many applications in fuel gas purification, wastewater treatment, and sludge hygienization.

Further industrial applications of electron linacs concern food sterilization via electron irradiation, non-destructive testing, non-destructive art-pieces and cargo inspection, and neutron production.

1.2 Accelerator-based neutron production

Since the late 1950s, research nuclear reactors built in numerous laboratories and universities have been used as neutron sources. These particles offer a wide range

of applications in diverse areas, including material science, nuclear medicine, spectroscopy, and imaging [31].

Reactor-based neutron sources plan to shut down soon primarily due to the fear of reactor-related incidents [32]. Therefore, there remains a need to supply high-intensity neutron beams, and accelerator-driven neutron sources have been constructed in the recent years to support and develop neutron activities.

In particular, two different types of accelerator-based neutron sources can be found: Spallation sources and Compact Accelerator-based Neutron Sources (CANS).

- **Spallation sources:** In the spallation process, protons are accelerated to very high energies to collide against a high atomic number material such as lead or mercury, producing neutrons among many other particles. Compared to reactors, these are 100 times more efficient [31], but they require expensive accelerators as protons have to reach hundreds of MeVs.

- **Compact accelerator-based neutron sources:** Compact accelerator-based neutron sources can rely on both electron or proton linacs. Proton-based machines produce neutrons via dedicated and controlled nuclear reactions such as the ^{7}Li(p,n)^{7}Be [33]. Electron-based machines rely on electron-induced spallation, where *Bremmstrahlung* photons are created which then induce photonuclear reactions. Further details will be discussed in Chapter 5.

  CANS have become highly competitive with existing medium flux fission or spallation-based sources. Since they cover a more moderated energy range, shielding issues are minimized and the emergent neutron spectrum can be more efficiently utilized. In this sense, these compact sources follow a *produce what you need* philosophy [34]. In addition, CANS are compact facilities that require less instrumentation and scale better at laboratory sizes.

The characteristics of some CANS and spallation sources can be found in Appendix A.1, and the highlights from this recapitulation are shown in Fig. 1.3.

1.3 Motivation and outline of the thesis

In the context of an uprising demand for neutron sources and increasing interest in Compact Accelerator-based Neutron Sources, this thesis explores the performance of normal-conducting compact electron linacs as drivers for neutron sources, aiming

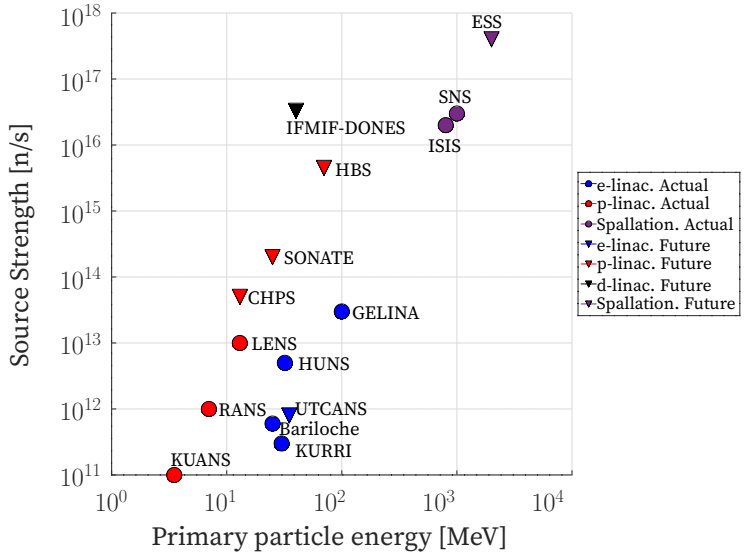

Figure 1.3: Source strength vs primary particle energy. Data from Tab. A.1 and [12, 35, 36, 37, 38, 39, 40, 41, 42, 43].

to present a beam-dynamics-based design of an X-band electron linac for neutron production.

To design an intense neutron source, the driver must provide an intense electron beam as well. In this scenario, charge-dependent collective effects are predominant, limiting the performance of the proposed source. One crucial phenomenon is the Beam Loading Effect, which effectively reduces the accelerating gradient of the structures. For this reason, Chapters 2-4 present a model to account for this effect and its implementation into the particle tracking code RF-TRACK, which will be used for the mentioned beam-dynamics based design.

In particular, Chapter 2 presents an overview of beam dynamics concepts to understand EM mode propagation in accelerating structures, the wakefield formulation of collective effects and the beam description in the phase- and trace-space. Chapter 3 presents the theoretical formulation of the BL effect in Travelling-wave (TW) and Standing-wave (SW), and shows the numerical implementation of this effect in RF-TRACK's tracking routine.

The performance of the developed tool is assessed by benchmark against other computational codes for TW structures, in Chapter 3, and against experimental measurements for both TW and SW structures in Chapter 4. Accordingly, this chapter intro-

duces the CERN Linear Electron Accelerator for Research (CLEAR) facility at CERN, and presents the methodology and results to perform BL measurements in this facility.

Chapter 5 examines neutron production with electron beams. An optimized tungsten target is presented for maximal neutron production, and two electron linac (S-band and X-band) are then evaluated as drivers of such target and compared with the state-of-the-art of accelerator-based neutron sources. In addition, a preliminary design of a target-moderator assembly for imaging applications is proposed.

Finally, Chapter 6 presents a beam-dynamics based design of a normal conducting, high intensity X-band linac for neutron production, where Beam Loading effects are of significant importance for compactness and energy-efficiency considerations. In addition, space charge effects and short range wakefield effects are considered to discuss static and dynamic imperfections, leading to a stable design whose neutron production is reported and compared with respect to the state-of-the-art.

2. Overview of electrodynamics and accelerator physics concepts

Linacs accelerate charged particles with electromagnetic fields by means of the Lorentz force:

$$\boldsymbol{F} = q(\boldsymbol{E} + \boldsymbol{v} \times \boldsymbol{B}), \tag{2.1}$$

with q being the charge of the considered particle, $\boldsymbol{v}$ its velocity and $\boldsymbol{E}$ and $\boldsymbol{B}$ the electric and magnetic fields acting upon it. Therefore, understanding the behavior of charged particles in accelerators requires a rigorous description of the EM fields affecting them as well as the physical observables which describe their evolution in the so-called phase space. The aim of this chapter is to introduce these concepts. This is a compilation of results from references [14, 44, 45, 46].

2.1 Beam phase space description

In accelerators, particles travel in large groups called *bunches*. Usual bunch populations range from $N = 10^9$ to 10^{11} particles. For each particle, namely i ($1 \leq i \leq N$), its possible states can be described by three position coordinates $(x_i, y_i, z_i) \in \mathbb{R}^3$, in units of mm, and three kinetic momenta coordinates $(p_x, p_y, p_z) \in \mathbb{R}^3$, in units of $\mathrm{MeV/c}$. Therefore, the description of such an ensemble requires $6N$ variables, which seems unpractical.

Given that N is a large quantity, bunches can be treated as continuous distributions characterized by a 6-dimensional *phase-space density*, Ψ [47]. For the chosen parametrization, (x, y, z, p_x, p_y, p_z)[1], Ψ has units of $\mathrm{mm^{-3}MeV^{-3}c^3}$. The domain

[1]Different sets of coordinates to describe the phase-space are reported in Refs [46, 48]. In particular, we emphasize the difference between the kinetic momentum, $p = \gamma m \beta c$, with the canonical momentum, $P = p + qA$, with A the corresponding EM vector potential. This last one is used when the

where this density function is defined is called *phase space*, in this case, the subset of $\mathbb{R}^6$ where all the possible descriptions of the particles in the bunch are enclosed. Ψ verifies the normalizing condition:

$$N = \int_{\mathbb{R}^3}\int_{\mathbb{R}^3} \Psi(\boldsymbol{r},\boldsymbol{p})\, \mathrm{d}^3\boldsymbol{r}\, \mathrm{d}^3\boldsymbol{p}. \tag{2.2}$$

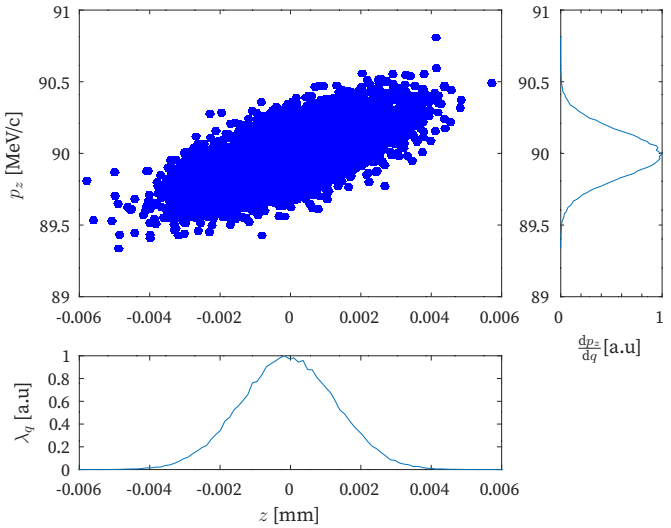

Figure 2.1: Longitudinal phase-space of an arbitrary bunch as the projection of the 6D phase-space over the coordinates (z, p_z). This bunch is characterized by $\langle p_z\rangle = 90\,\mathrm{MeV/c}$, $\sigma_\mathcal{E}/\mathcal{E} = 0.01$, $\langle z\rangle = 0$ and $\sigma_z = 1$ mm.

The definition of Ψ allows an statistical treatment of the bunch properties. Some quantities of interest that will be used through the document are:

$$\text{Volumetric charge density} \quad \rho(\boldsymbol{r}) \equiv \int_{\mathbb{R}^3} \Psi(\boldsymbol{r},\boldsymbol{p}) q(\boldsymbol{r},\boldsymbol{p})\, \mathrm{d}^3\boldsymbol{p} \qquad [\mathrm{C/m^3}] \tag{2.3}$$

$$\text{Linear charge density} \quad \lambda_q(z) \equiv \int_{\mathbb{R}}\int_{\mathbb{R}} \rho(x,y,z)\, \mathrm{d}x\, \mathrm{d}y \qquad [\mathrm{C/m}] \tag{2.4}$$

$$\text{Average bunch energy} \quad \langle\mathcal{E}\rangle \equiv \frac{1}{N}\int_{\mathbb{R}^3}\int_{\mathbb{R}^3} \Psi(\boldsymbol{r},\boldsymbol{p})\mathcal{E}(\boldsymbol{r},\boldsymbol{p})\, \mathrm{d}^3\boldsymbol{r}\, \mathrm{d}^3\boldsymbol{p} \qquad [\mathrm{MeV}] \tag{2.5}$$

$$\text{Bunch energy spread} \quad \sigma_\mathcal{E} \equiv \frac{1}{N}\sqrt{\int_{\mathbb{R}^3}\int_{\mathbb{R}^3} \Psi(\boldsymbol{r},\boldsymbol{p})(\mathcal{E}(\boldsymbol{r},\boldsymbol{p}) - \langle\mathcal{E}\rangle)^2\, \mathrm{d}^3\boldsymbol{r}\, \mathrm{d}^3\boldsymbol{p}}, \qquad [\mathrm{MeV}] \tag{2.6}$$

dynamics of the system are described in the EM Hamiltonian formalism.

$$\text{Longitudinal mean position} \quad \langle z \rangle \equiv \frac{1}{N} \int_{\mathbb{R}^3} \int_{\mathbb{R}^3} \Psi(\boldsymbol{r}, \boldsymbol{p}) z \, \mathrm{d}^3\boldsymbol{r} \, \mathrm{d}^3\boldsymbol{p} \quad [\mathrm{mm}] \tag{2.7}$$

$$\text{Longitudinal bunch size} \quad \sigma_z \equiv \frac{1}{N} \sqrt{\int_{\mathbb{R}^3} \int_{\mathbb{R}^3} \Psi(\boldsymbol{r}, \boldsymbol{p}) (z - \langle z \rangle)^2 \, \mathrm{d}^3\boldsymbol{r} \, \mathrm{d}^3\boldsymbol{p}}, \quad [\mathrm{mm}] \tag{2.8}$$

where q is the charge of each particle and $\mathcal{E}$ its total energy, which depends on its total kinetic momentum, $p = \sqrt{p_x^2 + p_y^2 + p_z^2}$, and rest mass, m_0, as $\mathcal{E} = \sqrt{(pc)^2 + (m_0 c)^2}$.

The prior definitions referred to the *longitudinal phase space* (z, p_z). The projection of the phase space over the coordinates (x, p_x, y, p_y) is called *transverse phase space*. Statistical quantities such as $\langle x \rangle$, $\langle y \rangle$, σ_x, σ_y, $\langle p_x \rangle$, $\langle p_y \rangle$, σ_{p_x}, and σ_{p_y}; can be defined by analogy with Eqs. (2.6) and (2.7). For ultrarelativistic bunches, the conjugated momenta are usually replaced by x' and y', defined as:

$$x' \equiv \frac{\mathrm{d}x}{\mathrm{d}s} = \frac{\mathrm{d}x}{\mathrm{d}t} \frac{\mathrm{d}t}{\mathrm{d}z} = \frac{p_x}{p_z} \simeq \frac{p_x}{p}, \tag{2.9}$$

$$y' \equiv \frac{\mathrm{d}y}{\mathrm{d}s} = \frac{\mathrm{d}y}{\mathrm{d}t} \frac{\mathrm{d}t}{\mathrm{d}z} = \frac{p_y}{p_z} \simeq \frac{p_y}{p}. \tag{2.10}$$

The study of the transverse properties of the beam is usually carried out in the *trace space* (x, x',y, y'). For simplicity, we consider only the (u, u') space in what follows, with $u = x, y$.

The *beam emittance*, ϵ_u, is defined as the area covered by the beam in the trace space divided by π [49]:

$$\epsilon_u = \frac{\text{Area trace space}}{\pi} = \frac{1}{\pi} \int \int \mathrm{d}u \mathrm{d}u'. \tag{2.11}$$

In practice, the emittance, which informs of the transverse beam quality, is defined in terms of the variances of the bunch as:

$$\epsilon_u = \sqrt{\langle u^2 \rangle \langle u'^2 \rangle - \langle u u' \rangle}. \tag{2.12}$$

According to the Liouville theorem, as long as all forces acting upon the system are conservative, the density of particles in the phase-space is preserved. From this result, the preservation of the phase-space volume can be derived [48]. From Eq. (2.10), assuming phase-space volume conservation, one obtains:

$$\text{Area phase space} = (\gamma m \beta c) * \text{Area trace space}, \tag{2.13}$$

where $\gamma = \mathcal{E}/m_0 c^2$ and $\beta = \sqrt{1 - \gamma^{-2}}$.

The implications of this equation manifest when the beam is accelerated adiabatically. In this case, the phase-space area remains almost constant, which forces trace-space area to diminish. To compare emittance values in different steps of acceleration, the *normalized emittance,* $\bar{\epsilon}_u$, is defined as:

$$\bar{\epsilon}_u \equiv \gamma\beta\epsilon_u. \tag{2.14}$$

The normalized emittance thus represents the transverse beam emittance corrected for relativistic effects. It remains invariant under acceleration in the absence of non-conservative forces and therefore provides a consistent measure of the intrinsic beam quality. This invariance makes $\bar{\epsilon}_u$ especially useful for comparing beam properties across different energies or accelerator stages.

2.2 Electromagnetic RF fields in lossless accelerating structures

Harmonic EM fields can be described in the phasorial formalism as [44]:

$$\boldsymbol{E}(\boldsymbol{r},t) = \text{Re}\left[\tilde{\boldsymbol{E}}(\boldsymbol{r})e^{j\omega t}\right], \tag{2.15}$$

$$\boldsymbol{B}(\boldsymbol{r},t) = \text{Re}\left[\tilde{\boldsymbol{B}}(\boldsymbol{r})e^{j\omega t}\right], \tag{2.16}$$

with $f = \omega/(2\pi)$ the excitation RF frequency, $j = \sqrt{-1}$ the complex imaginary unit, and $\tilde{\boldsymbol{E}},\ \tilde{\boldsymbol{B}}$ complex vectors called *phasors,* refering to the electric and magnetic field respectively.

This complex notation allows for a compact reformulation of the Maxwell's equations in free space, where the volumetric charge density, ρ, and the current density $\boldsymbol{J}$, are set to zero:

$$\begin{aligned} \boldsymbol{\nabla}\times\tilde{\boldsymbol{E}}(\boldsymbol{r}) &= -j\omega\tilde{\boldsymbol{B}}(\boldsymbol{r}) \qquad \boldsymbol{\nabla}\cdot\tilde{\boldsymbol{E}}(\boldsymbol{r}) = 0, \\ \boldsymbol{\nabla}\times\tilde{\boldsymbol{B}}(\boldsymbol{r}) &= +j\mu_0\varepsilon_0\omega\tilde{\boldsymbol{E}}(\boldsymbol{r}) \quad \boldsymbol{\nabla}\cdot\tilde{\boldsymbol{B}}(\boldsymbol{r}) = 0, \end{aligned} \tag{2.17}$$

with ε_0 the electric permittivity and μ_0 the magnetic permeability. When Eqs. (5.32) are combined, one gets that these fields are described by a Helmholtz wave equation:

$$(\boldsymbol{\nabla}^2 + \mu_0\varepsilon_0\omega^2)\tilde{\boldsymbol{E}}(\boldsymbol{r}) = 0, \qquad (\boldsymbol{\nabla}^2 + \mu_0\varepsilon_0\omega^2)\tilde{\boldsymbol{B}}(\boldsymbol{r}) = 0 \tag{2.18}$$

Accelerating structures, as an approximation, are cylindrical-symmetric conducting structures where a sinusoidal signal excites EM fields that propagate inside of it. The geometrical design of the cavity imposes different boundary conditions to Eq. (2.18),

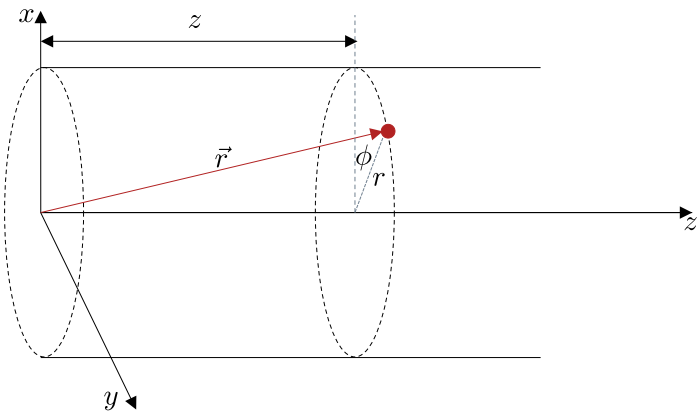

Figure 2.2: Cylindrical coordinates for the expression of the EM fields in an accelerating cavity.

which translate into different field shapes. Two sounded cases that will be analyzed in this section are the Travelling-wave structure and Standing-wave structure.

The starting point for the derivation of the EM field in both types of cavities is to consider a cylindrical waveguide where the electric field satisfies the following shape: $\tilde{\boldsymbol{E}}(\boldsymbol{r}) = \tilde{\boldsymbol{E}}(r,\phi)e^{\pm jk_z z}$, with k_z the wavenumber and (r,ϕ,z) the cylindrical coordinates as illustrated in Fig. 2.2.

The substitution of this ansatz into Eq. (2.18) leads to a complete set of solutions whose derivation and results can be consulted in [14, 45]. In particular, we will focus our attention on the Transverse Mode (TM), which exhibits a non-negligible longitudinal electric field given by:

$$\tilde{E}_z(r,\phi,z) = \sum_{n,m} \tilde{E}_{z_{n,m}}(r,\phi,z) = \sum_{n,m} A_{n,m} J_n(\kappa_{n,m} r)\cos(m\phi)e^{-jk_{z_{n,m}}z+j\varphi}, \tag{2.19}$$

where:

- $n \geq 0$, $m \geq 1$ are integers describing the different TM modes propagating along the structure.
- $A_{n,m} \in \mathbb{R}$ is the amplitude of the n,m mode.
- $\varphi \in [0, 2\pi)$ is the phase of the field at $t = 0$.
- J_n is the n-th Bessel function.

- $\kappa_{n,m}$ follows the characteristic relationship $\kappa_{n,m}^2 = \mu_0\varepsilon_0\omega^2 - k_z^2$. [2]

From this last point, several features regarding the propagation of the electric fields in the waveguide can be understood:

1. Only a discrete set of propagating modes (n, m) is able to travel through the structure. The wave number $k_{z_{n,m}}$ of each one is given by the following relationship, provided that the cavity is empty:

$$k_{z_{n,m}}^2 = \mu_0\varepsilon_0\omega^2 - \frac{\chi_{n,m}^2}{(d/2)^2} = \frac{\omega^2}{c^2} - \frac{\chi_{n,m}^2}{(d/2)^2} = \frac{1}{c^2}\left(\omega^2 - \frac{\chi_{n,m}^2}{(d/2)^2}c^2\right). \tag{2.20}$$

2. There is a cut off frequency $\omega_c := \min_{n,m} \frac{\chi_{n,m}}{(d/2)}c$, below which there can not be any propagating mode.

3. The phase velocity of any mode (n, m) is greater than the speed of light in vacuum, as it can be seen from its definition:

$$v_{\text{phase}_{n,m}} := \frac{\omega}{k_{z_{n,m}}} = c\frac{1}{\sqrt{1 - \left(\frac{\omega(d/2)}{c\chi_{n,m}}\right)^2}} > c. \tag{2.21}$$

2.2.1 Field propagation in Travelling-wave structures

Travelling-wave structures are designed such that the longitudinal electric field propagates as a travelling-wave whose phase velocity matches the particle's velocity. This is achieved by periodically loading the cylindrical waveguide with discs of a given aperture called *irises*. The irises form a set of connected sub-cavities called *cells*, whose length will be denoted as L. An example of this structure is shown in Fig. 2.3a.

For the non-periodical case, the fundamental mode (TM_{01}), that is, the mode in Eq. (2.19) given by $m = 0$ and $n = 1$, reads as:

$$\tilde{E}_z(r, z) = A_0 J_0(\kappa_{01} r)e^{-jk_{z01}z + j\varphi} \tag{2.22}$$

In the periodical case, the Floquet theorem states that, for a given mode of an infinite periodic structure, the fields at two different adjacent cells differ only by a constant

[2] Note that, in order to satisfy the boundary conditions at the ends of the waveguide, $J_n(\kappa_{n,m}d/2) = 0$ (here d stands for the cavity diameter). Therefore, the value of $\kappa_{n,m}$ is fixed and equals to $\kappa_{n,m} = \frac{\chi_{n,m}}{d/2}$, where $\chi_{n,m}$ is the m-th zero of the n-th Bessel function.

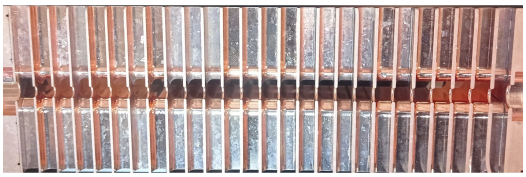

(a) X-band travelling wave structure sectional cut.

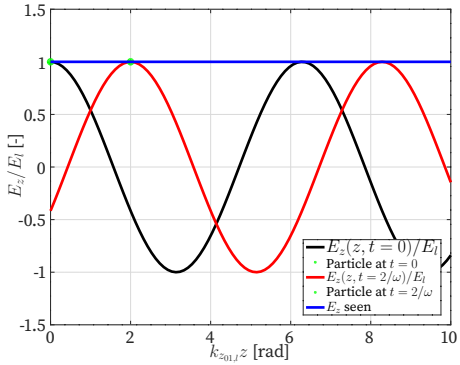

(b) Floquet mode of the on-z-axis longitudinal electric field with $v_{\text{phase}_{0,l}} \simeq c$ at different times and synchronization with the flight of a particle (in green).

Figure 2.3: Travelling-wave geometry and longitudinal electric field.

factor, which is in general a complex number. Such complex number corresponds to $\exp(-jk_{z01}L)$ [14]. In these terms, the longitudinal electric field phasor has to fulfill the following conditions:

$$\tilde{E}_z(\boldsymbol{r}) = \tilde{F}_z(r,z)e^{jk_{z01}z} \tag{2.23}$$

$$\text{with } \tilde{F}(r,z+L) = e^{-jk_{z01}L}\tilde{F}(r,z). \tag{2.24}$$

The phase advance, ϕ_{ad}, defined as:

$$\phi_{\text{ad}} = k_{z01}L, \tag{2.25}$$

gives the phase change in radians, when the field flows from a cell to the next. A structure is a travelling wave structure if $\phi_{\text{ad}} \in (\frac{\pi}{2}, \pi)$.

Since $\tilde{F}$ is periodic, it can be expanded in Fourier series, leading to the following expression [14, 45]:

$$\tilde{F}(r,z) = \sum_{l=-\infty}^{l=+\infty} a_l A_0 J_0(\kappa_l r) e^{\left(-j\frac{2\pi lz}{L}+j\varphi\right)}, \tag{2.26}$$

where a_l are the modal complex amplitudes that refer to the new modes introduced by the Floquet theorem and $\kappa_l^2 = (\omega/c)^2 - (k_{z01} + 2\pi l/L)^2$. Thereby, the TM_{01} accelerating mode is now degenerated and can be understood as the superposition of

several Floquet modes:

$$\tilde{E_z}(r,z) = \tilde{F}(r,z)e^{-jk_{z_{01}}z} = \sum_{l=-\infty}^{l=+\infty} a_l A_0 J_0(\kappa_l r) e^{\left(-j\frac{2\pi l z}{L} - jk_{z_{01}}z + j\varphi\right)}. \tag{2.27}$$

As it can be seen, each of the travelling wave propagating modes exhibits a different wave number $k_{01,l} = k_{01} + \frac{2\pi l}{L}$, which leads to a phase velocity, v_{phase_l}, of:

$$v_{phase_l} = \frac{\omega}{k_{z_{01}} + 2\pi l/L}. \tag{2.28}$$

Therefore, for certain values of l, one can find modes verifying $v_{phase_l} < c$. This allows the synchronization of the flight of the particles and the phase of the electric field, leading to optimal acceleration, as it is illustrated in Fig. 2.3b.

Analogously, the rest of the components of the EM fields read as [14]:

$$\tilde{E}_r(r,z) = j \sum_{l=-\infty}^{+\infty} E_l \frac{k_{01,l}}{\kappa_{01,l}} J_1(\kappa_{01,l} r) e^{j\left(\varphi - k_{01,l} z\right)}, \tag{2.29}$$

$$\tilde{B}_\theta(r,z) = j \sum_{l=-\infty}^{+\infty} E_l \frac{\omega}{\kappa_{01,l} c^2} J_1(\kappa_{01,l} r) e^{j\left(\varphi - k_{01,l} z\right)}, \tag{2.30}$$

where $A_0 a_l = E_l$ for compaction.

2.2.2 Field propagation in Standing-wave structures

Standing-wave cavities are periodic structures where the EM fields are confined in within a cell, i.e there is no power flow from one cell to another. For the case of periodic arrays, like the one exposed below, this can be achieved by imposing a phase advance of $\phi_{\text{ad}} = \pi$. In that case, the field is composed of backward and forward travelling waves whose superposition results in a stationary pattern in space which oscillates in time:

$$\begin{aligned}\tilde{E_z}(r,z) = \tilde{F}(r,z)e^{\left(-jk_{z_{01}}z\right)} &= \sum_{l=-\infty}^{l=+\infty} a_l A_0 J_0(\kappa_{01,l} r) e^{\left(-j2\pi l\frac{z}{L} - j\pi\frac{z}{L} + j\varphi\right)} \\ &= e^{j\varphi} \sum_{l=-\infty}^{l=+\infty} a_l A_0 J_0(\kappa_{01,l} r) e^{\left(-j\frac{z}{L}\pi[2l-1]\right)}.\end{aligned} \tag{2.31}$$

If the cavity is designed in such a way that $a_l = -a_{-l}$, the following expression for

the longitudinal electric field is obtained:

$$\begin{aligned}\tilde{E}_z(r,z) =& e^{j\varphi}\sum_{l=1}^{l=+\infty} a_l A_0 J_0(\kappa_{01,l} r)\left[e^{\left(-j\frac{z}{L}\pi[2l-1]\right)} - e^{\left(+j\frac{z}{L}\pi[2l-1]\right)}\right] \\ =& e^{j\varphi}\sum_{l=1}^{l=+\infty} 2a_l A_0 J_0(\kappa_{01,l} r)\sin\left(\frac{[2l-1]\pi z}{L}\right).\end{aligned} \tag{2.32}$$

This shows that the field cancels for every $z = kL/2$, with $k \in \mathbb{N}$, or in other words, that the field vanishes every cell-length. The regions in which the field is contained (and does not flow) are now chosen to be the cells, as shown in Fig. 2.4.

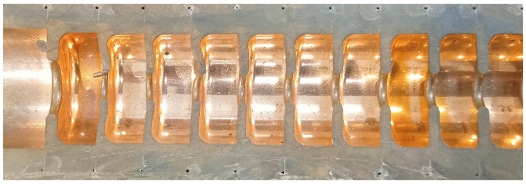

(a) S-band standing wave structure sectional cut.

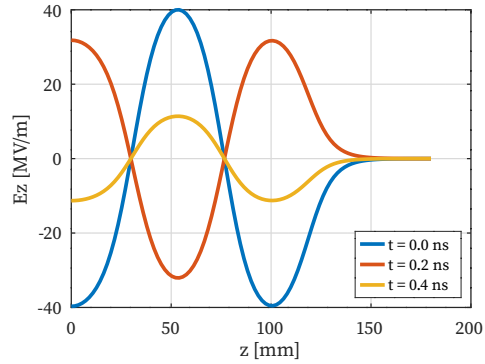

(b) On-axis electric field for an S-band injector.

Figure 2.4: Standing-wave geometry and longitudinal electric field.

A phase advance of π is advantegous from the point of view of acceleration efficiency, but it presents several drawbacks at operation time such as field equalization and structure operatibility [50, 51]. For this reason, other SW structures can be found, like Alvarez or Wideroe structures [52].

2.3 Wakefield and impedance formalism

When a beam of charged particles travels through an accelerating structure, surface currents are generated in the surrounding conducting walls. These currents create EM fields that act on the beam, thus deteriorating its properties [53, 54]. These beam-induced effects are described in the wakefield formalism, which considers the following set of assumptions:

1. Linearity of Maxwell's equations.

2. Straight linear motion through the region where the wake is generated.

3. Perturbative treatment of the effect of the wake.

4. Causality principle: The fields originated by a certain charge can only affect particles behind it. This is valid for ultrarelativistic beams ($v \simeq c$).

In this scenario, we consider the problem of describing the change of momentum that a test particle, q_t, suffers as a consequence of the EM fields originated by the currents in the wall that a source particle, q_s, creates when it passes through an accelerating structure, as illustrated in Fig. 2.5.

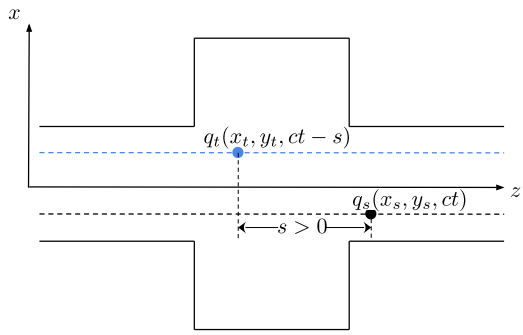

Figure 2.5: Accelerating cell scheme where a test particle goes inside of it after a source particle has travelled along the same. Both particles travel with a velocity $v \simeq c$ and are separated by a distance $s > 0$.

The source particle will originate EM fields whose action upon the test particle will result in a change of its momentum, $\Delta \boldsymbol{p}_t$, calculated as:

$$\Delta \boldsymbol{p}_t(x_s, x_t, y_s, y_t, s) = q_t \int_{-\infty}^{\infty} \mathrm{d}t \left[\boldsymbol{E}(x_t, y_t, ct - s, t) + c\hat{\boldsymbol{z}} \times \boldsymbol{B}(x_t, y_t, ct - s, t)\right]. \quad (2.33)$$

In this case, the *longitudinal*, w_l, and *transversal wake*, w_t, are defined as [54]:

$$w_l(x_s, y_s, x_t, y_t, s) \equiv -\frac{c}{q_s q_t} \Delta p_{t,z}(x_s, x_t, y_s, y_t, s) = \frac{c}{q_s} \int_{-\infty}^{\infty} \mathrm{d}t E_z(x_t, y_t, ct - s, t), \quad [\mathrm{V/C}] \quad (2.34)$$

$$\boldsymbol{w}_\perp(x_s, y_s, x_t, y_t, s) \equiv -\frac{c}{q_s q_t} \Delta \boldsymbol{p}_{t,\perp}(x_s, x_t, y_s, y_t, s) = \frac{c}{q_s} \int_{-\infty}^{\infty} \mathrm{d}t \left[\boldsymbol{E}_\perp(x_t, y_t, ct - s, t) + c\hat{\boldsymbol{z}} \times \boldsymbol{B}(x_t, y_t, ct - s, t)\right], \quad [\mathrm{V/C}] \quad (2.35)$$

where the symbol $\perp$ indicates the perpendicular direction to z. Since we are restricting ourselves to on-z-axis dynamics, the dependency on x_s, x_t, y_s, y_t can be neglected from now on. Causality implies that the following mathematical conditions hold:

$$w_l(s) = 0,\ s < 0 \qquad\qquad \int_0^\infty w_l(s)\mathrm{d}s = 0. \tag{2.36}$$

Energy loss of a bunch

w_l informs of the longitudinal momentum variation due to the effect of a single source particle, as it is shown in Eq. (2.34). In order to calculate the effect of a whole bunch upon one of its particles, the single-particle wake function w_l has to be convoluted with the linear charge density as follows:

$$\Delta p_z(z) = \frac{1}{e}\int_{-\infty}^{\infty} \lambda_q(z')\Delta p_{t,z}(s = z' - z)\ \mathrm{d}z' = -\frac{e}{c}\int_z^\infty \lambda_q(z')w_l(z' - z)\ \mathrm{d}z', \tag{2.37}$$

with e the single particle charge of the bunch. In the ultrarelativistic regime, the energy gain of any particle due to the wakefield interaction, $\Delta\mathcal{E}$, can be calculated as:

$$\Delta\mathcal{E}(z) \simeq c\Delta p_z(z) = -e\int_z^\infty \lambda_q(z')w_l(z' - z)\ \mathrm{d}z'. \tag{2.38}$$

The *wake potential of a bunch*, W_l, is defined as:

$$W_l(z) \equiv -\frac{\Delta\mathcal{E}(z)}{q_{\text{bunch}}e} = \frac{1}{q_{\text{bunch}}}\int_z^\infty \lambda_q(z')w_l(z' - z)\ \mathrm{d}z'.\ [\mathrm{V/C}] \tag{2.39}$$

The analogue transverse effect will be discussed in Sec. 2.5.

Impedance formalism

In many cases, it is convenient to work with the Fourier transform of the wake function. This quantity is called *impedance*, and it is defined through the wake function as follows:

$$Z_l(x_s, y_s, x_t, y_t, \omega) \equiv \frac{1}{c}\int_0^\infty \mathrm{d}s\ w_l(x_s, y_s, x_t, y_t, s)e^{j\omega s/c}, \qquad [\Omega] \tag{2.40}$$

$$\boldsymbol{Z}_\perp(x_s, y_s, x_t, y_t, \omega) \equiv \frac{1}{c}\int_0^\infty \mathrm{d}s\ \boldsymbol{w}_\perp(x_s, y_s, x_t, y_t, s)e^{j\omega s/c}. \qquad [\Omega] \tag{2.41}$$

Similarly, the reciprocal relationships are:

$$w_l(x_s, y_s, x_t, y_t, s) = \frac{1}{2\pi}\int_{-\infty}^\infty Z_l(x_s, y_s, x_t, y_t, \omega)e^{-j\omega s/c}\ \mathrm{d}\omega. \tag{2.42}$$

$$\boldsymbol{w}_\perp(x_s, y_s, x_t, y_t, s) = \frac{1}{2\pi}\int_{-\infty}^\infty \boldsymbol{Z}_\perp(x_s, y_s, x_t, y_t, \omega)e^{-j\omega s/c}\ \mathrm{d}\omega. \tag{2.43}$$

The longitudinal impedance allows a simpler calculation of the energy loss of the bunch:

$$\begin{aligned}\Delta\mathcal{E}_{\text{bunch}} =& \frac{1}{e}\int_{-\infty}^{\infty}\lambda_q(z)\Delta\mathcal{E}(z)\mathrm{d}z = -\int_{-\infty}^{\infty}\mathrm{d}z\lambda_q(z)\int_{-\infty}^{\infty}\mathrm{d}z'\lambda_q(z')w_l(z'-z)\\ =& \frac{-1}{2\pi}\int_{-\infty}^{\infty}\mathrm{d}z\lambda_q(z)\int_{-\infty}^{\infty}\mathrm{d}z'\lambda_q(z')\int_{-\infty}^{\infty}\mathrm{d}\omega Z_l(\omega)e^{-j\omega(z'-z)/c}\\ =& \frac{-1}{2\pi}\int_{-\infty}^{\infty}\mathrm{d}\omega Z_l(\omega)\int_{-\infty}^{\infty}\mathrm{d}z\lambda_q(z)e^{j\omega z/c}\int_{-\infty}^{\infty}\mathrm{d}z'\lambda_q(z')e^{-j\omega z'/c}\\ =& \frac{-q_{\text{bunch}}^2}{2\pi}\int_{-\infty}^{\infty}\mathrm{d}\omega Z_l(\omega)|\hat{F}(\omega)|^2.\end{aligned} \tag{2.44}$$

Here, $\hat{F}$ stands for the *bunch form factor*, and it is defined as the Fourier transform of the normalized charge distribution. This magnitude accounts for the bunch-size impact on the energy loss due to beam-excited EM modes, and for a gaussian bunch, it reads as $\hat{F} = e^{-\omega\sigma_z/2c}$.

2.4 Figures of merit

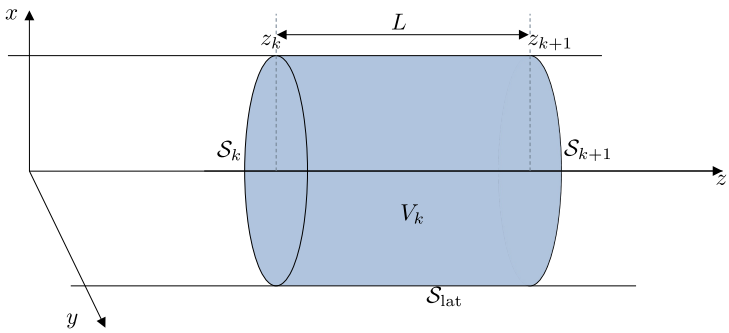

Figure 2.6: Cell schematic simplification as a cylindrical pillbox cavity with integration boundaries.

The performance of an accelerator is characterized by quantities called *figures of merit* [14, 45]. The first one to be considered is the *accelerating gradient*, G, in a cell $k \in \mathbb{N}$, defined as:

$$G(z_k) \equiv \frac{1}{L}\left|\int_{z_k}^{z_k+L}\tilde{E}_z(r=0,z)\,\mathrm{d}z\right|,\ [\mathrm{V/m}] \tag{2.45}$$

where $z_k = kL$ is the lower bound of the cell, as seen in Fig. 2.6. Another magnitude of interest is the *effective accelerating gradient*, G_{eff}, defined as the average electric field

seen by a particle travelling on-axis ($r = 0$) along a cell. It reads as:

$$G_{\text{eff}}(z_k) \equiv \frac{1}{L}\int_{z_k}^{z_k+L} E_z(z, t_q(z))\,\mathrm{d}z = \frac{1}{L}\int_{z_k}^{z_k+L} \mathrm{Re}\left[\tilde{E}_z(z)e^{j\omega t_q(z)}\right]\mathrm{d}z,\ [\mathrm{V/m}] \quad (2.46)$$

with t_q being the *time of flight* of a particle with charge q entering the k-th cell at a time t_0 with a velocity $v = \beta_r c$. Here β_r is the relativistic beta, and it is assumed to be constant in within a cell. The time of flight along the k-th cell is defined as:

$$t_q(z) \equiv t_0 + \frac{z - z_k}{\beta_r c}.\ [\mathrm{s}] \quad (2.47)$$

For ultrarelativistic particles entering lossless TW structures with $\varphi = \frac{\omega z_k}{c} - \omega t_0$ and with a privileged Floquet mode, l^*, with $v_{\text{phase}_{l^*}} \simeq c$, the following relationships hold:

$$\begin{aligned} G_{\text{eff}}(z_k) =& \frac{1}{L}\int_{z_k}^{z_k+L} \mathrm{Re}\left[\sum_{l=-\infty}^{+\infty} E_l e^{-jk_{01,l}z + j\omega t_q(z) + j\varphi}\right]\mathrm{d}z \\ =& \frac{1}{L}\sum_{l=-\infty}^{+\infty} E_l \int_{z_k}^{z_k+L} \cos\left(\frac{j2\pi(l-l^*)z}{L}\right)\mathrm{d}z \\ =& \sum_{l=-\infty}^{+\infty} E_l \left[\frac{\sin\left(2\pi(l-l^*)(k+1)\right)}{2\pi(l-l^*)} - \frac{\sin\left(2\pi(l-l^*)k\right)}{2\pi(l-l^*)}\right] = E_{l^*}. \end{aligned} \quad (2.48)$$

$$G(z_k) = \frac{1}{L}\left|\int_{z_k}^{z_k+L} E_l e^{-jk_{01,l}z + j\varphi}\mathrm{d}z\right| = \frac{1}{L}\sum_{l=-\infty}^{+\infty} E_l \int_{z_k}^{z_k+L} \cos\left(\frac{j2\pi(l-l^*)z}{L}\right)\mathrm{d}z = E_{l^*}. \quad (2.49)$$

Equation (2.49) gives a physical meaning for the accelerating gradient in lossless TW structures: It is the amplitude of the Floquet mode whose phase velocity is synchronized with the flight of the accelerated particles.

Figure 2.7 illustrates the definition of accelerating gradient for an arbitrary X-band fieldmap.

Equation (2.48) shows the case where the accelerated particle always sees the same accelerating field E_{l^*}, which is *on crest* (i.e at its maximum value, as seen in Fig. 2.3b). In any other scenario, the accelerated particle does not see the same phase of the RF field. The figure of merit accounting for such difference is the *time-transit factor*, $\mathcal{T}$:

$$\mathcal{T}(z_k) \equiv \frac{\int_{z_k}^{z_{k+1}} \mathrm{Re}\left[\tilde{E}_z(z)e^{j\omega t_q(z)}\right]\mathrm{d}z}{\left|\int_{z_k}^{z_{k+1}} \tilde{E}_z(z)\,\mathrm{d}z\right|}. \quad (2.50)$$

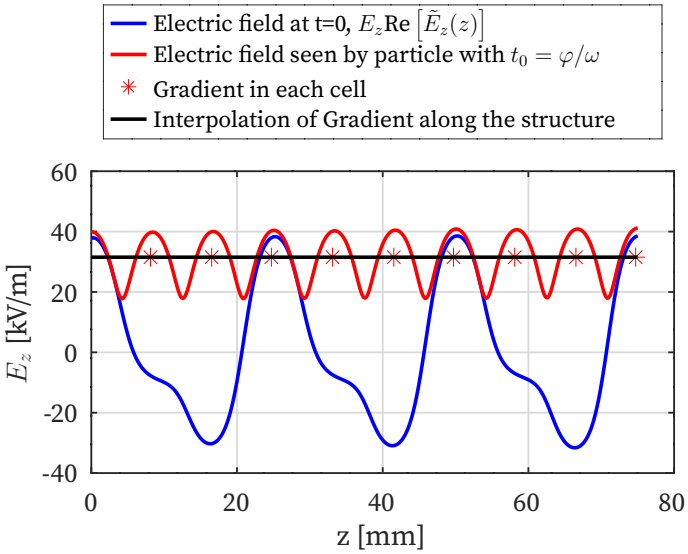

Figure 2.7: Effective electric field seen by an ultrarelativistic particle and its associated gradient for an X-band TW structure. The positive decelerating E_z values found at the extremes of the structure correspond to the SW behavior of the half-cell input powers, as seen in [7].

This quantity is always less than 1, being only equal for the case described in Eq. (2.49). These magnitudes are related to the *accelerating voltage*, V_{acc}, as follows:

$$V_{\text{acc}}(z_k) \equiv G_{\text{eff}}(z_k)L = G(z_k)\mathcal{T}(z_k)L = \int_{z_k}^{z_k+L} \text{Re}\left[\tilde{E}_z(z)e^{j\omega t_q(z)}\,\text{d}z\right]. \text{ [V]} \tag{2.51}$$

Another relevant figure of merit is the *time-averaged volumetric stored EM energy density*, $\bar{u}$, which in a cell with volume V_k in vacuum reads as:

$$\bar{u}(\boldsymbol{r}) \equiv \frac{1}{2}\varepsilon_0||\tilde{\boldsymbol{E}}(\boldsymbol{r})||^2_{\mathbb{C}^3} + \frac{1}{2}\mu_0||\tilde{\boldsymbol{H}}(\boldsymbol{r})||^2_{\mathbb{C}^3}, \text{ [J/m}^3\text{]} \tag{2.52}$$

Here, $||\boldsymbol{x}||^2_{\mathbb{R}^3\ (\mathbb{C}^3)} = \sum_{i=1}^{3} x_i^2$ is the squared norm of an arbitrary real (complex) vector $\boldsymbol{x} = (x_1, x_2, x_3) \in \mathbb{R}^3$ ($\mathbb{C}^3$). This allows the definition of the *stored energy per unit length*, w as:

$$w(z_k) \equiv \frac{1}{L}\int_{V_k} \bar{u}(\boldsymbol{r})\,\text{d}V, \text{ [J/m]} \tag{2.53}$$

Realistic structures suffer from resistive ohmic losses since EM fields, in the presence of metallic boundaries, penetrate the surrounding material, leading to power dissipation [44]. In the k-th cell, the *time-averaged dissipated power*, $\bar{P}_{\text{diss}}$, can be calculated

with the tangential magnetic field $\boldsymbol{H}_{\text{tan}}$ as:

$$\bar{P}_{\text{diss}}(z_k) \equiv \frac{1}{2}\int_{\text{V}_k} R_s ||\tilde{\boldsymbol{H}}_{\text{tan}}(\boldsymbol{r})||^2_{\mathbb{C}^3}\, \text{d}V \ [\text{W}], \tag{2.54}$$

where R_s is the surface resistance, defined as $R_s = (\sigma_s \delta)^{-1}$, being σ_s the surface electric conductivity and δ the skin depth penetration of the field in the conducting material. The *time-averaged dissipated power per unit length*, p_{diss}, is defined as:

$$p_{\text{diss}}(z_k) \equiv \frac{\bar{P}_{\text{diss}}(z_k)}{L}. \ [\text{W/m}] \tag{2.55}$$

Similarly, the *power flow per unit length*, p_{flow}, across a section of the structure can be defined in terms of the Poynting vector $\boldsymbol{S} = \boldsymbol{E} \times \boldsymbol{H}$ as:

$$p_{\text{flow}}(z) \equiv \frac{1}{L}\int_{\mathcal{S}_k} S_z(\boldsymbol{r})\, \text{d}\mathcal{S} \ [\text{W/m}] \tag{2.56}$$

The *group velocity*, v_g determine the velocity at which power flows along the structure. It can be defined as:

$$v_g(z_k) \equiv \frac{L p_{\text{flow}}(z_k)}{w(z_k)}. \ [\text{m/s}] \tag{2.57}$$

Power dissipation implies the diminution of the stored energy, and ultimately, the accelerating gradient. These figures of merit are related by the *quality factor*, Q, defined as [14]:

$$Q(z_k) \equiv \frac{\omega\, w(z_k)}{p_{\text{diss}}(z_k)}. \tag{2.58}$$

This definition is widely extended in accelerator physics [45], but it has its origin in resonating cavity theory [44]. In other words, from the figures of merit point of view, accelerating cells can be considered as resonators or pillbox cavities.

Shunt impedance and its physical meaning

The problem of studying the longitudinal wake of a resonator has been widely studied in references [46, 54] among others. Reference [46] presents its expression for ultrarelativistic particles as:

$$w_l(s) = \begin{cases} \dfrac{Z_0}{4\pi}\dfrac{3L^2}{(d_k/2)^2}\omega_r e^{-\alpha s/c}\cos\left(\dfrac{\bar{\omega}_r s}{c}\right) & \text{if } s > 0 \\ 0 & \text{otherwise} \end{cases} \tag{2.59}$$

Here, Z_0 is the vacuum impedance, d_k the diameter of the considered cell, ω_r the resonating frequency of the considered mode in the cavity, $\alpha = \omega_r/2Q$ characterises the damping of the given mode and $\bar{\omega}_r$ is:

$$\bar{\omega}_r = \sqrt{|\omega_r^2 - \alpha^2|}. \tag{2.60}$$

Fourier-transforming Eq. (2.59), one gets that the longitudinal impedance for a resonating cavity, for large values of Q, is:

$$Z_l(\omega, z_k) = \frac{R_{s,\text{eff}}(z_k)}{1 + jQ(z_k)\left(\frac{\omega_r}{\omega} + \frac{\omega}{\omega_r}\right)}, \tag{2.61}$$

with $R_{s,\text{eff}}$ the *effective shunt impedance*, defined as:

$$R_{s,\text{eff}}(z_k) \equiv \frac{3Q(z_k)L^2}{\pi d_k^2} Z_0 \ [\Omega]. \tag{2.62}$$

The impedance in Eq. (2.61) is the same as in an electrical parallel LCR circuit consisting of a resistance R_s, an inductance $L = \frac{R_s}{Q\omega_r}$ and a capacitance $C = \frac{Q}{R_s\omega_r}$ [46].

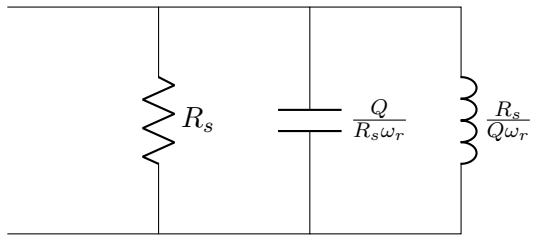

Figure 2.8: LCR equivalent circuit of the k-th cell.

In an LCR circuit, the impedance is dominated by the resistance when the operating frequency ω is close to the resonant frequency ω_r. Accelerating structures operate at the resonating frequency, and as a consequence, the analogy with an LCR circuit dominated by the resistance term can be established. In this case, the dissipated power in an accelerating cavity is defined as [14, 45, 50]:

$$P_{\text{diss}}(z_k) = \frac{V_{\text{acc}}(z_k)^2}{R_{s,\text{eff}}(z_k)}. \tag{2.63}$$

Therefore, we can define the *effective shunt impedance per unit length*, r_{eff}, making use of Eqs. (2.46), (2.55) and (2.63) as:

$$r_{\text{eff}}(z_k) \equiv \frac{R_{s,\text{eff}}(z_k)}{L} = \frac{V_{\text{acc}}(z_k)^2/L^2}{P_{\text{diss}}(z_k)/L} = \frac{G(z_k)^2\mathcal{T}(z_k)^2}{p_{\text{diss}}\,(z_k)}, \ [\Omega/\text{m}] \tag{2.64}$$

and the *shunt impedance per unit length*, r, as:

$$r(z_k) \equiv \frac{G(z_k)^2}{p_{\text{diss}}\,(z_k)}.\ [\Omega/\text{m}] \tag{2.65}$$

Lastly, the *normalized shunt impedance per unit length*, which depends only on the structure geometry and not on the quality of the surface of the cavity walls, is defined as:

$$\frac{r}{Q}(z_k) \equiv \frac{r(z_k)}{Q(z_k)}\ [\Omega/\text{m}]. \tag{2.66}$$

2.5 Transverse beam dynamics

2.5.1 Beam focusing and defocusing

RF effect: The longitudinal accelerating electric field presents associated transverse EM fields, as described in Eqs. (2.29) and (2.30). The resulting transverse Lorentz force in this case reads as:

$$\frac{F_r}{q} = E_r - vB_\theta = -\sum_{l=-\infty}^{l=+\infty} E_l \left(k_{01,l} - \frac{\beta\omega}{c}\right) \frac{J_1(\kappa_{01,l} r)}{\kappa_{01,l}} \sin\left(\omega t - k_{01,l} z + \varphi\right) \tag{2.67}$$

In the $r = 0$ vicinity, after manipulation, transverse force can be expressed as:

$$\frac{F_r}{q} = -(1-\beta)\frac{\omega}{c}\frac{r}{2}\sum_{l=-\infty}^{l=+\infty} E_l \sin\left(\omega t - k_{01,l} z + \varphi\right) - \frac{r}{2}\sum_{l=-\infty}^{l=+\infty} E_l \frac{2\pi l}{L} \sin\left(\omega t - k_{01,l} z + \varphi\right) \tag{2.68}$$

This force translates in a variation of the transverse momentum $p_r \equiv \sqrt{p_x^2 + p_y^2}$. Two particular cases are considered below:

- Case of SW ($\phi_{\text{ad}} = \pi$) with $l = 0$ predominant Floquet harmonic. Making use of trigonometric identities, the definitions in Eqs (2.47), (2.46), and (2.50); and assuming the origin of the z-field to be in the middle of the cell, the transverse momentum increase after a cell (k) reads as:

$$\begin{aligned}\Delta p_r &= \int_{z_k}^{z_k+L} F_r(z, t_q(z)) \frac{\mathrm{d}z}{\beta c} = -qr\frac{1-\beta}{\beta}\frac{\omega}{2c}\sin\varphi \int_0^L E_0 \cos\frac{\pi}{L} z \cos\omega t_q(z) \\ &= -\,qr\frac{1-\beta}{\beta}\frac{\omega}{2c} G(z_k) L \sin\varphi\end{aligned} \tag{2.69}$$

  This term is negligible at the ultrarelativistic limit. For low particle velocities, operation requires $\sin\varphi < 0$ [14], and the RF effect upon the beam is defocusing in this case. This effect is dominant in hadron linacs at low energies.

- TW Structures with rich harmonic contribution in the ultrarelativistic regime. In this case, the first term of Eq. (2.68) can be neglected, and the transvese force associated to this force is usually calculated as a ponderomotive term, i.e averaged over an RF period [55]. It shows the following dependencies [51]:

$$\bar{F}_r \propto -rq\frac{G(z_k)^2}{\gamma^2}\eta(\varphi); \qquad \Delta p_r \simeq \frac{\bar{F}_r L}{\beta c}, \tag{2.70}$$

with $\eta(\varphi)$ a factor depending on the RF phase.

An example of this case are ultrarelativistic electron beams in the periodic TW structures presented in Sec. 2.2.1, where the effect upon the beam is focusing, and its predominant for high-gradient structures.

Wakefield effect: In addition to the RF focusing/defocusing effects, the transverse wakefields presented in Sec. 2.3 provide a deflecting kick. In axisymmetric systems, the dipole wake (the predominant transverse wake) does not depend on the offset of the trailing particle and is proportional to the offset of the source particle [53]. Introducing $\bar{w}_x = \frac{w_x}{x}$, for the $r \simeq 0$ vicinity, the transverse kick provided by the dipolar wakefield reads as:

$$p_x(z) = \frac{e}{c}\int_{-\infty}^{\infty} \lambda_q(z')w_x(z'-z)\,\mathrm{d}z' \simeq \frac{e}{c}\int_{-\infty}^{\infty} x(z')\lambda_q(z')\bar{w}_x(z'-z)\,\mathrm{d}z'. \tag{2.71}$$

Quadrupoles and solenoid effect: Equations (2.69) and (2.71) illustrate detrimental effects that can increase the beam-size, σ_x, up to undesired values which could potentially lead to beam losses or significant quality degradation. To correct these issues, additional elements such as quadrupoles or solenoids are attached to the beamline.

Quadrupoles are magnets consisting in four pole tips with hyperbolic profiles that produce a constant transverse quadrupole gradient, $g = \frac{2NI}{\mu_0 R^2}$, with N the number of coils that power the magnet, I the intensity flowing through them, and R the inner radius. In this way, the magnetic field of a quadrupolar magnet reads as:

$$g = \frac{\partial B_x}{\partial y} = \frac{\partial B_y}{\partial x} \iff \boldsymbol{B} = g(y\hat{\boldsymbol{x}} + x\hat{\boldsymbol{y}}), \tag{2.72}$$

which produces a force upon a particle travelling on the longitudinal direction that is:

$$F_x = -qvgx; \qquad F_y = qvgy. \tag{2.73}$$

If qg is positive, the magnet focuses in x and defocuses in y.

Solenoids produce focusing in both planes, but the mathematical description of the force exterted upon particles is more complicated since focusing is a consequence of the interaction between the azimutal velocity component induced by fringe-fields in the entrace region, and the longitudinal magnetic field component in the central region. Further details can be found in [14, 46].

2.5.2 Solutions to the linear transverse equations of motion

In the x-direction, the relativistic equation of motion reads as:

$$F_x = \frac{\mathrm{d}p_x}{\mathrm{d}t} = \frac{\mathrm{d}}{\mathrm{d}t}\left(\gamma m v_x\right) = \gamma m \frac{\mathrm{d}v_x}{\mathrm{d}t} = \gamma m v^2 x'. \tag{2.74}$$

To deal with linear forces ($F_x \propto x$), it is convenient to define a *normalized strength* factor, $\kappa(s)$, as $\kappa(s) \equiv \frac{F_x(s)}{xvp}$. For quadrupoles, $\kappa = \frac{g}{p/q}$. Introducing this factor, we can rewrite Eq. (2.74) as:

$$x'' + \kappa(s)x = 0. \tag{2.75}$$

Equation (2.75) is called Hill's equation, and the Floquet's theorem states that it possesses a quasi-periodic solution, usually called phase-amplitude form [49], which is written as:

$$x(s) = \sqrt{\varepsilon\beta(s)}\cos(\mu(s) + \mu_0). \tag{2.76}$$

Here, $\beta(s)$ is the *amplitude function* (not to be confused with the relativistic beta) and $\mu(s)$ is the *phase function*, whereas ε and μ_0 are constants determined by the initial conditions.

The description of the transverse properties of the beam requires the definition of two additional functions: $\alpha(s)$ and $\gamma(s)$. Their definition, as well as an important relationship between $\beta(s)$ and $\mu(s)$, are listed below [14]:

$$\alpha(s) \equiv \frac{-\beta'(s)}{2}, \tag{2.77}$$

$$\gamma(s) \equiv \frac{1 + \alpha(s)^2}{\beta(s)}. \tag{2.78}$$

$$\mu(s) = \int_{s_0}^{s} \frac{\mathrm{d}s}{\beta(s)}. \tag{2.79}$$

The functions $\alpha(s)$, $\beta(s)$ and $\gamma(s)$ are called *Twiss functions*.

It can be proved that the solution $x(s)$ and its derivative $x'(s)$ satisfy the following relationship for all s values in the trajectory:

$$\gamma(s)x(s)^2 + 2\alpha(s)x(s)x'(s) + \beta(s)x'(s)^2 = \varepsilon. \tag{2.80}$$

Equation (2.80) defines ε as an invariant of motion called *Courant-Snyder invariant*. Four features are:

1. Equation (2.80) defines the envelope of an ellipse, and ε is defined in terms of the area of such ellipse as Area $= \pi\varepsilon$.

2. Periodic lattices demand $\beta(s) = \beta(s+L)$, $\alpha(s) = \alpha(s+L)$, and $\gamma(s) = \gamma(s+L)$. This implies that every time a particle moves one period in the length along s, its transverse position and slope (x, x') must lie on the same ellipse. This is illustrated in Fig. 2.9.

3. For a centered beam ($\langle x \rangle = 0$) with no correlation between phase and amplitude ($\langle \cos(\mu(s) + \mu_0) \rangle = \langle \sin(\mu(s) + \mu_0) \rangle = 0$), Eq. (2.78) allows to give a bunch-statistical meaning to the Twiss functions, even if these were initially found for the single-particle solution $x_i(s) = \sqrt{\varepsilon_i \beta(s)} \cos(\mu(s) + \mu_{0,i})$

   In this situation, the statistical moments can be calculated as in Eqs. (2.8) and (2.7). Averaging over all phases $\mu_{0,i}$, the quadratic terms satisfy ($\langle \cos^2(\mu(s) + \mu_0) \rangle = \langle \sin^2(\mu(s) + \mu_{0,i}) \rangle = \frac{1}{2}$. Therefore, we get [49]:

$$\sigma_x^2(s) = \frac{1}{2} \langle \varepsilon_i \rangle \beta(s) \tag{2.81}$$

$$\sigma_{x'}^2(s) = \frac{1}{2} \langle \varepsilon_i \rangle \gamma(s) \tag{2.82}$$

$$\langle xx' \rangle(s) = -\frac{1}{2} \langle \varepsilon_i \rangle \alpha(s). \tag{2.83}$$

   These relationships hold for arbitrary beams.

4. The following relationship between the Courant Snyder invariant and the emittance holds:

$$\epsilon_x = \sqrt{\sigma_x \sigma_{x'} - \langle xx' \rangle^2} = \frac{1}{2} \langle \varepsilon_i \rangle. \tag{2.84}$$

   For this reason, the beam size of a bunch will be generally described in terms of the rms-value of the Courant Snyder invariant, i.e the emittance, as $\sigma_x(s) = \sqrt{\epsilon_x \beta(s)}$.

   In practice, the particles are affected by non-linear forces, so the trace space cannot be described as an ellipse. However, there is a region of acceptance where such description can be carried out inheriting the formalism of the linear case.

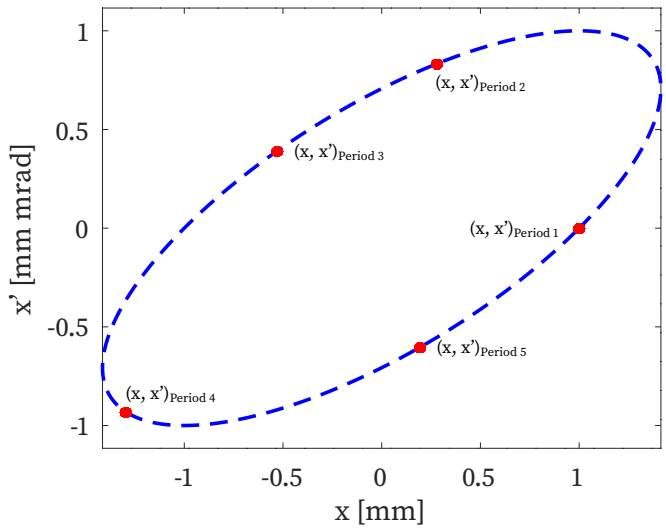

Figure 2.9: Illustration of the trace space of a single particle affected by linear transverse forces in a periodic lattice. Coordinates shown for a particle at a certain position s after several periods 1 to 5.

3. Power-diffusive model for the Beam Loading effect

Beam-cavity interaction results in the excitation of EM fields that act on the beam, as presented in Section 2.3. When a beam travels on-axis inside RF-cavities, the fundamental accelerating mode, in Eq. (2.27), is excited. This causes a reduction of the accelerating gradient known as *Beam Loading effect* [50, 56, 57].

The impact of the excitation of the fundamental mode upon the beam phase space can be calculated with the longitudinal wake function as shown in Eq. (2.38). Tracking codes like ELEGANT [58] or PLACET [59] implement wakefield calculations based on the single-cell damped oscillator model in Eq. (2.59). However, they do not account for the effect of cavity coupling, which is crucial when considering BL in TW structures where power flows from cell to cell.

ELEGANT and PLACET also offer the possibility of introducing externally-computed wakefield functions from EM solvers like CST STUDIO [60] or GDFIDL [61]. The biggest drawback of this approach is the computational time required by these calculations, which limits the applicability of these tools to practical beam dynamics simulations and parametric scans.

An alternative procedure for studying BL is to address gradient reduction and power consumption directly. In this regard, power-diffusive models have already been discussed in [50, 62, 63], where the BL effect is presented in terms of a power-diffusion Partial Differential Equation (PDE), which is analyzed for BL compensation in TW structures. This effect is also discussed in the phasorial formalism in [64] for SW structures.

This chapter aims to provide a unified description of the BL effect in both TW and SW structures, and to perform particle tracking simulations in realistic transient scenar-

ios, overcoming ultrarelativistic assumptions ($v \simeq c$) if needed.

3.1 Quasi-static phasorial formalism

The consideration of transient scenarios requires describing EM fields under the Quasi-static (QS) assumption [65]. In such case, E_z reads as:

$$E_z(\boldsymbol{r},t) = \mathrm{Re}\left[\tilde{E}_z(\boldsymbol{r},t)e^{j\omega t}\right]. \tag{3.1}$$

This extension of the standard phasorial formalism admits that the amplitude of the harmonic EM fields depends on time, being its variation much slower than the RF oscillation itselt, thus leading to some specific properties. To illustrate them, let $E_1 = E_1(z,t)$ and $E_2 = E_2(z,t)$ be two electric fields whose time dependent quasi-static phasors are $\tilde{E}_1$ and $\tilde{E}_2$ respectively. The following relationships hold [66]:

$$E_1(z,t)E_2(z,t) = \frac{1}{2}\left(\mathrm{Re}\left[\tilde{E}_1(z,t)\tilde{E}_2(z,t)^*\right] + \mathrm{Re}\left[\tilde{E}_1(z,t)\tilde{E}_2(z,t)e^{2j\omega t}\right]\right), \tag{3.2}$$

$$\overline{E_1(z,t)E_2(z,t)} = \frac{1}{2T}\int_t^{t+T} \mathrm{Re}\left[\tilde{E}_1(z,\tau)\tilde{E}_2(z,\tau)^*\right]\mathrm{d}\tau \simeq \frac{1}{2}\mathrm{Re}\left[\tilde{E}_1(z,t)\tilde{E}_2(z,t)^*\right], \tag{3.3}$$

$$\overline{\frac{\partial E_1(z,t)E_2(z,t)}{\partial t}} = \frac{\partial \overline{E_1(z,t)E_2(z,t)}}{\partial t}; \tag{3.4}$$

where the time-average of an oscillating function f with RF-period T is defined as:

$$\overline{f(t)} = \frac{1}{T}\int_t^{t+T} f(\tau)\mathrm{d}\tau. \tag{3.5}$$

Demonstration of the properties (3.2), (3.3), and (3.4):

(3.2): $E_1(z,t)E_2(z,t) = \mathrm{Re}\left[\tilde{E}_1(z,t)e^{j\omega t}\right]\cdot\mathrm{Re}\left[\tilde{E}_2(z,t)e^{j\omega t}\right] =$
$\frac{1}{4}\left(\tilde{E}_1(z,t)e^{j\omega t} + \tilde{E}_1^*(z,t)e^{-j\omega t}\right)\left(\tilde{E}_2(z,t)e^{j\omega t} + \tilde{E}_2^*(z,t)e^{-j\omega t}\right) =$
$\frac{1}{2}\left(\mathrm{Re}\left[\tilde{E}_1(z,t)\tilde{E}_2(z,t)^*\right] + \mathrm{Re}\left[\tilde{E}_1(z,t)\tilde{E}_2(z,t)e^{2j\omega t}\right]\right)$

(3.3): Follows directly from QS phasors being constant within an RF period.

(3.4): $\overline{\frac{\partial E_1(z,t)E_2(z,t)}{\partial t}} = \overline{\frac{\partial}{\partial t}\left(\frac{1}{2}\mathrm{Re}\left[\tilde{E}_1(z,t)\tilde{E}_2(z,t)^*\right]\right)} \simeq$
$\frac{\partial}{\partial t}\left(\frac{1}{2}\mathrm{Re}\left[\tilde{E}_1(z,t)\tilde{E}_2(z,t)^*\right]\right) = \frac{\partial \overline{E_1(z,t)E_2(z,t)}}{\partial t}.$

A first implication of the QS assumption is the temporal dependency of the EM quantities defined in Tab. 3.2. As a consequence, the figures of merit $\mathcal{T}$, V_{acc}, w, p_{diss}, p_{flow} inherit this time-dependency as can be observed from their definition in Eqs. (2.50, 2.51, 2.53, 2.55, 2.56).

Standard Phasorial Formalism	**QS Phasorial Formalism**
$\bar{u}(\boldsymbol{r}) \equiv \frac{1}{2}\varepsilon_0 \|\|\tilde{\boldsymbol{E}}(\boldsymbol{r})\|\|^2_{\mathbb{C}^3} + \frac{1}{2}\mu_0 \|\|\tilde{\boldsymbol{H}}(\boldsymbol{r})\|\|^2_{\mathbb{C}^3}$	$\bar{u}(\boldsymbol{r},t) \equiv \frac{1}{2}\varepsilon_0 \|\|\tilde{\boldsymbol{E}}(\boldsymbol{r},t)\|\|^2_{\mathbb{C}^3} + \frac{1}{2}\mu_0 \|\|\tilde{\boldsymbol{H}}(\boldsymbol{r},t)\|\|^2_{\mathbb{C}^3}$
$\bar{P}_{\text{diss}}(z_k) := \frac{1}{2}\int_{V_k} R_s \|\|\tilde{\boldsymbol{H}}_{\tan}(\boldsymbol{r})\|\|^2_{\mathbb{C}^3}\, \mathrm{d}V$	$\bar{P}_{\text{diss}}(z_k,t) \equiv \frac{1}{2}\int_{V_k} R_s \|\|\tilde{\boldsymbol{H}}_{\tan}(\boldsymbol{r},t)\|\|^2_{\mathbb{C}^3}\, \mathrm{d}V$
$G(z_k) = \frac{1}{L}\int_{z_k}^{z_k+L} \|\tilde{E}_z(z)\| \mathrm{d}z$	$G(z_k,t) = \frac{1}{L}\int_{z_k}^{z_k+L} \|\tilde{E}_z(z,t)\| \mathrm{d}z$
$G_{\text{eff}}(z_k) = \frac{1}{L}\int_{z_k}^{z_k+L} \mathrm{Re}\left[\tilde{E}_z(z)\exp\left(j\omega t_q(z)\right)\right] \mathrm{d}z$	$G_{\text{eff}}(z_k,t) = \frac{1}{L}\int_{z_k}^{z_k+L} \mathrm{Re}\left[\tilde{E}_z(z,t)\exp\left(j\omega t_q(z)\right)\right] \mathrm{d}z$

Table 3.2: Time-dependent figures of merit in the quasi-static approximation.

3.2 Energy conservation PDE

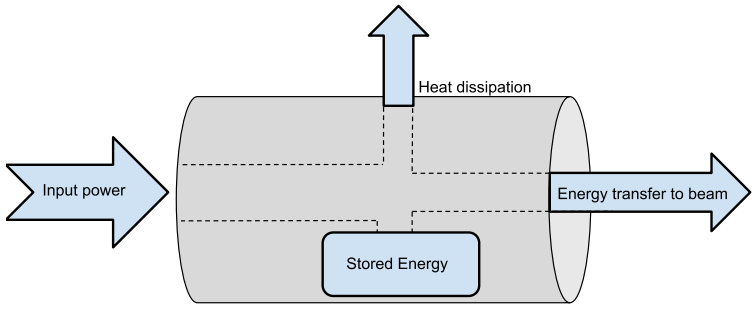

Figure 3.1: Energy conservation in an accelerating structure

The starting point for the derivation of a PDE describing gradient reduction in an accelerating structure is the Poynting theorem, which accounts for the instantaneous conservation of power along the structure. Upon the $k-$th cell (see Fig. 2.6), it reads as [44]:

$$-\frac{\partial u(\boldsymbol{r},t)}{\partial t} = \boldsymbol{\nabla}\cdot\boldsymbol{S}(\boldsymbol{r},t) + \boldsymbol{E}(\boldsymbol{r},t)\cdot\boldsymbol{J}(\boldsymbol{r},t),\ \boldsymbol{r}\in V_k,\ t\in[0,\infty) \tag{3.6}$$

with $\boldsymbol{S}$ the Poynting vector and $\boldsymbol{J}$ the current density. Assuming that particles travel much faster in the z direction than in the transverse plane (i.e paraxial approximation, $v_z \gg v_x, v_y$), the current density can be expressed as:

$$\boldsymbol{J}(\boldsymbol{r},t) \equiv \rho(\boldsymbol{r},t)\boldsymbol{v}(\boldsymbol{r},t) \simeq \rho(\boldsymbol{r},t)c\beta_z(z_k,t)\hat{\boldsymbol{z}}, \tag{3.7}$$

where ρ is the volumetric charge density and β_z is assumed to be constant in within a cell and period.

In first place, Eq. (3.6) shall be time-averaged over a period. From Eqs. (2.52) and (3.4), the following identity holds for the period-averaged EM density:

$$\overline{\frac{\partial u(\boldsymbol{r},t)}{\partial t}} = \frac{\partial \bar{u}(\boldsymbol{r},t)}{\partial t}, \tag{3.8}$$

which, along with the time-average definition in Eq. (3.5) and Eq. (3.7), leads to:

$$-\frac{\partial \bar{u}(\boldsymbol{r},t)}{\partial t} = \boldsymbol{\nabla}\cdot\bar{\boldsymbol{S}}(\boldsymbol{r},t) + \mathrm{Re}\left[\tilde{E}_z(z,t)\beta_z(z_k,t)\frac{1}{T}\int_t^{t+T} c\rho(\boldsymbol{r},\tau)e^{j\omega\tau}\,\mathrm{d}\tau\right]. \tag{3.9}$$

Secondly, Eq. (3.9) is divided by L and integrated over the cell volume. Making use of the definition of λ_q in Eq. (2.4), Eq. (2.53), and the divergence theorem; we can manipulate as follows:

$$\begin{aligned}
-\frac{\partial w(z_k,t)}{\partial t} =& \frac{1}{L}\int_{V_k}\boldsymbol{\nabla}\cdot\bar{\boldsymbol{S}}(\boldsymbol{r},t)\mathrm{d}V + \\
&\frac{1}{L}\int_{z_k}^{z_k+L}\mathrm{Re}\left[\tilde{E}_z(z,t)\beta_z(z_k,t)\frac{1}{T}\int_t^{t+T} c\left(\int_{\mathcal{S}}\rho(\boldsymbol{r},\tau)\right)e^{j\omega\tau}\,\mathrm{d}\tau\right]\mathrm{d}z; \\
-\frac{\partial w(z_k,t)}{\partial t} =& \frac{1}{L}\oint\bar{\boldsymbol{S}}(\boldsymbol{r},t)\cdot\mathrm{d}\boldsymbol{\mathcal{S}} \\
&+\frac{1}{L}\int_{z_k}^{z_k+L}\mathrm{Re}\left[\tilde{E}_z(z,t)\beta_z(z_k,t)\frac{1}{T}\int_t^{t+T} c\lambda_q(z,\tau)e^{j\omega\tau}\,\mathrm{d}\tau\right]\mathrm{d}z.
\end{aligned} \tag{3.10}$$

The mathematical representation of any moving function f with velocity v is $f(x-vt)$. For this reason, λ_q can be expressed as $\lambda_q(z,t) = q_{\text{bunch}}\, f(t-t_q(z))$, being f the shape of the normalized charge distribution. For instance, for a Gaussian bunch, the charge density is:

$$\lambda_q(z,t) = f(t-t_q(z)) = \frac{q_{\text{bunch}}}{\sqrt{2\pi}\sigma_z}\exp\left[-\frac{(t-t_q(z))^2}{2\sigma_z^2/c^2}\right]. \tag{3.11}$$

The bunch size, σ_z, is assumed to fullfill the condition $\sigma_z/c \ll T$, and $t_q(z) \in [t, t+T]$. This means that the considered bunch length is contained in an RF-period, as illustrated in Fig. 3.2. Therefore, we can manipulate and approximate the last term of Eq. (3.10) as follows:

$$\begin{aligned}
&\beta_z(z_k,t)\frac{1}{T}\int_t^{t+T} c\lambda_q(z,\tau)e^{j\omega\tau}\,\mathrm{d}\tau = \\
&e^{j\omega t_q(z)}\beta_z(z_k,t)\frac{q_{\text{bunch}}}{T}\int_t^{t+T} cf(\tau-t_q(z))e^{j\omega(\tau-t_q(z))}\,\mathrm{d}\tau \simeq
\end{aligned}$$

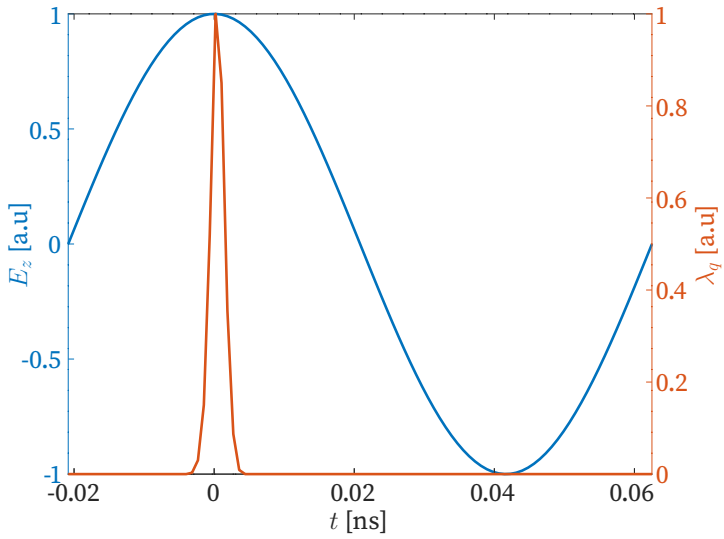

Figure 3.2: A 1-mm-σ_z Gaussian bunch λ_q (orange) and an X-band longitudinal electric field (blue). Both magnitudes have been normalised to their maximum values. In this case, the bunch is *on crest* and fully contained within an RF-period.

$$e^{j\omega t_q(z)}\beta_z(z_k,t)\frac{q_{\text{bunch}}}{T}\int_{-\infty}^{+\infty} cf(\tau - t_q(z))e^{j\omega(\tau - t_q(z))}\mathrm{d}\tau = \\ e^{j\omega t_q(z)}\beta_z(z_k,t)\frac{q_{\text{bunch}}}{T}F(\omega) = e^{j\omega t_q(z)}\tilde{I}(z_k,t;\omega), \tag{3.12}$$

with F the form factor and $\tilde{I} \equiv \frac{q_{\text{bunch}}}{T}F$ the period-averaged intensity.

Substituting Eq. (3.12) into Eq. (3.10), one gets that:

$$\frac{\partial w(z_k,t)}{\partial t} = \frac{1}{L}\oint \bar{\boldsymbol{S}}(\boldsymbol{r},t)\cdot \mathrm{d}\boldsymbol{\mathcal{S}} + \tilde{I}(z_k,t;\omega)\frac{1}{L}\int_{z_k}^{z_k+L}\mathrm{Re}\left[\tilde{E}_z(z,t)e^{j\omega t_q(z)}\right]\mathrm{d}z. \tag{3.13}$$

The second term of Eq. (3.13) can be rewritten according to the flux of the Poynting vector across the cell surface, which equals the net power balance in the cell. As it was introduced in Section 2.2, the main difference between TW and SW structures is whether they allow power flow from cell to cell or not. Thereby, a different expression is found for each type of accelerating structure.

Power diffusive PDE for TW structures

In a TW structure, the net power balance in a cell is given by:

$$\oint_{\mathcal{S}} \boldsymbol{S}(\boldsymbol{r},t)\cdot \mathrm{d}\boldsymbol{\mathcal{S}} = P_{\text{diss}}(z_k,t) + P_{\text{flow}}(z_k+L,t) - P_{\text{flow}}(z_k,t). \tag{3.14}$$

Inserting Eq. (3.14) in Eq. (3.13) and recalling the definitions given in Eqs. (2.46) and (2.55), we get that:

$$-\frac{\partial w(z_k,t)}{\partial t} = p_{\text{diss}}(z_k,t) + \frac{P_{\text{flow}}(z_k+L,t) - P_{\text{flow}}(z_k,t)}{L} + G_{\text{eff}}(z_k,t)\tilde{I}(z_k,t). \quad (3.15)$$

For structures exhibiting high resonant frequencies, their cells are short enough to assume the limit $L \to 0$. This leads to the following expression:

$$-\frac{\partial w(z,t)}{\partial t} = p_{\text{diss}}(z,t) + \frac{\partial \bar{P}_{\text{flow}}(z,t)}{\partial z} + G_{\text{eff}}(z,t)\tilde{I}(z,t). \quad (3.16)$$

Finally, inserting Eqs. (2.50), (2.56), (2.58) and (2.66) in (3.16), after manipulation, one obtains:

$$-\frac{\partial G(z,t)}{\partial t} = v_g(z)\frac{\partial G(z,t)}{\partial z} + \left(\frac{\partial v_g(z)}{\partial z} - \frac{v_g(z)}{\frac{r}{Q}(z)}\frac{\partial \frac{r}{Q}(z)}{\partial z} + \frac{\omega}{Q(z)}\right)\frac{G(z,t)}{2} + \frac{\omega \frac{r}{Q}(z)\mathcal{T}(z,t)\tilde{I}(z,t)}{2}. \quad (3.17)$$

Power diffusive PDE for SW structures

In a SW structure, the net power balance in a cell is given by:

$$\oint_{\mathcal{S}} \boldsymbol{S}(\boldsymbol{r},t)\cdot \mathrm{d}\boldsymbol{\mathcal{S}} = P_{\text{diss}}(z_k,t) - P_{\text{input}}(z_k,t), \quad (3.18)$$

where P_{input} is the input power provided by the external port which fills the k-th cell.

Inserting Eq. (3.18) in Eq. (3.13) and recalling the definitions given in Eqs. (2.46) and (2.55), we get that:

$$-\frac{\partial w(z_k,t)}{\partial t} = p_{\text{diss}}(z_k,t) - \frac{P_{\text{input}}(z_k,t)}{L} + G_{\text{eff}}(z_k,t)\tilde{I}(z_k,t). \quad (3.19)$$

Again, we can make the assumption $L \to 0$ and insert Eqs. (2.50), (2.58), and (2.66) in (3.19) to obtain:

$$-\frac{\partial G(z,t)}{\partial t} = \frac{\omega}{2Q(z)}G(z,t) - \frac{P_{\text{input}}(z,t)}{L}\frac{\omega \frac{r}{Q}(z)}{2G(z,t)} + \frac{\omega \frac{r}{Q}(z)\mathcal{T}(z,t)\tilde{I}(z,t)}{2}. \quad (3.20)$$

Equation (3.20) can be further simplified by providing an expression for P_{input}. For that, one has to consider that the feeding RF-signal provided by the port suffers several reflections until a targeted gradient G_{end} builds-up in the considered cell. In particular, phenomenology shows [14] that, for the unloaded case ($\tilde{I} = 0$), the gradient builds up as:

$$G(z,t) = G_{\text{end}}(z)\left(1 - e^{-\frac{\omega t}{2Q(z)}}\right). \quad (3.21)$$

Therefore, the input power follows the expression:

$$\frac{P_{\text{input}}(z_k,t)}{L} = \frac{G_{\text{end}}(z_k)^2}{r(z_k)}\left(1 - e^{-\frac{\omega t}{2Q(z)}}\right), \tag{3.22}$$

and, as a consequence, the PDE accounting for gradient reduction in SW reads as:

$$-\frac{\partial G(z,t)}{\partial t} = \frac{\omega}{2Q(z)}G(z,t) - \frac{\omega}{2Q(z)}G_{\text{end}}(z) + \frac{\omega\frac{r}{Q}(z)\mathcal{T}(z,t)\tilde{I}(z,t)}{2}. \tag{3.23}$$

Unlike Eq. (3.17), the quality factor of Eq. (3.23) is the loaded quality factor [14], which considers reflection of the RF signal with the input port.

Power-diffusive PDE features

As a consequence of energy conservation in accelerating structures, two power diffusive PDEs accounting for gradient reduction in TW and SW structures, Eqs. (3.17) and (3.23) respectively, have been derived. Both share some properties:

F1: The last term of Eqs (3.17) and (3.23), $\frac{\omega\frac{r}{Q}\mathcal{T}\tilde{I}}{2}$, is called the beam loading term, and it models the homonym effect. It shows that there is a gradient reduction which depends on the beam charge, more precisely, its averaged intensity $\tilde{I}$.

Such beam-induced gradient reduction depends on ω and r/Q. This means that the BL effect has a great impact in compact accelerating structures, whose cavities operate at high resonating frequencies and exhibit strong $\frac{r}{Q}$ values.

F2: The derivation of these equations uses the paraxial approximation and the quasi-static assumption. In addition, the shunt impedance introduced in Sec. 2.4, a concept inherited from the wakefield formalism, assumes causality of the beam-induced field with respect to the bunches. In other words, these equations are valid as long as the EM excitation induced by a bunch does not catch-up a bunch that entered the structure at an earlier time. This holds for ultrarelativistic scenarios, but a dedicated study should be carried out for non-ultrarelativistic scenarios. This will be presented in Chapter 4.

F3: In non-ultrarelativistic scenarios, $\tilde{I}$ exhibits a recursive dependency with the gradient G through β. For a charge e with rest mass m_0 and initial kynetic energy W_0, its expression is:

$$\beta(z,t) = \sqrt{1 - \left(\frac{m_0c^2}{m_0c^2 + W_0 + eLG_{\text{eff}}(z,t)}\right)^2} \tag{3.24}$$

When $\beta \simeq 1$ and $\mathcal{T} = 1$, i.e for TW structures with optimal phase-flight synchronization, as in Eq. (2.49), these terms are no longer dependent on G and Eq. (3.17) becomes a linear non-homogeneous PDE.

3.3 Fundamental theorem of Beam Loading

Equations (3.17) and (3.23) capture gradient reduction in the considered RF-structures as a consequence of the fulfillment of the Poynting theorem in the structure. This implies that, if energy is conserved in the beam-cavity system, then the stored EM energy of the beam-induced field should come from the energy lost by the beam itself.

To quantify this energy loss, one can consider a single charged particle, q, that enters an empty SW cavity on-axis with no RF input ($G_{\text{end}} = 0$) and with large Q, allowing to neglect ohmic dissipation. For simplicity, we assume a constant value of $\frac{r}{Q}$. In this case, Eq. (3.23) remains:

$$-\frac{\partial G(z,t)}{\partial t} = \frac{\omega \frac{r}{Q} \mathcal{T}(z,t) \tilde{I}(z,t)}{2}. \tag{3.25}$$

For a single charge that enters the cavity at $t = 0$ with $v \simeq c$, $\lambda_q(z,t) = q\delta(t - \frac{z}{c})$, with δ the Dirac-delta distribution. Therefore, $\tilde{I}$ reads as:

$$\tilde{I}(z,t) = \beta_z(z_k,t)\frac{1}{T}\int_t^{t+T} cq\delta\left(\tau - \frac{z}{c}\right) e^{j\omega(\tau - \frac{z}{c})}\, \mathrm{d}\tau = \frac{q}{T}(H(t) - H(t-T)), \tag{3.26}$$

with H the Heavyside function.

For an initially empty cavity, i.e $G(0) = 0$, the resolution of Eq. (3.25) leads to the following expression for the particle-induced gradient:

$$G_{\text{particle-induced}}(t) = \begin{cases} -\frac{\omega}{2}\frac{r}{Q}\mathcal{T} q \frac{t}{T} & 0 < t < T \\ -\frac{\omega}{2}\frac{r}{Q}\mathcal{T} q & t \geq T \end{cases} \tag{3.27}$$

Combining Eqs. (2.58), (2.66) and (3.27) , the stored EM energy in the cavity per unit length after the particle has left the structure, $t = T$, reads as:

$$w(T) = \frac{G_{\text{particle-induced}}(T)}{\frac{r}{Q}\,\omega} = \frac{\omega \frac{r}{Q} \mathcal{T}^2 q}{4}. \tag{3.28}$$

Energy conservation requires that the energy lost by the particle, ΔW, matches the stored EM energy. Therefore, using Eqs. (2.51), (3.27), and (3.28), we get that:

$$\Delta W + w(T)L = 0;$$
$$\Delta W = -\frac{\omega \frac{r}{Q} \mathcal{T}^2 q}{4} L = \frac{G_{\text{particle-induced}}(T)\mathcal{T}L}{2} = \frac{V_{\text{acc, particle-induced}}(T)}{2}. \tag{3.29}$$

Equation (3.29) shows that a particle looses energy at the expense of leaving a particle-induced gradient in the cavity. It also quantifies such energy loss to be half of the induced voltage.

If the cavity is initially empty, the only mechanism which makes the particle lose energy is the same EM field it excited. Therefore, such field must be excited in decelerating phase. This excitation induces a gradient reduction in the structure characterized by Eqs. (3.17) and (3.23). This phenomenon is called Beam Loading Effect.

3.4 Numerical implementation of the power diffusive Beam Loading model in RF-TRACK

RF-TRACK [67] is a tracking code developed at CERN, which allows arbitrary particle tracking under the effect of external and self-induced forces. It is written in parallel C++, and it is imported into Python and Octave as a pre-compiled library. This software offers a flexible accelerator description, handling complex 3D fieldmaps and computing self-consistent single-particle and collective effects such as space-charge, incoherent synchrotron radiation, and short-range wakefields, among others.

To perform particle tracking in RF-TRACK, two different strategies can be followed [68]:

- `Lattice`-like integration: All particles are assumed to lay on the same longitudinal plane ($z = z_0$ for a given $z_0 \in \mathbb{R}$) while their arrival time as longitudinal phase space dynamical variable. In this case, particles are always assumed to move forward, so the phase-space of the beam is updated in steps of $\mathrm{d}S$ where the longitudinal component evolves like: $S \to S + \mathrm{d}S$. This approach is preferable for ultrarelativistic dynamics.

- `Volume`-like integration: In this case, tracking occurs in steps of time, $\mathrm{d}t$, where the time of the particles is updated as $t \to t + \mathrm{d}t$. Therefore, particles are assumed to be at the same time t while their positions can differ one to another. This strategy is preferred for low energy space-charge-dominated regimes.

For either of the approaches, a general tracking routine must include:

1. **Beam definition:** Bunches of arbitrary charge and mass can be defined in RF-TRACK by specifying their initial phase-space coordinates. Bunches are treated as a set of macroparticles. Depending on the tracking strategy, one can define `Bunch6d` bunches for `Lattice` tracking, or `Bunch6dT` bunches for `Volume` tracking.

2. **Element and Tracking environment definition:** RF-TRACK offers the possibility to define symplectic-matrix based elements. In addition, RF-elements based on analytical or externally-imported complex 1D, 2D or 3D fieldmaps can be defined.

   The different elements shall be arranged in the tracking environments `Lattice` and/or `Volume`. `Lattice` restricts element placing to a sequence, where elements go one after the other. `Volume` offers more flexibility and enables superposition or spatial-rotation of the elements.

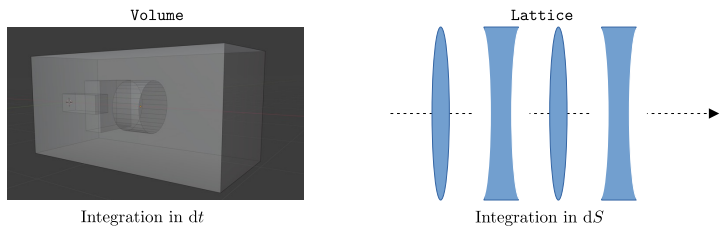

Figure 3.3: `Lattice` and `Volume` sketch [68].

3. **Collective Effects definition:** Collective effects can be defined as `Collective Effect` classes, which are attached to each element where such phenomena takes place. Their effect is modelled as an additional force which is superposed to the force associated to the element itself.

4. **Tracking:** The equations of motion can be integrated for the defined bunches with explicit algorithms such as Runge-Kutta-Fehlberg (4, 5). Among the different tracking options, two different tracking steps can be set: dt (or dS) for element tracking, and dt_{cfx} (or dS_{cfx}) for collective effects.

More details on how to set-up a particle tracking simulation with RF-TRACK and its capabilities can be found at [67].

To perform beam dynamics simulations in realistic beam-loaded scenarios, the

previously-derived power diffusive model has been implemented in RF-Track as a `Collective Effect`. Such implementation uses the solution of Eqs. (3.17) and (3.23) to compute the associated BL kick.

3.4.1 PDE resolution with the finite difference method

According to the feature F2, the BL term in Eqs. (3.17) and (3.23) exhibits a recursive dependency on the gradient itself in the non-ultrarelativistic regime. For this reason, theoretical methods, such as the Laplace transform in Ref [62], can only be deployed in ultrarelativistic scenarios where such dependency no longer exists.

As an alternative, Eqs. (3.17) and (3.23) were solved by using an explicit and forward finite-difference method. This approach is based on the discretization of the PDEs in temporal and spatial steps (as seen in Fig. 3.4), and it allows a flexible computation the evolution of the BL term in each time step.

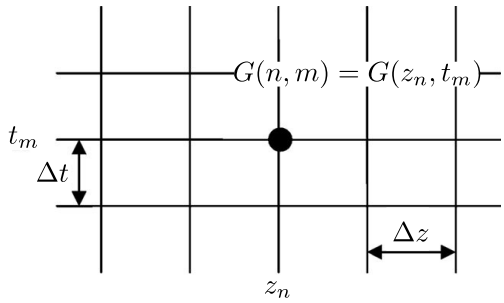

Figure 3.4: Discretized mesh of space and time.

The finite-difference method requires the discretization of the longitudinal and temporal domain in N and M nodes respectively. Therefore, the resolution domain translates in a set of $N \times M$ nodes $\{(z_n, t_m)\}_{n=1,m=1}^{N,M}$, where each coordinate depends on the longitudinal, h, and temporal, Δt, mesh-spacing as:

$$z_n = n \cdot h, \qquad \text{with } n = 1..N; \tag{3.30}$$

$$t_m = m \cdot \Delta t, \qquad \text{with } m = 1..M. \tag{3.31}$$

The mesh-spacings are defined from the considered RF-structure's length, L_{total}, and the beam-induced excitation duration, T_{end}, as:

$$h = \frac{L_{\text{total}}}{N-1}, \qquad \Delta t = \frac{T_{\text{end}}}{M-1}. \tag{3.32}$$

As a consequence of the domain discretization, the quantities involved in the PDEs, such as G, v_g, Q, $\frac{r}{Q}$, and $\tilde{I}$ are treated as arrays whose entries are their evaluation upon the nodes $\{(z_n, t_m)\}_{n=1,m=1}^{N,M}$. Moreover, the partial derivatives are discretized following the forward Euler method [69]. Table 3.3 shows the discretization of all of the terms in Eqs. (3.17) and (3.23).

Continuous form	**Discretized form**
$^{(1)}\ G(z,t)$	$\{G(n,m)\}_{n=1,m=1}^{N,M}, \quad G(n,m) = G(z_n, t_m)$
$^{(2)}\ \frac{r}{Q}(z)$	$\{\frac{r}{Q}(n)\}_{n=1}^{N}, \quad \frac{r}{Q}(n) = \frac{r}{Q}(z_n)$
$\frac{\partial G(z,t)}{\partial z}$	$\frac{G(n+1,m) - G(n,m)}{h}$
$\frac{\partial G(z,t)}{\partial t}$	$\frac{G(n,m+1) - G(n,m)}{\Delta t}$

Table 3.3: Forward-Euler discretization of the quantities in Eqs. (3.17) and (3.23).

The discretized version of Eqs. (3.17) and (3.23) reads as:

$$\text{For TW:} \quad G(n,m+1) = \Delta t B(n) G(n,m) + \Delta t \frac{v_g(z_n)}{\Delta z} G(n-1,m) - C(n,m), \tag{3.33}$$

$$\text{For SW:} \quad G(n,m+1) = \left(1 - \frac{\omega \Delta t}{2Q(z_n)}\right) G(n,m) - C(n,m) + \frac{\omega \Delta t}{2Q(z_n)} G_{\text{end}}(n), \tag{3.34}$$

with

$$B(n) = \frac{1}{2} \left.\frac{\mathrm{d}v_g}{\mathrm{d}z}\right|_{z_n} + \left.\frac{\mathrm{d}r/Q}{\mathrm{d}z}\right|_{z_n} \frac{v_g(z_n)}{2r/Q(z_n)} - \frac{\omega}{2Q(z_n)} - \frac{v_g(z_n)}{\Delta z} + \frac{1}{\Delta t}, \tag{3.35}$$

$$C(n,m) = \Delta t \frac{\omega \frac{r}{Q}(z_n) \mathcal{T}(z_n, t_m) \tilde{I}(z_n, t_m)}{2}. \tag{3.36}$$

Numerical stability

The numerical stability of Eq. (3.33) can be assessed with the Von Neummann analysis [69]. For that, we assume that the solution $G(n,m)$ is of the form:

$$G(n,m) = \tilde{G}(m) e^{jknh}, \tag{3.37}$$

where k is a real spatial wave number, which can have any value. Substituting Eq. (3.37) in Eq. (3.33), one gets:

$$\tilde{G}(m+1) e^{jknh} = \Delta t B(n) \tilde{G}(m) e^{jknh} + \Delta t \frac{v_g(z_n)}{\Delta z} \tilde{G}(m) e^{jk(n-1)h} - C(n,m); \tag{3.38}$$

$$\tilde{G}(m+1) = \underbrace{\left(\Delta t B(n) + \Delta t \frac{v_g(z_n)}{\Delta z} e^{-jkh}\right)}_{\xi(n)} \tilde{G}(m) - C(n,m) e^{-jknh}. \tag{3.39}$$

Equation (3.39) shows that the amplitude of the solution at t_{m+1} has a part that scales with the amplitude at t_m, ξ; and an independent term which does not scale with it. Therefore, for the solution to be stable, we shall study the condition $|\xi(n)|^2 \leq 1$:

$$\left(\Delta t B(n) + v_g(z_n)\frac{\Delta t}{h}\cos(kh)\right)^2 + v_g(z_n)^2\frac{(\Delta t)^2}{h^2}\sin^2(kh) \leq 1 \tag{3.40}$$

$$(\Delta t)^2 B(n)^2 + 2v_g(z_n)B(n)\frac{(\Delta t)^2}{h}\cos(kh) + v_g(z_n)^2\frac{(\Delta t)^2}{h^2} \leq 1; \tag{3.41}$$

For simplicity, we consider a constant impedance and constant group velocity structure. Also, we impose the condition $h = \Delta t$. Therefore, the stability condition remains:

$$\left(-\frac{\omega h}{2Q} - v_g + 1\right)^2 + 2v_g\left(-\frac{\omega h}{2Q} - v_g + 1\right)\cos(kh) + v_g^2 \leq 1; \tag{3.42}$$

Since k can take any real value, the extreme cases where $\cos(kh) = \pm 1$ shall be examined:

- $\cos(kh) = 1$. In this case:

$$\left(-\frac{\omega h}{2Q} - v_g + 1\right)^2 + 2v_g\left(-\frac{\omega h}{2Q} - v_g + 1\right) + v_g^2 \leq 1; \tag{3.43}$$

$$\left(-\frac{\omega h}{2Q} - v_g + 1 + v_g\right)^2 \leq 1 \iff \left(1 - \frac{\omega h}{2Q}\right)^2 \leq 1, \tag{3.44}$$

  which holds for realistic scenarios where $Q \gg 1$.

- $\cos(kh) = -1$. In this case:

$$\left(-\frac{\omega h}{2Q} - v_g + 1\right)^2 - 2v_g\left(-\frac{\omega h}{2Q} - v_g + 1\right) + v_g^2 \leq 1; \tag{3.45}$$

$$\left(-\frac{\omega h}{2Q} - 2v_g + 1\right)^2 \leq 1. \tag{3.46}$$

  Since $v_g < 1$ and $Q \gg 1$, condition (3.46) holds.

As it will be shown in Section 3.5, and Chapters 4 and 5, the TW structures that will be considered through this work do not show strong variations in v_g and $\frac{r}{Q}$, and the previous stability discussion is valid for these cases. Therefore, the numerical implementation of Eq. (3.17) requires the condition:

$$h = \Delta t. \tag{3.47}$$

To assess the numerical stability of Eq. (3.34), we iterate m times Eq. (3.34) and get the following expression for each value of n:

$$G(n,m+1) = \left(1 - \frac{\omega\Delta t}{2Q(z_n)}\right)^m G(n,0) - \sum_{j=0}^{m-1} \left(1 - \frac{\omega\Delta t}{2Q(z_n)}\right)^j \left(\frac{\omega\Delta t}{2Q(z_n)} G_{\text{end}}(n) - C(n,m)\right). \tag{3.48}$$

The stability of the numerical resolution is guaranteed if the growth associated to the amplitude of G is controlled, that is, if $|1 - \frac{\omega\Delta t}{2Q(z_n)}| \leq 1$. Therefore, the stability condition for the resolution of Eq. (3.34) is:

$$-1 \leq 1 - \frac{\omega\Delta t}{2Q(z_n)} \leq 1 \iff \frac{Q(z_n)}{\omega} \geq \Delta t \geq 0. \tag{3.49}$$

3.4.2 Beam Loading in RF-TRACK's version 2.2.3

The Beam Loading effect was implemented in RF-TRACK's version 2.2.3 as two different `Collective Effects` named `BeamLoading` and `BeamLoadingSW`. They both benefit from RF-TRACK's cubic interpolation routines as well as the numerical tools imported from the GNU Scientific Library (GSL) and the Fastest Fourier Transfor in the West (FFTW) libraries in C++.

In both scenarios, the BL kick applied to a particle of charge q at a longitudinal position z_{part} at time t_{part} reads as:

$$F_{z,\text{BL}}(z_{\text{part}}, t_{\text{part}}) = q\text{Re}\left[G_{\text{beam-induced}}(z_{\text{part}}, t_{\text{part}}) e^{j\omega[(t_{\text{part}} - \langle t\rangle_{\text{bunch}}) - (z_{\text{part}} - \langle z\rangle_{\text{bunch}})/c]}\right] \tag{3.50}$$

with $G_{\text{beam-induced}}$ the cubic interpolated value of the beam-induced gradient at (z_{part}, t_{part}), and $\langle t\rangle_{\text{bunch}}$, $\langle z\rangle_{\text{bunch}}$ the mean time and position of the considered bunch.

A few words on the two different implementations:

- `BeamLoading`: Assumes ultrarelativistic motion of the particles in a TW structure. For constant charge-per-bunch trains, the BL term in Eq. (3.36) can be known before tracking, and Eq. (3.33) can be calculated a priori. As specified in Fig. 3.5a, this requires knowledge of some beam information such as charge, population, and bunch-to-bunch spacing.

  In this case, the beam-induced gradient is calculated independently of the RF-structure to which the collective effect is attached. This calculation is performed before tracking, resulting into a fast and efficient implementation.

- `BeamLoadingSW`: Designed for SW cavities where particles do not necessarily travel with $v \simeq c$, like an electron gun. Here, Eq. (3.34) is solved at every tracking step. To calculate $\tilde{I}$ in each step, the user is required to provide information about the RF-structure to which the effect is attached.

  This method allows a flexible description of the considered beam since Eq. (3.34) is solved on the fly, allowing the simulation of non-homogeneous charge-per-bunch profiles.

A general schematic on the algorithm of both implementations is shown in Fig. 3.5. Further information and examples can be consulted in [67] and in Appendix A.2.

3.4.3 Beam Loading in RF-TRACK's version 2.3.0

The previous `BeamLoading` algorithm presented two limitations when applied to TW structures: The BL effect of trains of bunches with different charges per bunch cannot be calculated, as well as the superposition of the beam-induced fields from different species. To handle these scenarios, RF-TRACK's version 2.3.0 implements a

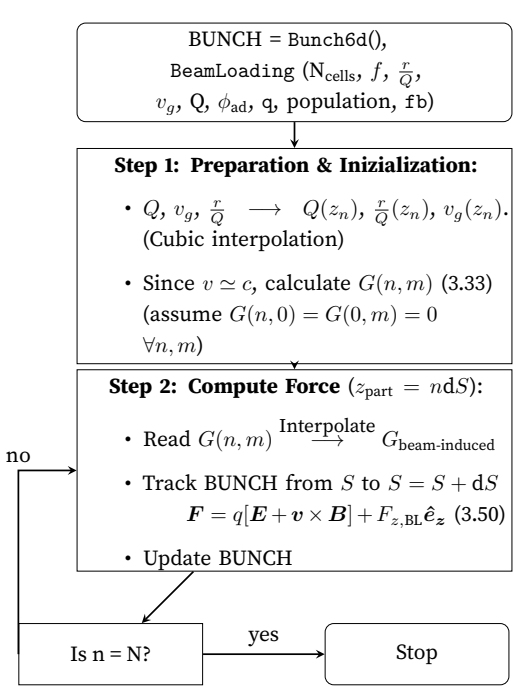

(a) `BeamLoading` schematic.

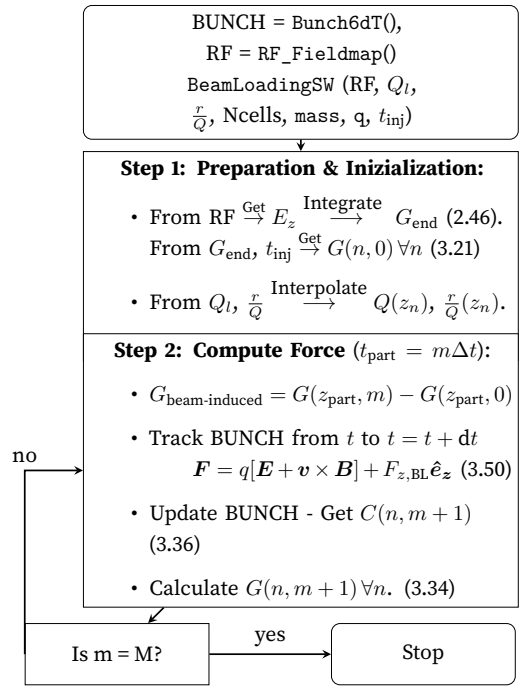

(b) `BeamLoadingSW` schematic.

Figure 3.5: Flowchart of the beam-loading algorithms in RF-Track v. 2.2.3.

more-flexible `BeamLoading` algorithm.

This new approach makes use of Eq. (3.33) to calculate the single-particle solution to Eq. (3.17), G_{single}. Because we are in the ultrarelativistic regime, Eq. (2.49) holds, and the on-axis single-particle-induced longitudinal electric field in an arbitrary TW structures reads as:

$$E_z(z,t) = \text{Re}\left[G_{\text{single}}(z,t)e^{j(\omega t - \frac{\omega}{c}z)}\right]. \tag{3.51}$$

Equation (3.51) can now be used to compute the longitudinal wake function, w_l, with Eq. (2.34). Equation (2.38) allows to define the BL kick as:

$$F_{z,\text{BL}}(z) = -\frac{1}{L_{\text{total}}}\int_{-\infty}^{\infty} \mathrm{d}s\lambda_q(s)w_l(z-s). \tag{3.52}$$

Long trains of bunches usually exhibit the following feature: The time-structure of a single bunch is two-three orders of magnitude lower than the bunch-to-bunch spacing. Figure. 3.6 shows an example where each bunch extends several picoseconds while the bunch-to-bunch spacing is of the order of a nanosecond. This allows to split the calculation of Eq (3.52) in two terms: The short-range-force term and the long-range-force term.

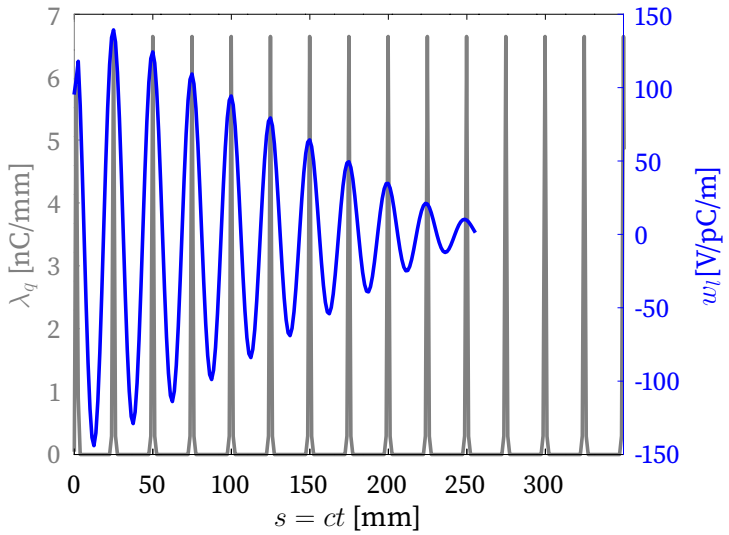

Figure 3.6: In blue, the longitudinal wake function for an X-band TW structure. In grey, a train of 15 Gaussian bunches with 8.33 nC/bunch, spacing of 25 mm and $\sigma_z = 1$mm per bunch.

Splitting the BL calculation in these two terms is specially advantageous when tracking long trains of bunches. Otherwise, RF-TRACK would need to store a large number of bins in memory to capture the beam density in detail to compute Eq (3.52), which would slow down significantly the simulations.

Computation of long-range and short-range effects

For a train of $N_{\text{bunches}} \in \mathbb{R}$ Gaussian bunches with total charge-per-bunch $q^{(i)}_{\text{bunch}}$, the linear charge density can be expressed as the sum of the linear charge density of each bunch $\lambda^{(i)}_q$ as:

$$\lambda_q(z) = \sum_{i=1}^{N_{\text{bunches}}} \lambda^{(i)}_q(z). \tag{3.53}$$

To compute the BL force upon a particle that belongs to the j-th bunch ($j \leq N_{\text{bunches}}$), we substitute Eq. (3.53) in Eq. (3.52) and separate the terms as follows:

$$\begin{aligned} F_{z,\text{BL}}(t_{\text{part}}) &= -\sum_{i=1}^{N_{\text{bunches}}} \frac{1}{L_{\text{total}}} \int_{-\infty}^{\infty} \mathrm{d}s \lambda_q(s)^{(i)} w_l(ct_{\text{part}} - s) \\ &= \underbrace{-\frac{1}{L_{\text{total}}} \int_{-\infty}^{\infty} \mathrm{d}s \lambda_q(s)^{(j)} w_l(ct_{\text{part}} - s)}_{\text{Short-range Force}} \underbrace{- \sum_{i \neq j} \frac{1}{L_{\text{total}}} \int_{-\infty}^{\infty} \mathrm{d}s \lambda_q(s)^{(i)} w_l(ct_{\text{part}} - s)}_{\text{Long-range Force}}. \end{aligned} \tag{3.54}$$

- To calculate the **short-range force** term in Eq. (3.54), the procedure is inherited from RF-TRACK's already-existing wakefield solver routine, which uses the Fast Fourier Transform (FFT) [69] algorithm and the Convolution Theorem [70]. This requires sampling the involved magnitudes, λ_q and w_l, in arrays of N elements and performing $N \log N$ operations.

- To calculate the **long-range force** term in Eq. (3.54), we model far bunches as point-like particles. In other words, $\lambda^{(i)}_q(z) = q^{(i)}_{\text{bunch}} \delta(z - z_i)$, with z_i the mean position of the i-th bunch. This leads to the following simplified expression:

$$\begin{aligned} F(t_{\text{part}})_{z,\text{BL, long-range}} &= -\sum_{i \neq j} \frac{1}{L_{\text{total}}} \int_{-\infty}^{\infty} \mathrm{d}s \, q^{(i)}_{\text{bunch}} \, \delta(ct_{\text{part}} - z_i) w_l(z_{\text{part}} - s) \\ &= -\frac{1}{L_{\text{total}}} \sum_{i \neq j} q^{(i)}_{\text{bunch}} \, w_l(ct_{\text{part}} - z_i). \end{aligned} \tag{3.55}$$

  Equation (3.55) allows a more efficient implementation of the long-range BL effects since the wake function w_l can be computed prior to tracking, so that Eq. (3.55) is calculated by cubic interpolation.

An schematic on the `BeamLoading` algorithm in version 2.3.0 is illustrated in Fig. 3.7. As it can be found in Ref [67], the major update of version 2.3.0 is the `Beam` structure, which allows to track an array of bunches in a go with long-range interactions as well as short-range effects.

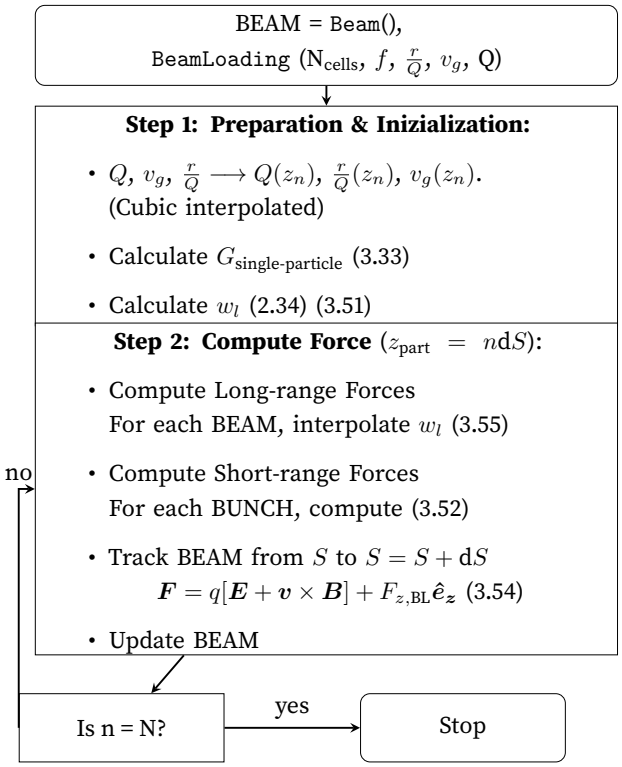

Figure 3.7: `BeamLoading` algorithm in RF-Track version 2.3.0.

Transverse forces

For the computation of the BL kick, only longitudinal forces are considered. This can be justified from two equivalent points of view:

- The longitudinal electric field that drives the BL force, in Eq. (3.51), corresponds to the floquet harmonic of the fundamental mode, in Eq. (2.27), with phase velocity c. For the same mode, the argument of the Bessel functions for the radial electric field and the azimutal magnetic field, in Eqs. (2.29) and (2.30) respectively, cancel out, and no transverse kick is provided by the BL force.

- Longitudinal and transverse wake functions are linked by the so-called Panofsky-Wenzel theorem [46]. For the fundamental longitudinal wakefield, it

is widely known that it exhibits no associated transverse wakefield, thus no kick in this direction is applied to the particles.

3.5 Benchmark against previous results

The performance of the new BL modules in RF-TRACK has been assessed by simulating three well-studied scenarios of CLIC based on X-band technology:

- CLIC Accelerating Structures (AS). They were conceived to accelerate the main beam.
- CLIC Power Extraction and Transfer Structures (PETS). These are passive cavities conceived for CLIC's drive beam deceleration due to the BL effect so that its power is extracted to feed CLIC AS.
- CLIC-K main accelerating structures, a klystron based alternative to CLIC AS.

The accelerating structures and beam specifications are shown in Table 3.4. For this benchmark, 20 bunches of the drive beam were simulated, instead of the nominal 2922.

3.5.1 Transient gradient reduction in CLIC Accelerating Structures

A train of 312 electron bunches with $q_{\text{bunch}} = -600\,\text{pC}$ and a bunch injection frequency of $f_b = 2.0\,\text{GHz}$ has been tracked along AS. Figure 3.8a shows the gradient reduction due to BL when such a train enters the structure. A similar curve is shown in Figure 3.8b, where the gradient reduction is calculated with the Laplace Transform of Eq. (3.17) for the case of $\mathcal{T} = \beta \simeq 1$. As seen in Ref [62], this method has also been successfully benchmarked with HFSS [72] simulations.

The solid blue line informs of the initial gradient along the structure, which for the input power of $61.3\,\text{MW}$ is $120\,\text{MV/m}$ in average. When the mentioned beam enters the structure, a gradient reduction (illustrated by red-dashed lines) occurs, until a steady state is reached (solid red line).

Figure 3.8 shows that the steady state, characterized by $\frac{\partial G}{\partial t} = 0$, occurs when an equilibrium between the power feeding the considered cell and the dissipated power is reached. Such balance is achieved at the so-called filling time t_{fill}, which is defined

Magnitude	Symbol	Units	CLIC AS / CLIC-K	CLIC PETS
Frequency	f	GHz	11.99	11.99
Number of cells	N_{cells}	-	27	34
Phase advance	ϕ_{ad}	rad	$\frac{2\pi}{3}$	$\frac{\pi}{2}$
Group velocity	v_g	$\%c$	(1.65, 1.2, 0.83)$^{(1)}$	0.453
Quality factor	Q	-	(5536, 5635, 5738)$^{(1)}$	7200
Shunt Impedance p.u.l	$\frac{r}{Q}$	kΩ/m	(14.59 16.22 17.95)$^{(1)}$	2700
Input power	P_{input}	MW	61.30	0.00
Nb. of bunches / train	N_{bunches}	-	312	2922
Charge per bunch	q_{bunch}	pC	-600	-8330
Bunch spacing	c/f_b	mm	150	25
Initial Energy	E_0	GeV	9.0	2.4
Initial bunch length	σ_t	mm/c	0.044	1.0
Initial norm. $x-$emitt.	ϵ_x	mm mrad	0.600	150
Initial norm. $y-$emitt.	ϵ_y	mm mrad	0.005	150

$^{(1)}$ (first, middle, last cell)

Table 3.4: CLIC nominal AS and PETS structure and beam parameters [7, 71].

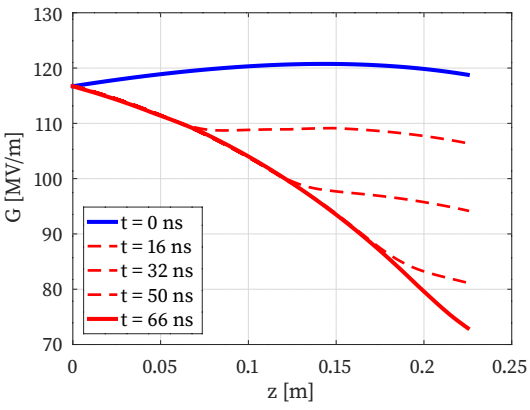

(a) RF-TRACK resolution of Eq (3.17) for CLIC AS in version 2.2.3 and 2.3.0.

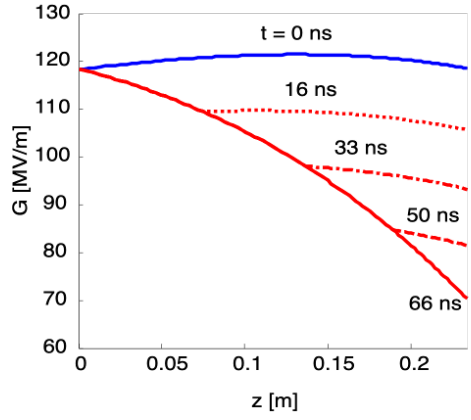

(b) Laplace Transform analytical resolution of Eq. (3.17). Extracted from [62].

Figure 3.8: Transient gradient reduction in CLIC AS for the beam specifications in Tab. 3.4.

in the following way for TW structures:

$$t_{\text{fill}} = \int_0^{L_{\text{total}}} \frac{\mathrm{d}z}{v_g(z)}, \tag{3.56}$$

which equals $66\,\mathrm{ns}$ in this case.

The transient nature of the beam-induced field implies that the beam does not gain energy uniformly. Instead, there is a beam-induced energy spread from first to last bunch as illustrated in Fig. 3.9.

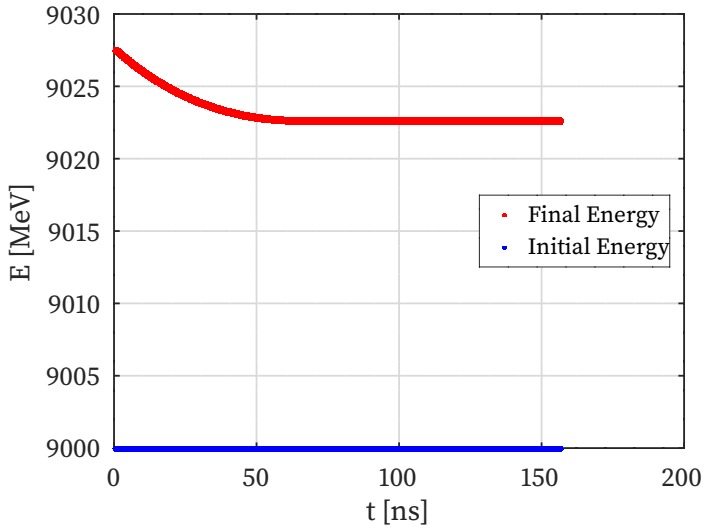

Figure 3.9: Longitudinal phase-space of the Beam specified in Tab. 3.4 after being tracked through CLIC AS. Simulation performed with 10^4 macroparticles per bunch.

Figure 3.9 shows the energy distribution of the 312 bunches, where the first 124 bunches are affected in a different way by the beam-induced gradient, while the rest experience the same energy gain of $\simeq 22\,\mathrm{MeV}$.

In many cases, there is interest in simulating only the steady state. For this reason, RF-Track also provides a routine which directly computes this regime. Figure 3.10a shows the steady state beam-induced gradient and its effect upon tracking of the previous bunch.

If we compare the mean energy of the last bunch of the train, $\langle E_{\mathrm{end}} \rangle$, obtained with the steady-state BL routine and the standard/transient BL routine, the deviation is:

$$\delta_{\langle E_{\mathrm{end}} \rangle} = \frac{|\langle E_{\mathrm{end}} \rangle_{\mathrm{transient}} - \langle E_{\mathrm{end}} \rangle_{\mathrm{steady}}|}{\langle E_{\mathrm{end}} \rangle_{\mathrm{transient}}} = 2.52 \times 10^{-3}\ \%, \tag{3.57}$$

which proves the solidity of the proposed algorithms.

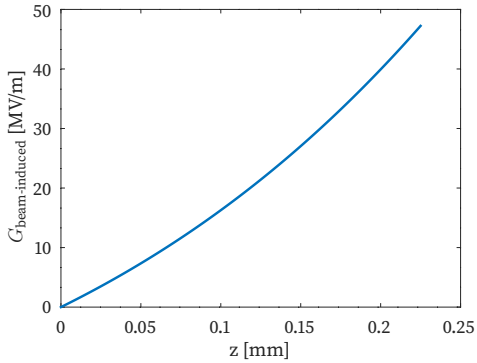

(a) Steady-state beam-induced gradient calculation with RF-TRACK.

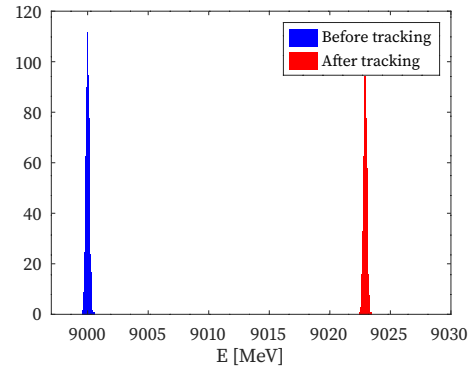

(b) Energy distribution prior and after tracking under the steady-state BL field.

Figure 3.10: Steady gradient reduction in CLIC AS for the beam specifications in Tab. 3.4.

3.5.2 Benchmark against PLACET for CLIC Power Extraction and Transfer Structures

A test beam of 20 bunches with $q_{\text{bunch}} = -8.33\,\text{nC}$, $f_b = 12.0\,\text{GHz}$ and an initial energy of $2.40\,\text{GeV}$ has been tracked through 1492 CLIC PETS. The results are shown in Fig. 3.11, where the longitudinal phase space of the beam (Figure 3.11a) and the last bunch (Figure 3.11c) are displayed.

In this case, the steady state is reached at $t_{\text{fill}} = 1.6\,\text{ns}$, coinciding with the time when the bunch 11 leaves the structure.

Good agreement is found comparing RF-TRACK's results with PLACET's results, shown in Figs. 3.11b and 3.11d. To compare both simulations, we study the power-extraction efficiency factor, η_{extr}, defined in terms of the minimum energy of the beam, E_{min}, as:

$$\eta_{\text{extr}} = \frac{E_0 - E_{\text{min}}}{E_{\text{min}}}. \tag{3.58}$$

The discrepancies between RF-TRACK and PLACET are shown in Tab. 3.5, showing nice agreement between both codes with a relative deviation between both η_{extr} of $0.67\,\%$.

In PLACET, PETS are conceived as specific elements through which a group-velocity-dependent flow of the longitudinal wakefield is admitted in this particular situation [71]. However, this wake flow strategy is not implemented in arbitrary TW structures,

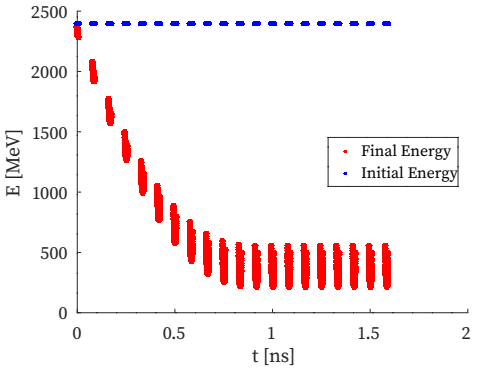

(a) Beam longitudinal phase-space after 1492 PETS simulated with RF-TRACK.

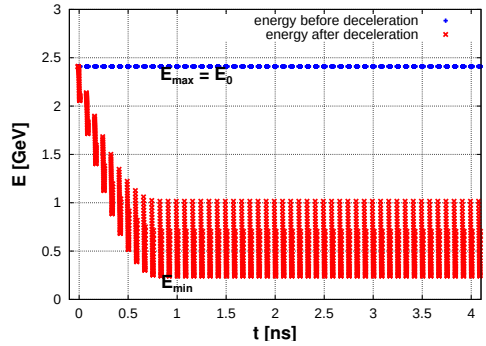

(b) Beam longitudinal phase-space after 1492 PETS simulated with PLACET [71].

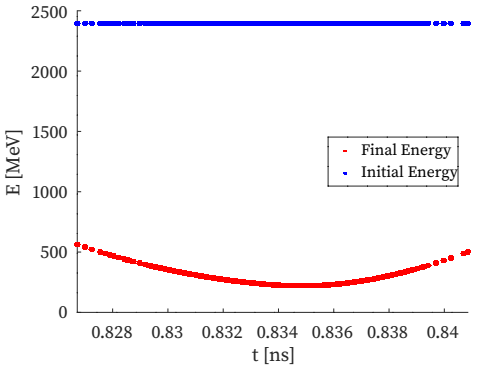

(c) 11-th bunch longitudinal phase-space after 1492 PETS simulated with RF-TRACK.

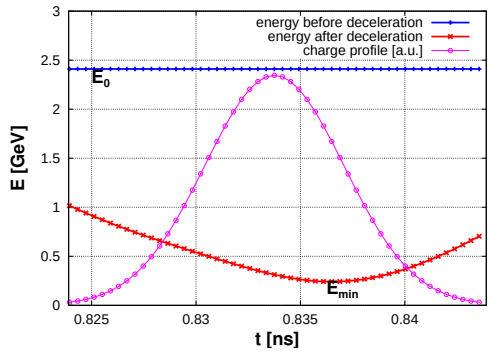

(d) 11-th bunch longitudinal phase-space after 1492 PETS simulated with PLACET [71].

Figure 3.11: Longitudinal phase-space after 1492 PETS for the beam and structure specifications in Tab. 3.4.

meaning that this effect cannot be computed in externally fed structures.

RF-TRACK provides an alternative to PETS simulation as an organic result of an implementation of BL general enough to consider arbitrary TW and SW structures. This enables more general beam dynamics simulations in regimes of strong BL.

3.5.3 Wakefield comparison with GDFIDL

This subsection compares RF-TRACK's calculation of the longitudinal wakefield from the fundamental mode with GDFIDL, a software designed and developed by W. Bruns that computes electromagnetic fields in 3D structures [61].

Tracking Code	E_{min} [MeV]	η_{extr} [%]
RF-TRACK	241.6	89.9
PLACET	240.0	90.0

Table 3.5: Power-extraction efficiency factor comparison between RF-TRACK and PLACET.

An alternative scenario for CLIC based on klystron structures, named CLIC-K, was designed in Ref [73] making use of GDFIDL for the calculation of the wakefields. The considered X-band TW structure, presented in Fig. 3.12, presents several loads that absorbe High-Order Modes (HOMs). Therefore, the main contribution expected in the longitudinal plane is the effect of the fundamental mode.

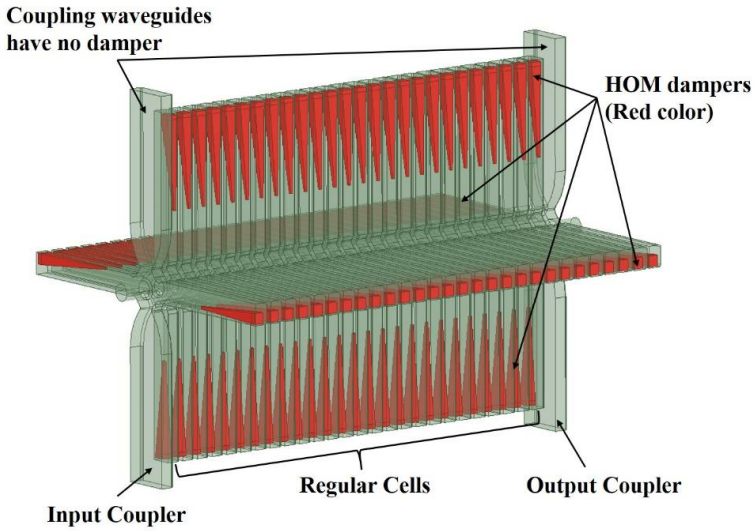

Figure 3.12: Geometry of the CLIC-K Accelerating Structure with damping HOMs loads. Figure extracted from [73]

From Eq. (2.39), the longitudinal wakefield is obtained from the wake potential that GDFIDL calculates. Figure 3.13a shows the calculation for a bunch of charge $q_{\text{bunch}} = 1\,\text{C}$ and $\sigma_z = 1.2\,\text{mm}$ travelling on-axis.

GDFIDL's wake potential calculation involves the computation of the 3D time-dependent EM fields excited by such bunch in the considered 3D geommetry. For this reason, despite GDFIDL being optimised for Multi-Core systems, the simulations took $16\,\text{days}$ in a 32-nodes server. In compensation, the retrieved spectrum contains infor-

mation of all of the HOMs that survive in the structure, as it can be seen in Fig. 3.13b.

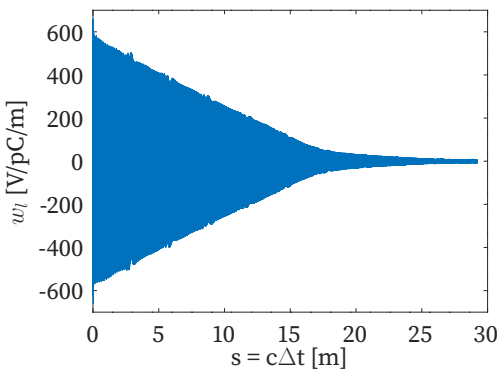

(a) Longitudinal wakefield.

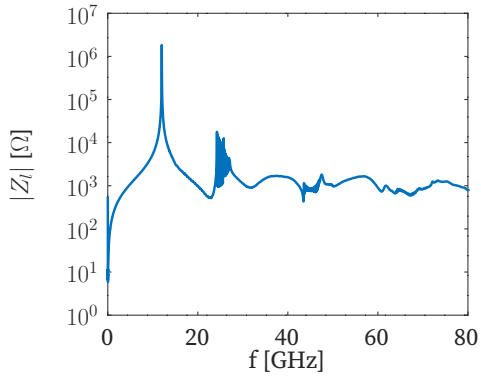

(b) Longitudinal impedance (modulus).

Figure 3.13: GdFidl calculation for the longitudinal beam-induced fields for CLIC-K Accelerating Structure.

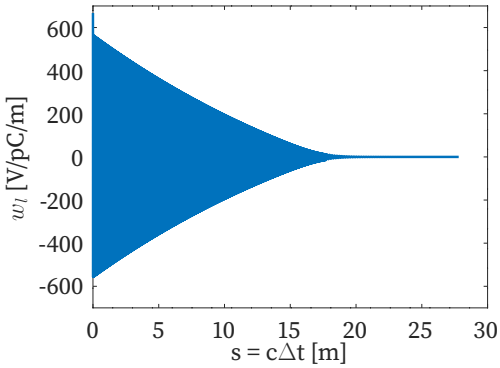

Figure 3.14: w_l from RF-Track.

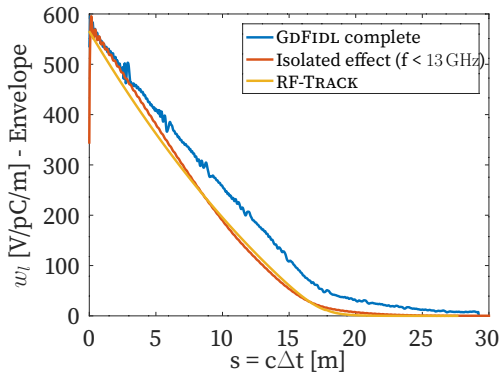

Figure 3.15: w_l amplitude comparison.

Figure 3.14 shows the longitudinal wake function calculated by RF-Track. Discrepancies with respect to Fig. 3.13a in the length and the amplitude are due to the fact that GdFidl's results consider HOMs that survive after the loads action. However, if the fundamental mode is isolated, the wake-function that corresponds only to the fundamental mode can be calculated by applying Eq. (2.42) to the filtered impedance spectrum.

Figure 3.15 shows the a comparison of the amplitude of the wakes calculated with RF-Track and GdFidl. Good agreement is found with the isolated effect from the fundamental mode, confirming the correctness of the module developed in RF-Track.

3.6 Compensation of the Beam Loading effect

The standard techniques for BL compensation rely on an understanding of the temporal dynamics of the EM fields described by Eqs (3.16) and (3.19). Indeed, an optimal choice of the initial and boundary conditions as well as the injection time of the bunches counteracts the beam-induced contribution in Eqs. (3.16) and (3.19).

3.6.1 Beam Loading compensation in standing-wave structures

The temporal build-up of EM fields in SW cavities depends on the characteristic time, τ, defined as:

$$\tau = \frac{2Q_l}{\omega}. \tag{3.59}$$

Figure 3.16 shows the solution of Eq. (3.19) for the unloaded case ($\tilde{I} = 0$), which stabilizes at its maximum value $G \simeq G_{\text{end}}$ when $t \gg \tau$. If a train of electron bunches is injected at a time t_{inj}, a beam-induced field builds up and the total gradient diminishes.

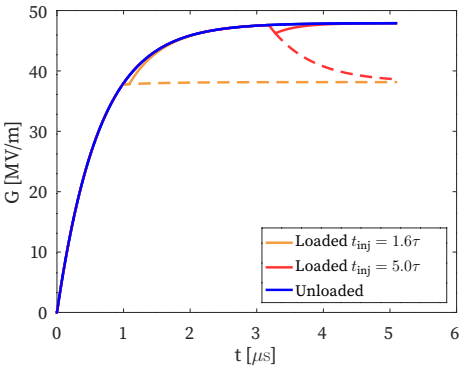

Figure 3.16: Gradient build-up in a 2.6 cell S-band SW photoinjector with $G_{\text{end}} = 48.0$ MV/m. The dashed lines represent the gradient reduction caused by an infinte train.

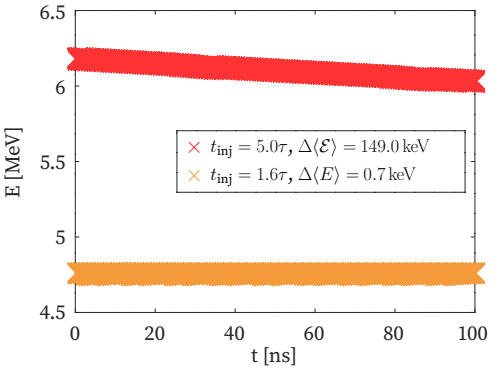

Figure 3.17: Longitudinal phase-space of two 150-bunch electron beams ($q_{\text{bunch}} = -300$ pC) injected at $t_{\text{inj}} = 5.0t_{\text{fill}}$ (red) and $t_{\text{inj}} = 1.6t_{\text{fill}}$ (orange) simulated with RF-Track.

One can find an optimal injection time t^*_{inj} where the beam-induced gradient reduction compensates the gradient rise in the early stages of the filling of the cavity. To account for this effect, the resolution of Eq. (3.19) was implemented in RF-Track's version 2.3.0 for $t < t_{\text{inj}}$ so that the previous behavior is captured. Therefore, the new

implementation requires the user to specify the injection time of the beam t_{inj} (see Appendix A.2).

Figure 3.17 shows the comparison between the long-range longitudinal phase-space of a train of 50 electron bunches injected with $q_{\text{bunch}} = -300$ pC in the SW structure at a time $t^*_{\text{inj}} = 1.6t_{\text{fill}}$ and a train injected at $t_{\text{inj}} = 5t_{\text{fill}}$. It shows that BL can be compensated by choosing an early injection time t^*_{inj} at the expense of not benefiting from the maximum energy gain.

3.6.2 Beam Loading compensation in travelling-wave structures

The idea behind BL compensation in TW structures is similar to the compensation in SW structures: to inject the beam into the structure in a way that the beam-induced gradient compensates the unloaded field build-up.

The creation and propagation of the fundamental accelerating mode in the structure, Eq. (3.16) for the unloaded case ($\tilde{I} = 0$), should be revised for the initial condition $G(z,t) = 0,\ z \in (0, L)$. This requires a spatial initial condition for the gradient of the first cell, which depends on the input power P_{input} provided by the coupling cell [62], which reads as:

$$G(z=0,t) = \sqrt{\frac{\omega \frac{r}{Q}(0) P_{\text{input}}(t)}{v_g(0)}},\ t \in [0, \infty). \tag{3.60}$$

Figure 3.18 presents the build-up in a CLIC TW accelerating structure. This structure is ramped-up from 0 to a desired value $P_{\text{input}}(t^*) = P_{\text{input,max}}$ (Fig. 3.18a) at time t^*, which gives an accelerating gradient in the first cell of $G(0, t^*) = G_{\text{end,0}}$ (Fig. 3.18b). Then, for $t \in [t^*, t^* + t_{\text{fill}})$, this final power configuration propagates through all the structure until a steady unloaded gradient is reached (Fig. 3.18c).

As shown in Appendix A.2, the developed BL module in RF-Track allows the calculation of unloaded gradient build-up for arbitrary P_{input} profiles. It also allows flexibility for the injection-time of the beam, which enables the compensation of this effect.

This is shown in in Fig. 3.19a, where the unloaded gradient associated to the previously described $P_{\text{input}}(t)$, in Fig. 3.18c, compensates the gradient induced by a beam of 312 bunches with $-600\,\text{pC/bunch}$ and $f_b = 2\,\text{GHz}$ injected at $t^* = 89\,\text{ns}$, in Fig. 3.18d. This results in a homogeneous energy profile in the long range longitudinal phase-space, as seen in Fig 3.19b.

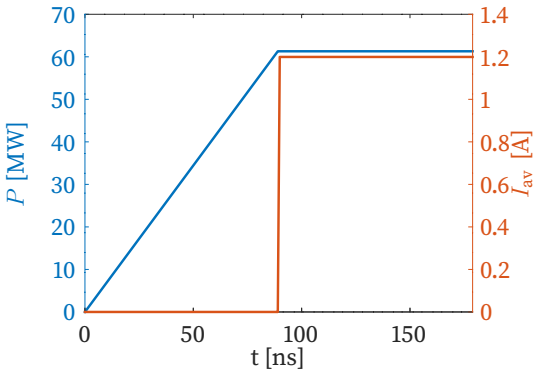

(a) Ramp-up input power until $P_{\text{input,max}} = 61$ MW.

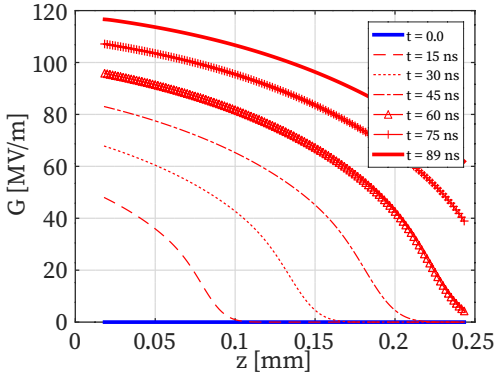

(b) Unloaded gradient rise until $G_{\text{end},0} = 117\,\text{MV/m}$ is achieved at $t^* = 89\,\text{ns}$.

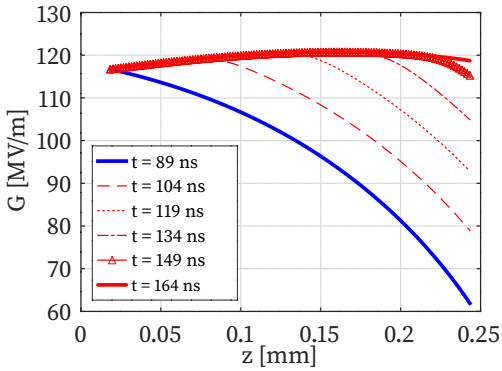

(c) Unloaded gradient rise until the steady state.

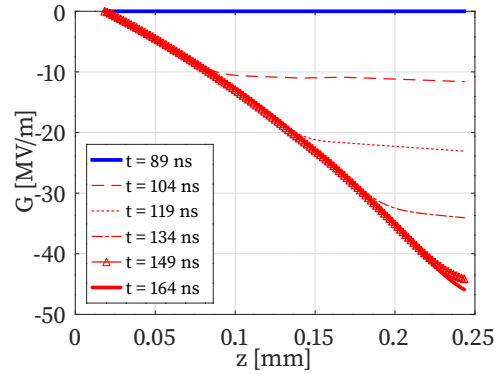

(d) Beam-induced field for $q_{\text{bunch}} = -600$ pC, $N_{\text{bunches}} = 312$ and bunch-spacing 0.5 ns.

Figure 3.18: Transient build-up of the gradient in a CLIC AS with $t_{\text{fill}} = 67$ ns.

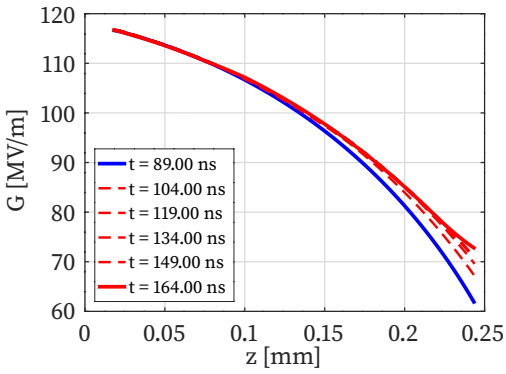

(a) Fig. 3.18c + Fig. 3.18d.

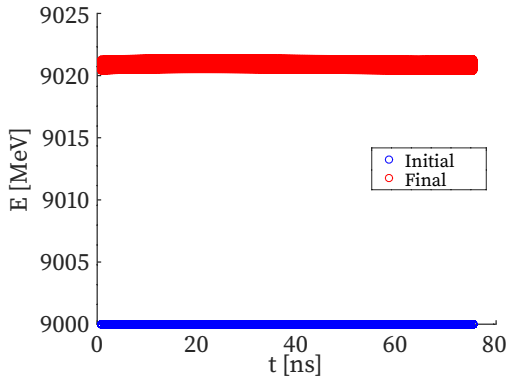

(b) Longitudinal phase space.

Figure 3.19: Compensated BL effect in CLIC AS for a beam of 312 electron bunches with q_{bunch} $-600\,\text{pC}$, bunch-spacing $0.5\,\text{ns}$, and $\langle E_0 \rangle = 90\,\text{MeV/bunch}$.

Charge-varying scenarios

The previous strategy for BL compensation in TW structures relies on the fact that beams of constant q_{bunch} induce a steady-state which can be compensated. However, when the charge per bunch is not constant, no steady-state is reached and, as a result, the energy gain along the structure is not constant for all bunches. This is shown in Fig. 3.20 for a beam of decreasing charge per bunch (whose intensity profile is shown in Fig. 3.21a).

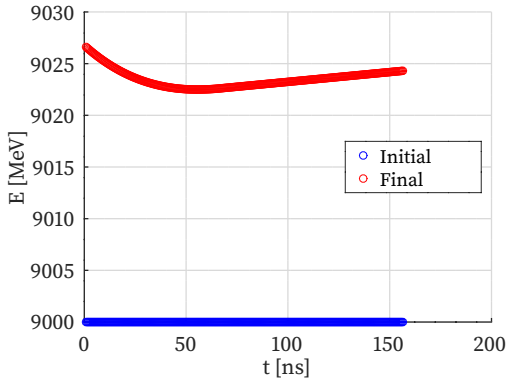

Figure 3.20: Longitudinal phase-space for a charge-varying beam entering CLIC AS at $t_{\text{inj}} = 155\,\text{ns}$.

In practice, bunches can have different charges because of losses in transmission, or by operation choice. Version 2.3.0 of RF-TRACK's BL implementation offers the flexibility to compute this effect for arbitrary charge profiles. To show this, we benefit from RF-TRACK's interface with Octave to use the "Nelder-Mead simplex method" [74], which is a single objective optimisation method in a multi-dimensional space and is named "fminsearch" in OCTAVE. The merit function to minimize the long-range BL contribution was defined as:

$$f = (\max_i \langle E_i \rangle - \min_i \langle E_i \rangle)^2, \tag{3.61}$$

where $\langle E_i \rangle$ is the mean energy of the $i-$th bunch.

The degrees of freedom to minimize Eq. (3.61) were t_{inj} and the coefficients a_1 and a_2 that define the input power spline as:

$$P_{\text{input}}(t) = \begin{cases} a_1 t^3 + a_2 t^2 + a_3 t & \text{if } t < t_{\text{inj}} \\ P_{\text{input, max}} & \text{if } t \geq t_{\text{inj}} \end{cases} \tag{3.62}$$

Here, a_3 was chosen to ensure continuity of Eq. (5.22) at $t = t_{\text{inj}}$.

The optimal parameters that result from the minimization are shown in Tab. 3.6, and the corresponding input power curve can be seen in Fig. 3.21a.

Parameter	Unit	Value
a_1	$\mathrm{MW/ns^3}$	-48.61
a_2	$\mathrm{MW/ns^2}$	122.3
a_3	$\mathrm{MW/ns}$	150.6×10^3
t_{inj}	ns	86.57

Table 3.6: Optimal Input Power Parameters.

Figure 3.21b illustrates the beam longitudinal phase-space for the compensated scheme, showing that the energy spread is reduced from $4.23\,\mathrm{MeV}$ in Fig. 3.20 to $1.55\,\mathrm{MeV}$, i.e an energy spread reduction of $63\,\%$.

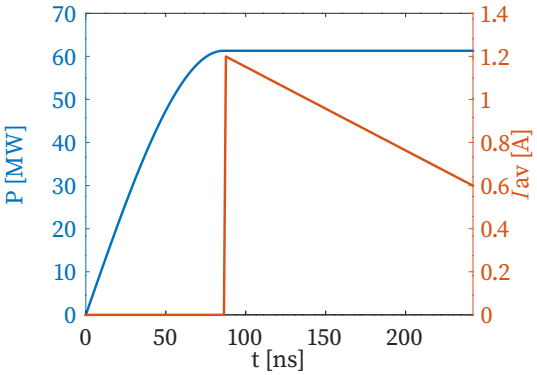

(a) Optimal input power and charge-varying intensity curves.

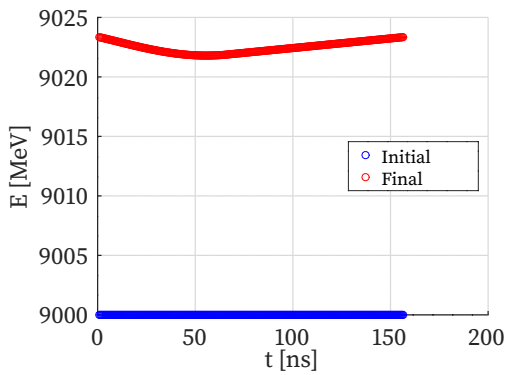

(b) Beam longitudinal phase-space.

Figure 3.21: Power optimization and bunch-to-bunch energy spread minimization for a charge-varying beam (600-300 pC).

4. Measurement of beam loading effects in CLEAR

The power-diffusive BL model presented in Chapter 3 has been benchmarked against previous results for TW structures. There remains the need to assess the performance of the SW BL module.

To our knowledge, no codes implement non-ultrarelativistic BL calculations in SW structures. Therefore, to test the accuracy of the developed tool, BL effects were measured in the CLEAR facility at CERN. This chapter presents the facility and the experimental procedure for the measurements, and compares the obtained results with RF-Track simulations, showing nice agreement and validating the SW module.

4.1 The CLEAR facility

The CERN Linear Electron Accelerator for Research is a stand-alone user facility which consists of a $200\,\mathrm{MeV}$ electron linac followed by an experimental beamline [75]. It is an adaptation of the CALIFES beamline (from the French, *Concept d'Accélérateur Linéaire pour Faisceau d'Electron Sonde*) [76] of the CLIC Test Facility 3 (CTF3) which previously demonstrated the feasibility of the CLIC key concepts, and whose operation finished at the end of 2016. CLEAR operation began in September 2017 [77]. Since then, the facility has been dedicated to:

- R&D studies of accelerator components and accelerating techniques for existing and possible future machines at CERN. Concrete examples of this are beam instrumentation prototyping [78], experiments on THz acceleration, or plasma-lens prototypes [79].
- Sample irradiation with high-energy electron beams, which allows testing elec-

tronic components [80] or assessing novel radiotherapy methods [81].

To serve these purposes, CLEAR offers to its users electron beams with a wide range of parameters, as shown in Tab. 4.1.

Magnitude	Units	Value
Beam Energy	MeV	30 to 200
Beam Energy Spread	% rms	< 0.2
Bunch length rms	ps	0.1 to 10
Bunch frequency	GHz	1.5 or 3.0
Bunch charge	nC	0.005 to 1.6
Norm. emmitance	$\mu m \cdot rad$	1 to 20
Bunches per pulse		1 to 200
Max. pulse charge	nC	87
Repetition rate	Hz	0.83 to 10

Table 4.1: Updated electron beam parameters. Data from [82].

Figure 4.1 shows a schematic of the accelerator layout. The first stage of acceleration is an RF photoinjector followed by three S-band TW accelerating structures and a focusing triplet of quadrupoles which extends up to $20\,\mathrm{m}$. At this point, a dipole deflects the beam to the first in-air test area called Very energetic Electron facility for Space Planetary Exploration missions in harsh Radiative environment (VESPER).

If the beam is not directed into VESPER, it continues to the user beamline, which extends for $16\,\mathrm{m}$ and consists of several in-vacuum test areas (for beam instrumentation, CLIC technology, and plasma lens development), as well as a final in-air area for irradiation experiments.

4.2 Preparation for Beam Loading measurements

The measurements of the BL effect were carried out in the first part of CLEAR, corresponding to the beamline shown at the top half of Fig. 4.1. More specifically, the BL effect in SW structures was measured in the RF gun, and SW and TW BL effects were measured in the VESPER line. This section details the preparation and calibration of these structures.

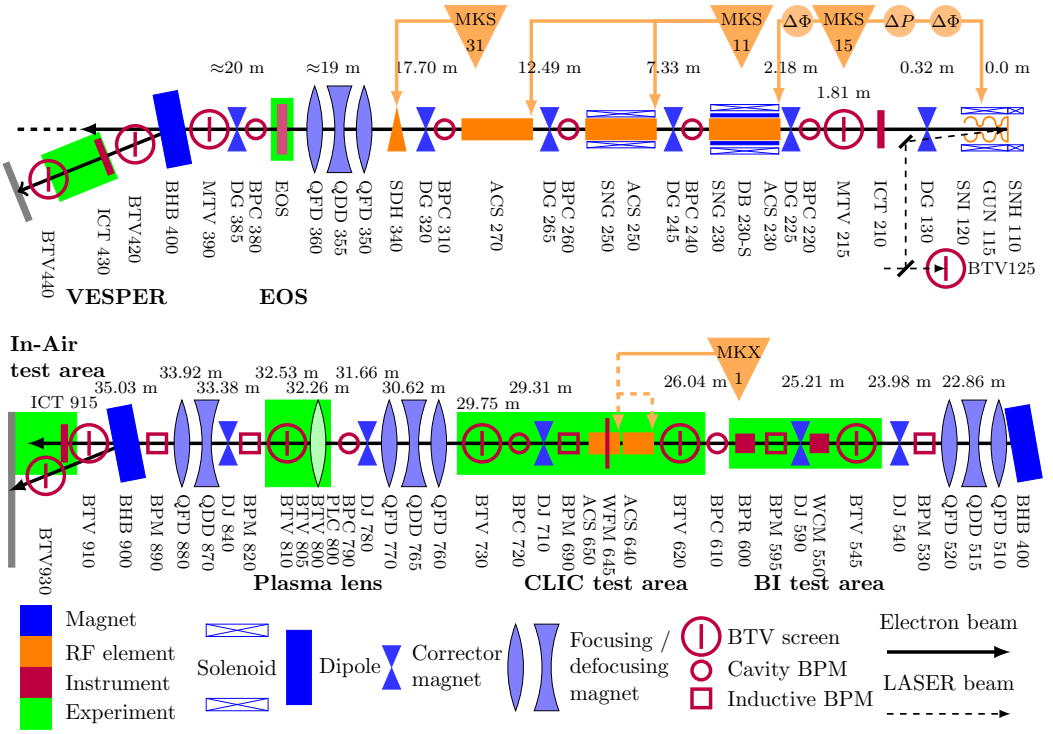

Figure 4.1: CLEAR beamline schematic. The beam goes from right to left, starting from the photoinjector at the top right corner. Extracted from [83].

4.2.1 Voltage calibration of CLEAR's electron gun

Figure 4.2 shows the CLEAR gun, where electrons are created via the photoelectric effect when a laser impinges upon a Cs_2Te photocathode. They are then captured by a 2.6 cell-long SW structure, which accelerates them while a solenoidal field focuses them. This high-quality bunch is transported to the entrance of the first TW structure with the help of orbit correctors, transport beampipes, position monitors, and screens, as seen in Fig. 4.2a.

BL effects in the electron gun were quantified by measuring voltage reduction in the voltage loop of the SW structure in the presence of the beam. However, it is uncalibrated, meaning that the obtained voltage signal has to be renormalised to the correct maximum value, V_{max}, for the optimal electric field phase. This value is inferred from the maximum energy gain of the electrons after the gun, $\mathcal{E}_{\text{max}} = eV_{\text{max}}$.

To measure the energy gain of the electrons after the accelerating structure, beam-rigidity measurements were performed with the orbit corrector of Fig. 4.2b and the

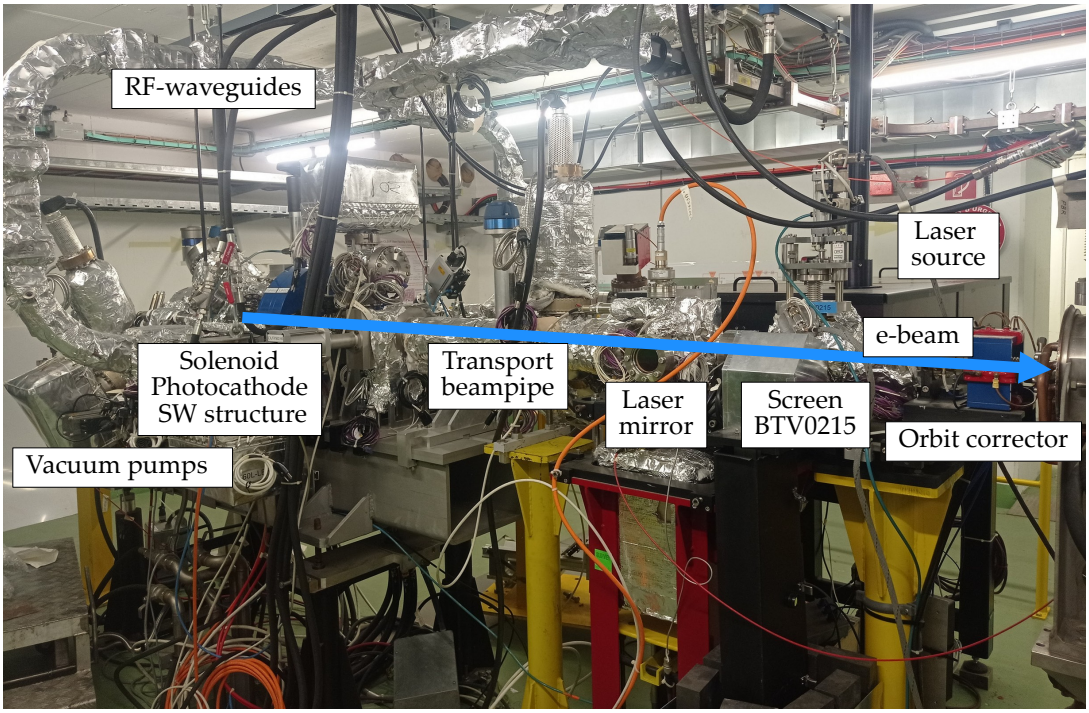

(a) CLEAR photoinjector from photocathode to first TW structure.

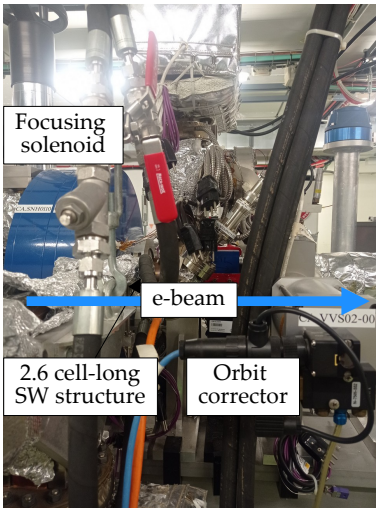

(b) CLEAR electron gun.

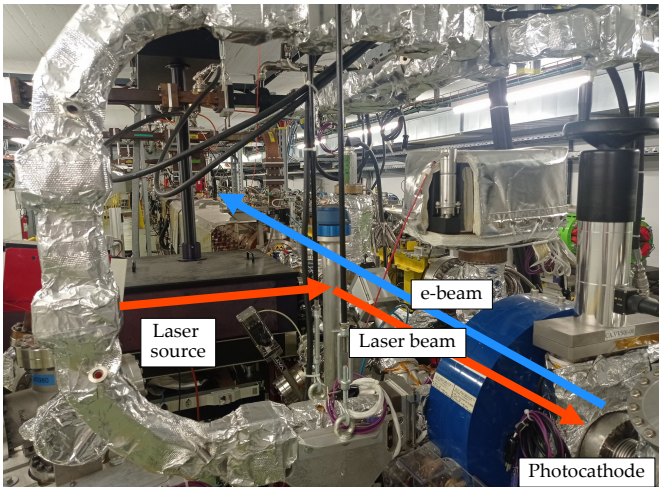

(c) Left view of CLEAR gun with laser source

Figure 4.2: CLEAR photoinjector.

screen shown in Fig. 4.2a. In the paraxial approximation, we can assume the motion of the electrons to be mainly longitudinal. Thereby, the orbit correctors can be set to

provide a perpendicular magnetic field. In this case, the Lorentz force, in Eq. (2.1), leads to the following expression for the curvature radius ρ:

$$\frac{1}{\rho[\mathrm{m}]} \simeq 0.3 \frac{B[\mathrm{T}]}{p[\mathrm{GeV/c}]}, \tag{4.1}$$

Figure 4.3 shows the geometry of the arrangement of the instrumentation and the flight of the electrons from the gun to the screen. For small bending angles θ, $\tan\theta \simeq \theta$ and we can express the curvature radius as:

$$\frac{1}{\rho} = \frac{\theta}{l_{\mathrm{kicker}}} \simeq \frac{\Delta x}{l_{\mathrm{kicker}} L}. \tag{4.2}$$

Here, l_{kicker} denotes the length of the corrector, L is the distance from the center of the corrector to the screen, and Δx relative position to the center of the screen where the electrons arrive.

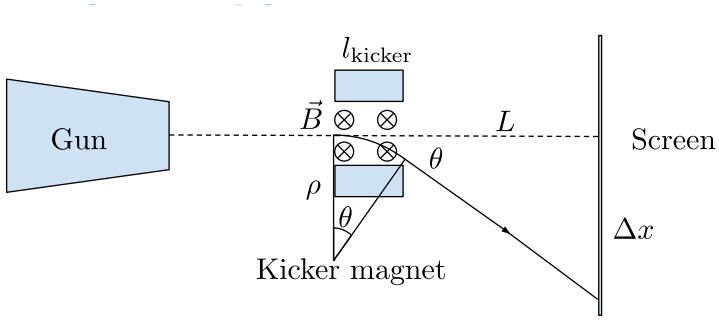

Figure 4.3: Sketch of the arrangement of the instrumentation from the RF gun to the screen

Combining Eqs. (4.1) and (4.2) and assuming a linear dependency of the magnetic field, B, with the intensity, I, that runs through the orbit corrector coils ($B = \frac{\partial B}{\partial I} I$), one finds out a linear relationship between the intensity running through the corrector coils and the position where the electron bunches arrive to the screen MTV0215:

$$\Delta x = \underbrace{0.3 \frac{\frac{\partial B}{\partial I} l_{\mathrm{kicker}} L}{p[\mathrm{GeV/c}]}}_{m} I[\mathrm{A}], \tag{4.3}$$

where m stands for the slope of the curve.

Methodology for voltage calibration of the RF gun:

1. For a bunch of $50\,\mathrm{pC}$ and a fixed phase φ_{gun}, measure $\{(I_k, \Delta x_k)\}_{k=1}^{N_I}$ for N_I different values of I.

2. Fit the previous set of data $\{(I_k, \Delta x_k\}_{k=1}^{N}$ to Eq. (4.3). For each value of φ_{gun}, the total momentum and energy of the particles can be calculated as:

$$p = 0.3 \frac{\partial B}{\partial I} \frac{l_{\mathrm{kicker}} L}{m} 10^3 \ [\mathrm{MeV/c}] \tag{4.4}$$

$$\mathcal{E} = \sqrt{(m_e c^2)^2 + (pc)^2} \ [\mathrm{MeV}] \tag{4.5}$$

3. Repeat 1 and 2 for N_φ different values of φ_{gun} to obtain the set of data $\{(\varphi_k, \mathcal{E}_k))\}_{k=1}^{N_\varphi}$.

4. Obtain the value of E_z^{max} by fitting the $\{(\varphi_k, \mathcal{E}_k)\}_{k=1}^{N_\varphi}$ data obtained in 3 to the curve $\mathcal{E}(\varphi_{\mathrm{gun}}; E_z^{\mathrm{max}})$. This merit function was calculated with RF-TRACK by computing the energy gain of a $50\,\mathrm{pC}$ bunch through the gun, whose fieldmap was obtained from SUPERFISH (Fieldmap courtesy of Dr. Avni Aksoy).

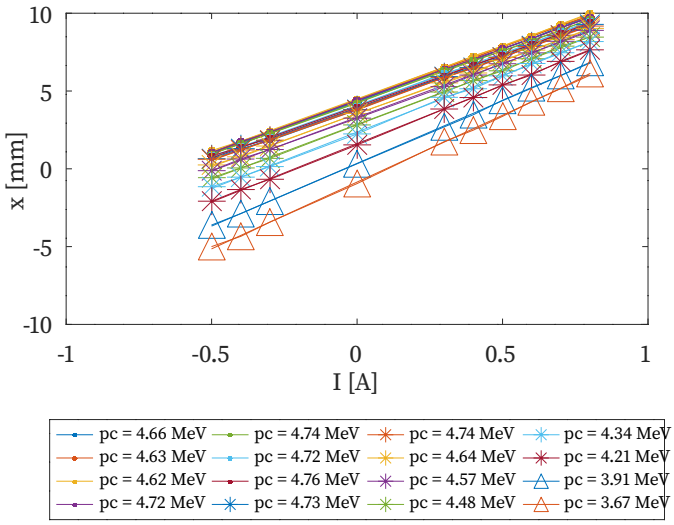

Figure 4.4: Current-screen position measurements for different phases and different energies. CLEAR data: $L = 1.49\,\mathrm{m}$, $l_{\mathrm{target}} = 160\,\mathrm{mm}$, $\frac{\partial B}{\partial I} = 4.45 \times 10^{-5}\,\mathrm{T/A}$.

Figure 4.4 shows the different $\{(I_k, \Delta x_k)\}_{k=1}^{N_I}$ measured and their linear fits for different φ values. Non-zero intercept values are obtained as a result of a misalignment of the centre of the screen with the beamline axis, which do not affect the calculation of $\mathcal{E}$ since it is only dependent on the slope of the curves.

Figure 4.5 presents the result of the non-linear fit of the experimental data with the $\mathcal{E}(\varphi; E_z^{\max})$ curve obtained from RF-TRACK. The fit shows good agreement with the experimental results across the entire range, although deviations are observed at the low-angle region. However, no definitive cause could be established. A plausible explanation for this behaviour is the influence of unwanted electron current emitted from the cavity walls, so-called dark currents [84], though further inspection should be carried out.

The value of the peak longitudinal field obtained from the non-linear fit, $E_z^{\max}$, is shown in Tab. 4.2.

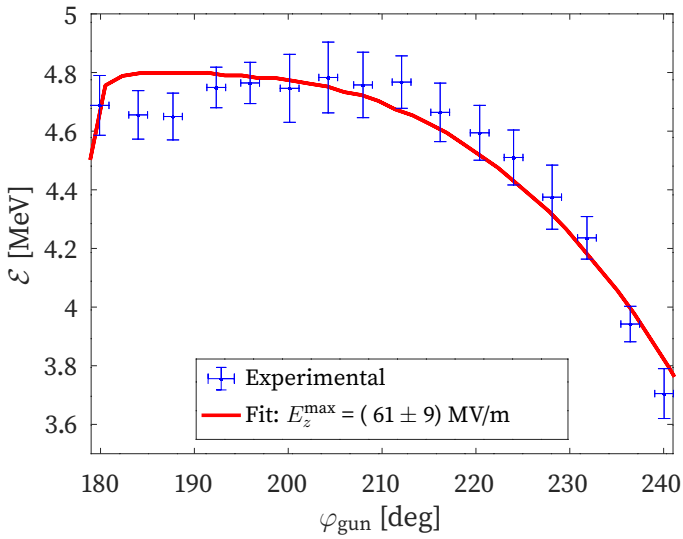

Figure 4.5: Gun Phase-voltage fitting of the experimental data with RF-TRACK.The non-linear fitting routine as well as the uncertainty calculation are detailed in Appendix A.3.

Magnitude	Units	Value
$E_z^{\max}$	MV/m	61 ± 9
r^2		0.94

Table 4.2: Fitting results for the RF gun for the set of data from Fig. 4.5.

4.2.2 VESPER spectrometer calibration

To assess the impact of BL after the TW accelerating structures, energy measurements were taken in the VESPER spectrometer. The physical setup is shown in Fig.

4.6, and a geometry sketch is depicted in Fig. 4.7.

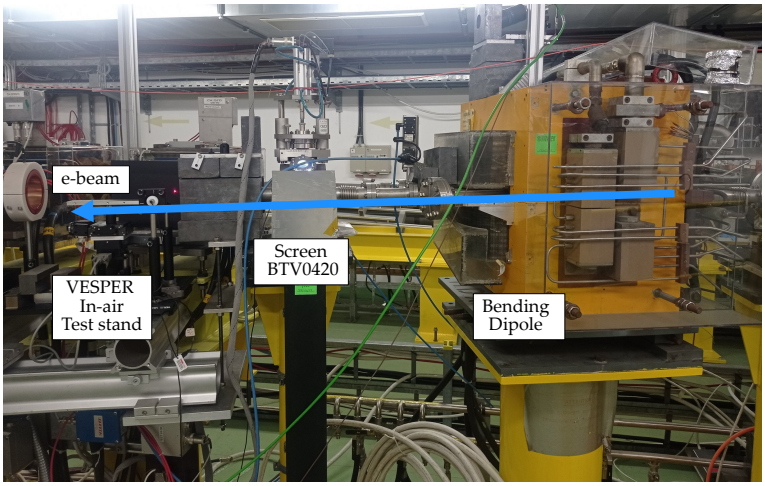

Figure 4.6: VESPER beamline lateral view.

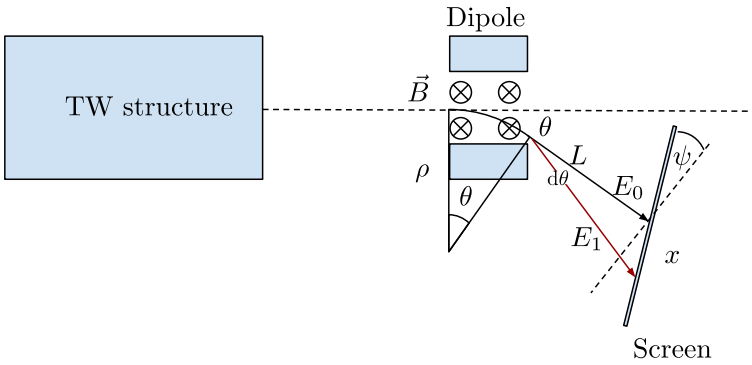

Figure 4.7: TW-to-screen geometry sketch in VESPER beamline

Calibrating the VESPER spectrometer requires correlating the arrival position of electrons to the BTV0420 screen with their energy. Based on Eq. (4.1), the momentum of a reference particle arriving to the center of the screen with energy E_0 and deflecting angle θ is:

$$p_0[\mathrm{MeV/c}] \simeq 0.3 \frac{\partial B}{\partial I} I[\mathrm{A}] \frac{l_{\mathrm{Dipole}}}{\theta}, \tag{4.6}$$

with l_{Dipole} the length of the dipole magnet.

Particles with different energies than the reference particle ($\mathcal{E}_1 \neq \mathcal{E}_0$) will be deflected differently an angle $\theta + \mathrm{d}\theta$. The ratio between the beam-rigidity relationship

of these two particles returns the following expression:

$$\mathrm{d}\theta = \theta\left(\frac{\mathcal{E}_0}{\mathcal{E}_1} - 1\right). \tag{4.7}$$

Here, two assumptions have been made: (1) The deflection towards the screen starts from the same starting point; and (2) The distance from the center of the screen to the dipole is much larger than the screen size, $L \gg \Delta x$.

Further trigonometrical considerations lead to the correlation of Δx and E_1:

$$\Delta x = \frac{\left[\frac{l_{\text{dipole}}}{\theta}\left(\frac{\mathcal{E}_1}{\mathcal{E}_0} - 1\right) + L\tan\left[\theta\left(\frac{\mathcal{E}_0}{\mathcal{E}_1} - 1\right)\right]\right]\cos\left[\theta\left(\frac{\mathcal{E}_0}{\mathcal{E}_1}\right)\right]}{\cos\left[\psi - \theta\left(\frac{\mathcal{E}_0}{\mathcal{E}_1}\right)\right]} \tag{4.8}$$

Equations (4.6) and (4.8) allow the measurement of the energy of the beam from the arrival position on the screen BTV0420 and the intensity of the dipole. An example of a calibrated measurement is shown in Fig. 4.8.

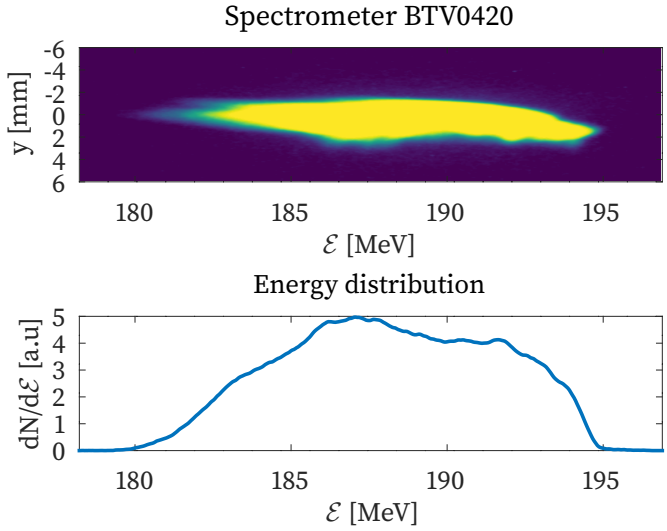

Figure 4.8: Energy measurements from beam position in screen BTV0420. Case of a train with 30 electron bunches with $q_{\text{bunch}} = 286\,\text{pC}$.

4.2.3 Accelerating structures calibration

CALIFES TW structures (in Fig. 4.9) have been operating for a very long time[1]. As a consequence, the power-to-gradient efficiency is not the original one, meaning that

[1]The CALIFES TW structures were part of the LEP injectors [85].

the translation between input power from the klystrons and accelerating gradient is not known *a-priori*. For this reason, a calibration of these structures is required before any BL measurement.

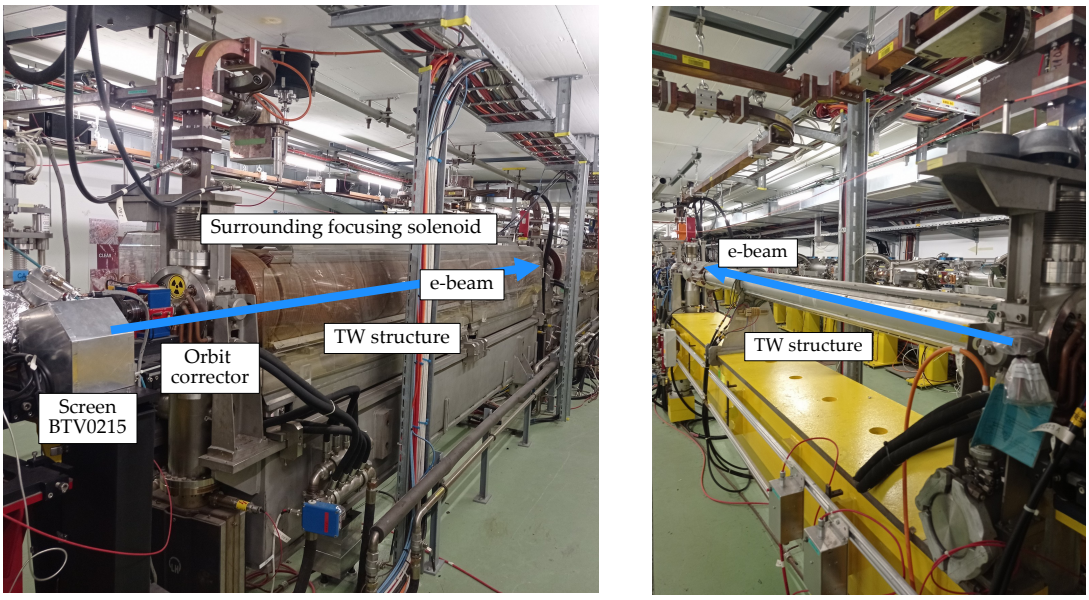

(a) First TW structure with surrounding solenoid.

(b) Third TW structure. No solenoid.

Figure 4.9: CLEAR TW structures.

To determine the accelerating gradient, or equivalently, the maximum longitudinal electric field, $E_z^{\max}$, the followed strategy was similar to the one presented in 4.2.1: To perform $\{(\varphi_k, \mathcal{E}_k)\}_k$ measurements in VESPER spectrometer to fit them to a theoretical curve $\mathcal{E}(\varphi; E_z^{\max})$, obtained with RF-Track.

Figure 4.1 shows that the first TW structure is fed by one klystron (MKS 15), while the second and third TW structures are fed by a different one (MKS 11). For this reason, the first TW structure was calibrated independently with MKS 11 off, and the second and third TW structure were calibrated together, with MKS 11 on and assuming equal phase and accelerating voltage in both of them.

The results of the calibrations for a single electron bunch of $285\,\mathrm{pC}$ are shown in Table 4.3, and the fitting of the experimental measurements and the theoretical curve are illustrated in Figs. 4.10a and 4.10b.

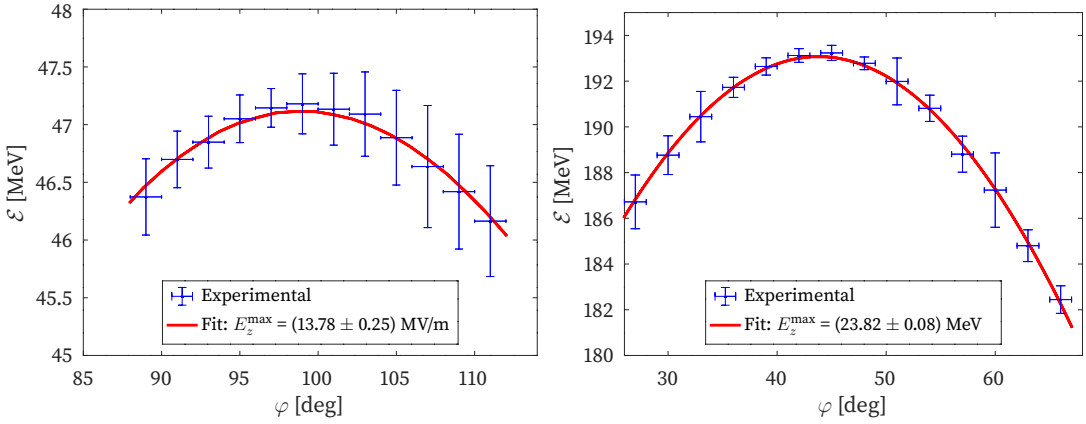

(a) First TW structure calibration.

(b) 2nd and 3rd TW structures calibration.

Figure 4.10: CLEAR TW structures calibration for an electron bunch with $q_{\text{bunch}} = (-285 \pm 21)$ pC. Each experimental point corresponds to the average of 20 $(\varphi_k, \mathcal{E}_k)$ measurements, and the uncertainty bars are calculated from the standard deviation of the set of measurements.

TW Structure	Magnitude	Units	Value
1st	$E_z^{\max}$	MV/m	13.78 ± 0.25
	r^2		0.97
2nd, 3rd	$E_z^{\max}$	MV/m	23.82 ± 0.08
	r^2		0.994

Table 4.3: Calibration results for the first, second and third TW structure.

4.3 Electron gun Beam Loading measurements

As a result of the calibration, the maximum accelerating voltage in the gun, V_{max}, is determined for each RF-gun phase, φ_{gun}. Therefore, voltage measurements could be performed at the gun's voltage loop, as shown in Fig. 4.11, at the accelerating phase of $\varphi_{\text{gun}} = (200 \pm 1)^\circ$.

According to Eq. (3.23), the BL effect translates in a voltage reduction of the cavity that is proportional to the beam charge. Consequently, the beam-induced voltage is calculated by comparing the voltage of an unloaded cycle, V_{ul}, with the voltage of a

beam-loaded cycle, V_l. We define the maximum beam-induced voltage as:

$$V_\mathrm{beam} = \max_t (V_\mathrm{ul}(t) - V_\mathrm{l}(t)). \tag{4.9}$$

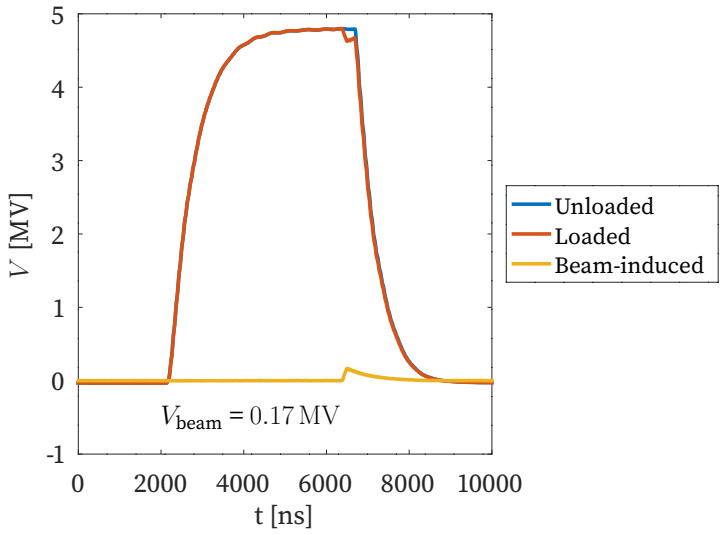

Figure 4.11: Comparison of the voltage measurement in the RF gun between the unloaded scenario and the case of a train of 150 electron bunches with (301 ± 11) pC/bunch.

Methodology for measurements of the beam-induced voltage in the gun: We measure the beam-induced voltage of different configuration of beams with N_bunches bunches of electrons with arbitrary charge per bunch q_bunch.

For each $(N_\mathrm{bunches}, q_\mathrm{bunches})$ configuration, a set of 20 data points $\{V^s_\mathrm{beam}\}_{s=1}^{20}$ was obtained. The results in Section 4.3.1 refer to the average value of the set, and the uncertainty bars cover 3σ, with σ being the standard deviation of the set of measurements.

The experimental results are compared with the ones obtained with the `BeamLoadingSW` algorithm introduced in section 3.4.2. The required arguments for the simulations with RF-TRACK are shown in Table 4.4, where the loaded quality factor has been obtained by fitting the unloaded voltage measurement with Eq. (3.21) as seen in Fig. 4.12.

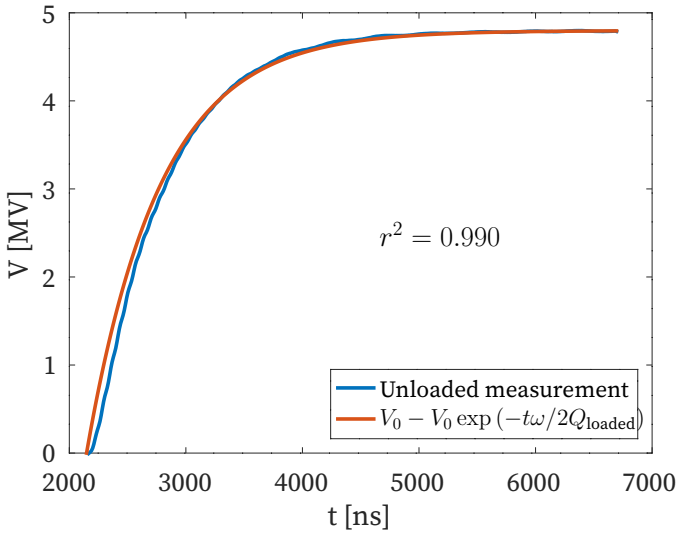

Figure 4.12: Unloaded measured voltage fit with Eq. (3.21).

Magnitude	Units	Value
r/Q	$k\Omega$/m	5.50
Q_{loaded}	10^1	597 ± 8
f_0	GHz	3.00
$\langle G \rangle$	MV/m	27.5
$\frac{d}{2}\Big\vert_{\text{min}}$	mm	10.0
σ_z	mm/c	1.0

Table 4.4: CLEAR RF gun parameters [86].

4.3.1 Results

A beam of 150 bunches with a bunch-to-bunch spacing of $200\,\text{mm}$ was injected into the CLEAR RF gun. For different q_{bunch} values, the beam induced energy losses have been measured with Eq. (4.9). The results are shown in Figure 4.13a.

The same scenario was simulated with RF-Track. It shows that the effect of BL is to induce a first-to-last bunch energy loss, $\mathcal{E}_{\text{BL, loss}}$, which is defined as:

$$\mathcal{E}_{\text{BL, loss}} = \langle E_1 \rangle - \langle E_{150} \rangle. \tag{4.10}$$

Figure 4.13b illustrates the dependency of $\mathcal{E}_{\text{BL, loss}}$ with q_{bunch}.

A linear dependency of the beam-induced energy loss with q_{bunch} is found, as re-

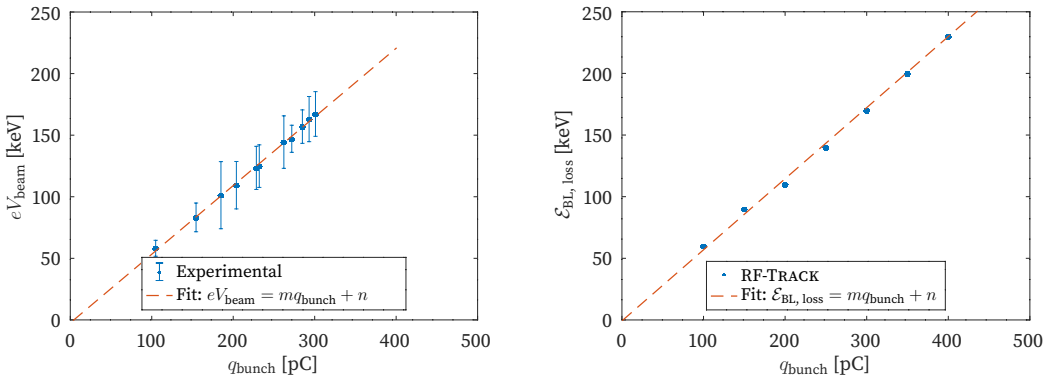

(a) Experimental measurements and linear fitting.

(b) Results with RF-TRACK and linear fitting.

Figure 4.13: V_{beam} for a train of 150 bunches with a bunch spacing of $200\,\text{mm}$ as a function of q_{bunch} in the Concept d'Accélérateur Linéaire pour Faisceau d'Electron Sonde (CALIFES) gun.

flected by the high value of the r^2 coefficient from the linear fit of both experimental and simulation data. This is consistent with the beam-loading term in Eq. (3.23), which depends linearly on $\tilde{I}$ and therefore on q_{bunch}.

Fitting parameter	**Units**	**Experimental**	**RF-TRACK**
m	keV/pC	0.56 ± 0.03	0.577 ± 0.024
r^2	-	0.998	0.9990

Table 4.5: Fitting parameters from Figs. 4.13a and 4.13b.

The positive sign of the slope, m, confirms that the higher the charge of the injected bunch, the larger the gradient reduction due to BL. A good agreement is found between the slopes obtained from the experimental data and RF-TRACK's simulation, as shown in Table 4.5. To quantify the agreement, the slope deviation, δ_m is defined and calculated for this case as:

$$\delta_m = \frac{|m_{\text{experimental}} - m_{\text{RF-TRACK}}|}{m_{\text{experimental}}} = 3.4\,\%. \tag{4.11}$$

Figure 4.14 shows the dependency of V_{beam} with the number of bunches when the charge per bunch is fixed to (294 ± 24) pC. A similar conclusion can be drawn from this comparison: larger charges lead to greater energy losses as a consequence of

beam-loading-induced gradient reduction, and accordance between simulations and measurement is obtained.

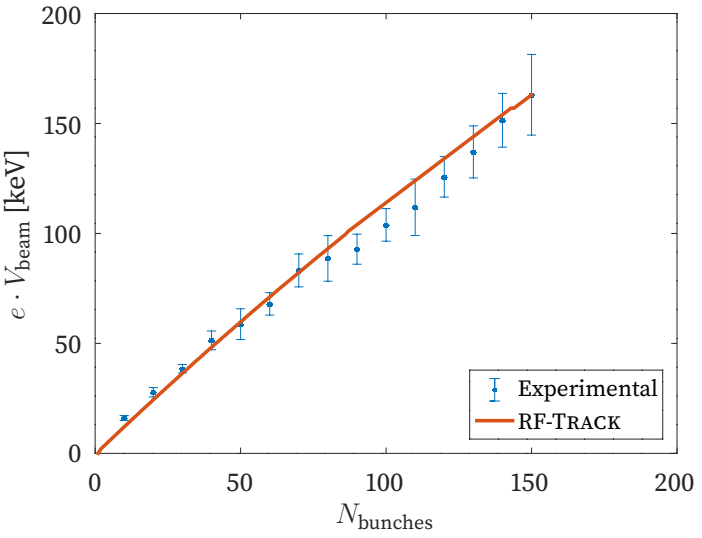

Figure 4.14: Beam-induced energy loss of a train with $q_{\text{bunch}} = (294 \pm 24)$ pC and bunch-to-bunch spacing $200\,\text{mm}$ as a function of the number of bunches in CLEAR RF-gun.

4.3.2 Validity of the model for non-ultrarelativistic scenarios

The power-diffusive model uses the definition of normalized shunt impedance per unit length. As discussed in Chapter 2, the shunt impedance is defined from the real part of the longitudinal wakefield, which is computed under the ultrarelativistic assumption, which implies wake causality.

Causality means that early bunches are not affected by the EM field induced by later particles. In principle, this could limit the application of the developed RF-TRACK's module for the CLEAR gun scenario. However, it can be seen that causality is not violated in this situation.

Figure 4.15 illustrates the catch-up condition for the causality violation: The EM wave front (illustrated as a triangle) originated by a late particle (in red) catches-up a sooner particle (in green) at a time t^*. For simplicity, we assume that the initial maximum distance between particles is s_0. In this case, the catch-up condition reads as:

$$\exists t^* \in \mathbb{R} \text{ so that } t^* = \frac{a}{c} + \frac{1}{c}\sqrt{a^2 + (s_0 + z(t^*))^2}, \tag{4.12}$$

where $z(t^*) = \int_0^{t^*} \beta(t) c \, \mathrm{d}t$ and a is the smaller inner radius in the cavity, as seen in Fig. 4.15.

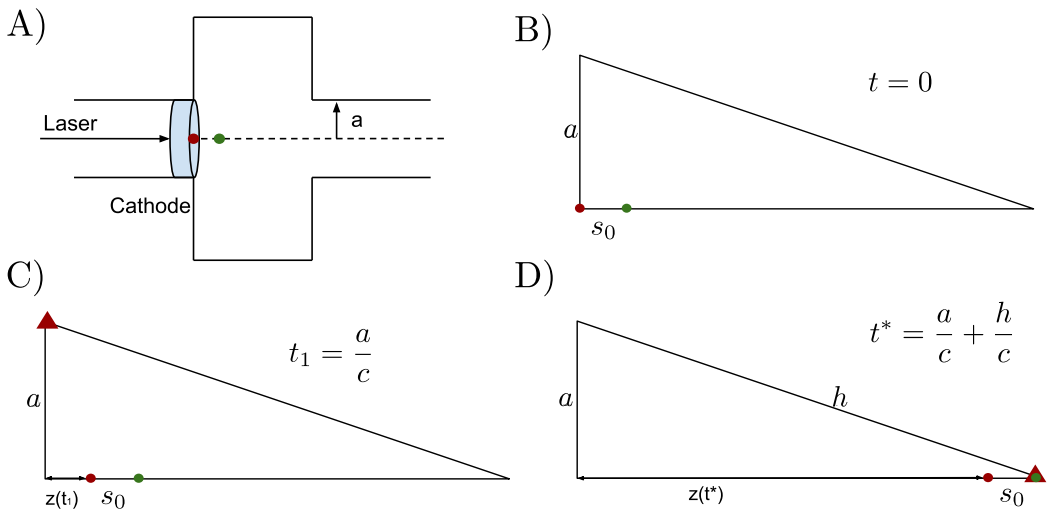

Figure 4.15: Wake catch-up condition illustration, with $h = \sqrt{a^2 + (s_0 + z(t^*))^2}$.

For the CLEAR RF-gun, the catch-up condition is illustrated in Fig. 4.16 for different s_0 values according to the bunch length in Tab. 4.1. It shows that, for $\langle G \rangle = 27.5\,\mathrm{MV/m}$ and $a = 4.6\,\mathrm{mm}$, the curve $f(t^*) = t^* - \frac{a}{c} + \frac{1}{c}\sqrt{a^2 + (s_0 + z(t^*))^2}$ does not cancel, meaning that the catch-up time t^* does not exist.

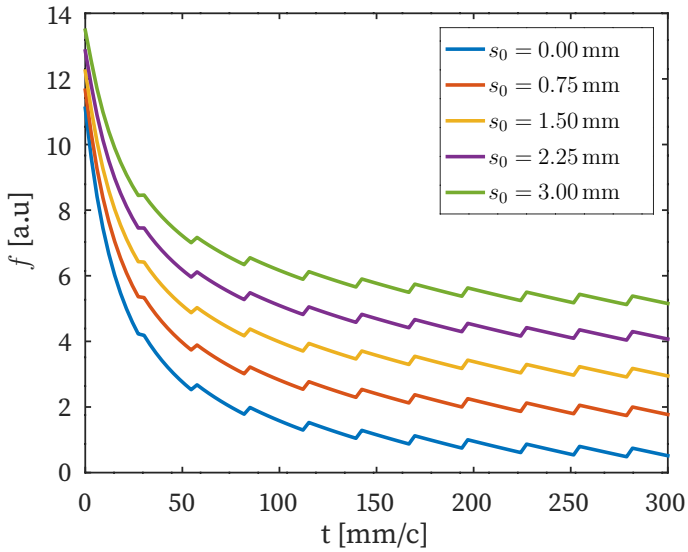

Figure 4.16: Catch-up condition for the CLEAR RF-gun

4.4 Start-to-end Beam Loading measurements at VESPER

Figure 4.8 presents the measurement of the beam energy at the screen BTV0420 after VESPER spectrometer, where the energy of the particles is obtained from the position in the screen according to the dispersing relationship in Eq. (4.8). From such measurement, the energy spectrum of the particles in the beam, $f_{\mathcal{E}}$, can be calculated, allowing to define the following quantities:

$$\langle \mathcal{E} \rangle_{\text{beam}} = \frac{1}{K} \int_{-\infty}^{\infty} \mathcal{E}\, f_{\mathcal{E}}(\mathcal{E}) \mathrm{d}\mathcal{E}, \tag{4.13}$$

$$\mathcal{E}_{\text{range}} = \min\{\mathcal{E} \in \mathbb{R} : F(\mathcal{E}) > 0.9K\} - \max\{\mathcal{E} \in \mathbb{R} : F(\mathcal{E}) < 0.1K\}, \tag{4.14}$$

$$\sigma_{\mathcal{E}} = \sqrt{\frac{1}{K} \int_{-\infty}^{+\infty} \mathcal{E} f_{\mathcal{E}}(\mathcal{E}) \mathrm{d}\mathcal{E} - \langle \mathcal{E} \rangle^2}, \tag{4.15}$$

with $F(\mathcal{E}) = \int_{-\infty}^{\mathcal{E}} f_{\mathcal{E}}(\mathcal{E}) \mathrm{d}\mathcal{E}$, and $K = F(\mathcal{E} \to \infty)$.

Methodology for measurements at VESPER: The BL effect after the TW structures is verified by measuring an intensity-dependent energy loss and energy spread at VESPER spectrometer for different beam intensities.

For each $(N_{\text{bunches}}, q_{\text{bunches}})$ configuration, a set of 20 measurements was obtained $\{\langle \mathcal{E} \rangle, \mathcal{E}_{\text{range}}, \sigma_{\mathcal{E}}\}_{s=1}^{20}$. The results in section 4.4.1 show the average values of these quantities, and the uncertainty bars cover three times the standard deviation of the given set of measurements.

The experimental results are compared with the ones obtained with the `BeamLoading` algorithm introduced in section 3.4.2. The required input values for the simulations with RF-TRACK are shown in Table 4.6.

Magnitude	Units	Value
f_0	GHz	3.00
ϕ_{ad}	rad	$2\pi/3$
N_{cells}	-	135
r/Q	$k\Omega$/m	(4.00, 4.40, 4.80)
Q	10^3 -	(15.3, 15.2, 15.1)
v_g	$\%c$	$(133^{-1}, 70.0^{-1}, 46.0^{-1})$

Table 4.6: Parameters for the three CLEAR TW structures [87].

4.4.1 Results

A beam of 50 bunches with a bunch-to-bunch spacing of 200 mm was injected in CLEAR, and its energy was measured at VESPER spectrometer. The results are shown in Figs. 4.17a and 4.17c for q_{bunch} values ranging from 100 to 400 pC. This scenario has been reproduced with RF-TRACK, and the $\langle\mathcal{E}\rangle_{\text{beam}}$ and $\mathcal{E}_{\text{range}}$ calculated from the simulation are presented in Figs. 4.17b and 4.17d.

Figure 4.17 proves the existence of an intensity-dependent $\langle\mathcal{E}\rangle_{\text{beam}}$ and $\mathcal{E}_{\text{range}}$, which is indicative of a gradient reduction of the accelerating structures which is reproducible with the `BeamLoading` module in RF-TRACK. Furthermore, the dependency of these magnitudes with q_{bunch} is found to be linear.

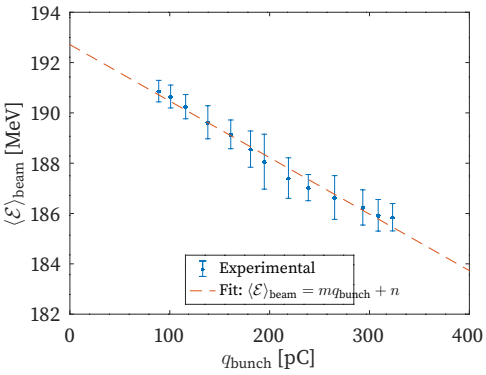

(a) Experimental $\langle\mathcal{E}\rangle_{\text{beam}}$.

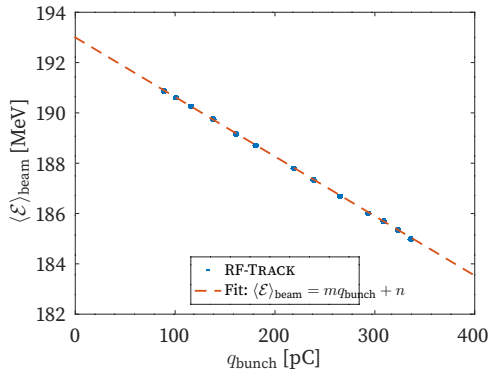

(b) RF-TRACK simulation $\langle\mathcal{E}\rangle_{\text{beam}}$.

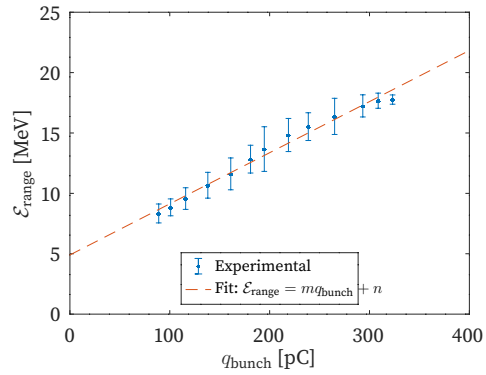

(c) Experimental $\mathcal{E}_{\text{range}}$.

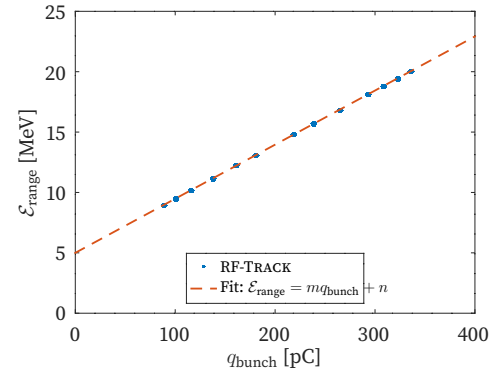

(d) RF-TRACK simulation for $\mathcal{E}_{\text{range}}$.

Figure 4.17: BL measurements for a train of 50 bunches with an injection frequency of 1.5 GHz going through CLEAR accelerating structures as function of the charge per bunch.

To assess the performance of RF-TRACK, the slopes resulting from the fitting of the

simulated and experimental data to a first-order polynomial fit were compared. The outcome of this analysis is shown in Table 4.7, where an agreement at 94% level is observed between simulation and experiments.

Case (y,x)	m_{exp} **[keV/pC]**	$m_{\text{RF-Track}}$ **[keV/pC]**	δ_m	r^2
$(\mathcal{E}_{\text{loss, BL}}\ ,\ q_{\text{bunch}})$	0.56 ± 0.03	0.577 ± 0.024	$3.4\ \%$	> 0.99
$(\mathcal{E}_{\text{loss, BL}}\ ,\ N_{\text{bunches}})$	-	-	-	0.98
$(\langle\mathcal{E}\rangle\ ,\ q_{\text{bunch}})$	-22.5 ± 2.4	-23.67 ± 0.17	$5.2\ \%$	> 0.98
$(\mathcal{E}_{\text{range}}\ ,\ q_{\text{bunch}})$	42 ± 5	44.8 ± 0.3	$5.9\ \%$	> 0.99

Table 4.7: Statistical indicators of simulation-measurement agreement

5. Electron linac based neutron sources

As discussed in Chapter 1, the demand for neutron sources has been increasing in the last years due to the wide range of applications of neutron science. An overview of these, as well as the required neutron energy and intensities, is shown in Fig. 5.1.

A few words on these applications:

- **Neutron and Gamma Activation**: Neutrons are used for nucleus excitation whose decay results in the emission of neutrons or gamma particles. These can be used for industrial processes such as nuclear fuel assay during production, explosive identification, and diverse applications in the oil industry.
- **Nuclear Physics research**: In the fast-neutron regime [88], fusion cross sections can be reproduced as well as astrophysics reactions. Moreover, in the ultra-cold regime, CP-violation experiments can be developed.
- **Software errors research**: Electronic devices suffer from Single Event Upset (SEU) due to the presence of unexpected charged particles in the circuits of memory chips. These arise from the nuclear reaction between a Si atom and a cosmic-ray-produced neutron. Facilities reproducing the cosmic-ray-produced neutron flux on Earth investigate these errors [89].
- **Imaging**: Neutrons constitute a complementary imaging technique to X-rays as they allow the visualisation of hydrogen-rich compounds and light elements.
- **Boron Neutron Capture Therapy (BNCT)**: The BNCT is a non-invasive cancer therapy conceived in 2 steps: First, a B-rich drug is delivered to the patient, which will adhere to the tumoral cell. Then, the patient is irradiated with neutrons so that the energy liberated in the ${}^{10}_{4}B + n$ reaction eliminates the tumour

[90]. The world's first medical BNCT device was set up in Japan in 2020 [91].

- **Radioisotope production**: An example is the production of ^{77}Lu, which is a β emitter radiopharmaceutical isotope which can be used to treat neuroendocrine tumours [92], which could be produced in the International Fusion Materials Irradiation Facility – Demo Oriented NEutron Source (IFMIF DONES) deuteron linac [35].
- **Elastic Scattering** and **Spectroscopy**: Neutron diffraction or emission allow the study of structural properties of condensed matter such as motions of atoms, the rotational modes of molecules, sound modes and molecular vibration, etc. [93]
- **Si-Doping**: For chip manufacturing.
- **Material Irradiation**: In these facilities, material resistance against neutron radiation can be tested for fusion or space missions, as mentioned in [35].

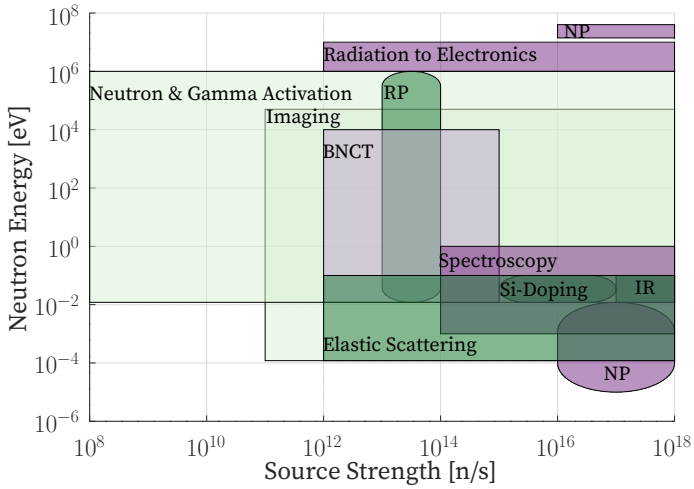

Figure 5.1: Neutron applications chart. Data extracted from [31] and [94]. The acronym NP stands for Nuclear Physics research, RP for Radioisotope Production, and IR for irradiation experiments.

This chapter intends to explore whether electron linacs are suitable drivers for neutron sources to satisfy the rising demand. In the first place, neutron production with electron beams is examined, and the neutron spectrum of an optimised tungsten target is presented. Then, the performance of different high-intensity electron linacs is examined, addressing the challenges in heat deposition as well as in energy con-

sumption. Finally, to explore low-energy applications, a preliminary thermal- and cold-moderator-target-assembly is proposed and different brightness values are discussed.

5.1 Neutron production with electron linear accelerators

5.1.1 Physical mechanisms for neutron production with electron beams

Neutron production with electron beams has already been demonstrated in facilities such as ORELA [95] (which operated from 1969 to 2008) and GELINA [36] (currently in operation). These facilities respectively rely on L-band (1.3 GHz) and S-band radiofrequency technologies (3.0 GHz) to accelerate beams up to 150 MeV.

In the case of CANS driven by electron accelerators, the neutrons are mainly produced via photonuclear reactions. First, electrons striking a high-Z-material target (e.g tungsten in GELINA [36]) generate *Bremmstrahlung* photons. Then, these photons interact with the target nuclei to produce neutrons. Photonuclear neutron production can be summarized in three predominant mechanisims:

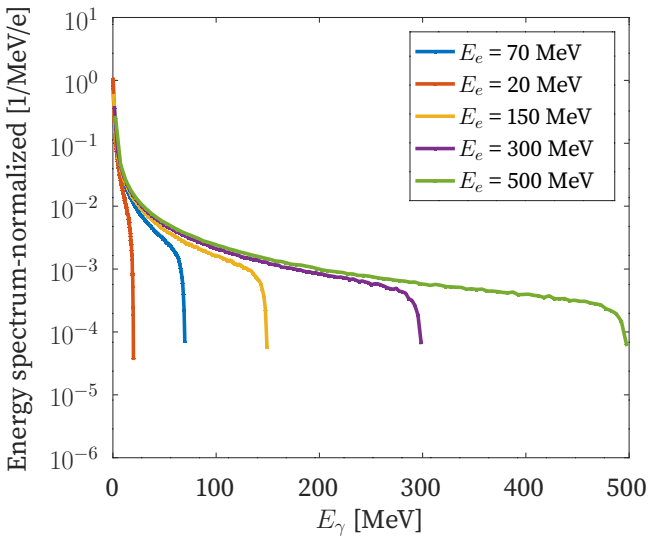

Figure 5.2: *Bremsstrahlung* photon spectrum of different electron beams against a 80mm-thick tungsten target. Simulations obtained with PENELOPE [96].

- **Giant Dipole Resonance (GDR) excitation:** Gamma photons from 7 MeV to 30 MeV increase the dipole momentum of the nucleus as an ensemble. This ex-

tra energy leads to a large number of de-excitation events such as neutron evaporation or gamma de-excitation, which result in the emission of neutrons [97].

- **Quasi-deuteron (QD) disintegration:** Occurs when a photon of high energy (40 MeV to 300 MeV) is absorbed by a pair of proton-neutron coming close together in the nucleus, forming a quasi-deuteron ensemble which disintegrates and emits a neutron [98, 99]

- **High Energy Physics (HEP) effects:** Gamma photons above 140 MeV lead to the formation of pions (so-called photo-pion effect [100]), which decay into high energy neutrons among other products. Protons and pions generated at these electron energies trigger intranuclear cascades which, in thick targets, result in an additional *Bremmstrahlung* photon spectrum, thus intensifying the GDR and QD photoneutron production [97].

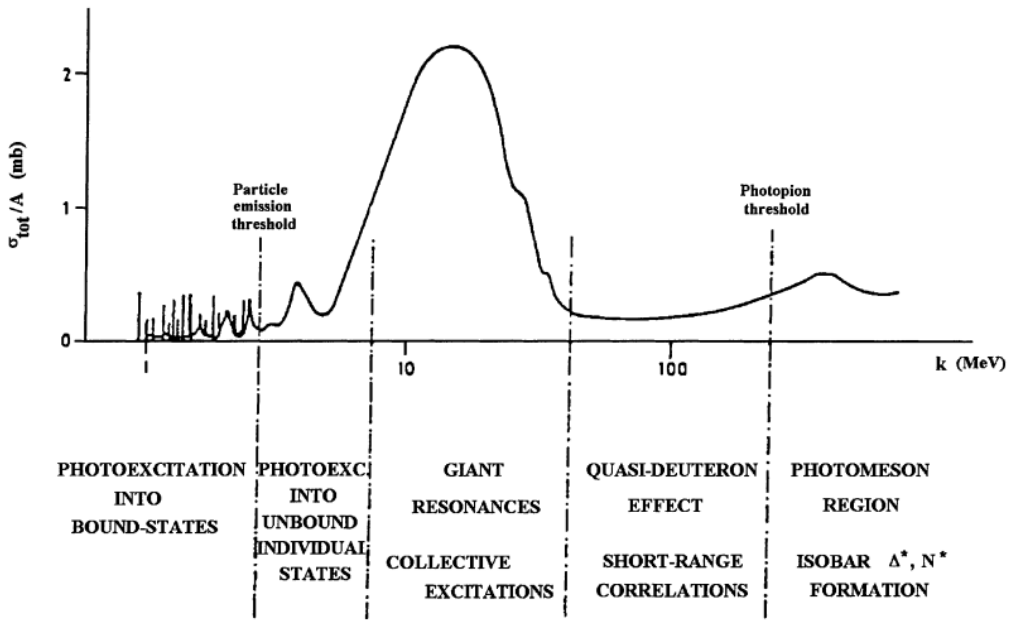

Figure 5.3: Photonuclear cross section for a tungsten target. Theoretical illustration from Ref [101].

5.1.2 Methodology

Description of neutron production

Figure 5.4 illustrates the setup for neutron production: Particles of charge q arrive to the center of a cylindrical target of radius r and length L with an angle θ_i. The resulting neutrons, which emerge in a solid angle Ω characterized by an azimutal, φ, and polar angle, θ, are detected by a detector whose surface, S_{detect}, is located at a distance r_{detect}.

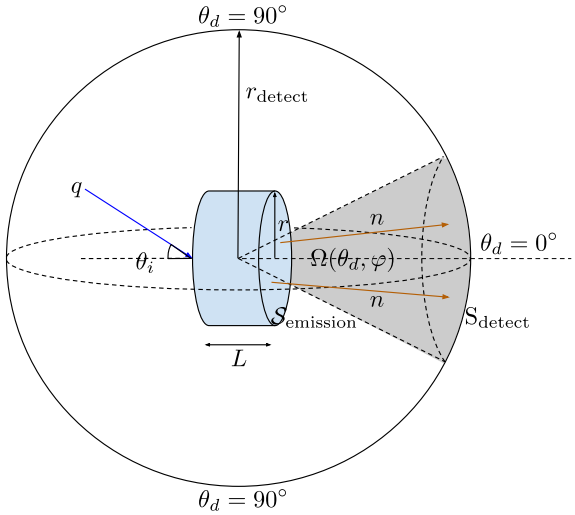

Figure 5.4: Spherical geometry for neutron production and detection when a charge q hits the tungsten target (in blue).

The figures of merit that describe neutron production are:

- The average neutron yield:

$$Y_n(\mathcal{E}_e) \equiv \frac{N_n(\mathcal{E}_e)}{N_e}\ [\text{n/e}], \tag{5.1}$$

  where N_n is the total amount of produced neutrons for a given electron energy, $\mathcal{E}_e$ and N_e the number of incident electrons.

- The solid-angle distribution, f_Ω:

$$f_\Omega(\varphi, \theta_d; \mathcal{E}_e) \equiv \frac{\mathrm{d}^2 Y_n}{\mathrm{d}\Omega}(\varphi, \theta_d)\ [\text{n/e/sr}], \tag{5.2}$$

  where $\mathrm{d}\Omega(\theta_d, \varphi) = \sin\theta_d\, \mathrm{d}\varphi\, \mathrm{d}\theta_d$ is the solid angle of detection with $0 \leq \varphi < 2\pi$ and $0 \leq \theta_d < \pi$.

- The polar-angle distribution, f_θ:

$$f_\theta(\theta_d;\mathcal{E}_e) \equiv \frac{1}{2\pi}\int_0^{2\pi} f_\Omega(\theta_d,\varphi)\mathrm{d}\varphi \ [\mathrm{n/e/sr}]. \tag{5.3}$$

- The azimuthal energy spectrum of the emergent neutrons, $f_{\theta,\mathcal{E}_n}$:

$$f_{\theta,\mathcal{E}_n}(\theta_d,\mathcal{E}_n;\mathcal{E}_e) \equiv \frac{\mathrm{d}f_\theta}{\mathrm{d}\mathcal{E}_n} \ [\mathrm{n/e/sr/MeV}]. \tag{5.4}$$

G4BEAMLINE simulations

The interaction of the electron beam in tungsten is modeled by G4BEAMLINE [102], a software which uses Monte Carlo sampling to study radiation-matter interaction. The simulations undertaken in this study use the physics option FTFP_BERT_HP, where hadron-nucleus interactions follow the FTF model [103]. Details on the G4BEAMLINE physics can be consulted in Appendix A.4.

For each simulation setup, unless explicitly mentioned, the emergent neutrons were detected in a sphere of radius $r_{\mathsf{detect}} = 1\,\mathrm{m}$, and the neutron yield was computed as:

$$Y_n = \frac{1}{N_e}\sum_{i=1}^{N_e}\chi_i, \tag{5.5}$$

where χ_i is the number of neutrons produced by the incident electron i. The uncertainty of the yield is calculated as $3\sigma_{Y_n}$, with [96]:

$$\sigma_{Y_n} \equiv \sqrt{\frac{1}{N_e}Y_n(1-Y_n)}. \tag{5.6}$$

The figures of merit in Eqs. (5.2-5.4) refer to continuous distributions, which from the simulation point of view are computed like histograms based on the associated stepwise constant functions. For instance, f_Ω was calculated as [96]:

$$f_\Omega(\varphi,\theta_d;\mathcal{E}_e) = f_{\Omega,j,k} \pm 3\sigma_{f_{\Omega,j,k}} \tag{5.7}$$

for $\theta_{d,j-1} < \theta_d < \theta_{d,j}$ and $\varphi_{k-1} < \varphi < \varphi_k$. Here, $\theta_{d,j} = j\Delta\theta_d$, and $\varphi_k = k\Delta\varphi$, with $0 < j,k < 100$, $\Delta\theta_d = \frac{\pi}{99}$rad and $\Delta\varphi = \frac{2\pi}{99}$ rad. Each bin value is expressed as:

$$f_{\Omega,j,k} = \frac{Y_{n,j,k}}{\sin\theta_{d,j}\Delta\theta_d\Delta\varphi} = \frac{1}{N_e}\sum_{i=1}^{N_e}\frac{\chi_{i,j,k}}{\sin\theta_{d,j}\Delta\theta_d\Delta\varphi}, \tag{5.8}$$

$$\sigma_{f_{\Omega,j,k}} = \frac{1}{\sin\theta_{d,j}\Delta\theta_d\Delta\varphi}\sqrt{\frac{1}{N_e}Y_{n,j,k}(1-Y_{n,j,k})}, \tag{5.9}$$

where $\chi_{i,j,k}$ is the number of neutrons per electron produced by the i-th electron in the solid angle $\mathrm{d}\Omega(\theta_{d,j},\varphi_k)$.

5.1.3 Characterization of a tungsten target

In this section, we will study neutron production upon arrival of the electrons to a cylindrical tungsten target of radius r and length L. For this reason, G4BEAMLINE simulations reproducing the geometry illustrated in Fig. 5.4 have been undertaken. The number of incident electrons simulated was 10^8, the mean energy $\langle \mathcal{E}_e \rangle$ ranged from $20\,\mathrm{MeV}$ to $500\,\mathrm{MeV}$; the relative energy spread $\sigma_{\mathcal{E}_e}/\mathcal{E}_e$ was 1%; and the incident angle, θ_i, was set to $0°$.

Figure 5.5a shows the neutron yield for different L and r values for an incident electron beam of $\langle \mathcal{E}_e \rangle = 500\,\mathrm{MeV}$. For all electron energies, the optimal dimensions leading to maximum yield were $L = 80\,\mathrm{mm}$ and $r = 40\,\mathrm{mm}$. Figure 5.5b presents the yield values for the optimal dimensions for $\langle \mathcal{E}_e \rangle$ ranging from 20 to 500 MeV. It shows that larger electron energies lead to greater neutron yields (always below $1\,\mathrm{n/e}$).

This arises from the fact that, for a fixed value of electron intensity, larger values of electron energy produce more *Bremmstrahlung* photons, both because the tail of the spectrum extends to higher energies and because of the effect of intranuclear cascades [97].

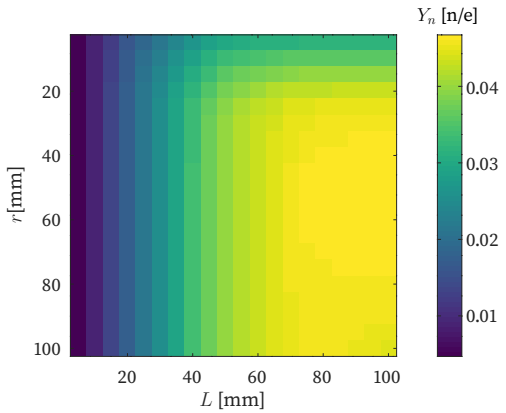

(a) Dimension scan for the neutron yield of a cylindrical tungsten target when $\langle \mathcal{E}_e \rangle$ = 500 MeV.

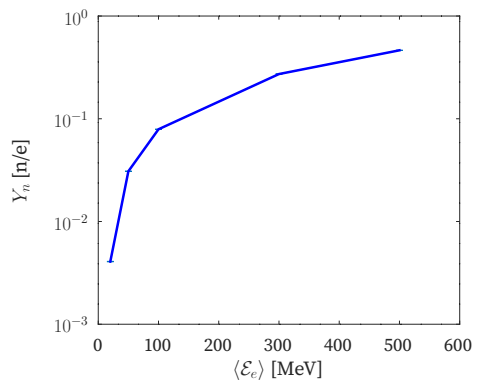

(b) Neutron yield for the optimal tungsten target ($L = 80\,\mathrm{mm}$, $r = 40\,\mathrm{mm}$).

Figure 5.5: Yield characterization of a cylindrical tungsten target.

Angular production

The polar angle distribution, f_θ, has been calculated for the optimal tungsten target for $\langle \mathcal{E}_e \rangle$ values of 20, 50, 100, 300 and 500 MeV. The results are illustrated in Fig. 5.6,

revealing that backward neutron production is larger than forward neutron production, being the direction of maximal production $\theta_d = 130$ deg. Consistent with Fig. 5.5b, the production is greater at larger $\langle \mathcal{E}_e \rangle$ energies.

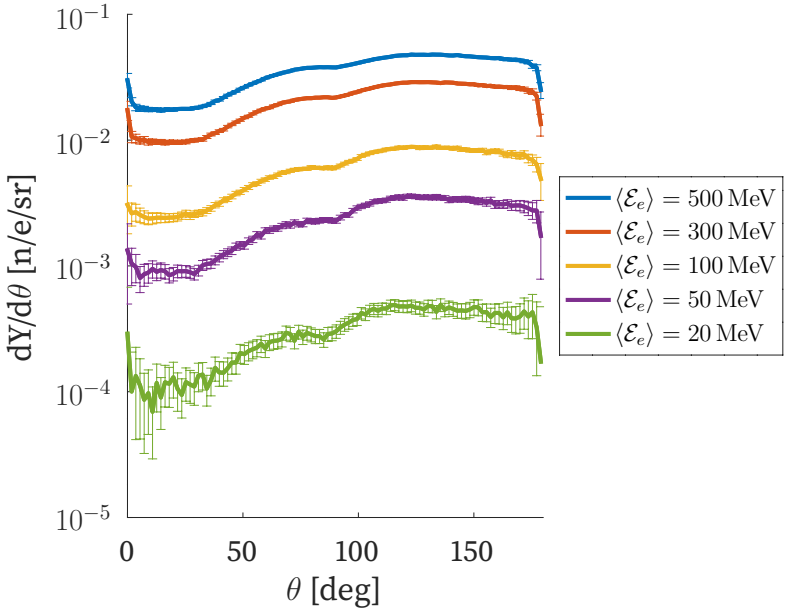

Figure 5.6: Neutron angular distribution for the optimal tungsten target ($L = 80$ mm, $r = 40$ mm) for different $\langle \mathcal{E}_e \rangle$ values.

Energy distribution

The neutron energy spectrum produced by the optimized tungsten target is calculated according to Eq. (5.4). Figure 5.7 shows the results of $f_{\theta,\mathcal{E}_n}$ for different $\langle \mathcal{E}_e \rangle$ values at the direction of maximum emission, $\theta_d = 130°$.

For all electron energies and detection angles, the low-energy region of the neutron spectrum resembles a Maxwellian distribution, with a peak near $0.5\,\mathrm{MeV}$, characteristic of evaporation neutrons originating from GDR-induced reactions [97]. The value of such peak, as shown in Table 5.1, increases with $\langle \mathcal{E}_e \rangle$, meaning that the amount of GDR-induced photoneutrons grows with the electron energy.

Given that the $\sim$ $0.5\,\mathrm{MeV}$ peak of $f_{\theta,\mathcal{E}_n}$, namely $f_{\theta,\mathcal{E}_{n,\mathrm{peak}}}$, corresponds to the evaporation-induced photoneutrons, an heuristic relative contribution of this mechanism can be calculated by comparison of the growth ratio of Y_n against the growth ratio of $f_{\theta,\mathcal{E}_n}$ for different $\langle \mathcal{E}_e \rangle$ values. We define the relative evaporation contribution,

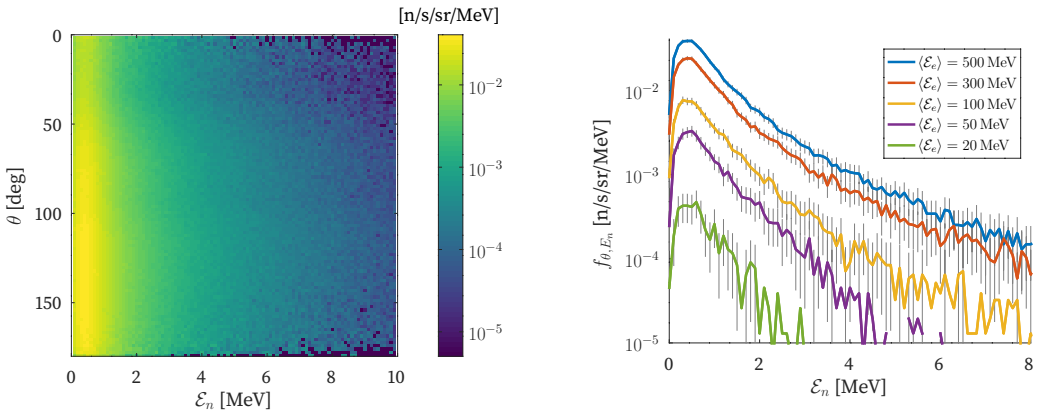

(a) $\mathcal{E}_n$ distribution for $\mathcal{E}_e = 500\,\mathrm{MeV}$.

(b) $f_{\theta,\mathcal{E}_n}$ distribution for $\theta_d = 130$ deg

Figure 5.7: Energy spectrum from the optimal tungsten target.

$\langle\mathcal{E}_e\rangle$ [MeV]	Y_n [10^{-1} n/e]	f_θ [10^{-2} n/e/sr]	max $\mathcal{E}_n$ [MeV]	$f_{\mathcal{E}_{n,\mathrm{peak}}}$ [10^{-2} n/e/sr/MeV]
20	0.041 ± 0.002	0.045 ± 0.005	0.6	0.047 ± 0.017
50	0.31 ± 0.05	0.350 ± 0.014	0.5	0.33 ± 0.4
100	0.79 ± 0.09	0.88 ± 0.02	0.3	0.77 ± 0.7
300	2.723 ± 0.014	2.89 ± 0.04	0.4	2.42 ± 0.12
500	4.644 ± 0.015	4.77 ± 0.05	0.4	3.89 ± 0.15

Table 5.1: Yield, f_θ, and $\langle\mathcal{E}_n\rangle$ for the neutrons emerging at $\theta_d = 130°$ for different electron energies.

w_{Evap}, as:

$$w_{\mathrm{Evap}}(\langle\mathcal{E}_e\rangle)_\theta \equiv \frac{f_{\theta,\mathcal{E}_{n,\mathrm{peak}}}(\langle\mathcal{E}_e\rangle)/f_{\theta,\mathcal{E}_{n,\mathrm{peak}}}(30\,\mathrm{MeV})}{Y_n(\langle\mathcal{E}_e\rangle)/Y_n(30\,\mathrm{MeV})}, \tag{5.10}$$

which compares the growth in Y_n and $f_{\theta,\mathcal{E}_{n,\mathrm{peak}}}$ at a given $\langle\mathcal{E}_e\rangle$ with respect to the GDR threshold of $30\,\mathrm{MeV}$. This indicator: (1) is computed from the cubic-interpolated values of Y_n and $f_{\theta,\mathcal{E}_{n,\mathrm{peak}}}$ at $30\,\mathrm{MeV}$, and (2) assumes that, at $30\,\mathrm{MeV}$, neutron production is dominated by evaporation (as reported in Ref [104] for $35\,\mathrm{MeV}$).

Table 5.2 presents the w_{Evap} values for different electron energies, showing that the neutron evaporation mechanism is predominant for all $\langle\mathcal{E}_e\rangle$ values. However, the decreasing tendency of w_{Evap} for higher electron energies informs of an increasing presence of non-evaporative processes, which generate higher energy neutrons which populate the tail of the distribution.

$\langle \mathcal{E}_e \rangle$ [MeV]	50	100	300	500
w_{Evap}	97%	89%	81%	76%

Table 5.2: w_{Evap} values for $\theta_d = 130\,^\circ$.

From Fig. 5.1, we see that these MeV neutrons could serve for electronics radiation studies, provided the source strength is large enough. For other applications including medical and industrial, these neutrons would require further moderation.

5.2 High-intensity electron linacs for neutron production

The strength of an electron-linac-based neutron source is defined in terms of the average electron intensity, $I_{\text{e, av}}$, as:

$$I_n \equiv Y_n I_{\text{e, av}} \tag{5.11}$$

Some neutron applications require pulsed spectra, and therefore benefit from pulsed linac operation. In this regard, CERN's ongoing efforts in developing normal-conducting linac technology, particularly within the framework of CLIC, provide a relevant basis for neutron production investigations.

To assess the neutron production of CANS driven by electron linacs with an optimized tungsten target, we consider optimizing the following linear accelerators as potential drivers: the CTF3 drive beam linac and the High-Pulse-Current-Injector (HPCI) linac. Both setups provide high-intensity electron beams with different injection schemes:

- The CTF3 drive-beam linac [105]: A thermionic gun followed by bunching and accelerating S-band travelling-wave structures. It was operated between 2004 and 2016, and accelerated electrons up to $150\,\text{MeV}$ to study the two-beam acceleration scheme of CLIC.
- The HPCI linac [106]: A photoinjector followed by an X-band travelling-wave linac optimized to provide high-quality and high-current electron beams. The HPCI is a conceptual design based on CLIC X-band technology with potential applications in ICS sources or novel radiotherapy schemes [107].

Table 5.3 presents the nominal parameters of the two high intensity electron linac proposals.

Magnitude	Units	HPCI linac	CTF3 drive beam linac
f	GHz	12.00	3.00
$f_{\text{RF-cycle}}$	Hz	100	100
r/Q	kΩ/m (av)	12.6	4.40
Q	- (av)	5717	4000
v_g	$\%c$ (av)	3.8	3.5
P_{max}	MW	26.7	29.8
q_{bunch}	nC	0.602	2.33
N_{bunches}		1000	2100
$I_{e,\text{av}}$	μA	28.50	489.3

Table 5.3: Specifications of the considered electron linacs [105, 106]

5.2.1 Full Beam Loading Operation

Equation (5.11) suggests that, for a given target at a given electron energy (i.e for a fixed yield value), the strength of a source can be maximized by transporting more charge through the electron linac. One key limiting factor is the BL effect. If the beam intensity is high enough, there is a limit where all EM energy is consumed and the structure cannot accelerate further bunches. This phenomenon is known as full beam loading.

CTF3 drive beam linac was designed to operate in a fully beam loaded mode, and its successful operation with $\geq 90\%$ percent of gradient reduction was proved in [108]. On the other hand, the designed q_{bunch} value of $285\,\text{pC}$ in Ref [106] for the HPCI linac does not reach the full beam loaded limit. For this reason, the full BL-induced gradient reduction was simulated with RF-TRACK for the HPCI linac. The full beam-loaded configurations for 95% percent of gradient reduction are shown in Tab. 5.4.

Since the HPCI injector is S-band, the proposed beam scheme is $q_{\text{bunch}} = 600\,\text{pC/bunch}$ with bunch-to-bunch spacing of $100\,\text{mm}$ ($3\,\text{GHz}$). Although the minimum number of bunches for the full BL to manifest is 165 in this case, the laser and photocathode technology reported in [106] allows the consideration of trains of 1000 bunches. Figure 5.8 shows the gradient reduction at the steady state for the considered HPCI-fully-loaded configuration, resulting in a loss of accelerating voltage of $10.08\,\text{MeV}$.

f_b [GHz]	q_{bunch} [pC]	**min.** N_{bunches}
12.00	150.6	657
6.00	301.2	329
4.00	451.8	219
3.00	602.4	165
2.00	903.6	110
1.50	1204.8	83

Table 5.4: Different train configurations resulting into full Beam Loading of HPCI linac.

RF-to-Beam Efficiency

The expression for the instantaneous RF-to-Beam efficiency reads as:

$$\eta_{\text{RF-beam}}(t) = \frac{\Delta P_{\text{beam}}(t)}{P_{\text{in}}(t)} = \frac{I(t)}{P_{\text{in}}(t)} \int_0^L G(z,t)\mathrm{d}z. \tag{5.12}$$

In practice, many RF-to-beam efficiency estimations are based in the maximum value of $\eta_{\text{RF-beam}}$ achieved during a full pulse duration. To compare the total useful output (beam energy) with the total input (RF energy) over the full pulse duration, the *average RF-to-Beam efficiency*, η_{av}, is defined as:

$$\eta_{\text{RF-beam, av}} \equiv \frac{\int_0^{T_{\text{pulse}}} \Delta P_{\text{beam}}(t)\ \mathrm{d}t}{\int_0^{T_{\text{pulse}}} P_{\text{in}}(t)\ \mathrm{d}t} = \frac{P_{\text{beam}}(t_{\text{out}} - t_{\text{in}})}{\int_0^{T_{\text{pulse}}} P_{\text{in}}(t)\ \mathrm{d}t}. \tag{5.13}$$

As seen in Eq. 5.13, the calculation of η_{av} requires knowledge of the power pulse shape, P_{in}. We propose the following pulse shape:

$$P_{\text{in}}(t) = \begin{cases} a_1 t^3 + a_2 t^2 + a_3 t & \text{for } t < t_{\text{inj}} \\ P_{\text{max}} & \text{for } t \geq t_{\text{inj}} \end{cases} \tag{5.14}$$

where the parameters that compensate BL in the HPCI linac were calculated by minimization the merit function in Eq.(3.61), following a similar procedure to the one presented in Sec. 3.6.2. Their value, and the corresponding RF-to-Beam efficiencies are shown in Tab. 5.5.

For the CTF3 drive beam linac, the RF-to-Beam efficiencies are $\eta_{\text{max}} = 0.93$ and $\eta_{\text{av}} = 0.90$ [105]. Figure 5.9 shows the shape of the optimal pulse as well as the beam power consumption.

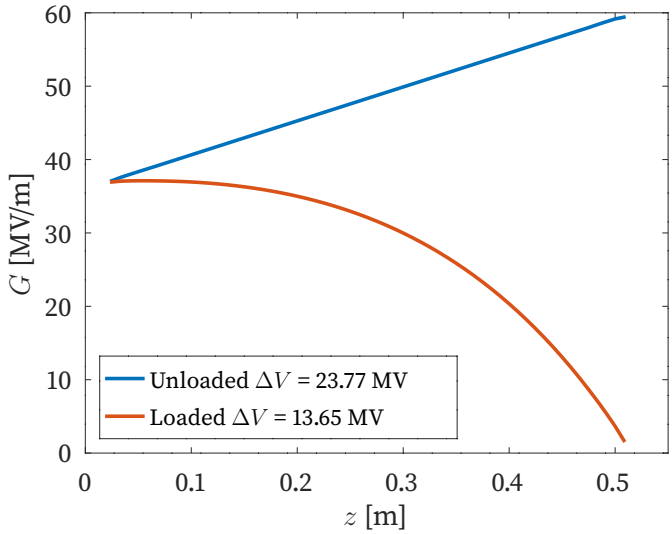

Figure 5.8: Unloaded and full beam loaded gradient of an HPCI X-band accelerating structure

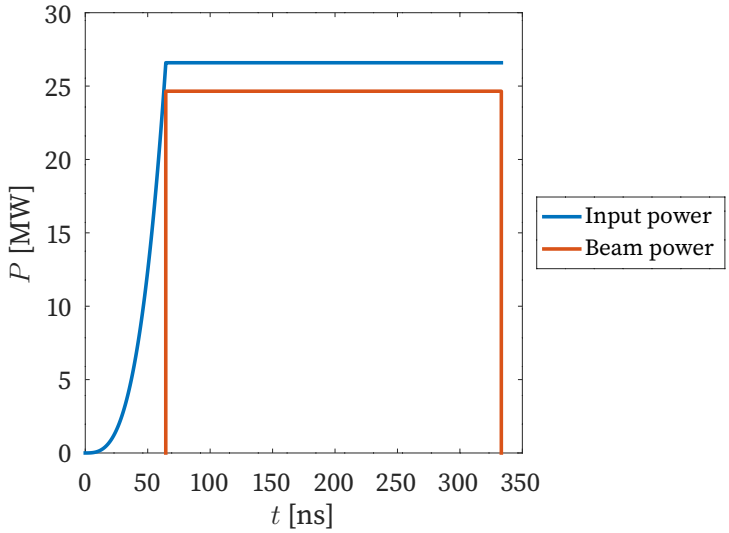

Figure 5.9: RF pulse and beam power for HPCI linac with N_{bunches} = 1000, q_{bunch} = 602.4 pC and f_b = 3.00 GHz.

5.2.2 Heat deposition in the target

One of the potential issues associated with the production of neutrons with heavy-loaded electron linacs is the heat deposition in the target. Such high-intensity beams

Parameter	Units	Value
a_1	$\mathrm{W/ns^3}$	98.33
a_2	$\mathrm{W/ns^2}$	41.35
a_3	$\mathrm{W/ns}$	260.7
t_{inj}	ns	63.46
$\eta_{\text{RF-beam, max}}$		0.927
$\eta_{\text{RF-beam, av}}$		0.879

Table 5.5: Beam Loading compensation parameters for HPCI linac.

lead to a non-uniform energy deposition in the target. As a consequence, mechanical stresses may arise, expanding the target up to a threshold where the deformation is no longer elastic, causing target failures [109].

The relationship between the beam deposited energy distribution in a pulse ($Q_m \equiv \mathrm{d}Q/\mathrm{d}m$, in units of $\mathrm{J/kg}$) and the associated temperature rise (ΔT_p, in Kelvin), is given by the specific heat capacity, c_p, by:

$$\Delta T_p = \frac{1}{c_p}\Delta Q_m. \tag{5.15}$$

These thermal gradients inside the target induce mechanical stresses, whose pressure can be calculated from the linear expansion coefficient, α, and the elastic modulus, E, as:

$$P_t \equiv \alpha \mathrm{E} \Delta T_p \, [\mathrm{Nm^{-2}}]. \tag{5.16}$$

For pure tungsten, the pressure value at which the deformation ceases to be elastic is $P_t^* = 54.6\,\mathrm{Nm^{-2}}$, which translates on a maximum temperature rise allowed of $\Delta T_p^* = 270\,\mathrm{K}$.

Despite c_p being temperature-dependent, for the case of pure tungsten in the range $25\,^\circ\mathrm{C}$ to $305\,^\circ\mathrm{C}$, its value is constant and equals $0.13\,\mathrm{J/g/K}$ [110]. Therefore, the maximum value of Q_m, namely Peak Energy Deposition Distribution (PEDD), after which the target suffers inelastic stresses is:

$$\mathrm{PEDD} = 35\,\mathrm{J/g}. \tag{5.17}$$

Methodology for PEDD calculations with G4Beamline: The setup in Fig. 5.4 was simulated with G4Beamline for $N_e = 10^7$ events. $N_z = 10$ cylindrical non-invasive

detectors of radius $40\,\mathrm{mm}$ and length L/N_z were placed along the z-axis. The center of each detector was at a position $z_k = (k-0.5)L/N_z$, $(k = 1, .., N_z)$. Each plane was meshed transversely $\{(x_i, y_j)\}_{i,j}^{N_x,N_y}$, with $N_x = N_y = 400$, $x_i = i\frac{2r}{N_x-1} - r$, and $y_i = i\frac{2r}{N_y-1} - r$.

Let $e_{n,m,ijk}$ denote the amount of energy deposited into the (x_i, y_j, z_k) node by the $m-$th particle of the $n-$th shower. The average energy deposited in the (x_i, y_j, z_k) node, $\Delta Q(i,j,k)$, and its uncertainty, are obtained as [96]:

$$\Delta Q(i,j,k) = \frac{1}{N_e}\sum_{n=1}^{N_e} e_{n,ijk}, \qquad \text{with} \qquad e_{n,ijk} = \sum_m e_{n,m,ijk}, \tag{5.18}$$

$$\sigma_{\Delta Q(i,j,k)} = \sqrt{\frac{1}{N_e}\left(\frac{1}{N_e}\sum_{n=1}^{N_e} e_{n,ijk}^2 - \Delta Q(i,j,k)^2\right)}. \tag{5.19}$$

This allows to compute the PEDD in a pulse as:

$$Q_m(i,j,k) = \frac{N_{\text{bunches}} q_{\text{bunch}}}{\rho e}\left(\frac{\Delta Q(i,j,k)}{\Delta x \Delta y \Delta z}\right), \tag{5.20}$$

$$\text{PEDD} = \max\{Q_m(i,j,k) : 1 \le i,j \le N_x, 1 \le k \le N_z\}. \tag{5.21}$$

with $\Delta z = \frac{L}{N_z}$, $\Delta_x = \Delta_y = \frac{2r}{N_x-1}$, and ρ the density of pure tungsten.

The results for the energy deposition calculations in the $z = 0$ and $z = 80\,\mathrm{mm}$ plane are shown in Fig. 5.10.

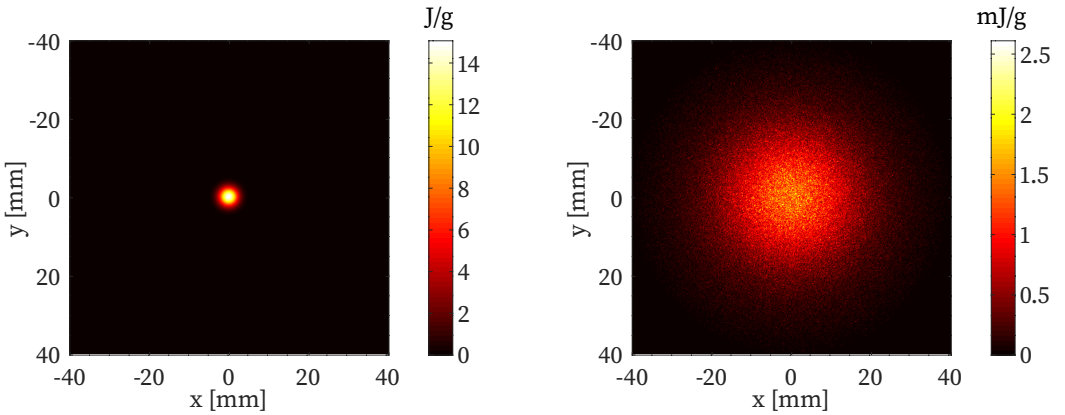

(a) $z = 0$ mm. (b) $z = 80$ mm.

Figure 5.10: Energy deposition in the tungsten target ($r = 40\,\mathrm{mm}, L = 80\,\mathrm{mm}$) when the HPCI $600\,\mathrm{pC/bunch}$ beam incides with $\langle \mathcal{E}_e \rangle = 500\,\mathrm{MeV}$, $\sigma_x = \sigma_y = 1.3\,\mathrm{mm}$.

Figure 5.11 presents the maximum value of the energy deposition in each detecting plane for the HPCI linac configuration ($602.4\,\mathrm{pC/bunch}$, $\sigma_x = \sigma_y = 1.3\,\mathrm{mm}$). It shows

that the maximum heat deposition occurs at the beam entrance. This is due to the fact that electrons, as well as their products, spread out as they travel through the target, leading to a reduction in the concentration of heat deposition. The same conclusion could be extracted by comparing Figs. 5.10a and 5.10b.

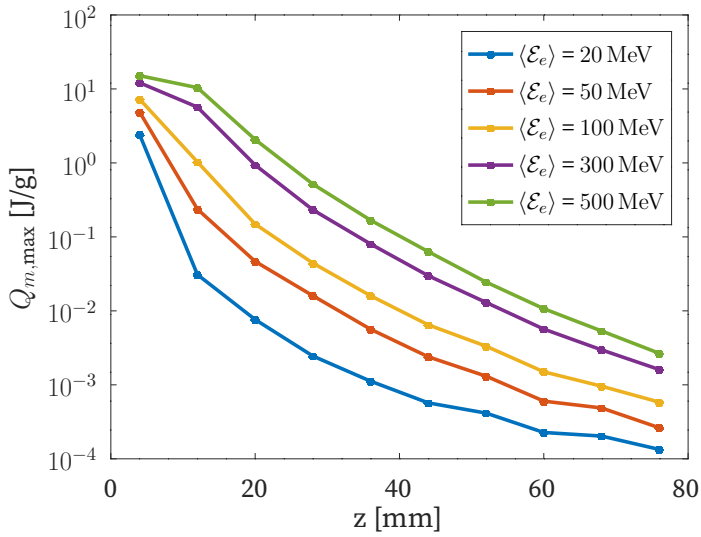

Figure 5.11: Energy deposition evolution with depth for HPCI-target configuration: $602.4\,\mathrm{pC/bunch}$, $\sigma_x = \sigma_y = 1.3\,\mathrm{mm}$.

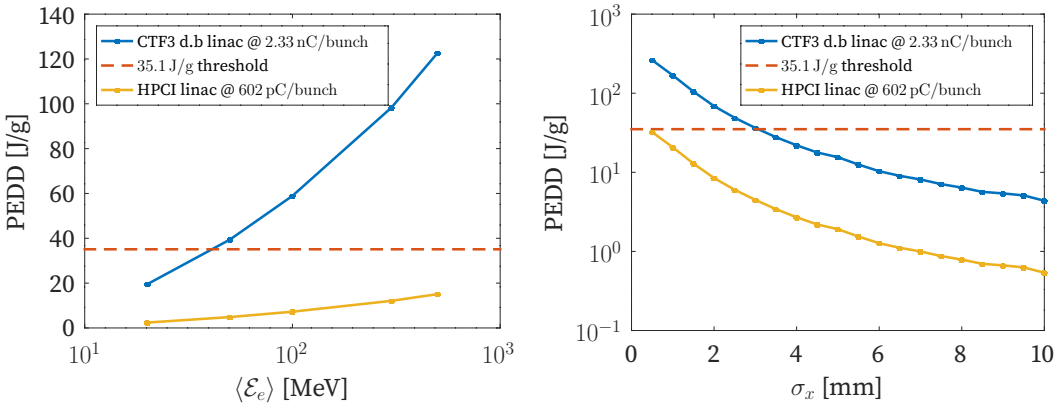

(a) $\sigma_x = \sigma_y = 1.3\,\mathrm{mm}$. (b) $\langle \mathcal{E}_e \rangle = 500\,\mathrm{MeV}$.

Figure 5.12: Peak Energy deposition for the different e-linac based sources proposed.

In Fig. 5.12, the PEDD values for the two electron-linac-based neutron sources under consideration are depicted. Figure 5.12a shows that, for beams of equal focus, the S-band proposal exceeds the 35.1 J/g threshold for $\langle \mathcal{E}_e \rangle > 40\,\mathrm{MeV}$ if a final beam size of

$\sigma_x = \sigma_y = 1.3\,\mathrm{mm}$ is considered. Figure 5.12b demonstrates the PEDD's dependency on σ_x (simulation performed for $\langle \mathcal{E}_e \rangle = 500\,\mathrm{MeV}$). Safe values for the CTF3 drive beam linac option are found for $\sigma_x \geq 3.5\,\mathrm{mm}$.

5.2.3 Comparison with state-of-the-art

So far, the proposed electron-linac-based neutron sources exhibit safe PEDD values, high RF-to-beam efficiency values and transport high q_{bunch} values without reaching BL saturation. In this Section, we discuss how their performance compares with already-existing or under design sources in the state-of-the-art. Figure 5.13 is a landscape plot that situates the CTF3- and HPCI-driven CANS within the context of existing facilities, with respect to source strength and primary particle energy.

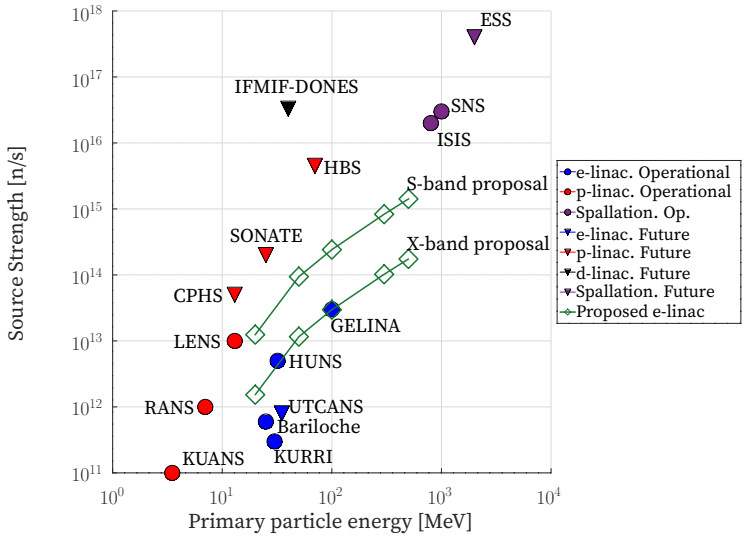

Figure 5.13: High-intensity electron linac comparison with the state-of-the-art.

The source strength of the proposed electron-linac-based CANS compares to some electron- and proton-linac-based compact sources, exhibiting a neutron strength up to $(1.51 \pm 0.07) \cdot 10^{15}$ n/s. This limit in neutron production can be understood considering the power of the primary particle's beam, defined as:

$$P_{\mathrm{beam}} \equiv I_{e,\mathrm{av}}[\mathrm{A}]\mathcal{E}_e[\mathrm{eV}]/\mathrm{e}\ [\mathrm{W}]. \tag{5.22}$$

Figure 5.14 shows the dependency of the source strength of the previous compact and spallation sources with the primary beam power. Among the considered sources in Fig. 5.14, the proposed e-linac facilities exhibit greater source strengths for beam

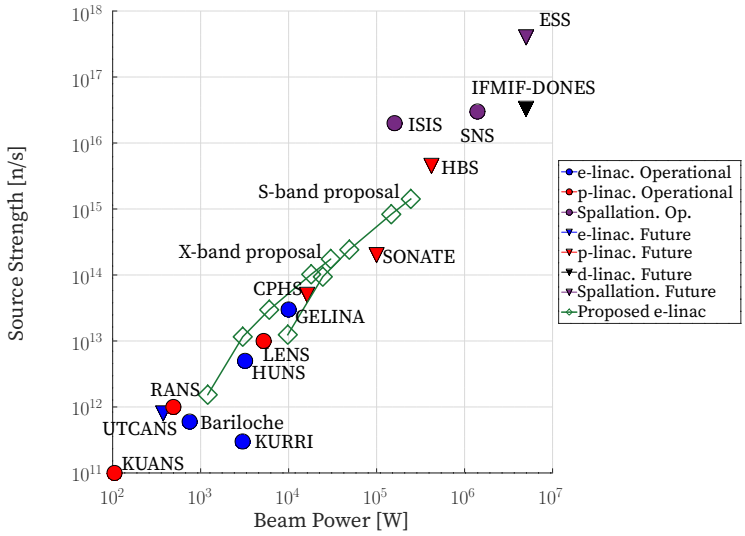

Figure 5.14: Beam power comparison for the state-of-the-art neutron sources.

powers ranging from $0.57\,\mathrm{kW}$ to $245\,\mathrm{kW}$, meaning that the optimized tungsten target is more efficient than other targets in this power regime, regardless the nature of the particle arriving to it.

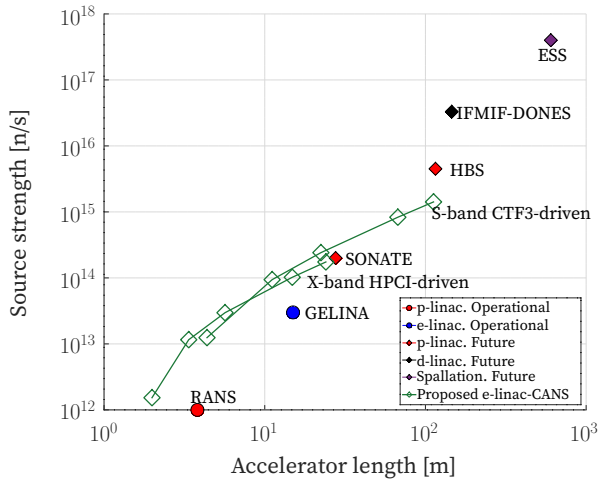

Figure 5.15: Source strength vs accelerator length. Data from Table A.2

Another quantity of interest to be considered when comparing different CANS is the accelerator length, L_{acc}. Figure 5.15 shows the dependency of the length of the accelerator-based sources with their strength.

5.2.4 Energy consumption and efficiency

The normalized shunt impedance, R/Q, scales with the frequency. In principle, this means that less energy is required to provide the same acceleration in X-band linacs with respect to S-band linacs. However, to estimate energy consumption in the neutron production process, the entire wall-to-beam process has to be considered, as it is illustrated in Fig. 5.16.

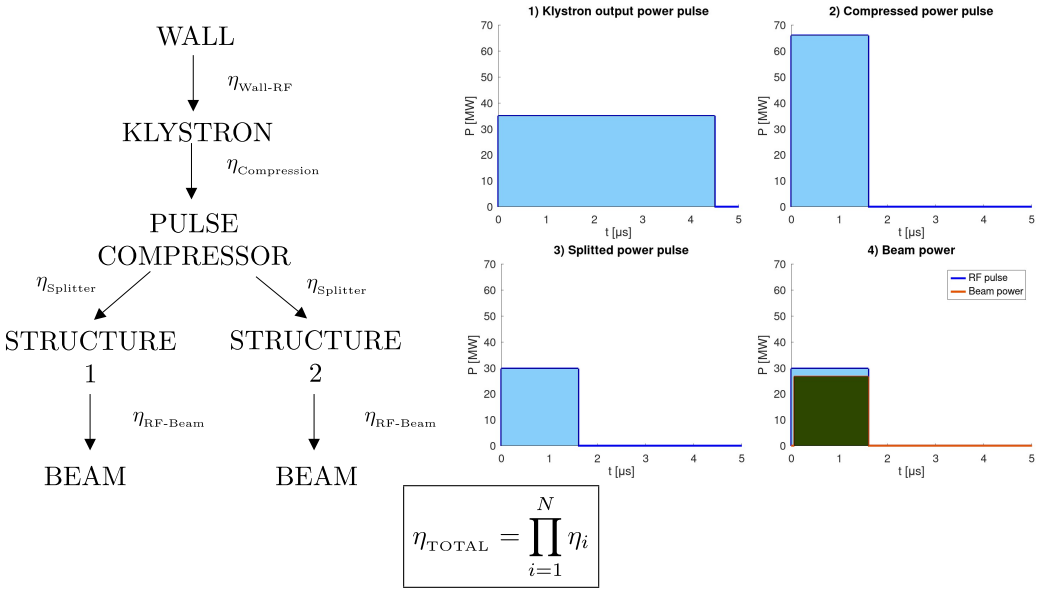

Figure 5.16: Wall-to-beam efficiency illustrated for CTF3 drive beam linac

The HPCI linac proposed and the CTF3 drive-beam linac share the same RF schematic: Each klystron produces an RF pulse which is compressed with a pulse compressor, and then splited to feed two independent TW structures. Losses are expected in each of the steps, and the total wall-to-beam efficiency, η_{TOTAL}, can be calculated as:

$$\eta_{\text{TOTAL}} = \eta_{\text{wall-RF}} \cdot \eta_{\text{compressor}} \cdot \eta_{\text{splitter}} \cdot \eta_{\text{RF-beam, av}} \cdot \tag{5.23}$$

Table 5.6 presents the total energy consumption for both electron-linac-based CANS proposals, as well as the energy consumed per neutron produced, E_{pn}. Both electron-linac-based sources have show similar wall-to-beam efficiencies, which translates into a similar energetic cost for neutron production, with X-band being more advantageous than S-band.

[1]Assumed 1 m of triplets and drifts between accelerating structures

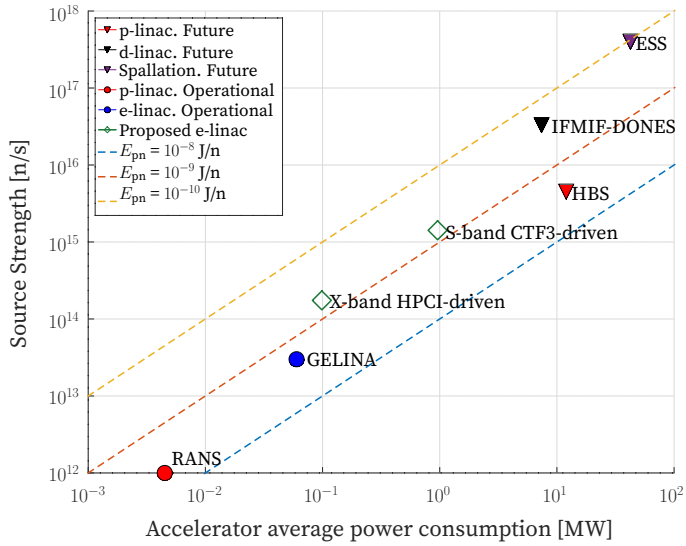

Figure 5.17: Average power consumption comparison for different neutron sources.

Magnitude	**Unit**	**HPCI X-band**	**CTF3 S-band**
Bunch power gain per structure	MW	24.6	26.6
Pulse length	μs	0.333	1.56
Energy required from 2 structures	J	16.86	82.93
Loaded gradient	MV/m	27.0	6.5
Pairs of structures		16	28
Total length [1]	m	24.0	112.1
η_{splitter}	-	0.9	0.9
$\eta_{\text{compressor}}$	-	0.56 [111]	0.66
$\eta_{\text{wall-RF}}$	-	0.6 [20]	0.45
η_{TOTAL}	-	0.27	0.24
Energy consumed by a train	J	986.2	9587
Average power consumption	kW	98.62	958.8
Yield	n/s	$1.74 \cdot 10^{14}$	$1.51 \cdot 10^{15}$
Energy consumed per neutron produced	J/n	$5.65 \cdot 10^{-10}$	$6.76 \cdot 10^{-10}$

Table 5.6: Efficiency considerations for $\langle \mathcal{E}_e \rangle = 500\,\text{MeV}$.

Figure 5.17 compares the RF average power consumption of different accelerator-based neutron sources with respect to their source strength. It shows that the

proposed electron-linac-based sources exhibit E_{pn} values one order of magnitude smaller than the others compact sources. This indicates that neutron generation using the proposed electron-based CANS is more energy-efficient than that of alternative compact sources, being this advantage is a consequence of the overall energy efficiency of the proposed high-gradient electron accelerators, η_{TOTAL}.

5.3 Preliminary proposal of a backscattering target for imaging applications

Without further moderation scheme, the proposed electron-linac-based sources offer very energetic neutron beams of the order of the MeVs as seen in Table 5.1. However, industrial and medical applications benefit from less energetic neutrons, thus requiring moderation. This is achieved by elastic scattering with hydrogen-rich compounds such as methane, polyethylene and liquid hydrogen.

In this section, a preliminary design of a thermal ($0.9\,\text{Å}$ to $2.6\,\text{Å}$) and cold ($2.6\,\text{Å}$ to $26.1\,\text{Å}$) target-moderator assembly is presented. To discuss its performance, the following figures of merit have to be defined:

- The wavelength spectrum, f_λ:

$$f_\lambda(\theta, \lambda; \mathcal{E}_e) \equiv \frac{\mathrm{d}^3 I_n}{\mathrm{d}S_{\text{emission}}\mathrm{d}\Omega\mathrm{d}\lambda}(\lambda)\ [\mathrm{n/s/cm^2/sr/Å}], \tag{5.24}$$

  where S_{emission} stands for the surface from which neutrons are emitted over the solid angle Ω, and λ is the associated neutron wavelength, calculated in terms of its energy as [88]:

$$\lambda \equiv \frac{9.045}{\sqrt{\mathcal{E}_n[\mathrm{MeV}]}}\ [\mathrm{Å}]. \tag{5.25}$$

  According to [34], f_λ is called *average brightness*. We note a discrepancy in the definition of this term compared to [43], where it is quoted as *brilliance*. In this document, f_λ denotes average brightness.

- The average brilliance, $\mathcal{B}$:

$$\begin{aligned}\mathcal{B}(\theta, \lambda; \mathcal{E}_e) &\equiv \frac{\int_{\lambda-\Delta\lambda/2}^{\lambda+\Delta\lambda/2} f_\lambda(\lambda')\mathrm{d}\lambda'}{1\%\frac{\Delta\lambda}{\lambda}} \\ &\simeq \frac{N_n^*}{S_{\text{emission}} \cdot \Omega \cdot (1\%\frac{\Delta\lambda}{\lambda})\Delta t}\ \left[\frac{\mathrm{n}}{\mathrm{s \cdot cm^2 \cdot sr \cdot 1\%BW}}\right],\end{aligned} \tag{5.26}$$

with N_n^* the number of neutrons emerging from the surface S_{emission} in a solid angle Ω with a wavelength spread of $\Delta\lambda$ in a time Δt. For $\Delta\lambda/\lambda \ll 1$, one can approximate as follows:

$$\mathcal{B} \simeq 100\,\lambda\, f_\lambda. \tag{5.27}$$

The brilliance depends on the direction as well as on the design of the target-moderator assembly, as seen in Eq. (5.26). According to Liouville's theorem, the volume in phase space is constant for lossless conservative optics, which implies that the brilliance at the sample position is identical to the brilliance of the source. This allows the comparison between facilities by just studying the target [31], and therefore, the average brilliance is the figure of merit assessing the quality of the neutron spectrum for imaging and diffractrometry applications.

- The peak brightness, $f_{\lambda,\,\text{peak}}$:

$$f_{\lambda,\,\text{peak}} \equiv \max_{t>0}\left(\frac{\mathrm{d}q_e}{\mathrm{d}t} \otimes g_{\lambda,t}\right)\,[\mathrm{n/s/sr/cm^2/\AA}], \tag{5.28}$$

where $\frac{\mathrm{d}q_e}{\mathrm{d}t}$ is the electron pulse, $\otimes$ denotes a convolution, and $g_{\lambda,t}$ for the neutron spectrum produced per single electron, defined as:

$$g_{\lambda,t} \equiv \frac{\mathrm{d}^4 Y_n}{\mathrm{d}S_{\text{emission}}\mathrm{d}\Omega\mathrm{d}\lambda\mathrm{d}t}\,[\mathrm{n/e/sr/cm^2/\AA/s}]. \tag{5.29}$$

5.3.1 Thermal Polyethylene Premoderator

To moderate neutrons to the thermal range, a polyethylene cylinder of thickness L_{thermal} is placed around the optimized tungsten target, as shown in Fig. 5.18a. To find the optimal value of L_{thermal}, the described setup was simulated with G4BEAMLINE choosing $N_e = 10^7$ and $\theta_i = 0^\circ$ for different values of L_{thermal} and different mean electron energies.

Figure 5.18b is a 2D histogram that shows the variation in neutron brightness observed at different thermal energies when the optimized tungsten target in Fig. 5.18a is driven by the CTF3 drive beam linac ($\langle\mathcal{E}_e\rangle = 500\,\mathrm{MeV}$) and surrounded by different lengths of moderator. There is a clear maximum in f_λ observed at $L_{\text{thermal}} = 60\,\mathrm{mm}$.

The thermal setup in Fig. 5.18a was simulated with $N_e = 10^8$ electrons for the electron beams of $\langle\mathcal{E}_e\rangle = 20,\,50,\,100,\,300,\,500\,\mathrm{MeV}$. The yield dependency with z is shown

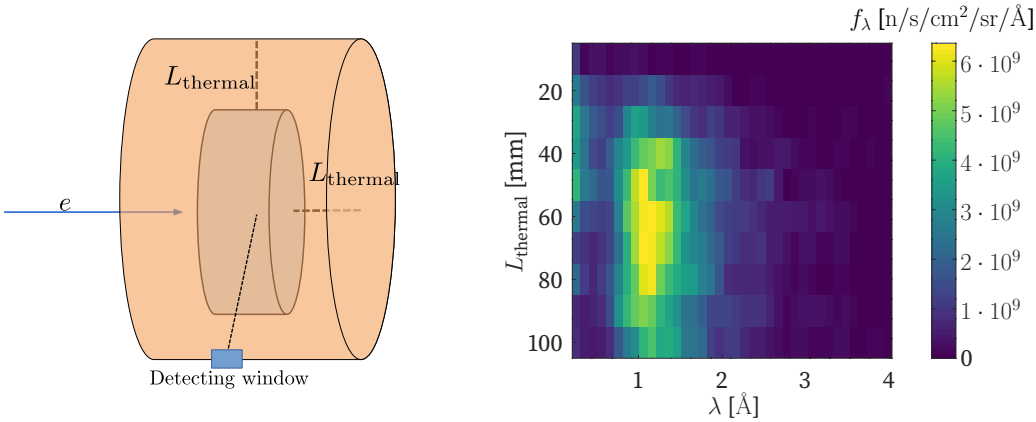

(a) Geometry sketch with arbitrary detecting window location.

(b) Dimension scan for maximum f_λ for the CTF3 drive beam linac 500 MeV.

Figure 5.18: Thermal moderator setup.

in Fig. 5.19a, revealing that the detecting window, i.e. the position where neutron emission is maximum, is located at $z < 0$. In addition, Fig. 5.19b shows that neutron emission is isotropic, consistent with the cylindrical symmetry of the setup.

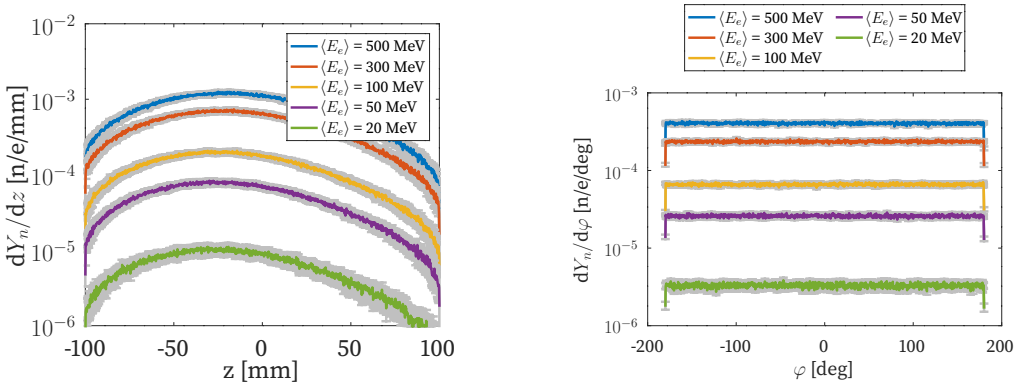

(a) Longitudinal position scan. Window located at $z \in (-30, -15)$ mm.

(b) Azimuthal isotropy of the yield.

Figure 5.19: Spatial and angular considerations for the location of the detecting window in the thermal moderator assembly.

Average brightness

For each electron energy, f_λ has been calculated by computing the histograms associated with Eq. (5.24) for the neutrons arriving at the detecting window in the previous simulation with $N_e = 10^8$ electrons. The results for both CTF3-drive-beam-linac-

based and HPCI-linac-based neutron sources are shown in Fig. 5.20.

Consistent with the neutron yield dependency with electron energy (see Fig. 5.5b), the average brilliance grows with the electron energy, and it shows a maximum value at $\lambda = 1.1$Å as seen in Fig 5.20.

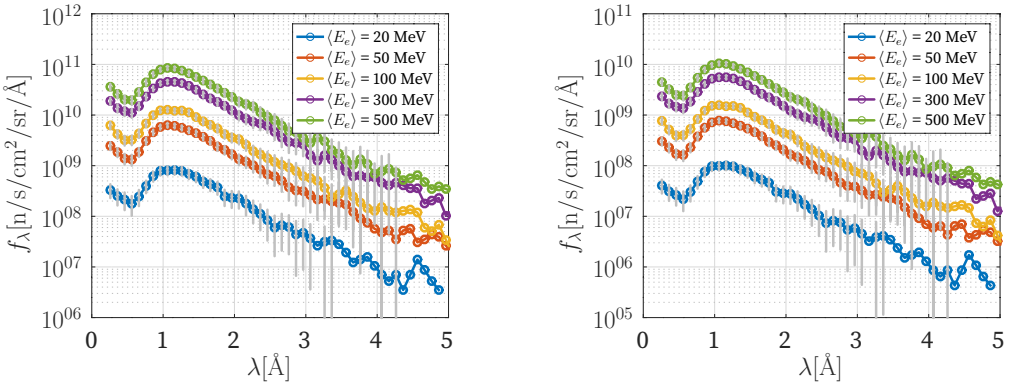

(a) CTF3-drive beam linac.

(b) HPCI linac.

Figure 5.20: f_λ (average brightness) distribution for the optimal thermal moderator assembly ($L_{\text{thermal}} = 60$ mm). Uncertainty bars in grey, computed based on Eq. (5.4).

Peak brightness

Figure 5.21 shows that $g_{\lambda,t}$ extends several microseconds for the considered CANS, while the electron pulses extend for only a few nanoseconds since the accelerator frequency is of the order of GHz as seen in Table 5.3. Therefore, Eq. (5.28) reads for this particular case as:

$$f_{\lambda,\,\text{peak}} = q_{\text{e train}} \cdot \max_{t>0} g_{\lambda,t}. \tag{5.30}$$

For a precise calculation of Eq. (5.30), the values of $g_{\lambda,t}$ obtained from the simulation have been fitted to the tail-weighted distribution functions f_X [113]:

$$f_X(x;a,b) = -f(x;a,b)\log\left(\int_0^x f(x';a,b)\mathrm{d}x'\right), \tag{5.31}$$

where the following distributions have been used:

$$\text{Maxwell-Boltzmann} \quad f(x;a,b) = a\sqrt{\frac{2}{\pi}}\frac{x^2}{b^3}e^{\frac{-x^2}{2b^2}} \tag{5.32}$$

$$\text{Rayleigh} \quad f(x;a,b) = a\frac{x}{b^2}e^{\frac{-x^2}{2b^2}} \tag{5.33}$$

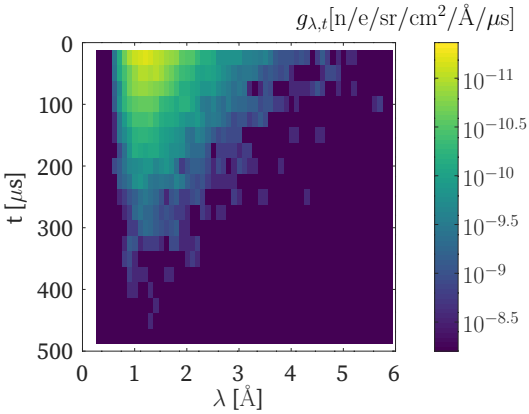

(a) $g_{\lambda,t}$ for $\langle \mathcal{E}_e \rangle = 20\,\mathrm{MeV}$ and $L_{\mathrm{thermal}} = 60$ mm.

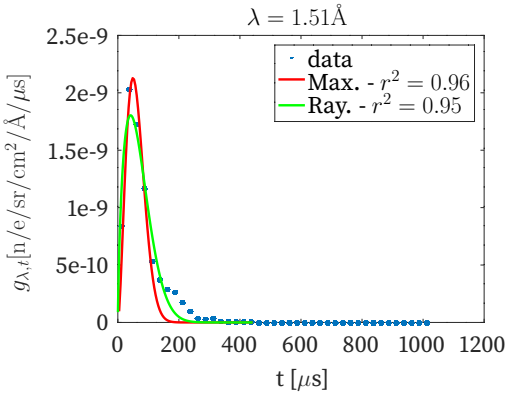

(b) $g_{\lambda,t}$ for $\langle \mathcal{E}_e \rangle = 20$ MeV and fits.

Figure 5.21: The fitting of the curves to the data was calculated with the Gauss-Newton method [112].

Figure 5.21b shows the values of $g_{\lambda,t}$ for an incident electron beam of $\langle \mathcal{E}_e \rangle = 20\,\mathrm{MeV}$ at the detecting window in Fig. 5.19a, and the fitting curves for both tail-weighted Maxwell-Boltzmann and Rayleigh distributions.

Figure 5.22 shows the peak brightness for the different electron accelerators considered through this work for $\langle \mathcal{E}_e \rangle$ ranging from $20\,\mathrm{MeV}$ to $500\,\mathrm{MeV}$. It can be seen that $f_{\lambda,\mathrm{peak}}$ depends on the electron energy, which is two orders of magnitude bigger than the average brightness.

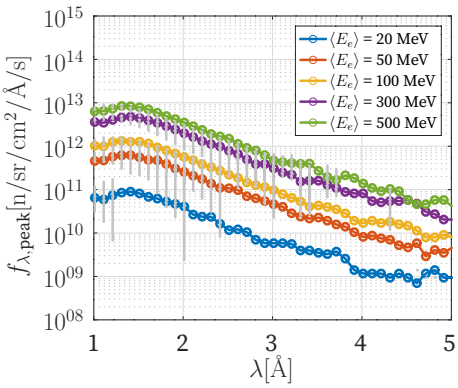

(a) CTF3-drive beam linac.

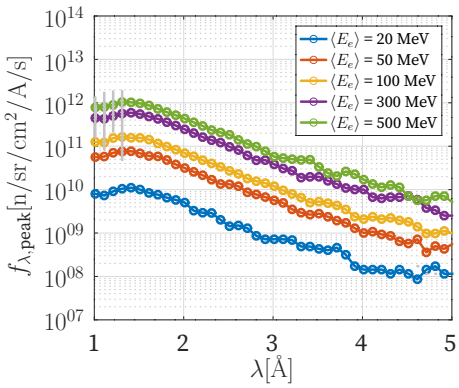

(b) HPCI linac.

Figure 5.22: $f_{\lambda,\mathrm{peak}}$ (peak brightness) distribution for the optimal thermal moderator assembly ($L_{\mathrm{thermal}} = 60\,\mathrm{mm}$). Uncertainty bars in grey, computed based on Eq. (5.4).

5.3.2 Cold Liquid Hydrogen Moderator

To moderate neutrons to the cold range, a liquid-hydrogen (20 K) cylinder of thickness L_{cold} can be placed around the optimized tungsten target in Sec. 5.3.1 as shown in Fig. 5.23a. To find the optimal value of L_{cold}, the described setup was simulated with $N_e = 10^7$ and $\theta_i = 0°$ for different values of L_{cold} and different mean electron energies. Figure 5.23b shows the values of f_λ in the detecting window for the case of the CTF3 drive beam linac at $\langle \mathcal{E}_e \rangle = 500\,\text{MeV}$. The optimal value of L_{cold} is 25 mm.

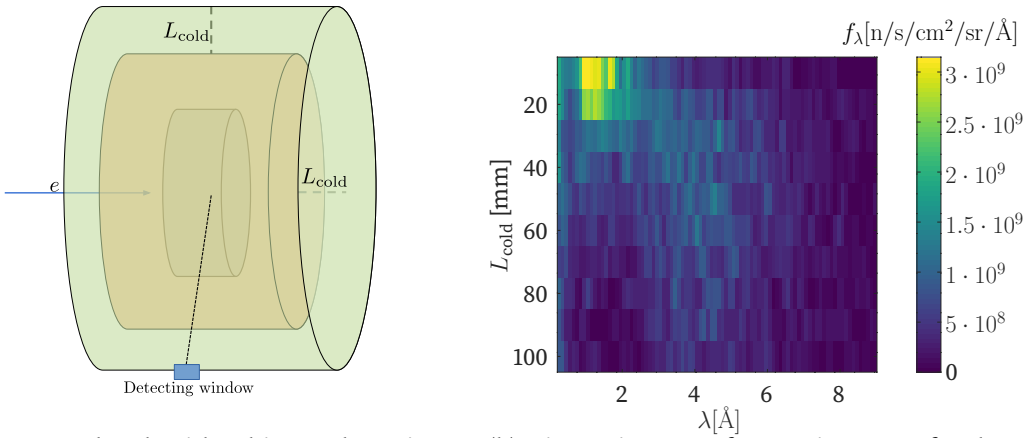

(a) Geometry sketch with arbitrary detecting window location.

(b) Dimension scan for maximum f_λ for the CTF3 drive beam linac 500 MeV.

Figure 5.23: Cold moderator setup.

Again, this choice of L_{cold} is assumed for all electron energies, and Fig. 5.24a shows that the detecting window where cold neutron emission is maximum is located at $z < 0$. The analysis of the neutron spectrum shows that the emission is isotropic (see Fig. 5.24b), consistent with the cylindrical symmetry of the problem.

Average and peak brightness

For the electron energies, $\langle \mathcal{E}_e \rangle = 20,\ 50,\ 100,\ 300,\ 500\,\text{MeV}$ and $L_{\text{cold}} = 25\,\text{mm}$, the cold setup in Fig. 5.23b was simulated with $N_e = 10^8$ electrons. The average and peak brightness of the cold neutrons arriving at the detecting window were calculated according to Eqs. (5.24) and (5.30) following the same procedure as in the case of the thermal moderator (in Sec. 5.3.1). The results are shown in Figs. 5.25 and 5.26.

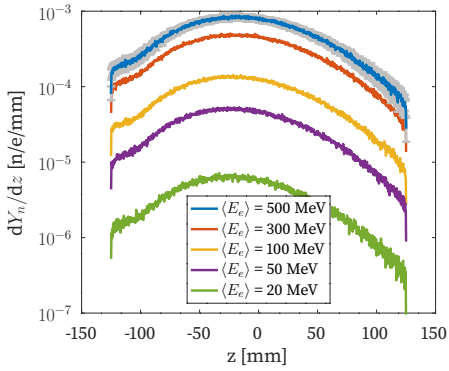

(a) Longitudinal position scan. Window located at $z \in (-30, -15)$ mm.

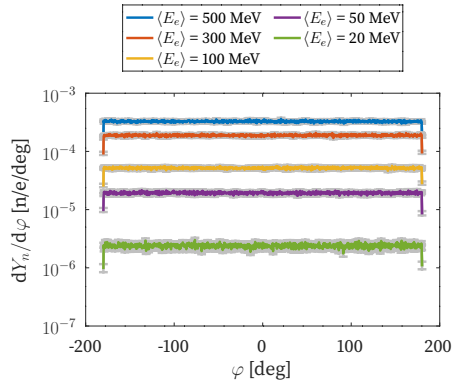

(b) Azimuthal isotropy of the yield.

Figure 5.24: Spatial and angular considerations for the location of the detecting window in the cold moderator assembly.

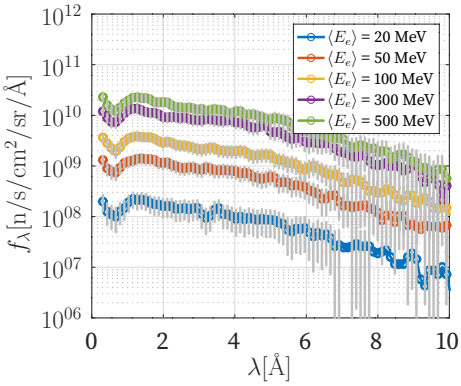

(a) CTF3-drive beam linac.

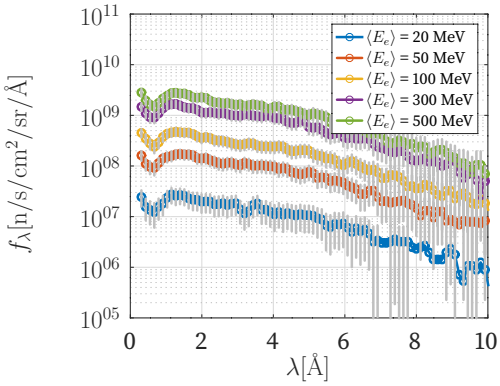

(b) HPCI linac.

Figure 5.25: f_λ (average brightness) distribution for the optimal cold moderator assembly ($L_{\text{cold}} = 25$ mm). Uncertainty bars in grey, computed based on Eq. (5.4).

5.3.3 Comparison with the state-of-the-art

The brightness of the already discussed electron-linac-based CANS is compared with future proposals of compact accelerator-based and spallation neutron sources in Fig. 5.27 and 5.28.

It can be seen that the CTF3 drive beam linac at $\langle \mathcal{E}_e \rangle = 500$ MeV, which features the highest beam power between the e-linacs proposed, reaches the state-of-the-art brightness for current neutron sources designs. However, The proposed electron-

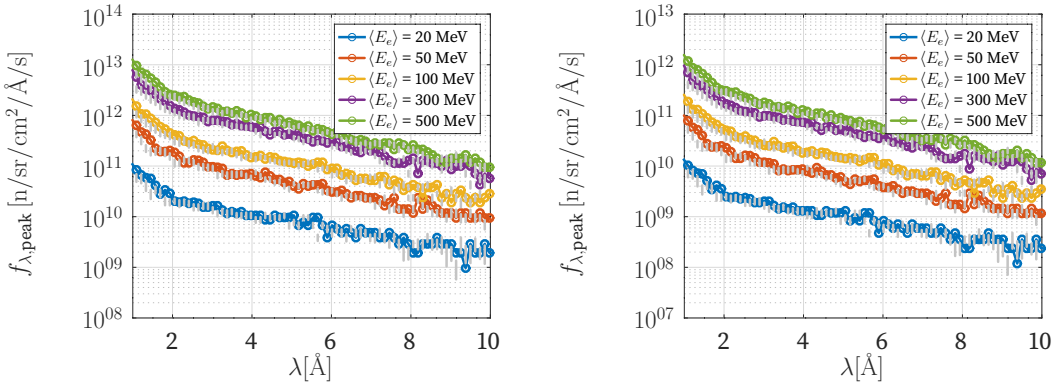

(a) CTF3-drive beam linac.

(b) HPCI linac.

Figure 5.26: $f_{\lambda,\text{peak}}$ (peak brightness) distribution for the optimal cold moderator assembly ($L_{\text{cold}} = 25$ mm). Uncertainty bars in grey, computed based on Eq. (5.4).

linac-based facilities provides less power to the electron beam than the rest of the facilities shown in Figs. 5.27 and 5.28, which explains why spallation sources and nuclear reactors provide up to two orders of magnitude more bright neutron beams.

To increase the peak and average brightness of the proposed sources there are two possibilities: Increasing the beam power, which maximizes the total neutron production, or optimizing the target so that moderating losses are reduced. In this sense, different moderating materials can be considered, like in HBS [43], where they propose 25%-paramagnetic liquid hydrogen.

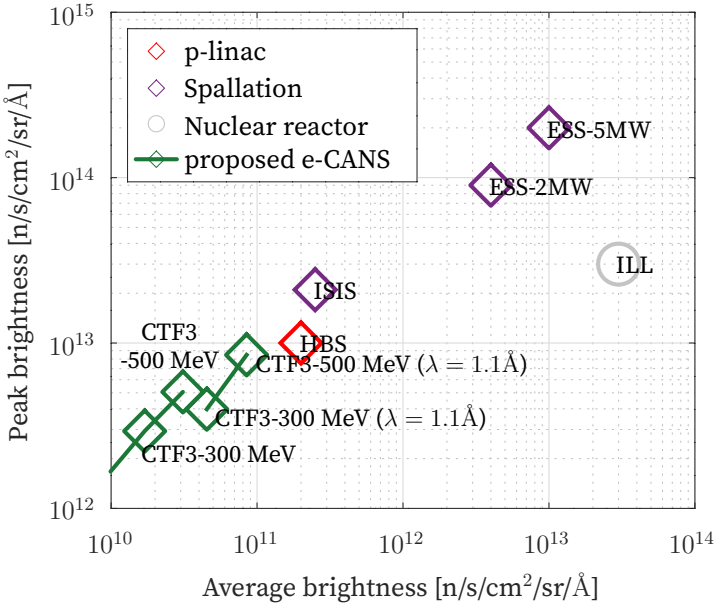

Figure 5.27: Brightness comparison with the state-of-the-art. Thermal neutron brightness ($\lambda = 1.8$ Å). Data from [34] and Figs. 5.20 and 5.22

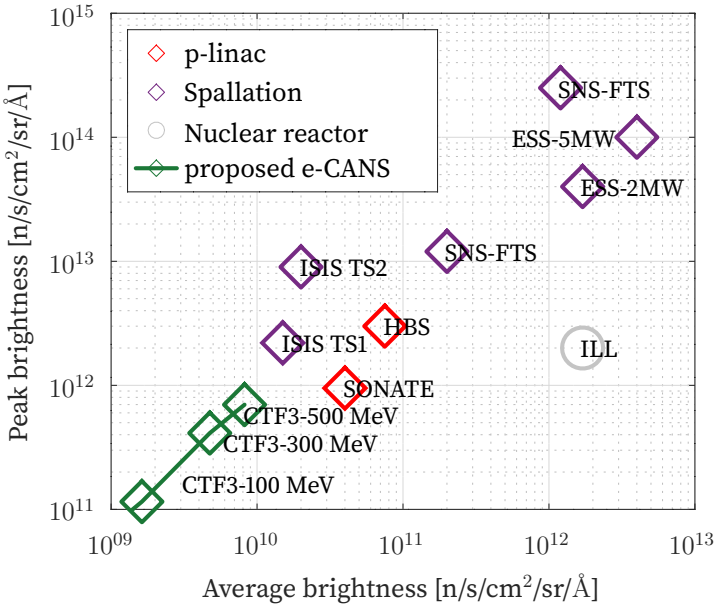

Figure 5.28: Brightness comparison with the state-of-the-art. Cold neutron brightness ($\lambda = 5.0$ Å). Data from [34] and Figs. 5.25 and 5.26.

6. Beam dynamics of a heavy-loaded electron linac for neutron production

Compact electron-linac-based neutron sources provide a useful neutron spectrum for a wide range of applications, as discussed in Chapter 5. Two normal-conducting linacs were examined as drivers for these sources: HPCI, and CTF3 drive beam's linac.

While CTF3 drive beam's linac operation was already proved, it remains unclear whether X-band technology can be used to transport intense beams of $600\,\mathrm{pC/bunch}$ without losses and with stability. In addition, attention should be paid to the final focusing system to prevent the target from local overheating, which could lead to its malfunctioning.

Accordingly, this chapter analyses the challenges of high-intensity stable operation of the HPCI linac from the beam dynamics point of view. In particular, it presents a preliminary beam-dynamics-based design of an X-band accelerator, which delivers an electron beam with a mean final energy of $\simeq 500\,\mathrm{MeV}$ for neutron production. Finally, the performance of the proposed source is discussed.

6.1 Transverse stability challenges for high-intensity beams in X-band structures

X-band's high frequency operation translates into small apertures, as it is the case of the HPCI linac, with a tapered aperture from $4.6\,\mathrm{mm}$ to $3.0\,\mathrm{mm}$. To avoid losses, and therefore guarantee safe operation from the radiation protection point of view, the

beam envelope has to be contained within those limits.

Section 2.5.1 presented two main focusing mechanisms in X-band linacs that control the growth of the transverse dimensions of the bunch: Quadrupole and solenoidal focusing, and the ponderomotive RF focusing in high-gradient structures. These mechanisms help to compensate for the detrimental impact of the charge-dependent collective effects that arise. For the particular case we will consider, two of them are highlighted: Space-charge effects and short-range wakefields.

Space charge effects are predominant in the low-energy regions, causing an increase in both beam emittance and energy spread as a consequence of the Coulomb interaction between particles within the same bunch. A detailed description of these effects can be found in Refs. [14, 46], and their implementation in RF-TRACK is discussed in Ref. [114].

Short-range wakefield effects, on the other hand, affect the bunches at higher energies, causing head-to-tail energy spread as well as emittance blowup.

6.1.1 Karl Bane's wakefield model

Although these structures incorporate RF-loads that mitigate HOMs, similar to the ones in Fig. 3.12, these survive for a short fraction of time in the structure and affect bunches in the so-called short range. Therefore, short-range wakefield effects arise, which, in high gradient structures, can be described by the approximation given by K.Bane in Ref [115], where he proposes the following expressions:

$$\bar{w}_t(s) = \frac{4Z_0 c s_{\perp 0}}{\pi a^4}\left[1 - \left(1 + \sqrt{\frac{s}{s_{\perp 0}}}\right)\exp\left(-\sqrt{\frac{s}{s_{\perp 0}}}\right)\right], \qquad [\mathrm{V/pC/m/mm}] \tag{6.1}$$

$$w_l(s) = \frac{4Z_0 c}{\pi a^2}\exp\left(-\sqrt{\frac{s}{s_{\parallel 0}}}\right). \qquad [\mathrm{V/pC/m}] \tag{6.2}$$

Here, Z_0 is the impedance of free space, a is the average aperture radius of the structure, g is the gap length, d is the length of the cell, $s_{\parallel 0}$ and $s_{\perp 0}$ are

$$s_{\parallel 0} = 0.41\,\frac{a^{0.18} g^{1.6}}{d^{2.5}}, \qquad\qquad s_{\perp 0} = 1.69\,\frac{a^{1.79} g^{0.38}}{d^{1.17}},$$

respectively.

6.1.2 Chromatic effects and RF-phase compensation

The primary consequence of the short-range longitudinal wake is an energy spread, which arises from the fact that the particle at the head of the bunch only loses a small

fraction of its energy (given by the fundamental theorem of BL in Sec. 3.3), while the particles at the tail lose a greater amount as they suffer from the effect of the entire bunch, as demonstrated in Eq. (2.38). As a consequence, the bunch head's energy is larger than the tail's.

As introduced in Sec. 2.5.1, the focusing strength of the quadrupoles depends on the beam energy. Therefore, two particles with different energies will undergo different quadrupolar forces, and their trajectories will be described by the solution of different Hill's equations, see Eq. (2.75). As a consequence, each particle will experience a different phase advance in the trace space as it travels through the accelerator. This phenomenon, which translates into an increase in the associated transverse emittance, is known as chromaticity.

To mitigate this effect, one can modify the RF phase of the accelerating field. For simplicity, we assume in the following a longitudinal electric field with $E_z = E_0 \cos(-kz + \omega t + \varphi)$, and an ultrarelativistic two-particles beam with injection times t_1 (leading particle) and t_2 (trailing particle), with $t_1 < t_2$. Both particles have charge e, and their time of flight is given by $t_{q,i} = z/c + t_i$ $(i = 1, 2)$. Without loss of generality, we consider $t_1 = 0$. Consequently, the energy gain and energy spread after the structure are:

$$\mathcal{E}_{\text{gain},i} = eLE_0 \cos(\varphi + \omega t_i) \tag{6.3}$$

$$\Delta\mathcal{E}_{\text{RF}} = \mathcal{E}_{\text{gain},1} - \mathcal{E}_{\text{gain},2} \simeq eLE_0 \sin(\varphi)\omega t_2, \tag{6.4}$$

where the assumption $(t_2 - t_1)\omega \ll 1$ has been made.

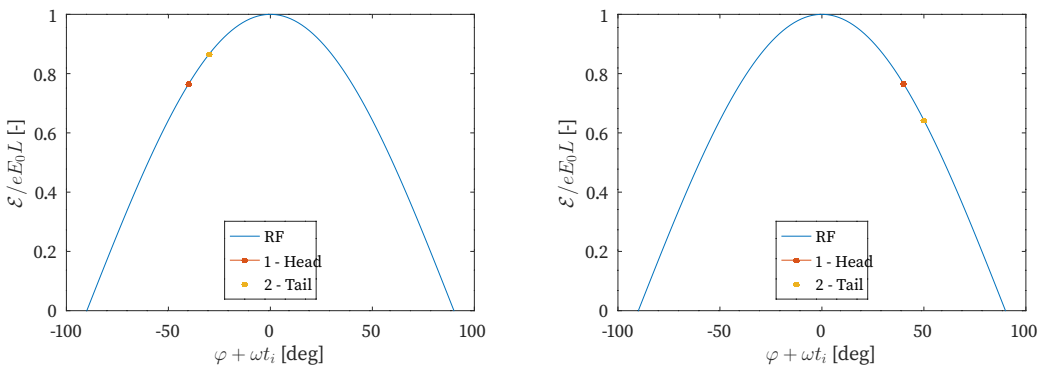

(a) $\varphi < 0$, $\Delta\mathcal{E} < 0$.

(b) $\varphi > 0$, $\Delta\mathcal{E} > 0$.

Figure 6.1: Energy spread dependency with accelerating RF-phase

On the other hand, making use of Eq. (2.38), the w_l-induced energy spread, $\Delta\mathcal{E}_{\text{wake}}$, is:

$$\mathcal{E}_{\text{gain},1} = -\,e^2\frac{w_l(0)}{2}L \qquad \mathcal{E}_{\text{gain},2} = -e^2\frac{w_l(0)}{2}L - e^2 w_l\left(ct_2\right)L. \tag{6.5}$$

$$\Delta\mathcal{E}_{\text{wake}} = e^2 w_l\left(ct_2\right)L. \tag{6.6}$$

To achieve compensation, we choose an RF-phase φ^* such that $\Delta\mathcal{E}_{\text{RF}} = -\Delta\mathcal{E}_{\text{wake}}$, that is:

$$\varphi^* = -\sin^{-1}\left(\frac{e^2 w_l(ct_2)}{E_0\,\omega t_2}\right) < 0. \tag{6.7}$$

6.1.3 Single-bunch Beam Breakup Instability and BNS damping

Likewise, the transverse short-range wakefield has an impact upon beam stability, leading to the so-called *Single-bunch Beam Breakup Instability (BBU)*. To understand this phenomenon, we consider the transverse equation of motion of a particle travelling through a linear accelerator. On the one hand, the forces affecting the particle in the ultrarelativistic regime are:

$$F_x(s) = -\gamma mc^2\kappa(s)x + F_{x,\text{wake}}(s) = -\gamma mc^2\kappa(s)x + e\int_{-\infty}^{\infty} x(s',t)\lambda_q(s')\bar{w}_x(s'-s)\,\mathrm{d}s, \tag{6.8}$$

where κ is the focusing strength associated to the lattice quadrupoles, in Eq. (2.73), and the RF-transverse effect, in Eq. (2.70); and $\bar{w}_x$ is normalized to the driver's offset and the accelerator length as in Eq. (6.1).

On the other hand, for a lattice with acceleration, we get that:

$$F_x = \frac{\partial(\gamma m v_x)}{\partial t} = \dot{\gamma}m\frac{\partial x}{\partial t} + \gamma m\frac{\partial^2 x}{\partial t^2}. \tag{6.9}$$

Combining Eqs. (6.8) and (6.9), one gets the following system of equations for the ultrarelativistic two-particle beam from Sec. 6.1.2:

$$\frac{\partial^2 x_1(s,t)}{\partial t^2} + \frac{\dot{\gamma}}{\gamma}\frac{\partial x_1(s,t)}{\partial t} + \underbrace{c^2\kappa(s)}_{\omega^2_{\beta,1}(s)}x_1(s,t) = 0 \tag{6.10}$$

$$\frac{\partial^2 x_2(s,t)}{\partial t^2} + \frac{\dot{\gamma}}{\gamma}\frac{\partial x_2(s,t)}{\partial t} + \underbrace{c^2\kappa(s)}_{\omega^2_{\beta,2}(s)}x_2(s,t) = \frac{e^2}{\gamma m}x_1(ct_2+s,t)\bar{w}_x(ct_2). \tag{6.11}$$

Here, $\omega_{\beta,i}$ represents the betatron frequency of each particle. This frequency does not have to be the same for all particles, as they can undergo different focusing forces

depending on their energy, as discussed previously. For simplicity, we will asume a constant $\omega_{\beta,i}$ value ($\omega_{\beta,i} \equiv \langle \omega_{\beta,i}(s) \rangle$).

Following the solution for the case without acceleration, in Eq. (2.75), we seek solutions in the form, $x_1(s,t) = a(s,t)e^{j\omega_{\beta,1}t}$, where we have included complex notation for simplicity. However, the final solution is the real part of the complex ansatz. Here, a is assumed to be quasi-static, and therefore satisfies the following expression:

$$-2j\omega_{\beta,1}\frac{\partial a(s,t)}{\partial t} - \frac{\dot{\gamma}}{\gamma} j\omega_{\beta,1} a(s,t) = 0, \tag{6.12}$$

whose solution, assuming an initial amplitude $a(s,0)$ at $t=0$, is:

$$a(s,t) = a(s,0)\sqrt{\frac{\gamma_0}{\gamma(t)}}. \tag{6.13}$$

$$x(s,t) = a(s,0)\sqrt{\frac{\gamma_0}{\gamma(t)}}\cos\omega_{\beta,1}t \tag{6.14}$$

The reduction of the oscillation amplitude when the beam gets accelerated is called *adiabatic damping*. This effect is beneficial as it keeps the beam size small, but it is not enough to counteract the wakefield effect. To see this, we focus our attention on Eq. (6.11), which now reads:

$$\frac{\partial^2 x_2(s,t)}{\partial t^2} + \frac{\dot{\gamma}}{\gamma_2}\frac{\partial x_2(s,t)}{\partial t} + \omega_{\beta,2}^2 x_2(s,t) = \underbrace{\frac{e^2}{\gamma_2 m} a(ct_2+s,0)\sqrt{\frac{\gamma_0}{\gamma_1(t)}}\bar{w}_x(ct_2)}_{F_0(s,t)}\cos\omega_{\beta,1}t, \tag{6.15}$$

which is the equation of a damped oscillator with an external driving force $F_0(s,t)\cos\omega_{\beta,1}t$ with a quasi-static amplitude. As discussed before, the damping term is *small enough* so the natural frequency of the system remains $\omega_{\beta,2}$. In this case, assuming $x_1(s,0) = x_2(s,0)$ and $\dot{x}_1(s,0) = \dot{x}_1(s,0) = 0$, the solution is [14, 48]:

$$x_2(s,t) = a(s,0)\sqrt{\frac{\gamma_0}{\gamma_2(t)}}\cos\omega_{\beta,2}t + \frac{F_0(s,t)}{\omega_{\beta,2}^2 - \omega_{\beta,1}^2}(\cos\omega_{\beta,1}t - \cos\omega_{\beta,2}t). \tag{6.16}$$

To illustrate the BBU instability and its compensation technique, we consider the following two cases:

a) Beam Breakup Instability when $\omega_{\beta,1} = \omega_{\beta,2} = \omega_\beta$.

In this case, taking the limit when $\omega_{\beta,2} \to \omega_{\beta,1}$, Eq. (6.16) is:

$$x_2(s,t) = a(s,0)\sqrt{\frac{\gamma_0}{\gamma(t)}}\cos\omega_\beta t + \frac{F_0(s,t)t}{2\omega_\beta}\sin\omega_\beta t, \tag{6.17}$$

where the first term's amplitude is bounded by $a(s,0)$ and is subjected to adiabatic damping, while the second term is several orders of magnitude larger, as shown in Figure 6.2. Here, the evolution of the amplitude of x_2 is illustrated for the HPCI X-band linac and a bunch charge of $-600\,\mathrm{pC}$. Three cases are considered: (1) No wake effect (x_1's amplitude, in yellow); (2) Wake effect without acceleration (in red); and (3) Wake effect with acceleration ($\frac{F_0(s,t)t}{2\omega_\beta}$, in blue). The wake effect increases the amplitude of the oscillations several orders of magnitude despite being asymptotically controlled by adiabatic damping in this two-particle toy model.

This amplitude growth is known as *Single-Bunch Beam Breakup Instability*, and is a consequence of the resonance between the natural betatron frequency of the particles in the tail, and the wake force induced by the particles at the head of the bunch, which oscillate with the same ω_β.

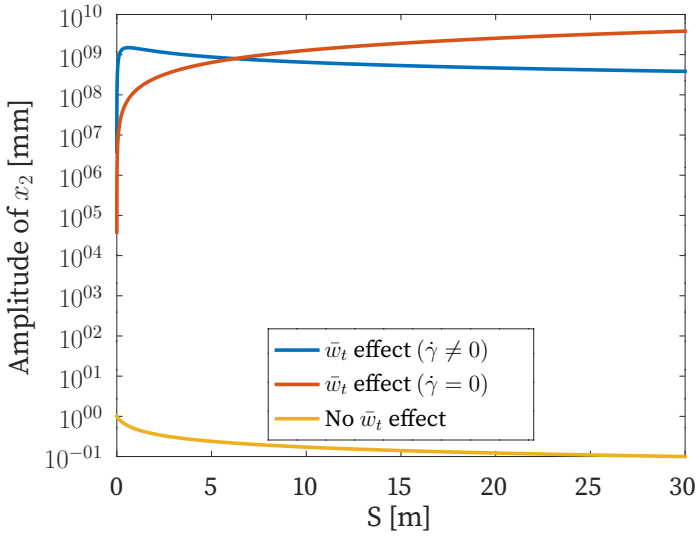

Figure 6.2: BBU instability for two particles in the HPCI linac with $-300\,\mathrm{pC}$ per macroparticle, $a(s,0) = 1\,\mathrm{mm}$, $t_1 = 0$, $t_2 = 1\,\mathrm{mm/c}$ and $\langle\beta(s)\rangle = 1\,\mathrm{m}$.

b) BNS damping technique when $\omega_{\beta,1} \neq \omega_{\beta,2}$.

To avoid this resonance, a linear energy chirp can be introduced so that $\omega_{\beta,1} \neq \omega_{\beta,2}$. This idea was proposed in 1983 by Balakin, Novokhatski, and Smirkov [116], and it is known under the name of *BNS damping*.

If the betatron frequency shift, $\Delta\omega_\beta$, is small enough, we can approximate

$\omega_{\beta,2}^2 - \omega_{\beta,1}^2$ as $2\omega_{\beta,1}\Delta\omega_\beta$, and calculate $\Delta\omega_\beta$ to suppress the instability:

$$\frac{F_0(s,t)}{2\omega_{\beta,1}\Delta\omega_\beta} = \sqrt{\frac{\gamma_0}{\gamma_1(t)}}; \implies \Delta\omega_\beta = \frac{e^2}{2\gamma_2(t)m\omega_{\beta,1}} a(ct_2+s,0)\bar{w}_x(ct_2). \tag{6.18}$$

For a single harmonic TW electric field like the one in Sec. 6.1.2, the betatron frequency shift depends on the RF-phase as $\Delta\omega_\beta = \frac{\omega_\beta}{2}\tan(\varphi)\omega_{RF}t_2$. Therefore, assuming one could control ω_β along the trajectory, one could seek a compensating RF-phase, φ^*, which for the case of our model reads as:

$$\varphi^* = \tan^{-1}\left(\frac{e^2/\omega_{RF}t_2}{\gamma_2(t)m\omega_\beta^2} a(ct_2+s,0)\bar{w}_x(ct_2)\right) > 0. \tag{6.19}$$

6.2 Beam dynamics accelerator design

This section presents the design of an accelerator lattice based on the HPCI linac, which targets neutron production by delivering high-intensity, high-energy electron bunches to the optimised tungsten target described in Sec. 5.1.3. Due to the simultaneous presence of collective effects such as space charge, beam loading and short- and long-range wake fields, the lattice design was carried out in RF-Track, which incorporates these effects.

6.2.1 Photoinjector

Before the accelerating TW structures, the beam is created at a Cs_2Te photocathode and accelerated by a 2.6-cell S-band electron gun, similar to the CLEAR setup described in 4.2.1 with an on-axis electric peak field of $90\,\mathrm{MV/m}$. A solenoid is found in the first $70\,\mathrm{cm}$ to compensate for the defocusing effect of space-charge, which dominates this low energy regime. A sketch of the gun section arrangement is shown in the bottom part of Fig. 6.3.

To transport bunches of 600, 550, and $500\,\mathrm{pC}$ with minimal emittance and beam-size, a multi-objective optimization of the injector was carried out using the following degrees of freedom: the laser spot size $\sigma_{x,\mathrm{laser}}$ and the pulse length $\sigma_{t,\mathrm{laser}}$ at the cathode; the RF gun phase ϕ_{RF}; the solenoid strength B_{max}; and the position of the linac start with respect to the cathode, L.

Table 6.1 shows the optimal degrees of freedom for the proposed gun setup, along with the beam properties at the entrance of the linac sector. For the three different

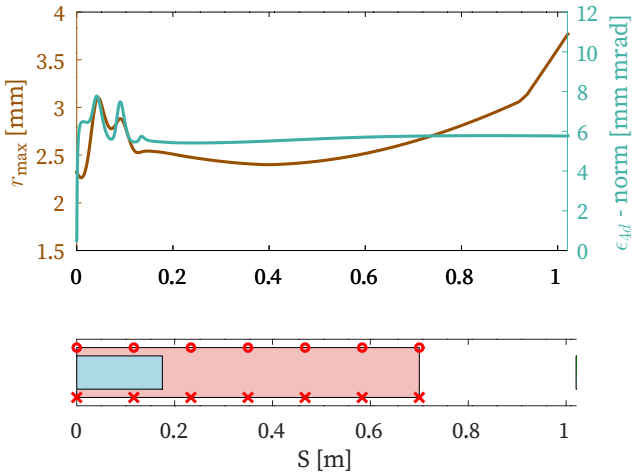

Figure 6.3: Beam envelope, r_{max}, and normalised emittance evolution in the gun section for $550\,\text{pC/bunch}$. In blue, the RF gun. In red, the extent of the solenoid field, including the fringe region.

Parameter	**Units**	$q_{\text{bunch}} = 600\,\text{pC}$	$q_{\text{bunch}} = 550\,\text{pC}$	$q_{\text{bunch}} = 500\,\text{pC}$
$\sigma_{x,\text{laser}}$	mm	1.19	0.56	0.53
$\sigma_{t,\text{laser}}$	10^{-3} mm/c	3.26	1.89	3.74
ϕ_{RF}	deg	-61.6	-65.9	-61.6
B_{max}	10^{-1} T	1.48	1.87	1.85
L	m	1.02	1.02	1.04
$\langle\mathcal{E}\rangle$	MeV	3.92	4.22	4.43
σ_x	mm	2.03	1.39	1.64
σ_y	mm	2.03	1.39	1.64
$\sigma_{\mathcal{E}}$	keV	98.0	97.0	94.0
$\epsilon_{x,\,\text{norm}}$	mm mrad	9.91	5.75	5.64
$\epsilon_{y,\,\text{norm}}$	mm mrad	9.88	5.76	5.65
$\epsilon_{4\text{d},\,\text{norm}}$	mm mrad	9.89	5.76	5.64
r_{max}	mm	4.52	3.76	3.73
r_{99}	mm	4.33	2.84	3.57

Table 6.1: Optimal injector parameters and beam properties before the linac entrance for different q_{bunch}-based optimizations. Simulations with 10^4 macroparticles.

configurations, a centred beam with a beam envelope below $4.6\,\text{mm}$ is found. The

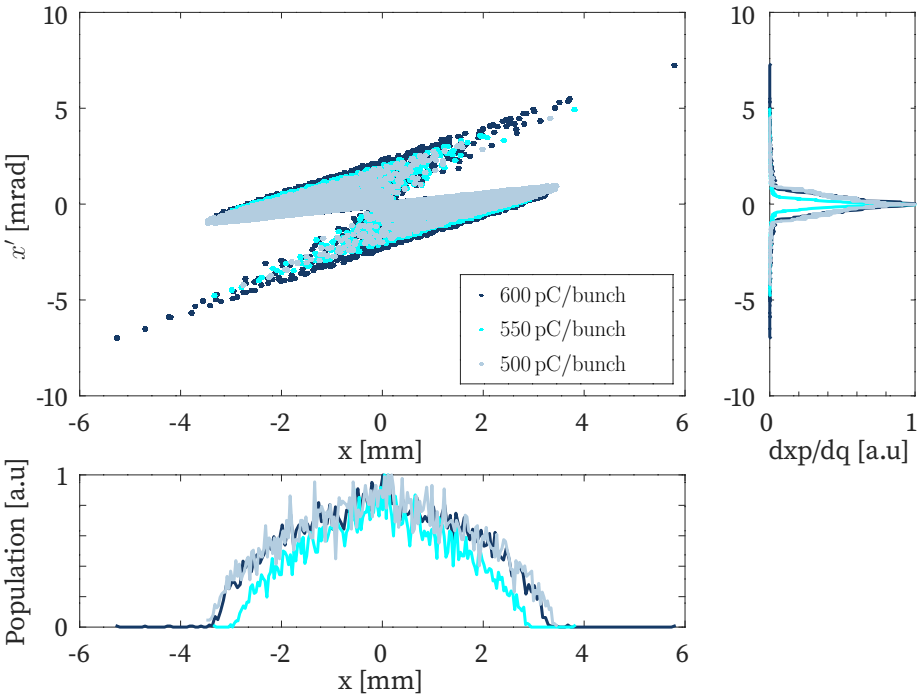

Figure 6.4: Transverse phase-space for the different charge configurations.

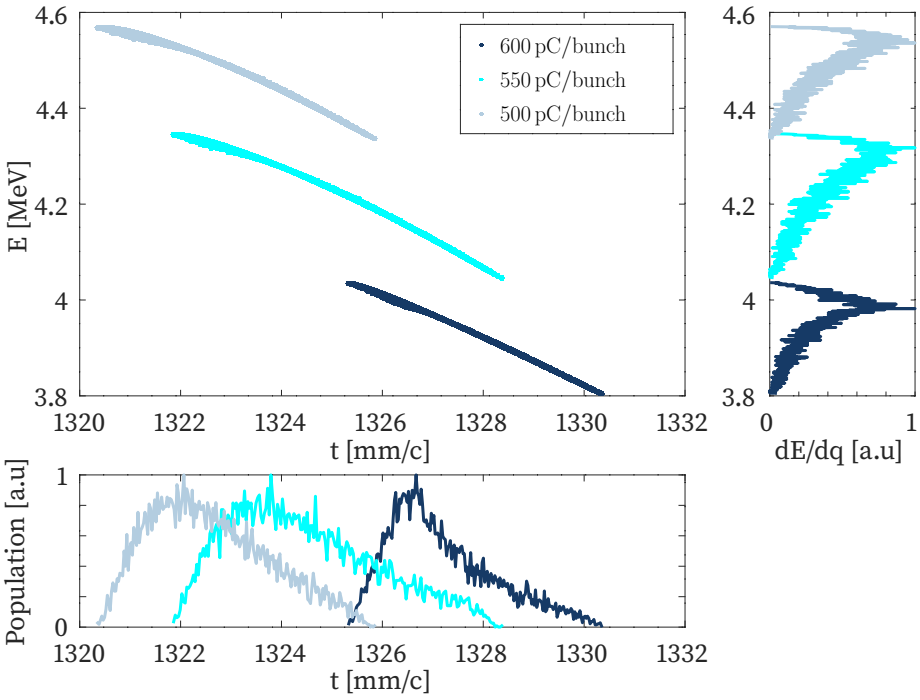

Figure 6.5: Longitudinal phase-space for the different charge configurations.

influence of charge-dependent collective effects is observed, since smaller envelopes and emittance values are obtained for lower charges per bunch.

The final transverse trace space is shown in Fig 6.4. All three cases show a divergent beam, which follows from the fact that $30\,\mathrm{cm}$ to $60\,\mathrm{cm}$ of drift space was left empty for beam instrumentation after the solenoid. Regarding the longitudinal trace space, in Fig. 6.5, bunches exhibit different energies as a consequence of Beam Loading effects in the gun, which reduce the mean energy from $4.43\,\mathrm{MeV}$ for the $500\,\mathrm{pC/bunch}$ case to $3.92\,\mathrm{MeV}$ for the $600\,\mathrm{pC/bunch}$ configuration.

6.2.2 X-band linear accelerator

To accelerate the electron beam up to $500\,\mathrm{MeV}$, 42 HPCI X-band accelerating TW structures, described in Table 5.3, were arranged as shown in Fig. 6.6. In addition to the RF structures, a lattice of focusing and defocusing quadrupoles was placed along the lattice to control beam size and emittance. The spacing between consecutive elements has been set to $10\,\mathrm{cm}$, allowing for the placement of flanges, bellows, but also screens and Beam Position Monitors (BPMs).

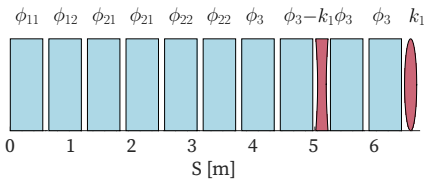

(a) First part sketch.

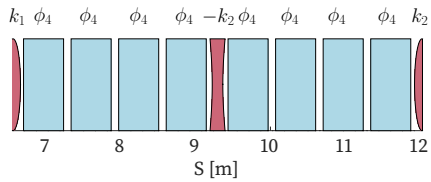

(b) FODO(ϕ_4, k_2) sketch.

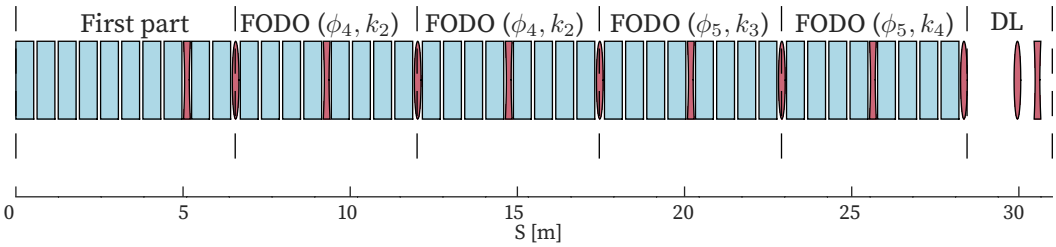

(c) Full X-band linac sketch. DL stands for delivery line.

Figure 6.6: X-band linac lattice layout. In blue, the RF accelerating structures. In red, the (de)focusing quadrupoles.

The optimisation of the lattice, which targeted $100\,\%$ transmission and maximal beam power, was divided into three parts:

- Capture, quadrupole-free section: It consists of ten TW structures with minimal spacing ($10\,\mathrm{cm}$) to avoid divergence in the drifts and keep the beam within the $4.6\,\mathrm{mm}$ to $3.0\,\mathrm{mm}$ limits. To achieve this, the manipulated degrees of freedom in the optimization were the RF phases ϕ_{11}, ϕ_{12}, ϕ_{21}, ϕ_{22}, ϕ_3, and the quadrupole strength k_1, as shown in Fig. 6.6a.

- On-crest-accelerating FODO cells: It consists of four FODO cells which accelerate and focus the beam up to a final energy of $509\,\mathrm{MeV}$. The degrees of freedom for the optimisation of this part were the RF phases ϕ_4, ϕ_5, and the quadrupole strengths k_2, k_3, and k_4, as seen in Fig. 6.6b.

- Delivery line: This part consists of a quadrupole doublet with strengths k_5 and k_6, placed $1.5\,\mathrm{m}$ after the last FODO cell, with an spacing of $0.5\,\mathrm{m}$ quadrupole-quadrupole and quadrupole-target, which bring the electron beam to the target with a beam-size $\sigma_y = \sigma_x > 0.4\,\mathrm{mm}$. The element spacing is enough to place a screen and a mass spectrometer. [1]

As previously mentioned, the optimisation process aimed to maximise transmission, beam power, and minimise emittance, while ensuring the final round beam size was at least $0.4\,\mathrm{mm}$. A bunch charge of $550\,\mathrm{pC}$ enabled these requirements to be satisfied for the on-axis bunch presented in Table 6.1, as well as for the different off-axis configurations to be discussed in the "Sensitivity to beam jitter" section. Therefore, the results that follow refer to the case of an electron beam with $1000\,\mathrm{bunches}$ with $q_{\text{bunch}} = 550\,\mathrm{pC/bunch}$ and bunch-to-bunch spacing $100\,\mathrm{mm}$, as detailed in Table 6.1.

Table 6.2 presents the optimal values of the RF phases and quadrupole strengths, along with an interval which tolerates neutron intensity losses up to 1%, as illustrated in Fig. 6.7. To calculate such a threshold, we study variations in the neutron strength, making use of Eq. (5.11):

$$\Delta I_n = \left|\frac{\partial I_n}{\partial P}\right| \Delta P = \left|\frac{\partial Y_n}{\partial P} I_e + Y_n \frac{\partial I_e}{\partial P}\right| \Delta P = \left|\frac{\partial Y_n}{\partial \mathcal{E}} e + \frac{Y_n}{\mathcal{E}} e\right| \Delta P \tag{6.20}$$

To achieve the condition $\Delta I_n \leq 0.01 I_n$, we find out that it is enough to require that

[1] For a $1\,\mathrm{T}$ dipole, the bending radius, given by Eq. (4.1), is $1.6\,\mathrm{m}$. If a bending angle of $30\,\mathrm{deg}$ is desired, then the length of the spectrometer should be $1\,\mathrm{m}$ according to Eq. (4.2).

the final beam power verifies:

$$\Delta I_n = \left|\frac{\partial Y_n}{\partial \mathcal{E}} e + \frac{Y_n}{\mathcal{E}} e\right| \Delta P \leq \left|\frac{\partial Y_n}{\partial \mathcal{E}} e \Delta P\right| + \left|\frac{Y_n}{\mathcal{E}} e \Delta P\right| \leq 0.01 I_n \implies$$
$$\implies \Delta P \leq \min\{\frac{0.005 I_n}{e\frac{\partial Y_n}{\partial \mathcal{E}}}, 0.005 P\}. \tag{6.21}$$

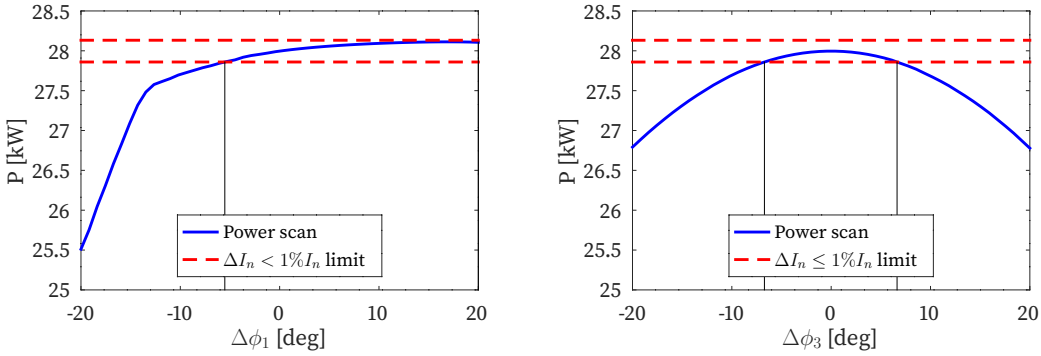

(a) Scan for ϕ_1.

(b) Scan for ϕ_3.

Figure 6.7: Parametric scan to ensure $\Delta I_n / I_n \leq 1\%$.

Parameter	Units	Nominal value	Tolerance for $\Delta I_n \leq 1\% I_n$
ϕ_{11}	deg	-52.7	$(-58.2,\ -32.7)$
ϕ_{12}	deg	-59.7	$(-62.9,\ -52.7)$
ϕ_{21}	deg	43.2	(39.8, 46.1)
ϕ_{22}	deg	4.83	$(-15.21,\ 16.07)$
ϕ_3	deg	-9.97	$(-19.22,\ 9.44.)$
ϕ_4	deg	-4.67	$(-11.40,\ 1.96)$
ϕ_5	deg	-4.66	$(-11.38,\ 2.07)$
k_1	m^{-2}	0.60	(0, 2.59)
k_2	m^{-2}	1.43	(0, 2.74)
k_3	m^{-2}	3.60	(1.60, 5.60)
k_4	m^{-2}	8.74	(6.88, 9.00*)
k_5	m^{-2}	-2.40	Only affects beam quality
k_6	m^{-2}	7.28	Only affects beam quality

Table 6.2: Optimal parameters of the lattice elements for the transport of a train of 1000 bunches with $550\,\mathrm{pC/bunch}$.

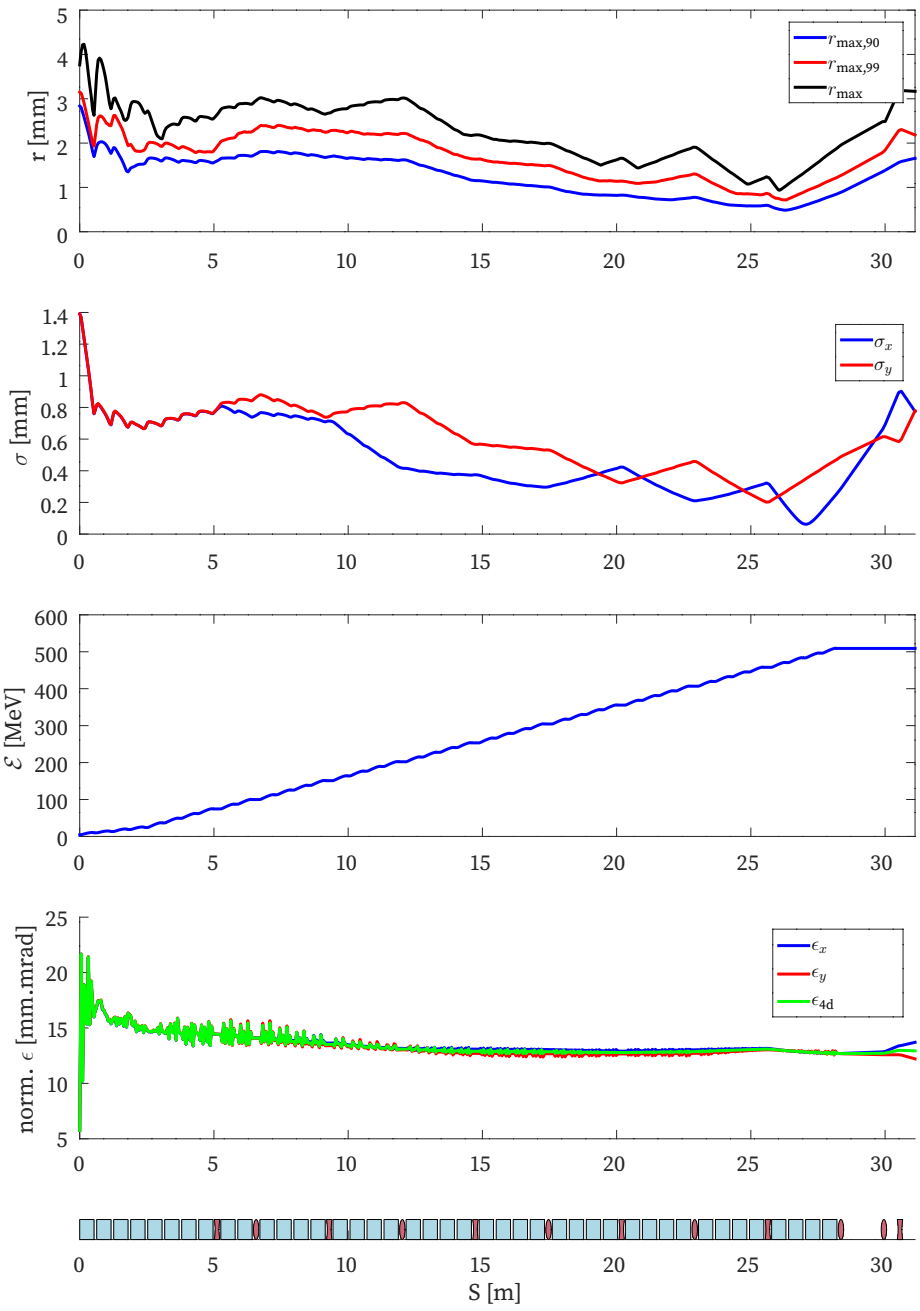

Figure 6.8: Evolution of beam properties along the designed X-band linac for $q_{\text{bunch}} = 550\,\text{pC}$, simulated with 10^4 macroparticles as discussed in Table 6.1.

Due to the incoming energy spread (see Fig. 6.5), a negative RF phase was found by the simplex algorithm to minimise the associated chromaticity, as explained in Sec. 6.1.2. Positive RF-phase values for ϕ_{21} are found for BNS damping, as shown in Eq. (6.19), since early stages of the acceleration process manifest larger emittance blow-ups as a consequence of the BBU instability, as seen in Fig. 6.2 and Fig.6.8. To increase the beam energy up to $509\,\mathrm{MeV}$, the remaining RF phases are set closer to the crest to provide greater energy gain, and ultimately, a larger beam power and neutron production.

Regarding the quadrupole strengths, it can be seen that the strength is larger as the beam is accelerated, resulting in a decrease in size due to adiabatic damping and RF focusing. Smaller sizes enable the strong quadrupolar forces to be effective without losses associated to their defocusing force.

Figure 6.8 shows the evolution of the beam properties along the linac, where a beam envelope below the aperture limit is found. The beam size is controlled and matched to a round beam with safe PEDD values, since $\sigma_x = 0.77\,\mathrm{mm}$ and $\sigma_y = 0.78\,\mathrm{mm}$. Despite an initial emittance blow-up, due to BBU instability as well as chromatic effects, the normalised emittance is well controlled and preserved along the linac, which translates into stable operation.

Sensitivity to beam jitter

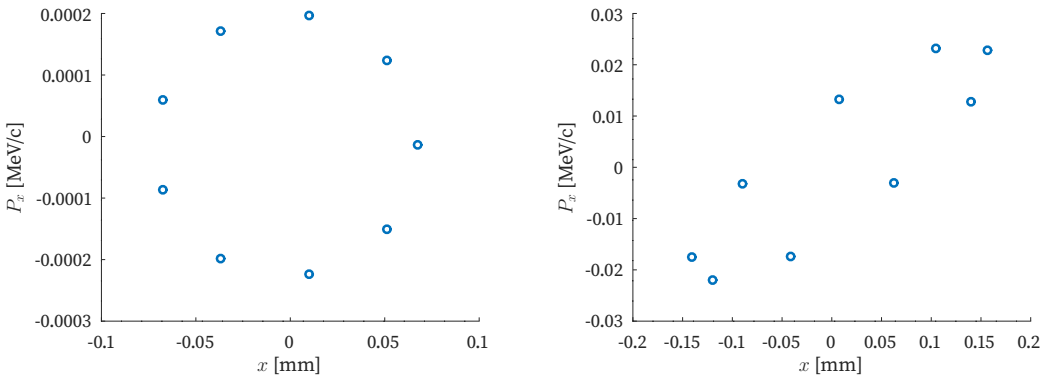

(a) Initial.

(b) Final.

Figure 6.9: Transverse phase space for the baricenter of 10 off-axis bunches injected in the linac for $\alpha = 0.05$.

Sensitivity studies are dedicated to assessing whether the variations in the parameters of the machine provide acceptable beams for neutron production or not. In

this section, we examine beam jitter by tracking off-axis bunches with longitudinal offset Δx in position and $\Delta x'$ in angle, satisfying the relationship for a given offset coefficient α:

$$\sqrt{(\Delta x/\sigma_{x0})^2 + (\Delta x'/\sigma_{x'0})^2} = \alpha, \tag{6.22}$$

with σ_{x0} and $\sigma_{x'0}$ referring to the on-axis beam at the entrance of the linac.

In the presence of an incoming transverse beam jitter, the transverse short-range wakefields amplify the jitter-induced betatron oscillation, deflecting the beam off-axis further and increasing the amplitude of the oscillation [117]. This is quantified by the jitter amplification factor, JA, defined as the square root of the ratio between the "action" at the linac end and the "action" at the linac start:

$$\text{JA} = \sqrt{\frac{A_{\text{final}}}{A_{\text{initial}}}}, \tag{6.23}$$

where the action is the area of the phase-space ellipse in Fig. 6.9.

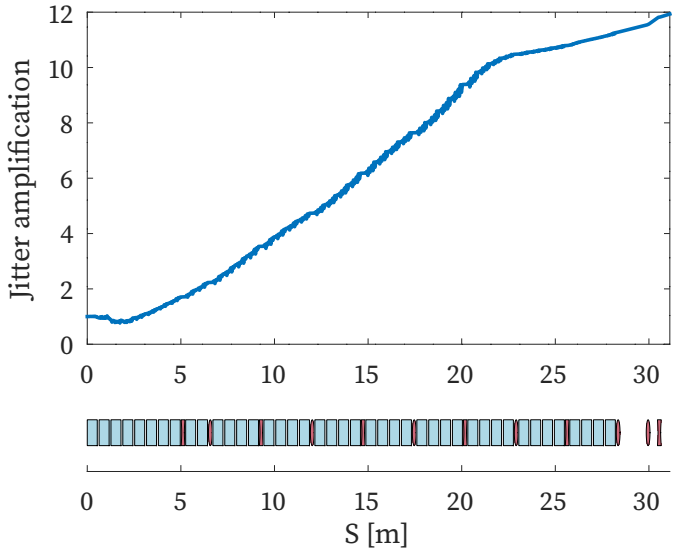

Figure 6.10: Jitter amplification for $\alpha = 0.05$.

Figure 6.10 shows the evolution of jitter amplification for the case $\alpha = 0.05$. For RF phases close to the on-axis values, larger energy dispersions are induced, and therefore, the chromatic effects increase, which ultimately increases the JA.

Fortunately, beam quality is not spoiled dramatically by this effect for $\alpha = 0.05$ since adiabatic damping occurs simultaneously, preserving low divergency and beam size. The competition of both effects can be examined in Fig. 6.11, which shows that, for

values up to $\alpha = 0.07$, JA does not lead to significant beam losses that could compromise neutron production.

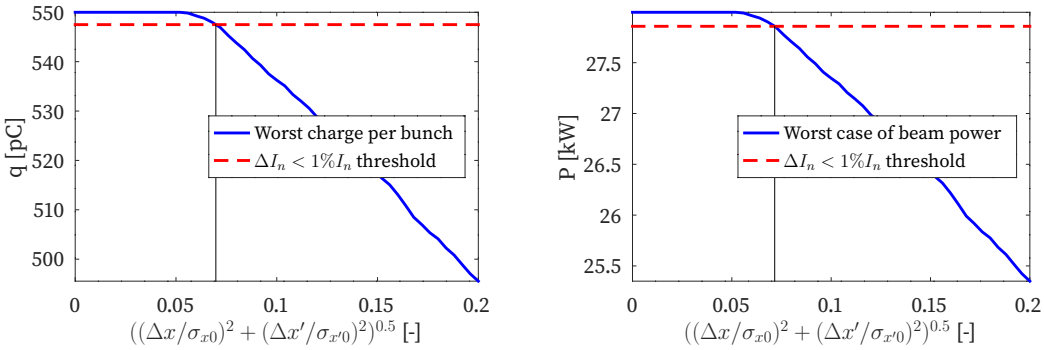

(a) Transmission.

(b) Power.

Figure 6.11: Bunch charge and beam power dependency with α.

Sensitivity to misalignments

Quadrupoles and RF structures misalignments are unavoidable, causing beam quality degradation as a consequence of the off-axis wakefield effects, transverse dipole kicks, and skew-quadrupolar effects. To simulate the misalignments for the sensitivity study, we assume a rms misalignment of $100\,\mu\mathrm{m}$ of the edges of each element. Then, the values of the RMS-centre misalignment, $\sigma_{t,\mathrm{center}}$, and the pitch, yaw angle misalignments are calculated as:

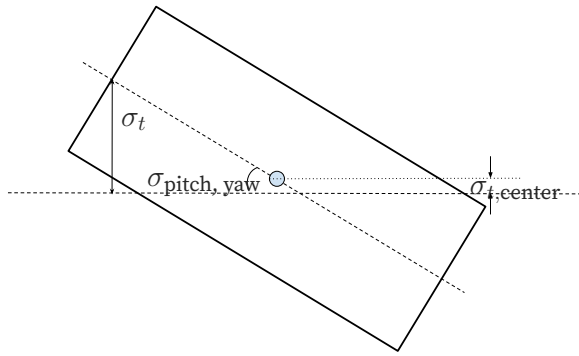

Figure 6.12: Schematic of the misalignments.

$$\sigma_{t,\mathrm{center}} = \frac{\sigma_t}{\sqrt{2}}, \tag{6.24}$$

$$\sigma_{\text{yaw,pitch}} = \frac{\sigma_t \sqrt{2}}{\Delta L}. \tag{6.25}$$

Element	σ_t [μm]	ΔL [mm]	$\sigma_{t,\text{center}}$ [μm]	σ_{roll} [μrad]	$\sigma_{\text{pitch, yaw}}$ [μrad]
Quadrupole	100	10	70.7	300	1000
TW Structure	100	530	70.7	300	188.7

Table 6.3: RMS misalignment values of the LINAC components. The values of σ_t and σ_{roll} are assumed, while the rest are computed from Eqs. (6.24) and (6.25).

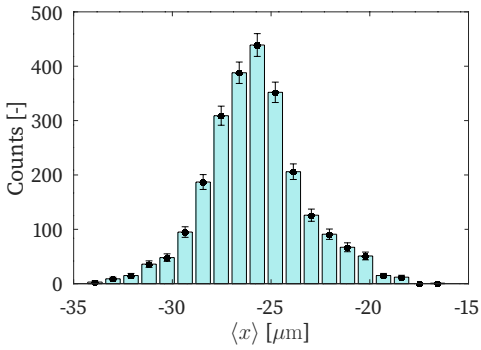

(a) Average x-position.

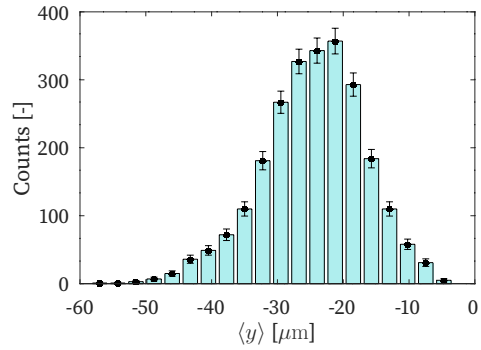

(b) Average y-position.

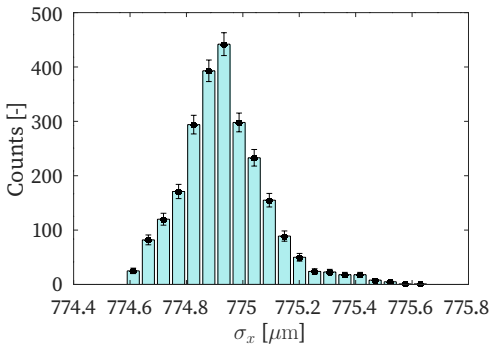

(c) x-size.

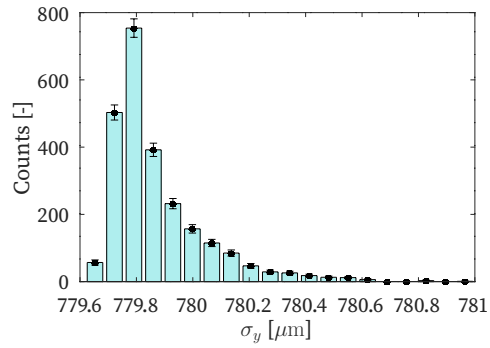

(d) y-size.

Figure 6.13: Histogram of the bunch properties for 2520 randomly misaligned lattices according to the parameters in Table 6.3.

2520 beams were tracked through misaligned lattices where elements were placed following a normal distribution with the RMS values shown in Table 6.3. Figure 6.13 shows histograms for the transverse average position and size of the resulting beams at the end of the delivery line, showing that there is no significant degradation of the

beam quality as the deviation is minimal compared to the on-axis case. This can be checked in Table 6.4 as well.

6.2.3 Electron beam characterisation at the target

Parameter	Units	Nominal Value	Worst 5%− -jitter bunch	Average with 100 μm rms- -misaligned lattice
σ_x	μm	774.8	949.0	774.9
σ_y	μm	779.7	843.4	779.9
$\langle\mathcal{E}\rangle$	MeV	509.0	509.0	509.0
$\sigma_\mathcal{E}$	MeV	10.4	10.4	10.4
ϵ_x	mm mrad	13.7	20.4	13.7
ϵ_y	mm mrad	12.2	12.4	12.2
ϵ_{4d}	mm mrad	12.9	15.9	13.0
r_{max}	mm	3.17	4.59	3.18
r_{99}	mm	2.18	3.31	2.19

Table 6.4: Electron beam parameters at the end of the linac.

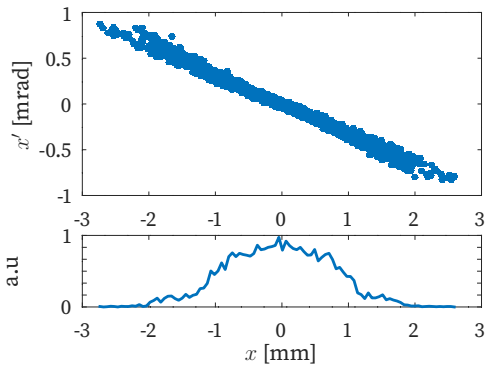

(a) x-trace-space and x-distribution..

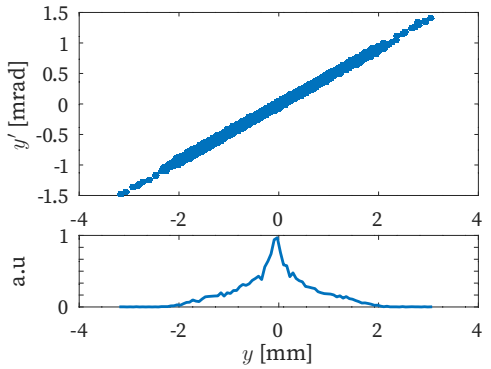

(b) y-trace-space and y-distribution.

Figure 6.14: Beam transverse trace space at target.

Table 6.4 shows the beam parameters at the end of the delivery line where the electrons collide against the tungsten target. The transverse trace spaces can be found in Fig. 6.14. A round beam is achieved at the centre of the circular face of the cylindrical tungsten target ($r = 4\,\mathrm{cm}$) with a mean energy of $509\,\mathrm{MeV}$. These features remain stable for the considered misalignments and beam jitter studies.

6.3 Performance of the proposed neutron source

To discuss neutron production of the proposed source, we carried out G4BEAMLINE simulations with a similar setup to the one shown in Sec. 5.1.2, where the beam input is specified in Table 6.4 with 10^6 macroparticles.

Table 6.5 presents the final set of parameters of the proposed source. For the neutron yield and the angular and energetic neutron spectrum, similar values to the ones found in Table 5.1 are obtained, since the cylindrical symmetry of both scenarios is guaranteed and the electron energies values are close ($\langle\mathcal{E}\rangle = 500\,\mathrm{MeV}$ and $509\,\mathrm{MeV}$ respectively).

Magnitude	**Units**	**Value**
Y_n	10^{-1} n/e	4.53 ± 0.02
f_θ (at $\theta_d = 130\,^\circ$)	10^{-2} n/e/sr	4.81 ± 0.02
$\max \mathcal{E}_n$	MeV	0.41 ± 0.01
$\langle\mathcal{E}_n\rangle$	MeV	1.28
$f_{\mathcal{E}_{n,\mathrm{peak}}}$ (at $\theta_d = 130\,^\circ$)	10^{-2} n/e/sr/MeV	4.0 ± 0.5
Source Strength	10^{14} n/s	1.56 ± 0.07
$P_{\text{beam, av}}$	kW	28.0
$f_{\text{RF-cycle}}$	Hz	100
N_{bunches}	-	1000
Length gun-target	m	32.1
PEDD	J/g	7.86
Average power consumption	kW	133.2
E_{pn}	10^{-10} J/n	8.57 ± 0.03

Table 6.5: Final set of parameters for the proposed source.

Figure 6.15 shows the f_θ and $f_{\theta,\mathcal{E}_n}$ neutron spectra, which also agree with Figures 5.6 and 5.7a respectively. As anticipated, neutron emission is larger in the backwards direction than in the forward direction, with a maximal neutron production at $\theta_d = 130 \pm 1^\circ$. Regarding the energy spectrum, it exhibits a Maxwellian behaviour with a peak energy of $\mathcal{E}_n = 0.41 \pm 0.01\,\mathrm{MeV}$, consistent with what was anticipated in Sec. 5.1.3.

Figure 6.16 compares the neutron strength of the proposed source with the state-of-the-art presented in Fig. 5.14, showing that the proposed target is as efficient from the

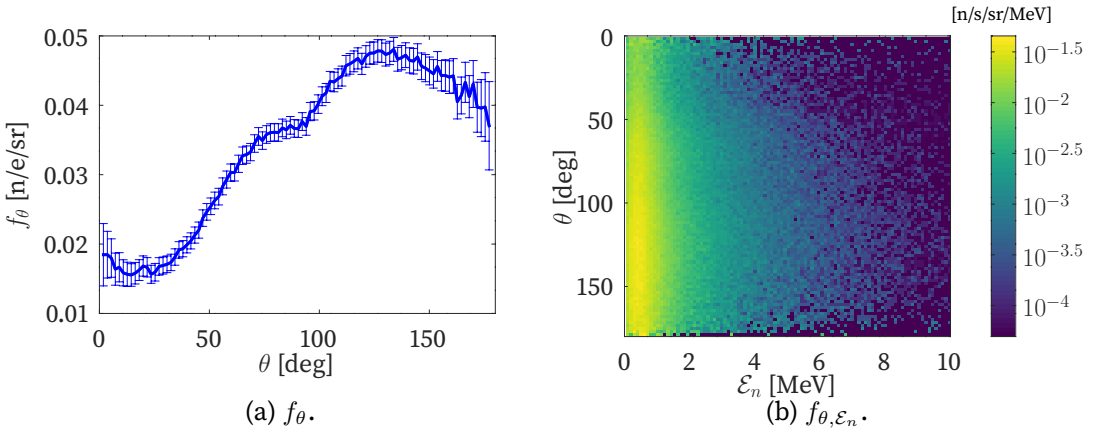

Figure 6.15: Angle and energy neutron distribution at $50\,\mathrm{cm}$ from the target.

neutron production point of view as the rest of the examined CANS. This is verified because the differences in neutron production are due to the beam power achieved by each driving accelerator, being the exception of the spallation sources.

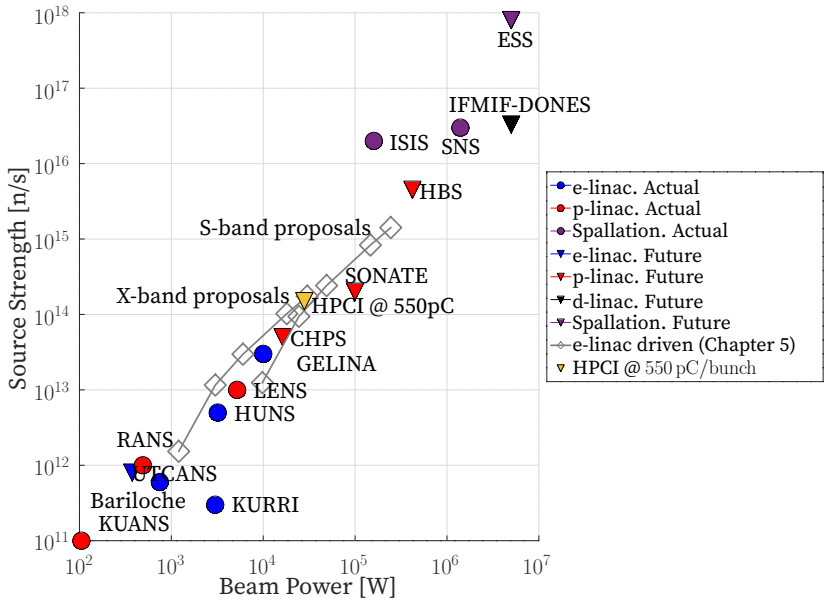

Figure 6.16: Beam power comparison for the state-of-the-art neutron sources with the HPCI-beam-dynamic-based design proposal at $550\,\mathrm{pC/bunch}$.

The average power consumption of the driving accelerator was calculated, making use of the wall-to-RF, compressing and splitting efficiencies shown in Table 5.6 for the HPCI linac. Due to the transverse beam stability requirements, the bunch per

charge of the proposed design is $550\,\mathrm{pC/bunch}$, leading to an rf-to-beam efficiency of $\eta_{\text{RF-beam}} = 83.4\,\%$. In addition, since stable operation requires off crest operation (see Table 6.2), 42 RF structures are needed to achieve the targeted final energy, which leads to a larger energy consumption than the one presented in Table 5.6 for the on-crest $600\,\mathrm{pC/bunch}$ case.

Nevertheless, an efficient value of $E_{\text{pn}} = (8.57 \pm 0.03) \cdot 10^{-10}$ J/n is obtained, leading to a cheaper neutron production when compared to the compact middle-flux neutron sources in Fig. 6.17.

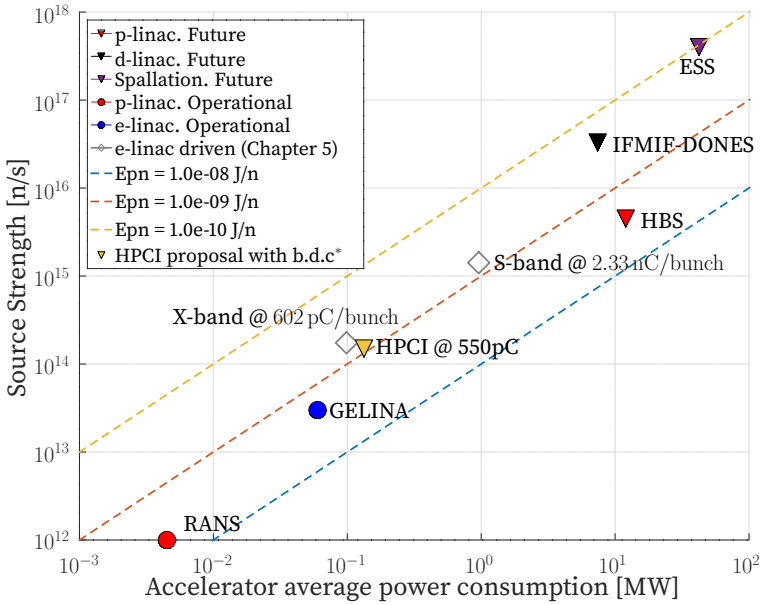

Figure 6.17: Average power consumption comparison for different neutron sources. * b.d.c stands for beam dynamics considerations

To conclude this section, Fig. 6.18 presents the neutron application landscape of Fig. 5.1, showing where the proposed source stands. Without any further moderation scheme, as expected, the proposed source meets the requirements to act as a radiation to electronics facility for testing SEU events [80]. With similar target-moderator assemblies to those presented in Sec. 5.3, and convenient manipulation of q_{bunch} or $\langle \mathcal{E} \rangle$, further applications can be targeted, such as Boron Neutron Capture Therapy, Neutron activation experiments or Spectroscopy and Imaging, among others.

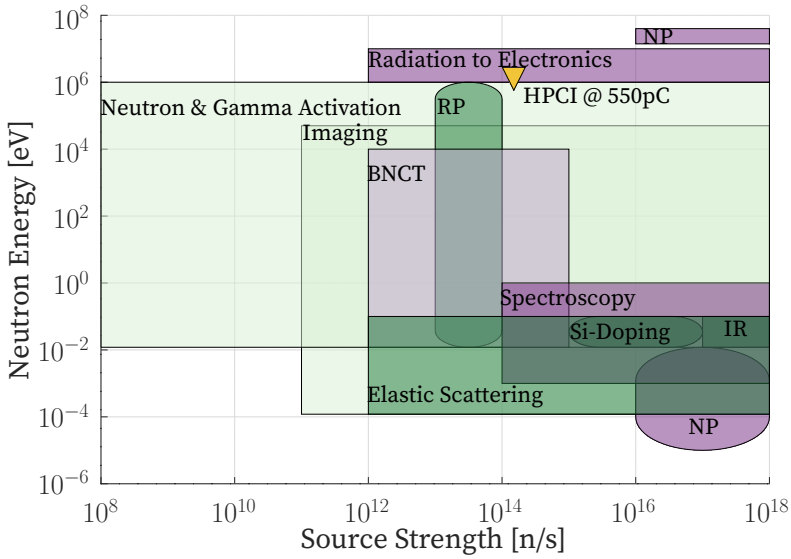

Figure 6.18: Neutron applications chart with HPCI @550 pC/bunch beam-dynamics-based design performance. The acronym NP stands for Nuclear Physics research, RP for Radioisotope Production, and IR for irradiation experiments.

7. Summary and Conclusions

The need to achieve high energies in particle accelerators has led to the development of new accelerator technologies. One particular example is the high-gradient, normal-conducting X-band accelerating structures, developed within the CLIC collaboration and elsewhere. The compactness and energy-efficiency of this technology make it a suitable candidate for future research linacs, compact inverse Compton scattering X-ray sources, medical linacs, and compact neutron sources. This PhD thesis has focused on the latter, where high beam intensities are required. In this scenario, Beam Loading effects occur, and an intensity-dependent gradient reduction affects the accelerated beam as a consequence of its interaction with the surrounding cavity.

The first objective of the thesis, addressed in Chapters 2-4, is the implementation of a Beam Loading module in the tracking code RF-Track. This was achieved by deriving a power-diffusive model starting from the Poynting theorem, valid for both TW and SW structures. Since this effect presents a transient response, the figures of merit describing accelerator performance had to be revised and re-formulated under the quasi-static assumption, thus limiting the validity of the derived model to scenarios where the amplitude decay of the EM fields is much slower than the RF oscillation itself.

The power-diffusive PDE is solved with a stable, forward-derivative Finite Difference scheme, and its solution can be interpreted as the gradient of the Floquet harmonic, l^*, of the fundamental mode, TM_{01}, whose propagation is synchronised with the flight of the particle. Therefore, the longitudinal wake associated with this mode can be calculated, which allows the computation of this effect on the long and short range. Computational efficiency is achieved by modelling long-range interactions as bunch-to-particle interactions. Therefore, the long-range BL calculations, available in RF-Track since its 2.3.0 version, shall be utilised when such hypothesis can be

granted, i.e. when the beam is bunched and bunches do not overlap.

Moreover, studying the initial and boundary conditions of the power-diffusive PDE, compensation techniques for this effect in both TW and SW structures have been discussed. Its implementation in RF-Track consists of the resolution of these equations for times before injection, which reproduces the unloaded build-up of the accelerating EM fields and compensates for the beam-induced fields.

Benchmarking against previous theoretical BL studies in ultra-relativistic TW structures reveals that the designed tool captures the transitivity of the BL effect. It also reflects how this transition to a steady state depends on the filling time of the structure. The BL-influenced particle tracking performance is compared by studying the power-extraction coefficient in the CLIC-PETS, previously calculated with Placet. Comparison shows that it is reproduced by RF-Track with a $< 1\%$ deviation. In addition, the longitudinal wakefield calculation is successfully benchmarked against GdFidl, reproducing the excitation of the fundamental mode in only a few seconds of computational time.

To test the accuracy of the SW module and to provide further evidence of the validity of the TW module, experimental measurements of the BL effect were carried out in the CLEAR facility at CERN. When reproducing the same measurements with RF-Track, it is found that the developed module reproduces the charge-dependent voltage reduction at the gun and energy loss at the end of the linac with deviations in the results only up to 5.9%.

All of this results in a flexible module, which is able to consider this effect for multi-beam species, arbitrary charge profiles, and arbitrary injection times and input-power profiles, aligning with the modular spirit of RF-Track. This opens the doors to novel accelerator designs where the BL effect is relevant, such as the positron sources for future colliders (CLIC and FCC-ee), X-band-based ICS sources, or the optimisation of the CLIC RTML (Rings to Main Linac) sections. In particular, the developed tool has been used for the work presented in references [118] and [119]

The second objective is addressed in Chapter 5, where it is shown that normal-conducting high-intensity electron linacs are suitable drivers for compact neutron sources. First, we presented the optimization and characterization of a tungsten target based on extensive G4beamline simulations, being the optimal dimensions $L = 80\,\mathrm{mm}$ and $r = 40\,\mathrm{mm}$ and showing maximal neutron emission for the backward direction $\theta_d = 130\,\mathrm{deg}$.

Then, the particular performance of the CTF3 drive beam linac (S-band) and HPCI linac (X-band) was examined. It was found that increasing the bunch charge up to the full beam loading regime allows maximizing the neutron emission up to $1.51 \times 10^{15}\,\mathrm{n/s}$ as well as the RF-to-beam efficiency up to $91\,\%$. In addition, despite the high beam intensity, safe values of heat deposition in the target are found provided that the focusing is not too strong ($\sigma_x \geq 3.5\,\mathrm{mm}$, well below the target radius).

The comparison with the state-of-the-art shows that electron-accelerator-based sources are, in general, equally compact and more efficient than proton-based or deuteron-based sources, making them valuable alternatives for moderate neutron production scenarios, like medical and industrial applications.

In particular, the proposed neutron sources offer very energetic neutron beams of the order of the MeV, which could serve mostly for electronic irradiation studies. To serve for further industrial and medical applications, where moderation is required, a preliminary design of a target-moderator assembly was proposed, showing that it can reach brightness values comparable to the compact sources designs in the state-of-the-art. However, further work should aim at the mechanical design of such an assembly for a specific neutron application, where aspects such as neutron delivery, radiation shielding, or target-moderator-assembly cooling should be inspected.

Finally, Chapter 6 analyses the stability challenges of the high-intensity operation required for neutron production with the HPCI linac. A beam-dynamics based design of a beamline accelerating electrons up to $509\,\mathrm{MeV}$ is presented, constraining bunch charge up to $550\,\mathrm{pC}$, bunch-to-bunch spacing to $100\,\mathrm{mm/c}$, and the number of bunches to 1000. The resulting design exhibits a tolerance of initial position beam jitter up to 7%, meaning that deviations below this threshold lead to a loss of beam power inferior to 1%. Complementarily, the sensitivity to TW structures and quadrupole misalignments has been tested, ensuring lossless operation with minimal orbit deviation for an element rms offset of $100\,\mu\mathrm{m}$. This linac would drive neutron generation for a source with a strength of $I_n = (1.56 \pm 0.07) \cdot 10^{14}$ n/s and an energy per neutron produced of $E_{\mathrm{pn}} = (8.57 \pm 0.03) \cdot 10^{-10}$ J/n, being a compact and efficient alternative for neutron production for medical and industrial purposes.

A. Appendices

A.1 Detailed CANS state-of-art recompilation

Source	Driver	Source strength I_n , E_{range}	Applications
GELINA	S-band e-linac + W	$3.4 \cdot 10^{13}$	Imaging
Belgium [36]	100 MeV / 100μA	$10^{-4} - 10^{6}$ eV	
HUNS	S-band e-linac + Pb	$5 \cdot 10^{12}$ n/s	Irradiation, Imaging
Japan [38, 120]	32 MeV / 100 μA	$1 - 10^{-4}$ eV	Astrophysics
KURRI-LINAC	L-band e-linac + Ta	$3 \cdot 10^{11}$	γ-act, Spectroscopy
Japan [38, 39]	46 MeV / 1μA		Isotope production
Bariloche Linac	e-Linac + Pb	$6 \cdot 10^{11}$ n/s	Nuclear Physics
(Argentina)	25 MeV / 30μA		Diffraction, Scattering
RANS	p-linac + Be	10^{12} n/s	Imaging
Japan [38]	7 MeV / 70 μA	$10^{3} - 10^{-4}$ eV	Solid-state-phys
KUANS	p-linac + Be	10^{11} n/s	Imaging
Japan [38]	3.5 MeV / 30 μA	$10^{3} - 10^{-2}$ eV	Detector R&D
LENS	p-linac + 2RFQ + Be	10^{13} n/s	Radiation effects
USA [40]	13 MeV/ 20 mA		Imaging [34]
Sources under study or ongoing development			
CPHS	p-Linac + Be	$5 \cdot 10^{13}$ n/s	Imaging
China [41]	16 MeV / 1.25μA		Detector R&D
LENOS	p-RFQ + Li	10^{15} n/s	Nuclear physics
Italy	5 MeV/ 50 mA	not moderated	Imaging
IFMIF-DONES	d-linac+RFQ+SRF+Li	$5 \cdot 10^{14}$ n/s/cm^2	Material irradiation
Spain [35]	40 MeV / 125 mA	@source, forward	
UTCANS	X-band e-linac + W	$8 \cdot 10^{11}$ n/s	Nuclear physics
Japan[40]	35 MeV / 250 mA (peak)	$(C_2H_4)_n$ moderator	Fukushima analysis
SONATE	p-linac+Li/Be	$3.1 \cdot 2 \cdot 10^{14}$ n/s	Material Science
France [42]	20 MeV/ 7 mA		
HBS	p-linac+ Ta	$9.1 \cdot 10^{14}$ n/s/mA	Quantum materials
Germany [43]	70 MeV / 7 mA	$\langle E_n \rangle = 0.45$ MeV	Imaging, scattering
Dual-target sources under study or ongoing development			
UTCANS	X-band e-linac + W	$2 \cdot 10^{9}$ n/s	Nuclear physics
Japan[40]	3.95 MeV / 95 mA (peak)	$(C_2H_4)_n$ moderator	
[121]	S-band e-linac+W+Be	$9.94 \cdot 10^{9}$ n/s	Non-destructive assay
Japan	10 MeV / 0.1 mA		
[122]	S-band e-linac+W+Be	$2.133 \cdot 10^{-6}$ n/e	
India	6 MeV / 130 mA	< 2 MeV	

Table A.1: Compact accelerator-driven neutron sources specifications.

Facility	Accelerator length [m]	RF Average power consumption [MW]
RANS	3.8 [123]	0.0045 [124]
GELINA [125]	15.0	0.06
HBS [43]	115.4 [1]	12
IFMIF DONES	141.6 [126]	7.4 [2] [127]
ESS [128]	602.4	42.1 [2]

[1] Assumed 0.5 m drift between structures.

[2] Cryogenic cooling system power consumption included.

Table A.2: State-of-the-art: Length and power consumption.

A.2 Beam Loading documentation in RF-Track

This appendix presents the extracts of RF-Track's user-guide [67] where the Beam Loading module usage is described.

A.2.1 Beam Loading in RF-Track version 2.2.3

Beam loading in travelling-wave structures

The beam loading effect in travelling-wave structures is considered using the collective effect `BeamLoading()`. The following constructors apply to ultra-relativistic bunches ($v \simeq c$) and distinguish between transient and steady-state depending if the bunch is injected before or after the structure is filled (t_{fill}):

Constructors

```
% Steady state beam loading — For bunches entering after tfill
BL = BeamLoading(TWS, Pactual, vg, Q, ph_ad, q, particles_bunch, fb,
    ffactor);
BL = BeamLoading(Ncells, freq, r_Q, vg, Q, ph_ad, q, particles_bunch, fb
    , ffactor);
% Transient beam loading — For bunches entering before tfill
BL = BeamLoading(TWS, Pactual, vg, Q, ph_ad, q, particles_bunch, fb,
    Nbunches, ffactor);
BL = BeamLoading(Ncells, freq, r_Q, vg, Q, ph_ad, q, particles_bunch, fb
    , Nbunches, ffactor);
```

The possible arguments are:

`TWS`	RF-Element with the TW field map	
`Ncells`	Number of cells of the TW structure	
`freq`	RF-Frequency	[Hz]
`Pactual`	Steady input power of the structure	[W]
`vg`	Group-velocity array	[c]
`Q`	Quality factor array	
`r_Q`	Normalised shunt impedance per unit length array (r/Q)	[Ω/m]
`ph_ad`	Phase advance	[rad]

`q`	Single particle charge	[e]
`particles_bunch`	Number of particles per bunch	
`fb`	Bunch injection frequency	[Hz]
`Nbunches`	Number of bunches of the train	
`ffactor`	Bunch form factor	

The most common bunch distributions and associated form factors are given below:

$$\text{GAUSSIAN} \qquad F(\omega) = \exp -\frac{\omega^2 \sigma_z^2}{2c^2}$$

$$\text{UNIFORM} \qquad F(\omega) = \frac{\sin x}{x}, \text{ with } x = \frac{1}{2}\omega t_b$$

Here, σ_z refers to the longitudinal single-bunch energy spread and t_b is the time-range of it. If no `ffactor` is given, the default value is `ffactor = 1`.

Get methods

Some structure-relevant magnitudes, as well as the beam-induced and unloaded gradients, can be retrieved from the constructors as follows:

```
%Structure information
BL.get_Lcell(); % Cell length, m
BL.get_tfill(); % Filling time, mm/c
BL.get_z0(); % Starting longitudinal coordinate, m
BL.get_z1(); % Ending longitudinal coordinate, m

% Interpolated splines of figures of merit along the structure
BL.get_vg(); % Group velocity, c
BL.get_dvg(); % Group velocity spatial derivative, c/mm
BL.get_Q(); % Quality factor
BL.get_rho(); % Normalized shunt impedance per unit length, Ohm/m
BL.get_drho(); % Normalized shunt impedance p.u.l derivative, Ohm/m/mm

% Structure gradient
BL.get_G(); % Transient beam-induced gradient, V/m
BL.get_G_steady(); % Steady beam-induced gradient, V/m
BL.get_G_unloaded(); % Transient unloaded gradient, V/m
BL.get_G_unloaded_steady(); % Steady unloaded gradient, V/m
BL.get_dt(); % Time-step in transient gradient matrices, mm/c
```

Beam loading compensation

A common technique for beam loading compensation in travelling-wave structures is injection during structure filling. The following constructor allows the simulation of beam-loading effects at arbitrary times after the structure is powered with an arbitrary time profile:

```
BL = BeamLoading(TWS, Pinput, dt_Pinput, inj_delay, vg, Q, ph_ad, q,
    particles_bunch, fb, Nbunches, ffactor);
```

In this case, the following new arguments have to be considered:

`Pinput`	Input power spline	[W]
`dt_Pinput`	Time-step of `Pinput` spline	[mm/c]
`inj_delay`	Injection time with respect to `Pinput` origin	[mm/c]

Beam loading in standing-wave structures

The beam loading effect in standing-wave structures is taken into account using the collective effect `BeamLoadingSW()`, which accepts the following arguments:

```
% Transient beam loading in SW structures
BL = BeamLoadingSW(SWS, Q, r_Q, Ncells, mass, q, tinj);
```

In this case, the arguments are:

`SWS`	RF-Element with the SW field map	
`Q`	Quality factor array	
`r_Q`	Normalized shunt impedance per unit length array (r/Q)	[Ω/m]
`Ncells`	Number of cells of the TW structure	
`mass`	Particle mass	[MeV/c^2]
`q`	Single particle charge	[e]
`tinj`	Injection time of the bunch	[mm/c]

Get methods

The following quantities can be obtained from the `BeamLoadingSW()` collective effect:

```
BL.get_Lcell(); % Cell length, m
```

```
BL.get_tfill(); % Filling time, mm/c
BL.get_TT1(); % Time-transit factor array for the first cell
BL.get_TT2(); % Time-transit factor array for any complete cell
```

A.2.2 Beam Loading in RF-Track version 2.3.0

This version of RF-Track improves the previous beam loading module by simplifying the sintax and implementing the flexible wake-based kick computation presented in Sec. 3.4.3 and the compensation technique for SW structures.

Beam loading in ultrarelativistic scenarios

The beam loading effect in ultrarelativistic scenarios ($v \simeq c$) is considered for both travelling-wave structures and standing-wave structures using the collective effect `BeamLoading()`. The following constructors distinguish between transient and steady-state:

Constructors

```
% Steady state beam loading - For trains entering after tfill. Fixed
    charge per bunch
BL = BeamLoading(Ncells, freq, ph_ad, Q, r_Q, vg, q, particles_bunch, fb
    , nbins);
% Transient beam loading - For bunches entering before tfill. No
    assumption on the train distribution
BL = BeamLoading(Ncells, freq, ph_ad, Q, r_Q, vg, nbins);
```

The possible arguments are:

`Ncells`	Number of cells of the TW structure	
`freq`	RF-Frequency	[Hz]
`ph_ad`	Phase advance	[rad]
`Q`	Quality factor array	
`r_Q`	Normalised shunt impedance per unit length array (r/Q)	[Ω/m]
`vg`	Group-velocity array	[c]
`nbins`	Number of bins for single-bunch longitudinal slicing	
`q`	Single particle charge	[e]
`particles_bunch`	Number of particles per bunch	
`fb`	Bunch injection frequency	[Hz]

If no `nbins` value is provided, the default value is `nbins=16`.

Solve methods

For trains with bunches of equal charge and fixed spacing, the beam-induced gradient exhibits a transient behaviour which, after a certain time (t_{fill} for TW structures or 5τ for SW structures), stabilises at the so-called steady state. In this case, the beam-induced gradient be retrieved with the following constructors:

```
BL.solve_pde_steady(q_bunch, fb, ffactor);
BL.solve_pde_transient(q_bunch, fb, Nbunches, ffactor);
```

The possible arguments are:

`q_bunch`	Total charge per bunch	[e]
`Nbunches`	Number of bunches of the train	
`ffactor`	Bunch form factor	

The most common bunch distributions and associated form factors are given below:

$$\begin{aligned} &\text{GAUSSIAN} && F(\omega) = \exp -\frac{\omega^2 \sigma_z^2}{2c^2} \\ &\text{UNIFORM} && F(\omega) = \frac{\sin x}{x}, \text{ with } x = \frac{1}{2}\omega t_b \end{aligned}$$

Here, σ_z refers to the longitudinal single-bunch energy spread and t_b is the time-range of it. If no `ffactor` is given, the default value is `ffactor = 1`.

Set methods

There are two common strategies for beam loading compensation: Injecting bunches early in the structure prior to its RF-filling, and optimising the input-power pulse shape in TW structures. Bunch injection and input-power profile can be arbitrarily defined in RF-Track prior to tracking with the following constructors:

```
% Set unloaded gradient according to Pinput for BL compensation in TW
    structures
BL.set_unloaded_gradient(Pinput, dt_Pinput, t_inj, RF_Structure );
% Set early injection time for BL compensation in SW structures
BL.set_early_injection(t_inj, RF_Structure );
```

The required arguments are:

`Pinput`	Input power spline	[W]
`dt_Pinput`	Time step associated to the `Pinput` spline	[mm/c]
`t_inj`	Injection time with respect to the origin of `Pinput`	[mm/c]
`RF_Structure`	RF-Element with the TW/SW fieldmap	

Get methods

Some structure-relevant magnitudes, as well as the beam-induced and unloaded gradients, can be retrieved from the constructors as follows:

```
%Structure information
BL.get_Lcell(); % Cell length, m
BL.get_tfill(); % Filling time, mm/c
BL.get_z0(); % Starting longitudinal coordinate, m
BL.get_z1(); % Ending longitudinal coordinate, m
BL.get_wake_function(); % Longitudinal wakefield, V/pC/m

% Interpolated splines of figures of merit along the structure
BL.get_vg(); % Group velocity, c
BL.get_dvg(); % Group velocity spatial derivative, c/mm
BL.get_Q(); % Quality factor
BL.get_rho(); % Normalized shunt impedance per unit length, Ohm/m
BL.get_drho(); % Normalized shunt impedance p.u.l derivative, Ohm/m/mm
```

```
% Structure gradient - After solve methods
BL.get_G(); % Transient beam-induced gradient, V/m
BL.get_G_steady(); % Steady beam-induced gradient, V/m

% Structure gradient - After Set methods
BL.get_G_unloaded(); % Transient unloaded gradient, V/m
BL.get_G_unloaded_steady(); % Steady unloaded gradient, V/m
BL.get_dt(); % Time-step in transient gradient matrices, mm/c
```

The function `BL.get_wake_function()` retrieves the longitudinal wakefield associated to the excitation of the fundamental mode, which is the one on which the implementation of the BL kick is based as discussed in Sec. 3.4.2.

Further longitudinal short-range effects arising from higher-order modes can be simulated with `ShortRangeWakefield`, as it is presented in [67]. To avoid overlap of the effects, the following constructors allow to enable/disable the short-range BL force:

```
BL.disable_short_range();
BL.enable_short_range();
```

Beam loading in standing-wave structures

The beam loading effect in standing-wave structures for non-ultrarelativistic scenarios is taken into account using the collective effect `BeamLoadingSW()`, which accepts the following arguments:

```
% Transient BL in SW structures
BL = BeamLoadingSW(SWS, Q, r_Q, Ncells, mass, q, tinj);
```

In this case, the arguments are:

`SWS`	RF-Element with the SW field map	
`Q`	Loaded quality factor array	
`r_Q`	Normalized shunt impedance per unit length array (r/Q)	[Ω/m]
`Ncells`	Number of cells of the TW structure	
`mass`	Particle mass	[MeV/c^2]
`q`	Single particle charge	[e]

`tinj`	Injection time of the bunch	$[\tau]$

For SW structures, $\tau = \frac{2Q}{\omega}$.

Get methods

The following quantities can be obtained from the `BeamLoadingSW()` collective effect:

```
BL.get_Lcell(); % Cell length, m
BL.get_tfill(); % Filling time, mm/c
BL.get_tinj();  % Injection time, mm/c
BL.get_TT1(); % Time-transit factor array for the first cell
BL.get_TT2(); % Time-transit factor array for any complete cell
```

A.3 Curve-fitting and statistical data treatment

Monte Carlo as well as experimental results have been shown with their corresponding uncertainties. For direct measurements, the uncertainty is the precision of the instrument or the standard deviation of a set of measurements as explained in Chapter 4. On the other hand, the uncertainties of Monte Carlo-based quantities follow the expressions shown in Sec. 5.1.2.

To calculate the uncertainty of an indirect measurement, f, depending on N direct measurements a_i ($i \leq N$), we used quadratic error propagation, which reads as:

$$\Delta f(x;\vec{a}) = \sqrt{\sum_{i=1}^{N} \left(\frac{\partial f}{\partial a_i}\right)^2 \Delta(a_i)^2}. \tag{A.1}$$

Curve fitting

To correlate the experimental measurements with theoretical predictions, or to asseverate the linear dependency of a set of data, we made use of curve fitting methods to obtain the value of some coefficients, namely b_j ($j < M$), that provide the closest match of the function $F(x;\vec{b})$ to the experimental data $\{(x_s, y_s)\}_{s=1}^{S}$.

Curve fitting algorithms solve non-linear least square problems, i.e, for a given residual vector, $\vec{r} \in \mathbb{R}^S$, defined as $r_s = y_s - F(x_s;\vec{b})$, they minimize the norm of that vector as:

$$\min_{\vec{b}\in\mathbb{R}^M} ||\vec{r}(\vec{b})|| = \min_{\vec{b}\in\mathbb{R}^M} \sum_{s=1}^{S} (y_s - F(x_s;\vec{b}))^2. \tag{A.2}$$

Two strategies were followed along the document to minimize Eq. (A.2):

- The Gauss-Newton Method: Which implements a gradient-descent strategy to converge quadratically to the solution. It was implemented in Sec. 4.2.1, and the iterative algorithm searches for an optimal value of $\vec{b}$, $\vec{b}^*$, with the recursive formula [112]:

  $$\vec{b}^{\mathtt{iter}+1} = \vec{b}^{\mathtt{iter}} - (J_r^T J_r)^{-1} J_r^T \cdot \vec{r}(\vec{b}^{\mathtt{iter}}), \text{ where } (J_r)_{sj} = \frac{\partial r_s(\vec{b}^{\mathtt{iter}})}{\partial b_j}. \tag{A.3}$$

  Here, `iter` stands for the iteration, and the algorithm requires an initial estimate $\vec{b}^0$, and stops when $||\vec{b}^{\mathtt{iter}+1} - \vec{b}^{\mathtt{iter}}|| < \varepsilon$ for a given $\varepsilon > 0$.

- The polyfit function in OCTAVE, which makes use of Vandermonde matrices to solve the overfitted system of equations $\vec{y} = A(\vec{b})\vec{x}$ when the targeted function is a polynomial, i.e $F(\vec{x};\vec{b}) = A(\vec{b})\vec{x}$, with $A \in \mathbb{R}^{M\times S}$.

The minimization in Eq. (A.2) is equivalent to a Maximum Likelihood Estimation (MLE) if the residuals $r_s = y_s - F(x_s, \vec{b})$ are assumed to be independently and identically distributed (i.i.d.) and normally distributed, $r_s \sim \mathcal{N}(0, \sigma^2)$. The theory that follows has been extracted from Ref [129].

Under this assumption, the least-squares estimator ($\vec{b}^*$) is the MLE of the parameters $\vec{b}$. The covariance matrix of the estimated parameters is then given by

$$\text{Cov}(\vec{b}) = \hat{\sigma}^2 (J_r^T J_r)^{-1}, \tag{A.4}$$

where:

- J_r is the Fisher Information Matrix associated to this model, which for the Gauss Newton Method can be approximated using the Jacobian of the residuals, as shown in Eq. (A.3).
- $\hat{\sigma}^2$ is the estimated residual variance:

$$\hat{\sigma}^2 = \frac{||\vec{r}(\vec{b}^*)||}{S - M}. \tag{A.5}$$

This matrix allows to calculate the standard error (SE) of the coefficients by taking the square root of its diagonal entries, that is, that is, $\text{SE}(b_j) = \sqrt{(\text{Cov}(\vec{b}))_{jj}}$.

Because the number of degrees of freedom, ν, is small, the centered confidence intervals for the parameters b_j are constructed using the Student's t-distribution as:

$$b_j \pm t_{\frac{\alpha}{2},\nu}\, \text{SE}(b_j), \tag{A.6}$$

where $t_{\frac{\alpha}{2},\nu}$ is the percentile $1 - \alpha$ of the T-student distribution, α is the so-called confidence level, and $\nu = S - M$ are the degrees of freedom.

A.4 G4beamlines simulations

G4BEAMLINE is a particle tracking and simulation program based on the Geant4 toolkit that is specifically designed to easily simulate beamlines and related systems [102]. It exhibits a simpler user interface which allows the study of radiation-matter interaction, in our case, neutron production with electron beams. As explained in Sec. 5.1.2, the nuclear mechanisms that result in neutron production are modeled using the physics option FTFP_BERT_HP.

The FTFP_BERT_HP allows the simulation of Bremsstrahlung processes where photons are produced from the interaction of the electron beam with tungsten's nuclei and inner shell electrons. G4BEAMLINE makes use of the `G4eBremmstrahlung` class of Geant4, which produces an energy spectrum which follows the Bethe-Heitler distribution, peaking at low energies but extending up to the energy of the electron.

To model the photonuclear processes described in Sec. 5.1.2, the FTFP_BERT_HP physics option imports the Geant4 classes `G4PhotoNuclearProcess` and `G4CascadeInterface`. The first one models hadron production when photons up to $5\,\mathrm{GeV}$ interact with tungsten nuclei. The second option implements the Bertini Cascade algorithm to simulate the hadron multiple scattering and emission of secondaries like neutrons, pions, etc. It models the cascade as a sequence of two-body collisions inside the nucleus as described in Ref [130].

Finally, neutron transport is taken into account with the following high-precision Geant4 classes: `G4NeutronHPInelastic`, `G4NeutronHPElastic`, `G4NeutronHPCapture`, `G4NeutronHPFission`. These classes simulate the mentioned processes by evaluating nuclear data libraries (like ENDF/B or JENDL) for neutron interactions [131].

A summary of these key processes is shown in Table A.5.

Process	**Responsible Model / Class**	**Energy Range**
Bremsstrahlung	`G4eBremmstrahlung`	EM range
Photonuclear (γ, n)	`G4PhotoNuclearProcess`, `G4CascadeInterface`	$< 5\,\mathrm{GeV}$
Neutron transport	`G4NeutronHPInelastic`, `G4NeutronHPElastic`, `G4NeutronHPCapture`, `G4NeutronHPFission`	$< 20\,\mathrm{MeV}$

Table A.5: Summary of Key Processes.

Geometry and beam transport

To simulate the interaction of particles with matter, G4BEAMLINE requires the definition of a geometry where the different materials are arranged. The list of materials that can be simulated with G4BEAMLINE can be found in Ref [102]. The materials have to be arranged in geometrical shapes that do not overlap one with eachother (i.e only a 2D boundary between elements is accepted).

In such setup, particles are tracked individually in steps until they leave the volume or get absorbed by the material. Let us consider the case of a particle entering a volume with energy $\mathcal{E}$. Then, in the absence of EM forces (which can also be considered in G4BEAMLINE, see Ref [102]), such particle follows a straight motion until a process occurs.

In a differential approach, the path length of the particle from the original position until the next event occurs follows an exponential probability density given by:

$$f(s) = \frac{1}{\lambda(\mathcal{E})} \exp - \frac{s}{\lambda(\mathcal{E})}, \quad \text{with} \quad \lambda(\mathcal{E}) = \left(\sum_i n_i \sigma_i(\mathcal{E}) \right)^{-1}, \tag{A.7}$$

where $\sigma(Z_i, \mathcal{E})$ is the total cross section per atom of the process and $\sum_i$ runs over all elements composing the material. Here, λ refers to the mean free path. Further details of the transport can be found at Ref [132].

It should be noted that, if a particle crosses a media during its flight, it is only tracked until the boundary. Here, a new process, determined by the cross section corresponding to the new material, takes place, determining the amount, energy, and direction of subproducts (if any), which are tracked following the trajectory determined by Eq. (A.7) . Figure A.1 illustrates this process for a neutron penetrating a material media.

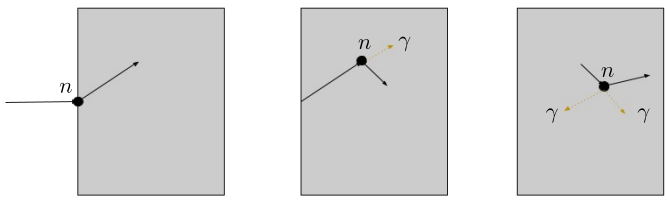

Figure A.1: Illustration of Monte Carlo differential tracking strategy for neutron transport in materials.

Bibliography

[1] P. C. A. Nassiri, B. Chase, "History and Technology Developments of Radio Frequency (RF) Systems for Particle Accelerators," *IEEE Transactions on Nuclear Science*, vol. 63, pp. 707–750, Nov 2015.

[2] E. O. Lawrence and M. S. Livingston, "The Production of High Speed Light Ions Without the Use of High Voltages," *Phys. Rev.*, vol. 40, pp. 19–35, Apr 1932.

[3] V. I. Veksler, "New method for the acceleration of relativistic particles," in *Doklady Akademii Nauk USSR*, vol. 43, pp. 346–348, 1944.

[4] D. W. Kerst, "The Acceleration of Electrons by Magnetic Induction," *Phys. Rev.*, vol. 60, pp. 47–53, Jul 1941.

[5] D. A. Edwards and M. J. Syphers, *An introduction to the physics of high energy accelerators*. John Wiley & Sons, 2008.

[6] FCC CDR website. `https://fcc-cdr.web.cern.ch/`. Accessed the 10th of March, 2024.

[7] M. Aicheler, P. Burrows, M. Draper, T. Garvey, P. Lebrun, K. Peach, N. Phinney, H. Schmickler, D. Schulte, and N. Toge, "A Multi-TeV linear collider based on CLIC technology: CLIC Conceptual Design Report," tech. rep., SLAC National Accelerator Lab., Menlo Park, CA (United States), 2014.

[8] ILC official website. `https://linearcollider.org/`. Accessed the 10th of March, 2024.

[9] K. Black, S. Jindariani, D. Li, F. Maltoni, P. Meade, D. Stratakis, D. Acosta, R. Agarwal, K. Agashe, C. Aime, *et al.*, "Muon collider forum report," *Journal of Instrumentation*, vol. 19, no. 02, p. T02015, 2024.

[10] M. Altarelli, R. Brinkmann, M. Chergui, W. Decking, B. Dobson, S. Düsterer, G. Grübel, and W. Graeff, *The European X-Ray Free-Electron Laser Technical design report*. DESY XFEL Project Group, July 2007.

[11] S. Benedetti, A. Grudiev, and A. Latina, "High gradient linac for proton therapy," *Phys. Rev. Accel. Beams*, vol. 20, p. 040101, Apr 2017.

[12] V. Santoro, K. Andersen, P. Bentley, M. Bernasconi, M. Bertelsen, Y. Beßler, A. Bianchi, T. Brys, D. Campi, A. Chambon, *et al.*, "The HighNESS Project at the European Spallation Source: Current Status and Future Perspectives," *Nuclear Science and Engineering*, vol. 198, no. 1, pp. 31–63, 2024.

[13] J.P.Blewett, *Linear Accelerators*, ch. The History of Linear Accelerators. Lapostolle, P.M. and Septier. Ed. Amsterdam, Holland: A.L North Holland Publishing, 1970.

[14] T. P. Wangler, *RF Linear accelerators*. John Wiley & Sons, 2008.

[15] A. Gurevich, "Theory of RF superconductivity for resonant cavities," *Superconductor Science and Technology*, vol. 30, no. 3, p. 034004, 2017.

[16] A. Caldwell, E. Adli, L. Amorim, R. Apsimon, T. Argyropoulos, and R. A. et. al., "Path to AWAKE: Evolution of the concept," *Nuclear Instruments and Methods in Physics Research Section A: Accelerators, Spectrometers, Detectors and Associated Equipment*, vol. 829, pp. 3–16, 2016. 2nd European Advanced Accelerator Concepts Workshop - EAAC 2015.

[17] W. Wuensch, C. Achard, S. Dobert, H.-H. Braun, I. Syrachev, M. Taborelli, and I. Wilson, "A demonstration of high-gradient acceleration," *Conf. Proc. C*, vol. 030512, p. 495, 2003.

[18] P. Martinez-Reviriego, D. Esperante, A. Grudiev, B. Gimeno, C. Blanch, D. González-Iglesias, N. Fuster-Martínez, P. Martín-Luna, E. Martínez, A. Menendez, and J. Fuster, "Dielectric assist accelerating structures for compact linear accelerators of low energy particles in hadrontherapy treatments," *Frontiers in Physics*, vol. 12, 2024.

[19] Y. Kim, S. Saitiniyazi, M. Mayierjiang, M. Titberidze, T. Andrews, and C. Eckman. `https://www.jlab.org/conferences/FLS2012/talks/Thur/isu_jlab39_fls2012_57_final.PDF`. Oral contribution to ICFA Workshop on Future Light Sources March 5-9, 2012.

[20] P. Alonso Arias, A. Chauchet, C. Marrelli, I. Syratchev, M. Webber, M. Boronat, M. Jones, N. Catalan-Lasheras, S. González-Antón, and U. N. Zaib, "Validation of high efficiency klystron technology," *JACoW*, vol. LINAC2024, p. THPB015, 2024.

[21] P. Morales Sanchez, A. Gerardin, A. Moros, A. T. Perez Fontenla, A. Magazinik, E. Rodriquez Castro, N. Catalan-Lasheras, and S. Gonzalez Anton, "Smartcell X-band normal conducting accelerator structure prototype fabrication," *JACoW*, vol. LINAC2024, p. THPB016, 2024.

[22] W. Herr and B. Muratori, "Concept of luminosity," 2006. CERN report https://cds.cern.ch/record/941318. DOI: 10.5170/CERN-2006-002.361.

[23] M. Vretenar, J. Vollaire, R. Scrivens, C. Rossi, F. Roncarolo, S. Ramberger, U. Raich, B. Puccio, D. Nisbet, R. Mompo, S. Mathot, C. Martin, L. A. Lopez-Hernandez, A. Lombardi, J. Lettry, J. B. Lallement, I. Kozsar, J. Hansen, F. Gerigk, A. Funken, J. F. Fuchs, N. Dos Santos, M. Calviani, M. Buzio, O. Brunner, Y. Body, P. Baudrenghien, J. Bauche, and T. Zickler, *LINAC4 design report*, vol. 6 of *CERN Yellow Reports: Monographs*. Geneva: CERN, 2020.

[24] O. S. Brüning, P. Collier, P. Lebrun, S. Myers, R. Ostojic, J. Poole, and P. Proudlock, *LHC Design Report*. CERN Yellow Reports: Monographs, Geneva: CERN, 2004.

[25] Z. Vostrel and S. Doebert, "Design of an electron source for the FCC-ee with top-up injection capability," *Nuclear Instruments and Methods in Physics Research Section A: Accelerators, Spectrometers, Detectors and Associated Equipment*, vol. 1063, p. 169261, 2024.

[26] CERN Courrier. https://cerncourier.com/a/linacs-to-narrow-radiotherapy-gap/. Consulted on April 2025.

[27] G. Kraft, "Medical application of accelerators in tumor therapy," in *CERN Accelerator School. Fifth advanced Accelerator Physics Course*, CERN, 1995.

[28] A. Degiovanni and U. Amaldi, "History of hadron therapy accelerators," *Physica medica*, vol. 31, no. 4, pp. 322–332, 2015.

[29] Universidad de Valencia Press. uv.es/uvweb/uv-news/en/news/. Consulted on April 2025.

[30] A. Latina, E. Cormier, R. Corsini, L. Dyks, E. Granados, A. Grudiev, V. Musat, G. Santarelli, S. Stapnes, and W. Wuensch, "A Compact Inverse Compton Scattering Source Based on X-Band Technology and Cavity-Enhanced High-Average-Power Ultrafast Lasers," *JACoW*, vol. LINAC2022, pp. 44–46, 2022.

[31] Y. Kiyanagi, "Neutron applications developing at compact accelerator-driven neutron sources," *AAPPS Bulletin*, vol. 31, pp. 1–19, 2021.

[32] J. M. Carpenter, "The development of compact neutron sources," *Nature Reviews Physics*, vol. 1, no. 3, pp. 177–179, 2019.

[33] M. S. Herrera, G. A. Moreno, and A. J. Kreiner, "Revisiting the 7Li(p,n)7Be reaction near threshold," *Applied Radiation and Isotopes*, vol. 88, pp. 243–246, 2014. 15th International Congress on Neutron Capture Therapy Impact of a new radiotherapy against cancer.

[34] LENS Ad-hoc Working Group CANS, "Low energy accelerator-driven neutron sources," tech. rep., League of Advanced European Neutron Sources, Nov 2020.

[35] I. Podadera, A. Ibarra, D. Jiménez-Rey, J. Molla, C. de la Morena, C. Oliver, N. Bazin, N. Chauvin, J. Dumas, S. Chel, *et al.*, "The accelerator system of IFMIF-DONES multi-MW facility," in *Proceedings of 12th International Particle Accelerator Conference (IPAC'21), Campinas, Brazil*, pp. 1910–1913, 2021.

[36] GELINA official website. `https://joint-research-centre.ec.europa.eu/laboratories-z/jrc-neutron-time-flight-facility_en`. Accessed on April 2025.

[37] ISIS official website. `https://www.isis.stfc.ac.uk/Pages/home.aspx`. Accessed on April 2025.

[38] J. website. `https://www.jcans.net/rans.html`. Accessed on April 2025.

[39] K. linac website. `https://www.eng.hokudai.ac.jp/labo/QBMA/LINAC/performance-e.html`. Accessed on April 2025.

[40] I. Anderson, C. Andreani, J. Carpenter, G. Festa, G. Gorini, C.-K. Loong, and R. Senesi, "Research opportunities with compact accelerator-driven neutron sources," *Physics Reports*, vol. 654, pp. 1–58, 2016.

[41] T. Sano, J.-i. Hori, Y. Takahashi, H. Yashima, J. Lee, and H. Harada, "Analysis of energy resolution in the KURRI-LINAC pulsed neutron facility," in *EPJ Web of Conferences*, vol. 146, p. 03031, EDP sciences, 2017.

[42] F. Ott, A. Menelle, and C. Alba-Simionesco, "The SONATE project, a French CANS for materials sciences research," in *EPJ Web of Conferences*, vol. 231, p. 01004, EDP Sciences, 2020.

[43] T. Brückel, T. Gutberlet, J. Baggemann, S. Böhm, P. Doege, J. Fenske, M. Feygenson, A. Glavic, O. Holderer, S. Jaksch, *et al.*, *Conceptual Design Report-Jülich High Brilliance Neutron Source (HBS)*. Forschungszentrum Jülich GmbH, Zentralbibliothek, Verlag, 2020.

[44] J. D. Jackson, *Classical electrodynamics*. John Wiley & Sons, 2021.

[45] M. Weiss, "Introduction to rf linear accelerators," *Cern Accelerator School Proceedings*, 1994.

[46] A. Wolski, *Beam dynamics in high energy particle accelerators*. World Scientific, 2014.

[47] H. Wiedemann, *Particle accelerator physics*. Springer Nature, 2015.

[48] H. Goldstein, *Classical mechanics*. Addison-Wesley, 1980.

[49] W. Hillert, "Transverse Linear Beam Dynamics," in *CAS - CERN Accelerator School 2019: Introduction to Accelerator Physics*, 7 2021.

[50] J. E. Leiss, "Beam loading and transient behavior in traveling wave electron linear accelerators.," *pp 147-72 of Linear Accelerators. /Lapostolle, Pierre M. (ed.). Amsterdam North-Holland Publishing Co. (1970).*, 1 1970.

[51] D. Alesini, "Linear accelerator technology," *CERN Yellow Reports: School Proceedings*, vol. 1, pp. 79–79, 2018.

[52] A. Nassiri, B. Chase, P. Craievich, A. Fabris, H. Frischholz, J. Jacob, E. Jensen, M. Jensen, R. Kustom, and R. Pasquinelli, "History and technology developments of radio frequency (rf) systems for particle accelerators," *IEEE Transactions on Nuclear Science*, vol. 63, pp. 1–1, 11 2015.

[53] G. Stupakov and G. Penn, *Classical mechanics and electromagnetism in accelerator physics*, vol. 61. Springer, 2018.

[54] A. W. Chao, "Physics of collective beam instabilities in high energy accelerators," *Wiley series in beam physics and accelerator technology*, 1993.

[55] S. C. Hartman and J. B. Rosenzweig, "Ponderomotive focusing in axisymmetric RF linacs," *Phys. Rev. E*, vol. 47, pp. 2031–2037, Mar 1993.

[56] G. Saxon, "Theory of electron beam loading in linear accelerators," *Proceedings of the Physical Society. Section B*, vol. 67, no. 9, p. 705, 1954.

[57] J. Leiss, S. Penner, J. Rose, and J. Broberg, "Transient beam loading in electron linear accelerators," *IEEE Transactions on Nuclear Science*, vol. 16, no. 3, pp. 1027–1030, 1969.

[58] K. Amyx, J. King, I. Pogorelov, M. Borland, and R. Soliday, "Current Status of the GPU-accelerated ELEGANT," in *Proc. 5th Int. Part. Accel. Conf.*, pp. 454–456, 2014.

[59] A. Latina, Y. Levinsen, D. Schulte, and J. Snuverink, "Evolution of the Tracking Code PLACET," in *4th International Particle Accelerator Conference*, p. MOPWO053, 2013.

[60] C. M. Studio, "CST Microwave studio," *CST Studio Suite*, 2008.

[61] W. Bruns, "Improvements in GdFidl," in *Proceedings of the 1999 Particle Accelerator Conference (Cat. No. 99CH36366)*, vol. 4, pp. 2767–2768, IEEE, 1999.

[62] A. Lunin, V. Yakovlev, and A. Grudiev, "Analytical solutions for transient and steady state beam loading in arbitrary traveling wave accelerating structures," *Physical Review Special Topics-Accelerators and Beams*, vol. 14, no. 5, p. 052001, 2011.

[63] R. M. Jones, V. A. Dolgashev, and J. W. Wang, "Dispersion and energy compensation in high-gradient linacs for lepton colliders," *Physical Review Special Topics-Accelerators and Beams*, vol. 12, no. 5, p. 051001, 2009.

[64] P. Wilson, "Transient beam loading in electron-positron storage rings," tech. rep., 1978.

[65] V. Venkatasubramanian, "Tools for dynamic analysis of the general large power system using time-varying phasors," *International Journal of Electrical Power & Energy Systems*, vol. 16, no. 6, pp. 365–376, 1994.

[66] G. Dôme, "Basic rf theory, waveguides and cavities," CERN, 1992.

[67] A. Latina, "RF-Track Reference Manual," tech. rep., CERN, Geneva, Switzerland, 2024.

[68] A. Latina. https://indico.cern.ch/event/1138716/contributions/5558677/attachments/2731786/4750073/WEA3C1_talk.pdf. Oral contribution to HB2023 Workshop, Luzern, Switzerland.

[69] W. H. Press, *Numerical recipes 3rd edition: The art of scientific computing*. Cambridge university press, 2007.

[70] E. W. Weisstein. MathWorld–A Wolfram Web Resource. Convolution Theorem.

[71] E. Adli, *A study of the beam physics in the CLIC drive beam decelerator*. PhD thesis, U. Oslo, 2009.

[72] O. El Mrabet, "High frequency structure simulator (HFSS) tutorial," *IETR, UMR CNRS*, vol. 6164, pp. 2005–2006, 2006.

[73] J. Liu and A. Grudiev, "RF design of accelerating structure for the main linac of the klystron-based first stage of CLIC at 380 GeV," tech. rep., CERN, Geneva, 2018.

[74] J. A. Nelder and R. Mead, "A simplex method for function minimization," *The Computer Journal*, vol. 7, pp. 308–313, 01 1965.

[75] R. Corsini, L. A. Dyks, W. Farabolini, P. Korysko, A. Malyzhenkov, V. Rieker, and K. Sjobak, "Status of the CLEAR User Facility at CERN and its Experiments," *JACoW*, vol. LINAC2022, pp. 753–757, 2022.

[76] W. Farabolini *et al.*, "CTF3 probe beam LINAC commissioning and operations," in *25th International Linear Accelerator Conference*, p. MOP001, 2011.

[77] D. Gamba, R. Corsini, S. Curt, S. Doebert, W. Farabolini, G. Mcmonagle, P. Skowronski, F. Tecker, S. Zeeshan, E. Adli, C. Lindstrøm, A. Ross, and L. Wroe, "The CLEAR user facility at CERN," *Nuclear Instruments and Methods in Physics Research Section A: Accelerators, Spectrometers, Detectors and Associated Equipment*, vol. 909, pp. 480–483, 2018. 3rd European Advanced Accelerator Concepts workshop (EAAC2017).

[78] J. J. Bateman, E. Buchanan, R. Corsini, W. Farabolini, P. Korysko, R. G. Larsen, A. Malyzhenkov, I. O. Ruiz, V. Rieker, A. Gerbershagen, and M. Dosanjh, "Development of a novel fibre optic beam profile and dose monitor for very high

energy electron radiotherapy at ultrahigh dose rates," *Physics in Medicine & Biology*, vol. 69, p. 085006, apr 2024.

[79] K. N. Sjobak, E. Adli, R. Corsini, W. Farabolini, G. Boyle, C. A. Lindstrøm, M. Meisel, J. Osterhoff, J.-H. Röckemann, L. Schaper, and A. E. Dyson, "Strong focusing gradient in a linear active plasma lens," *Phys. Rev. Accel. Beams*, vol. 24, p. 121306, Dec 2021.

[80] G. Lerner, A. Coronetti, J. M. Kempf, R. G. Alía, F. Cerutti, D. Prelipcean, M. Cecchetto, A. Gilardi, W. Farabolini, and R. Corsini, "Analysis of the Photoneutron Field Near the THz Dump of the CLEAR Accelerator at CERN With SEU Measurements and Simulations," *IEEE Transactions on Nuclear Science*, vol. 69, no. 7, pp. 1541–1548, 2022.

[81] L. Whitmore, R. I. Mackay, M. van Herk, P. Korysko, W. Farabolini, A. Malyzhenkov, R. Corsini, and R. M. Jones, "CERN-based experiments and Monte-Carlo studies on focused dose delivery with very high energy electron (VHEE) beams for radiotherapy applications," *Sci. Rep.*, vol. 14, no. 1, p. 11120, 2024.

[82] P. Korysko, A. Malyzhenkov, A. Aksoy, C. Robertson, J. Bateman, K. Sjobak, M. Dosanjh, R. Corsini, V. Rieker, and W. Farabolini, "The CLEAR user facility: a review of the experimental methods and future plans," *JACoW*, vol. IPAC2023, p. MOPL141, 2023.

[83] K. Sjobak, E. Adli, M. Bergamaschi, S. Burger, R. Corsini, A. Curcio, S. Curt, S. Döbert, W. Farabolini, D. Gamba, L. Garolfi, A. Gilardi, I. Gorgisyan, E. Granados, H. Guerin, R. Kieffer, M. Krupa, T. Lefèvre, C. Lindstrøm, A. Lyapin, S. Mazzoni, G. McMonagle, J. Nadenau, H. Panuganti, S. Pitman, V. Rude, A. Schlogelhofer, P. Skowroński, M. Wendt, and A. Zemanek, "Status of the CLEAR electron beam user facility at CERN," p. MOPTS054, 2019.

[84] R. Huang, D. Filippetto, C. F. Papadopoulos, H. Qian, F. Sannibale, and M. Zolotorev, "Dark current studies on a normal-conducting high-brightness very-high-frequency electron gun operating in continuous wave mode," *Phys. Rev. ST Accel. Beams*, vol. 18, p. 013401, Jan 2015.

[85] J. H. B. Madsen, "LEP injector linacs 1989," tech. rep., CERN, Geneva, 1989.

[86] C. P. B. M. R. Roux, G. Bienvenu. `https://cds.cern.ch/record/941433/files/note-2004-034-PHIN.pdf`. CALIFES-PHIN photoinjector report.

[87] R.Belbeach, G. Bienvenu, J. Bourdon, P. Brunet, R. Chaput, R. Chehab, S.Costa, V. Dabin, and G. Danon. https://cds.cern.ch/record/136636/files/lal-rt-82-01.pdf. Rapport d'etudes sur le projet des linacs injecteur de LEP (LIL).

[88] "PSI online resources: Neutron energies clasification." Accesed the 6th of November, 2023.

[89] H. Iwashita, H. Sato, K. Arai, T. Kotanigawa, K. Kino, T. Kamiyama, F. Hiraga, K. Koda, M. Furusaka, and Y. Kiyanagi, "Accelerated Tests of Soft Errors in Network Systems Using a Compact Accelerator- Driven Neutron Source," *IEEE Transactions on Nuclear Science*, vol. 64, no. 1, pp. 689–696, 2017.

[90] J. R. Centre, I. for Energy, Transport, W. Sauerwein, and R. Moss, *Requirements for boron neutron capture therapy (BNCT) at a nuclear research reactor*. Publications Office, 2009.

[91] N. Hu, R. Kakino, A. Sasaki, S. Yoshikawa, K. Akita, S. Takeno, Y. Yoshino, T. Aihara, K. Nihei, M. Nojiri, N. Matsubayashi, T. Takata, H. Tanaka, M. Suzuki, and K. Ono, "Clinical evaluation of performance, stability, and longevity of an accelerator system designed for boron neutron capture therapy utilising a beryllium target," *Nuclear Instruments and Methods in Physics Research Section A: Accelerators, Spectrometers, Detectors and Associated Equipment*, vol. 1072, p. 170126, 2025.

[92] E. López-Melero, F. García-Infantes, I. L. Casas, F. A. de Saavedra, I. Porras, A. Roldán, L. F. Maza, and J. Praena, "Production of 177Lu with deuterons at IFMIF-DONES facility," 11 2021.

[93] ILL official website. https://www.ill.eu/. Accessed the 6th of November, 2023.

[94] I. A. E. AGENCY, *Compact Accelerator Based Neutron Sources*. No. 1981, Vienna: TECDOC Series, 2021.

[95] T. S. Bigelow, C. Ausmus, D. Brashear, K. Guber, J. Harvey, P. Koehler, R. B. Overton, J. A. White, and V. Cauley, "Recent operation of the ORELA electron LINAC at ORNL for neutron crosssection research," in *Proceedings of the Linear Accelerator Conference (LINAC)*, no. 21, pp. 79–81, 2006.

[96] F. Salvat, J. M. Fernández-Varea, J. Sempau, *et al.*, "PENELOPE-2006: A code system for Monte Carlo simulation of electron and photon transport," in *Workshop proceedings*, vol. 4, p. 7, Citeseer, 2006.

[97] C. Sunil and P. Sarkar, "Empirical estimation of photoneutron energy distribution in high-energy electron accelerators," *Nuclear Instruments and Methods in Physics Research Section A: Accelerators, Spectrometers, Detectors and Associated Equipment*, vol. 581, no. 3, pp. 844–849, 2007.

[98] S. Fujii, "Note on the quasi-deuteron model for nuclear photo-disintegration," *Il Nuovo Cimento (1955-1965)*, vol. 25, pp. 995–1007, 1962.

[99] M. B. CHADWICK, P. G. YOUNG, and S. CHIBA, "Photonuclear angular distribution systematics in the quasideuteron regime," *Journal of Nuclear Science and Technology*, vol. 32, no. 11, pp. 1154–1158, 1995.

[100] V. Petwal, V. Senecha, K. Subbaiah, H. Soni, and S. Kotaiah, "Optimization studies of photo-neutron production in high-Z metallic targets using high energy electron beam for ADS and transmutation," *Pramana*, vol. 68, pp. 235–241, 2007.

[101] F. Jallu, A. Lyoussi, E. Payan, H. Recroix, A. Mariani, G. Nurdin, A. Buisson, and J. Allano, "Photoneutron production in tungsten, praseodymium, copper and beryllium by using high energy electron linear accelerator," *Nuclear Instruments and Methods in Physics Research Section B: Beam Interactions with Materials and Atoms*, vol. 155, no. 4, pp. 373–381, 1999.

[102] T. Roberts, "G4Beamline user's guide," *Muons, Inc*, pp. 3468–3470, 2013.

[103] G. L. official website. `https://geant4.web.cern.ch/documentation/dev/plg_html/PhysicsListGuide/reference_PL/FTFP_BERT.html`. Consulted on April 2025.

[104] R. Beyer, E. Birgersson, Z. Elekes, A. Ferrari, E. Grosse, R. Hannaske, A. Junghans, T. Kögler, R. Massarczyk, A. Matić, R. Nolte, R. Schwengner, and A. Wagner, "Characterization of the neutron beam at nelbe," *Nuclear Instruments and Methods in Physics Research Section A: Accelerators, Spectrometers, Detectors and Associated Equipment*, vol. 723, pp. 151–162, 2013.

[105] G. Geschonke and A. Ghigo, "CTF3 design report," tech. rep., CERN, 2002.

[106] A. Latina, V. Muşat, R. Corsini, L. A. Dyks, E. Granados, A. Grudiev, S. Stapnes, P. Wang, W. Wuensch, E. Cormier, and G. Santarelli, "A compact inverse Comp-

ton scattering source based on X-band technology and cavity-enhanced high average power ultrafast lasers," in *67th ICFA Adv. Beam Dyn. Workshop Future Light Sources Conference Proceedings*, pp. 257–260, 2023.

[107] C. R. et al., "The Deep Electron FLASH Therapy facility," in *Proc. 32nd Linear Accelerator Conference (LINAC2024)*, no. 32 in International Linear Accelerator Conference, pp. 551–556, JACoW Publishing, Geneva, Switzerland, 08 2024.

[108] R. Corsini, M. Bernard, G. Bienvenu, H. Braun, G. Carron, A. Ferrari, O. Forstner, T. Garvey, G. Geschonke, L. Groening, E. Jensen, R. Koontz, T. Lefèvre, R. Miller, L. Rinolfi, R. Roux, R. D. Ruth, D. Schulte, F. A. Tecker, L. Thorndahl, and A. D. Yeremian, "First Full Beam Loading Operation with the CTF3 Linac," 2004.

[109] X. Artru, V. N. Baier, R. Chehab, M. Chevallier, M. S. Dubrovin, A. Jejcic, and J. Silva, "Positron Sources Using Channeling: A Comparison with conventional Targets," *Part. Accel.*, vol. 59, pp. 19–41, 1998.

[110] D. Agrawal and V. Menon, "Grüneisen's law for the classroom," *Physics Education*, vol. 36, pp. 495–496, 01 2001.

[111] L. M. Wroe. Internal Communication with.

[112] Å. Björck, *Numerical methods for least squares problems*. SIAM, 2024.

[113] H. M. de Oliveira and R. J. Cintra, "A new information theoretical concept: Information-weighted heavy-tailed distributions," *arXiv preprint arXiv:1601.06412*, 2016.

[114] A. Latina, "RF-Track: Beam tracking in field maps including space-charge effects, features and benchmarks," p. MOPRC016, 2017.

[115] K. L. Bane, "Wakefields of sub-picosecond electron bunches," *International Journal of Modern Physics A*, vol. 22, no. 22, pp. 3736–3758, 2007.

[116] V. E. Balakin, A. V. Novokhatsky, and V. P. Smirnov, "VLEPP: TRANSVERSE BEAM DYNAMICS," *Conf. Proc. C*, vol. 830811, pp. 119–120, 1983.

[117] A. Latina, "Studies of single and multi-bunch instabilities in linacs using RF-Track," *JACoW LINAC*, vol. 2024, p. MOPB039, 2024.

[118] N. Mesbah, S. Doebert, M. Dayyani Kelisani, A. Latina, Y. Zhao, and J. O. Herrador, "Optimisation of the CLIC positron capture LINAC taking into account Beam Loading effects," *EPJ Web Conf.*, vol. 315, p. 02001, 2024.

[119] Y. Zhao and A. Latina, "Optimization of the Compact Linear Collider rings-to-main-linac at 380 GeV," *Phys. Rev. Accel. Beams*, vol. 28, p. 021003, Feb 2025.

[120] HUNS official website. `https://www.eng.hokudai.ac.jp/labo/QBMA/LINAC/performance-e.html`. Accessed on April 2025.

[121] A. Murata, S. Ikeda, and N. Hayashizaki, "Design of an electron-accelerator-driven compact neutron source for non-destructive assay," *Nuclear Instruments and Methods in Physics Research Section B: Beam Interactions with Materials and Atoms*, vol. 406, pp. 260–263, 2017.

[122] B. Patil, S. Chavan, S. Pethe, R. Krishnan, V. Bhoraskar, and S. Dhole, "Design of 6 Mev linear accelerator based pulsed thermal neutron source: FLUKA simulation and experiment," *Applied Radiation and Isotopes*, vol. 70, no. 1, pp. 149–155, 2012.

[123] D. L. Friesel and W. Hunt, "Performance of an AccSys Technology PL-7 Linac as an Injector for the IUCF Cooler Injector Synchrotron," in *Proceedings of 19th International Linear Accelerator Conference (LINAC'98), Chicago, IL, US*, 1998.

[124] Y. Otake, "RIKEN accelerator-driven compact neutron systems, RANS project and their capabilities," *Neutron News*, vol. 31, no. 2-4, pp. 32–36, 2020.

[125] J. Clendenin, L. Rinolfi, K. Takata, and D. Warner, "Compendium of scientific linacs," *CERN/PS*, vol. 96, p. 32, 1996.

[126] W. Królas, A. Ibarra, F. Arbeiter, F. Arranz, D. Bernardi, M. Cappelli, J. Castellanos, T. Dézsi, H. Dzitko, P. Favuzza, *et al.*, "The IFMIF-DONES fusion oriented neutron source: evolution of the design," *Nuclear Fusion*, vol. 61, no. 12, p. 125002, 2021.

[127] D. Regidor, C. de la Morena, D. Iriarte, F. Sierra, S. Dragaš, P. Marini, J. Sanz, J. Molla, and A. Ibarra, "IFMIF-DONES RF System," *Fusion Engineering and Design*, vol. 167, p. 112322, 2021.

[128] K. Andersen, "ESS Technical Design Report," tech. rep., European Spallation Source, 2012.

[129] G. Casella and R. L. Berger, *Statistical Inference*. rooks/cole, Cengage Learning, 2002.

[130] D. Wright and M. Kelsey, "The GEANT4 bertini cascade," *Nuclear Instruments and Methods in Physics Research Section A: Accelerators, Spectrometers, Detectors and Associated Equipment*, vol. 804, pp. 175–188, 2015.

[131] E. Mendoza, D. Cano-Ott, T. Koi, and C. Guerrero, "New standard evaluated neutron cross section libraries for the geant4 code and first verification," *IEEE Transactions on Nuclear Science*, vol. 61, no. 4, pp. 2357–2364, 2014.

[132] G. Collaboration *et al.*, "Physics reference manual," *Version: geant4*, vol. 9, no. 0, 2020.

Acronym list

BL	Beam Loading
RF	Radiofrequency
linac	Linear Accelerator
FCC	Future Circular Collider
CLIC	Compact Linear Collider
ILC	International Linear Collider
ESS	European Spallation Source
EM	Electromagnetic
TRL	Technology Readiness Level
CERN	European Organization for Nuclear Research
LHC	Large Hadron Collider
FEL	Free Electron Laser
ICS	Inverse Compton Scattering
CANS	Compact Accelerator-based Neutron Sources
TW	Travelling-wave
SW	Standing-wave
CLEAR	CERN Linear Electron Accelerator for Research
TM	Transverse Mode

PDE Partial Differential Equation

QS Quasi-static

GSL GNU Scientific Library

FFTW Fastest Fourier Transfor in the West

FFT Fast Fourier Transform

AS Accelerating Structures

PETS Power Extraction and Transfer Structures

HOMs High-Order Modes

CTF3 CLIC Test Facility 3

CALIFES Concept d'Accélérateur Linéaire pour Faisceau d'Electron Sonde

VESPER Very energetic Electron facility for Space Planetary Exploration missions in harsh Radiative environment

SEU Single Event Upset

BNCT Boron Neutron Capture Therapy

IFMIF DONES International Fusion Materials Irradiation Facility – Demo Oriented NEutron Source

HEP High Energy Physics

GDR Giant Dipole Resonance

QD Quasi-deuteron

HPCI High-Pulse-Current-Injector

PEDD Peak Energy Deposition Distribution

BBU Beam Breakup Instability

BPMs Beam Position Monitors

keV Kilo electron-volt

MeV Mega electron-volt

XFEL X-Ray Free-Electron Laser Facility

TULIP Turning Linac for Proton Therapy

SPS Super proton Synchrotron

HL-LHC High Luminosity Large Hadron Collider

PS Proton Synchrotron

HERA Hadron-Electron Ring Accelerator

FCC-hh Hadron-Hadron Future Circular Collider

FCC-ee Electron-Positron Future Circular Collider

LEP Large Electron-Positron Collider

PIP Proton Improvement Plan

AGS Alternating Gradient Synchrotron

HUNS Hokkaido University Neutron Source

RANS RIKEN Accelerator-driven compact Neutron Source

KUANS Kyoto University Accelerator based Neutron Source

LENS Low energy Neutron Source

CPHS Compact Pulsed Hadron Source

LENOS Legnaro Neutron Source Facility

UTCANS University of Tokio Compact Accelerator-based Neutron Source

HBS High Brilliance Source